ACOUSTIC EMISSION MONITORING OF PROPULSION SYSTEMS: A LABORATORY STUDY ON A SMALL GAS TURBINE

Mohamad Shadi Nashed

Submitted for the degree of doctor of philosophy on completion of research in the
School of Engineering and Physical Sciences, Mechanical Engineering,
Heriot-Watt University

November 2010

Abstract

The motivation of the work is to investigate a new, non-intrusive condition monitoring system for gas turbines with capabilities for earlier identification of any changes and the possibility of locating the source of the faults. This thesis documents experimental research conducted on a laboratory-scale gas turbine to assess the monitoring capabilities of Acoustic Emission (AE). In particular it focuses on understanding the AE behaviour of gas turbines under various normal and faulty running conditions.

A series of tests was performed with the turbine running normally, either idling or with load. Two abnormal running configurations were also instrumented in which the impeller was either prevented from rotation or removed entirely. With the help of demodulated resonance analysis and an ANN it was possible to identify two types of AE; a background broadband source which is associated with gas flow and flow resistance, and a set of spectral frequency peaks which are associated with reverberation in the exhaust and coupling between the alternator and the turbine.

A second series of experiments was carried out with an impeller which had been damaged by removal of the tips of some of the blades (two damaged blades and four damaged blades). The results show the potential capability of AE to identify gas turbine blade faults. The AE records showed two obvious indicators of blade faults, the first being that the energy in the AE signals becomes much higher and is distinctly periodic at higher speeds, and the second being the appearance of particular pulse patterns which can be characterized in the demodulated frequency domain.

Acknowledgments

Table of Contents

Lists of Tables

Lists of Figures

Nomenclature

α	Attenuation coefficient (dB/m)
γ	adiabatic index of gas
ρ	Density (kg/m^3)
σ	Standard deviation
A_i, A_{1i}, A_{2i}	Amplitude of AE signal (dB or V)
A_r	Relative amplitude (dB)
C	sound speed in gas (m/sec)
E	Energy content (V^2.s)
$E(x)$	Energy at distance, x (V^2.s)
E_o	Energy of the source (V^2.s)
F_{crit}	Variance within the group
F_{value}	Variance between the group
f	the reverberating frequency (Hz).
k	Attenuation factor or Attenuation coefficient (m^{-1})
$Kurt$	Kurtosis
M	molar mass in kilograms per mole
P1-P4	Sensor positions
R	molar gas constant (J·mol^{-1}·K^{-1})
rms	RMS energy at each window
$Skew$	Skewness
S1-9	Turbine running speed(RPS)
t	Time (s)
$v(t)$	Amplitude of signal (V)
Var	Variance
x	Distance (m)

Abbreviations

AE	Acoustic emission
ANN(s)	Artificial neural network(s)
CWT	Continuous wavelet transform
GG	Gas generator turbine
FFT	Fast Fourier Transform
FOD	Foreign object damage
FPT	Free power turbine
HCF	High cycle fatigue
ICA	Independent component analysis
LCF	Low cycle fatigue
MLP(s)	Multilayer perceptron(s)
NDT	Non-destructive testing
PNN	Probabilistic neural network
PCA	Principal component analysis
PSD	Power spectrum density
RMS, rms	Root mean square
SNR	Signal to noise ratio
SOM	Self-organising mapping
STFT	Short Time Fourier Transform
WDA	Wear Debris Analysis
WNG	White noise generator
WT	Wavelet transform
LGPA	linear gas path analysis
NLGPA	non-linear gas path analysis

Chapter 1 Introduction

This work relates to the condition monitoring of turbines using acoustic emission (AE). A small, laboratory-scale turbine has been instrumented using AE sensors and recordings made of the AE as a function of position on the machine for various normal operating conditions and fault conditions, as well as for some idealized conditions to understand the source of AE in the machine. This chapter introduces the technological background and significance of the work as well as presenting the motivation for the research.

1.1. Background to condition monitoring of gas turbines

The application of condition monitoring techniques to machinery allows earlier diagnosis and prompt repair of any malfunction and avoidance of breakdown caused by faulty components, which is its most critical use for process plant and machinery. Moreover, condition monitoring systems can be used to identify the machine condition in order to achieve economic performance through increased availability and reduced component replacement costs through predictive maintenance. Generally the main methods which have been developed for condition monitoring of gas turbines are performance analysis[1], oil analysis [2], and vibration analysis [3].

Performance analysis is widely used on rotating machines, and specifically on gas and steam turbines. Performance analysis is based on the idea that any deterioration in the machine will produce changes in the operating parameters from their ideal values [4]. The combination of performance analysis with other artificial intelligence techniques constitutes a good tool for providing information about the degradation severity of the machine components. One of the limitations is that measurement quality has a critical influence on the reliability of a performance analysis condition monitoring system, and most measured data are contaminated by sensor noise, disturbances, instrument degradation, and human error to a greater or lesser extent.

Wear Debris Analysis (WDA) involves examining the debris suspended in lubricating oil in order to predict machine condition [5]. One drawback of this technique is that it is inappropriate for certain machines and/or operations, such as electrical machinery and switch gear, which can be monitored by acoustic emission and ultrasonic techniques.

Another disadvantage of WDA is the difficulty of applying it to sealed systems where obtaining a sample of fluid is difficult and usually not recommended. A further demerit is the inability to identify the precise location of the fault and several faults from different components can cause confusion. Finally, the necessary analysis is normally performed in batches in a laboratory rendering it not particularly amenable to continuous or on-line monitoring. The most prominent advantage of WDA is that it directly diagnoses wear, which is not usually achievable economically using other techniques.

Vibration analysis [6] is one of the most widely applied condition monitoring techniques for rotating and reciprocating machines. Generally, vibration analysis starts by drawing a comparison between historical measurements and recent values using some kind of trending. A wide range of features are conventionally extracted from the recorded signals from the time domain, the frequency domain, and the quefrency domain [7]. Vibration signals are sensitive to low frequency environmental noise such as machine resonances or ancillary equipment. Although, the vibration method is indirect but it has the potential benefit of source location.

The above techniques including performance analysis, oil analysis, and vibration monitoring are all indirect in that they measure the changes in some aspect of the machine operation from which an attempt is made to deduce condition. Furthermore, these approaches are generally unable to give information about the exact locations of changes in the turbine. Acoustic Emission (AE) sources include impacts, wear, crack propagation and gas flow all of which can occur in gas turbine operation. As a non intrusive technique, AE has two potential advantages over other techniques; (a) its ability of early identification of any changes, (b) the potential to locate the source of the emission [8]. Acoustic emission (AE) has been used successfully for condition monitoring of machinery and has proven to be a useful tool for monitoring a number of rotating machinery types such as gas turbines, steam turbines, and pumps. Detailed reported examples include the diagnosis of faults on the inner and outer races of gas turbine bearings [9, 10], rubbing and bearing damage in a steam turbine [11], the transmissibility of acoustic emission across very large-scale turbine rotors[12], and detecting cavitation in pumps [13].

1.2. Aims and objectives:

Turbine engines are extremely difficult to monitor with high operating temperatures and huge centrifugal speeds and loads. They are subject to a range of failure mechanisms which might be expected to modify the flow through the machine. AE has been used successfully for machinery monitoring in lower speed rotating machines, reciprocating engines, bearings, fuel injection and combustion, where the fundamental sources are similar to those expected in a gas turbine. Therefore using AE to monitor gas turbine engines to enable classification of the operating parameters and fault diagnosis is the main aim of this research.

The detailed aims are therefore:
1. To understand the fundamental mechanisms generating AE signals in gas turbines.
2. To study the effect of operating conditions on AE signals and develop recognition approaches.
3. To identify potential benefits of AE monitoring over conventional turbine monitoring approaches.
4. To demonstrate the potential of AE technique for diagnosing gas turbine blade defects.

To pursue these aims, the following objectives were set:
1. Calibrate AE sensors on a standard steel block and on gas turbine rig.
2. Study AE propagation characteristics in the gas turbine rig.
3. Categorize the AE signatures under various normal running conditions of the gas turbine.
4. Understand and explain the complex AE behavior of gas turbine during normal operation.
5. Simulate various blade defects and characterize the AE signature in time and frequency domains.

1.3. Thesis outline

This thesis is organized in 7 chapters, the contents of which are summarized as follows.

Chapter 1: Introduction

This chapter introduces the general background of condition monitoring of gas turbines and the place of AE monitoring in this context. The objectives of the research and the claimed contribution to knowledge are also identified.

Chapter 2: Literature review

This chapter describes the general physics of AE wave propagation including wave types, wave propagation speed, effects of AE wave attenuation, AE sensor calibration procedures, and AE analysis techniques in the time and frequency domains. The main part of the chapter is a critical review of condition monitoring methods on gas turbines and other machinery with emphasis on the advanced diagnostic methods used for fault monitoring of gas turbines. The AE application with advanced diagnostic methods on gas turbine has been reviewed in this chapter. A summary of common gas turbine faults is also included in this chapter.

Chapter 3: Experimental apparatus and procedures

This chapter describes the experimental apparatus, data acquisition methods, experimental set-up and experimental procedure for the laboratory tests of AE calibration on steel block, AE calibration on the gas turbine, AE propagation on the gas turbine, as well as monitoring the gas turbine under various operating conditions with and without simulated impeller faults. The results of the calibrations and attenuation tests are also summarized here.

Chapter 4: Results: normal running tests and tests without functioning impeller

This chapter shows the results of simple time- and frequency-domain analyses of four different test configurations; idling with the speed being controlled by fuel and air flow, or under load at fixed fuel and air flow as well as two abnormal running tests in which the impeller was either prevented from rotating or removed entirely.

Chapter 5: Analysis and discussion of normal running tests

This chapter extends the preliminary analysis of chapter 4 in order to explain the complex AE behavior in the gas turbine for the idling and load tests. Pattern recognition

techniques using artificial neural networks have been applied to aid the understanding of the characteristics of AE behaviour of gas turbine.

Chapter 6: Faulty impeller condition monitoring tests

The results of the tests conducted on with a faulty free power turbine are described in this chapter. These are analysed using time- and frequency-domain processing to indicate how pulse train analysis can be used to track blade faults in turbines.

Chapter 7: Conclusions and future work

The main findings and achievements of this research are detailed here along with recommendations for possible future studies.

1.4. Original contribution

The overall outcome of improved monitoring capabilities of gas turbine processes based upon analysis of AE signals is the specific area in which a contribution to knowledge is claimed. As far as the author is aware, detailed study on the complex pattern recognition of acoustic emission from gas turbines using artificial neural network has not previously been attempted. Furthermore, the study has developed and used a technique based on the demodulated frequency analysis to diagnose gas turbine blade faults. Some success is claimed also in identifying the fluid-mechanical sources of the AE in turbines which is of generic interest to turbine and machinery monitoring.

Chapter 2 Literature Review

2.1. Introduction:

This chapter aims at providing a summary of the state of knowledge of the areas relevant to the condition monitoring of gas turbines using AE. Condition monitoring is here considered to be any tool for providing an assessment of machinery condition based on collecting sensor data, and interpreting it with regard to any deterioration that could affect machine life. A successful monitoring system will have the potential to minimise the cost of maintenance, improve operational safety, and reduce the incidence of in-service machine failure or breakdown.

The review is divided into six parts, commencing with an outline of how engineering AE measurements are made, followed by a critical discussion of the conventional analysis approaches. Next the role of other condition monitoring techniques such as vibration monitoring, performance analysis, and oil analysis in gas turbines is evaluated in preparation for a comparison of their strengths and weaknesses compared with what is currently known about AE monitoring of turbines. In view of its relevance to this work, a summary of the use of artificial neural networks in condition monitoring is provided. Finally in this chapter, the range of commonly-encountered gas turbine faults is explained with a view to identifying those which might reasonably be monitored using AE.

2.2. Acoustic emission measurements:

The term acoustic emission (AE) is normally reserved to describe high frequency stress waves generated on the surface or within a material. The stress wave propagates in, or on, the material and can be detected externally by mounting a sensor on an appropriate surface. The degree to which one or more sensors can be used to determine the characteristics of the source depends on a number of factors, such as AE wave propagation, AE attenuation, and AE sensor calibration, as well as a number of practical issues, all of which are discussed in this section.

2.2.1. AE sources and waves:

Sources of AE can be categorized as fundamental material sources and pseudo sources[14]. Crack growth, slip, twinning and phase transformation are examples of the first type, while pseudo sources include phenomena which give rise to the fundamental sources, such as leaks [15], mechanical impact [16], sliding contact, turbulent fluid flow, fluid cavitation [17], wear and friction[18]. Apart from crack growth, all of the sources of potential interest in turbines are in the latter category and this is common to most machinery monitoring applications.

AE sources can also be categorized depending on the type of signals they produce, which can be either discrete or continuous. A single burst of energy produced by a fracture or an impact leads to a discrete signal, whereas sources occurring rapidly to the extent that they overlap in time and/or continuous sources lead to a continuous or quasi-continuous signal. Examples of the latter are the AE signals associated with such phenomena as fluid flow, fluid leaks, some chemical processes and sleeve bearings.

AE sources can further be categorised in terms of how they are stimulated, (a) structural testing where a load is applied for the purpose of inspection, (b) process monitoring, for example of machines such as engines, turbines and rotating machines, (c) materials testing where the AE is used as a diagnostic of material behavior.

In the monitoring application, AE can be regarded as passive ultrasound, i.e. the AE events are self-generated and the recorded ultrasound is not the result of a pulse or wave injected into the component as occurs in ultrasonic non-destructive testing. One of the oft-cited advantages of AE is its ability to reveal faults at an early stage, giving an opportunity for intervention before sudden failure [19]. The reason this is essentially that AE is generally sensitive to the processes that cause degradation as opposed to the symptoms of degradation having occurred, one example being that AE can detect bearing wear processes as opposed to, say, acceleration monitoring which might be more sensitive to the looseness arising from excessive wear having occurred.

When an AE signal is generated by a source, the stress waves (approximate frequency range of 100 kHz to 1.2 MHz) radiate and propagate to the boundaries of the structure where they may be dissipated or reflected back into the structure, depending on the

nature of the structure, particularly the material and the size and shape. At any point on a surface, arriving waves may have suffered refraction, scattering, and attenuation [20] and may have been reflected once or more from boundaries, all of which makes interpretation difficult.

AE waves propagate in solid media in one or more of four classes: longitudinal waves, shear waves, Rayleigh waves and Lamb waves [21, 22]. The wave modes [23] constitute a complete orthogonal set of eigenfunctions, which is to say that each one propagates independently without losing energy to the other. Longitudinal and shear waves are plane waves and are the only ones which propagate in infinite media. The particle movement in the longitudinal wave in isotropic materials is parallel to the direction of wave propagation but in shear waves it is perpendicular (Figure 1.1). Longitudinal waves are faster than shear waves because the elastic modulus is greater with that kind of deformation. Rayleigh waves propagate in media considered to be semi-infinite and require a free surface. The velocity is a little lower than a shear wave and the particles move in ellipses. Lamb waves are plane waves in an infinite medium and the particles move in ellipses during its propagation [22]. The Lamb wave velocity varies with frequency, a phenomenon known as velocity dispersion [21, 22, 24]. There are two families of Lamb waves which are essentially coupled surface waves, symmetric (often called extensional waves) (s_0) and asymmetric (often called flexural waves) (a_0). Both wave modes propagate at various speeds, which are dependent on both frequency and plate thickness. The extensional mode has a lower amplitude than the flexural component and occurs as a small amplitude precursor to the larger flexural wave. In practical situations, the AE energy is carried in one or more mode and each mode can be converted to another at a boundary. It is not common to treat AE waves as pure modes and, for many applications (including the current one), the AE can be treated as a packet of mixed frequency propagating at a specific group velocity.
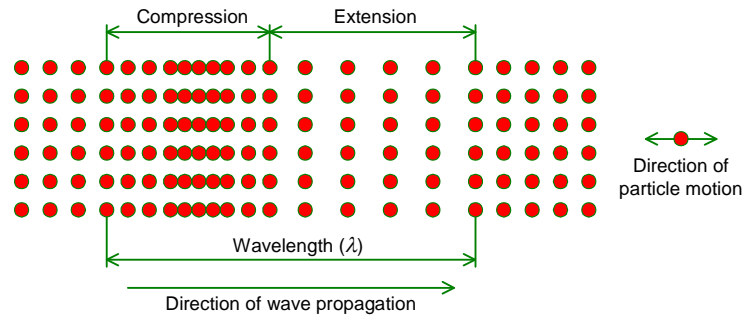
(a) Dilatational wave (Longitudinal wave)
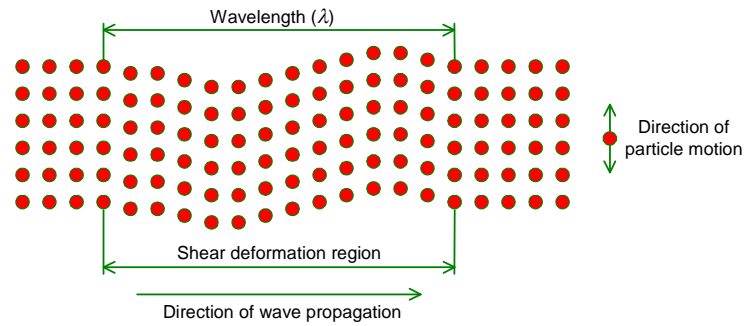
(b) Distortional wave (Shear wave)
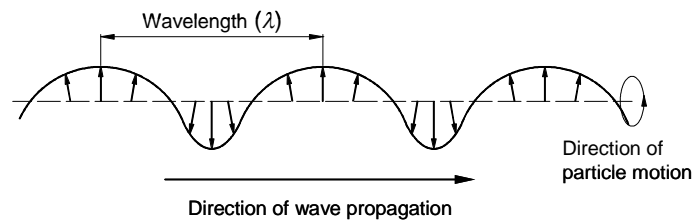
(c) Rayleigh wave or surface wave

Figure 2. 1: The main wave types: dilatational wave, and distortional wave and Rayleigh wave (or surface wave).

2.2.2. Attenuation:

AE waves are subject to attenuation during their propagation inside a material [14, 25, 26], which manifests itself as a loss of amplitude as a wave propagates. There are four main mechanisms of attenuation:

- Geometric spreading of the wave with constant energy whereby the amplitude of the wave decreases with increasing distance from the source
- Wave dispersion, in which the shape of the pulse changes as it propagates
- Scattering and diffraction which are manifest as a decrease in amplitude when waves encounter medium boundaries such as holes, slots, cavitation bubbles,

inclusions and cracks. Scattering occurs when the AE waves propagate through the finite void or inclusion, while diffraction occurs when AE waves propagate at edges, whereas some of the energy of the propagated wave through these boundaries will scatter or diffract.

- Internal friction, which is due to the damping capacity of the material itself [27, 28]. Internal friction dominates [22] the attenuation in the far field and can be described by an exponential relationship for amplitude with distance, giving much steeper attenuation close to the source. In plates and shells, the transition distance at which internal friction starts to dominate over geometric spreading is given by 4.34/ α, where α is a (measured) attenuation factor (dB/m) [22].

Graham and Alers [29] have measured attenuation of AE waves on various structures such as steel, aluminum and alumina ceramic plates, and a large pressure vessel using a white noise generator (WNG) as an AE source. The AE signals were acquired at various distances from the source then the loss in amplitude as a function of distance was obtained using equation 2.2. They found that attenuation on the large pressure vessel follows the expected form for geometrical spreading and varies with 1/ r in the near-field zone. In the far-field zone, the attenuation of the signal is caused by absorption with a limited amount of dispersion. Holford and Carter [27], working with long, structural steel I-beams, found that the attenuation of waves was sharpest in the near-field zone at around 10 dB over 0.5 m (20 dB/m) and lower for longer source-sensor distances (1 dB/m). They attributed the higher attenuation in the near-field zone to geometric spreading, and that in the far-field zone to absorption or conversion of AE wave energy into heat. Prosser [30] found that the larger effect on the flexural waves on a graphite/epoxy composite plate were attenuated more than extensional waves and attributed the greater attenuation to dispersion. McIntire [14] used a simple power law to describe AE attenuation in steel tubes:

$$A = A_0 x^{\alpha} \qquad\qquad (2.1)$$

Where A is the signal amplitude at a distance, x, from the source and A_0 is the amplitude of the source. He found that the exponent, α, for steel tube of 150 mm diameter was for 8.1 dB/m the near field and 1.9 dB/m for the far field. Shehadeh et al [31] estimated automatically the arrival times of two AE components, a fast and a slow component, using an array of sensors on a steel pipe. Their technique relied upon the balance of high- and low-frequency components of the signal as a function of time to determine

arrival time. They applied three techniques i.e. cross correlation, wavelet transform, filtering technique, and found that the best technique was cross correlation which located the source with error less than 3%.

2.2.3. AE sensors and sensor calibration:

Acoustic emission (AE) is a passive non-destructive testing (NDT) technique that has been used widely since the 1970s. Generally the stress wave arrives at the sensor at a frequency in the approximate range of 100 kHz to 1.2 MHz with surface elevations in the nm range. AE sensors [32] are mechanical-electrical transducers which convert this mechanical disturbance to an electrical signal, and, in this sense, the measurement is indirect. Furthermore, the AE signal measured at the sensor will be influenced by the sensor's response to the forcing transient waves, which is, in turn, influenced by the sensor construction, including the piezoelectric properties of the sensing element as well as its size, shape and backing, which govern the amplitude sensitivity and associated self-resonance. As well as this, the propagation path from source to sensor and the nature of the coupling between the sensor and the surface will affect what is recorded.

The successful use of piezoelectric AE sensors in industry over other transduction technologies such as capacitive, electromagnetic and laser-optical measurement comes from the fact that AE sensors have proven to be sufficiently sensitive and robust to be used in a variety of environments. The material most often used for the active element in piezoelectric AE sensors is lead zirconate titanate (PZT), although it has been shown that other piezo-active materials such as quartz and even polymers like polyvinylidene diflouride (PVDF) are equally feasible [33]. Figure 2.2 shows a schematic diagram of a typical AE sensor. For AE sensors, there is always a compromise between bandwidth and sensitivity, i.e. when the bandwidth of the application is known to be narrow then a higher sensitivity can be achieved by adjusting the geometry of the piezoelectric element. However, if a broad bandwidth is needed such as for machinery monitoring, the sensitivity of the sensor over the range will be lower. Commercial AE sensors are sensitive to frequencies above 100 kHz, whereas resonant sensors in the region of 150 kHz to 300 kHz are probably the most widely used in AE applications. The highest frequencies likely to be of interest to users of AE transducers are in the range of 800 kHz to 1.2 MHz and transducers with bandwidths which extend above this range are not normally used. Analogue band-pass filters are essential with AE systems to ensure that electronic

noise outside the frequency range of interest is kept to a minimum. Another essential component for AE systems is pre-amplification which is provided either integrally to the sensor or very close to it using a separate pre-amplifier.
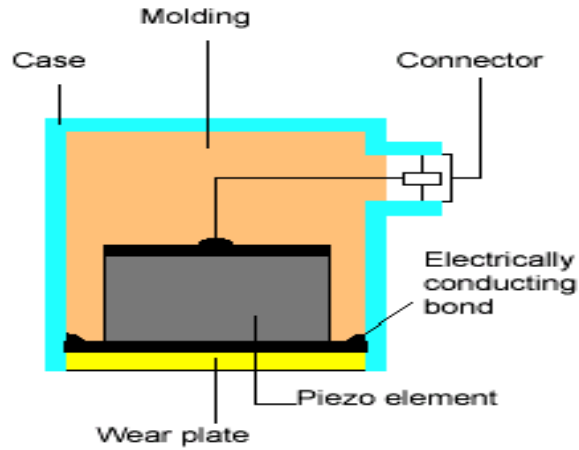
Figure 2. 2: Schematic of an AE sensor, from Vallen [34].

The main limitation to the application of piezoelectric AE sensors is that they do not give an absolute measurement of stress wave amplitude, unlike capacitive or laser-based measurements. Although this disadvantage is somewhat unavoidable, it is tolerable, since these sensors present the most practical means of measuring emissions and a certain degree of calibration is possible, for examples against standardised sources or machine running conditions. Nevertheless, the lack of a universally accepted and applied method of signal calibration means that the direct quantitative comparison of test results obtained from different detection systems is highly questionable. Some "standard" sources, such as pencil-lead breaks, glass capillary breaks and helium gas jets [32, 35], are used to give a kind of calibration, although they are actually more often used to check the functioning of the AE detection system and to confirm the quality of sensor coupling. A further use for these reproducible sources is to investigate AE propagation in structures, in which case the acquired signals need normalization of the source energy.

Calibration, as defined by international standards (BSI, 1995) is "*a set of operations that establish, under specified conditions, the relationship between values of quantities indicated by a measuring instrument or measuring system, or values represented by a material measure or a reference material, and the corresponding values realized by standards*". Using a large steel block with a pencil lead break source can provide a way of characterizing a sensor reproducibly and discriminatingly that is low cost, and provides a

very simple calibration [36]. Such a test can confirm the uniformity of a set of nominally identical sensors used in a given lab or provide a cross-calibration between different sensors used for the same task. If carefully specified, the test can also be used to compare AE data from different tests in different laboratories, using different instrumentation.

2.2.4. Practical implications of AE monitoring of machinery:

In general, the structures of machines such as gas turbines will consist of a number of parts of varying geometric complexity, some joints and other features, such as webs and welds. In addition, the internal surfaces may be in contact with oil or hot gases. AE wave propagation will therefore be much more complex than simpler plate- and block-like structures. Some authors such as Miller and McIntire[14], Pollock [22] and Kolsky [37], have suggested an approach to studying the attenuation in such complex structures by acquiring AE signals at different positions relative to a source. Thereafter, the attenuation is described by using peak amplitude and a logarithmic relative amplitude scale, (A_r) [22, 27, 29] :

$$A_r = 20.\log\left(\frac{A_i}{A_0}\right) \qquad (2.2)$$

where A_i is the maximum signal amplitude (V) at a receiver sensor at distance x from the source, and A_0 is the maximum signal amplitude (V) at the source position.

The amplitudes can be measured in volts provided that the amplifiers are consistently calibrated. Then, wave attenuation can be determined from a plot of the relative amplitude versus distance and can be expressed as decibels per unit distance [14], determined by:

$$\alpha = \frac{20}{x}.\log\left(\frac{A_2}{A_1}\right) = \frac{A_r}{x} \qquad (2.3)$$

where α is attenuation coefficient (dB/m)

A_1 is amplitude of signal at a position P1 (V)

A_2 is amplitude of signal at a position P2 (V) and;

x is distance between P1 and P2 (m)

In this work, a similar approach is used, where the energy of the AE signal can be calculated simply by integrating the square of the amplitude over a fixed time, t, as follows:

$$E = \int_0^t v^2(t)dt \qquad (2.4)$$

where $v(t)$ is the amplitude of the AE waveform in volts (V); t is time in seconds (s); E is acoustic emission energy in V².s.

In a semi-infinite medium, the acoustic emission energy can be considered to be lost as the wave travels according to a simple absorption law:

$$E(x) = E_o e^{-kx} \qquad (2.5)$$

where $E(x)$ is acoustic emission energy at distance x from the source (V².s);

   E_0 is the energy of the source (V².s);

   k is an attenuation factor (m^{-1});

and x is the source-sensor distance (m)

Figure 2.3 shows an example of the amplitude attenuation of two sensors on the turbine rig, where the distance between two sensors is 450 mm.
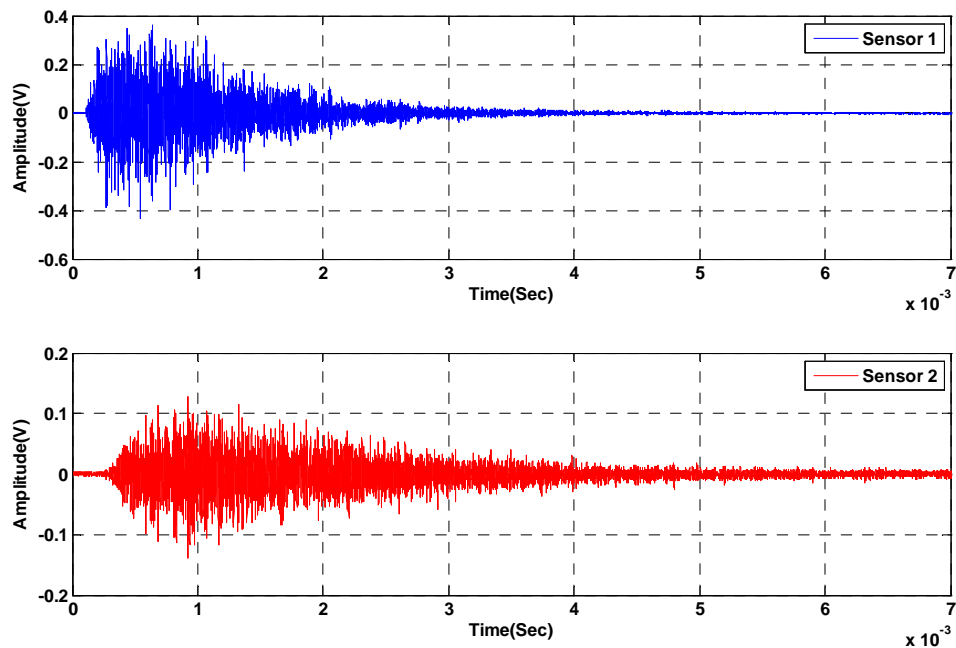
Figure 2. 3: Attenuation example of AE signal on turbine rig.

A few investigators have studied attenuation on machinery structures where interfaces play a more important part. Mba and Hall [12] have measured the attenuation on a large industrial gas turbine and suggested that AE could detect rubbing in the turbine at sensor positions up to 2 m from the source and AE may be detectable on the bearing housing. Nivesrangsan *et al* [38, 39] studied the attenuation and AE propagation on diesel engines and a number of simpler objects (Figure 2.4) and found that the attenuation increases with distance from the source and that more complicated transmission paths and geometries give higher attenuation factors. In structures of small extent, such as a strip of dimensions 58×483×5 mm more "reverberant" wave field resulted with very low attenuation. These authors used equation 2.5 and measured attenuation factors, *k*, to be typically around 8 to 12 for a small (road-going freight vehicle) engine block and around 2 for a very large marine engine structure (10 MW) used for district power generation. Finally, the attenuation of the small engine with water in the cooling galleries was slightly higher than without water which leads to the conclusion that the added water increases the losses from the structure when waves encounter interfaces, but that dominant transmission paths remain through the cast iron structure of the engine block.
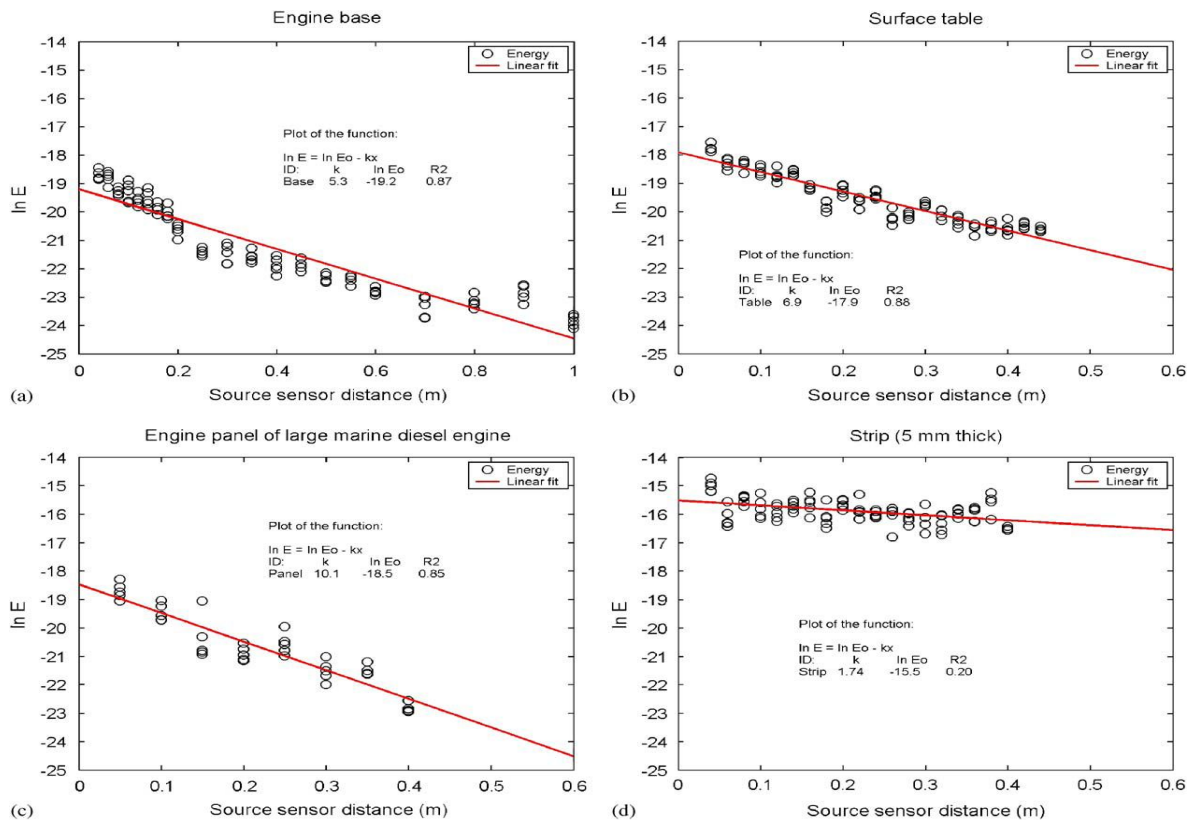
Figure 2. 4: Examples of attenuation characteristics on various cast iron structures (from Nivesrangsan *et al* [38, 39]).

2.3. Acoustic emission analysis techniques:

For processing purposes, it is conventional to class AE signals as of burst type or continuous type, although some acknowledge a mixture of the two. In the first kind, the signal consists of clearly defined 'events' characterized by amplitudes significantly larger than the background level, while the continuous kind occurs when burst generation is so rapid that the resolution of individual events is not possible. Obviously, this basic distinction has a fundamental bearing on the type of analysis that is used.

The analysis technique used can also depend on the application itself. For some applications statistical time domain analysis to extract time-based features is sufficient, while, for other applications, frequency domain analysis is needed. In some cases simple time and frequency domain analysis is not adequate requiring the use of higher-level analysis techniques such as artificial neural networks, fuzzy logic and expert systems.

2.3.1. AE features and extraction:

Extracting time features from raw AE signals is considered a first level of signal processing. Normally, time features are used to describe characteristics of time series data from random, stationary, ergodic and continuous processes. Table 2.1 summarises a typical set of time-based features that might be used for continuous signals.

Feature	Summary description
Maximum value (x_{max})	- Indicates the maximum value of discrete time series data
Minimum value (x_{min})	- Indicates the minimum value of discrete time series data
Mean value ($\bar{x}$) or the first moment of amplitude distribution function $$\bar{x} = \frac{1}{N}\sum_{i=1}^{N} x_i \qquad (2.6)$$ where N is the number of data points; and x_i is the data at each discrete point in time.	- Measures the central distribution of discrete time series data.
Root mean square (RMS) value $$rms = \sqrt{\frac{\sum_{i=1}^{N} x_i^2}{N}} \qquad (2.7)$$	- Measures square root of mean square in discrete time series data. - Indicates energy contained in continuous AE data.
Variance (Var) or the second moment of the amplitude distribution function. $$Var = \sigma^2 = \frac{1}{N}\sum_{i=1}^{N}[x_i - \bar{x}]^2 \qquad (2.8)$$	- Indicates the spread or dispersion or distribution of discrete time series data.
Standard deviation (σ) $$\sigma = \sqrt{\frac{1}{N}\sum_{i=1}^{N}[x_i - \bar{x}]^2} \qquad (2.9)$$	- Indicates the spread or dispersion or distribution of discrete time series data.
Skewness ($Skew$) or the third moment of amplitude distribution function $$Skew = \frac{1}{N}\sum_{i=1}^{N}\left[\frac{x_i - \bar{x}}{\sigma}\right]^3 \qquad (2.10)$$	- Measures the lack of symmetry of distribution of discrete time series data. - $Skew = 0$ represents normal distribution - For, $Skew < 0$ the left tail of distribution is heavier than the right tail and opposite for. $Skew > 0$
Kurtosis ($Kurt$) or the fourth moment of amplitude distribution function. $$Kurt = \frac{1}{N}\sum_{i=1}^{N}\left[\frac{x_i - \bar{x}}{\sigma}\right]^4 - 3 \qquad (2.11)$$	- Measures the degree of peakedness of distribution of discrete time series data. - $Kurt > 0$ represents a peaked distribution. - $Kurt < 0$ represents a flat distribution. - $Kurt = 0$ represents normal distribution.

Table 2. 1: Summary of typical statistical parameters used for continuous signals

For discontinuous (burst) signals, a specific set of features have evolved. These include:

- the AE event count, which is the number of times that the burst signal crosses a preset threshold

- the AE event rate, which is the time rate at which AE event counts occur

- the AE count or ringdown count is the number of times the burst signal amplitude exceeds the preset threshold

- the count rate, which is the number of AE counts per unit time
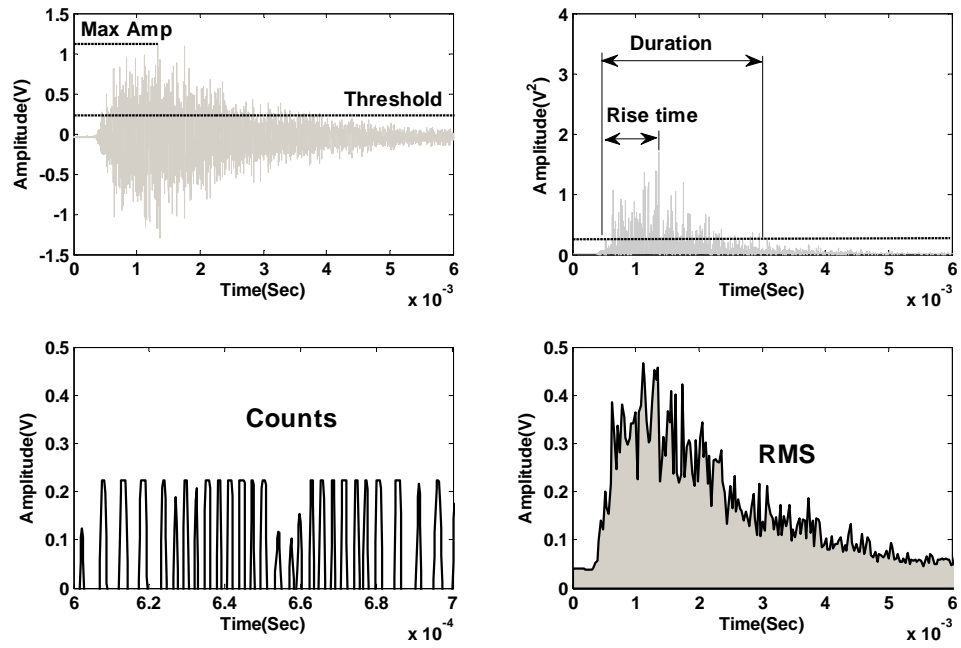
Figure 2. 5: Typical time domain features of AE signals

Frequency analysis depends on decomposing the time series signal into the frequency domain., most commonly done using a Fast Fourier Transform (FFT) algorithm [40]. The FFT algorithm can be used to estimate the distribution of the signal energy in the frequency domain, using the Power Spectral Density (PSD) and Welch's PSD estimate [41]. Frequency analysis can be used in machinery fault diagnosis as part of an approach which uses known repeat times to filter out effects, such as running speed, and resonance, from those of unknown origin for normal and faulty conditions. Furthermore, some sources of AE can be masked by noise and filtering can again be used to separate the noise from the signal, thus enhancing the signal-to-noise ratio. Dealing with non-stationary signals, such as AE, where frequency can vary substantially with time, techniques such as the Short Time Fourier Transform (STFT),which combines time and frequency analysis, can be used [42]. This implements the FFT algorithm at time increments throughout the signal using a sliding window approach. Other methods for time-frequency analysis include wavelet decomposition [43-46]. The wavelet transform is a powerful method that analyses the signal using multi-scaling where the resolution of time and frequency vary in the time-frequency plane. Longer time intervals give more precise low frequency information and shorter time intervals give high frequency information. Therefore, a high resolution of time frequency representation can be obtained[46].

One further application of the FFT of particular use for rotating machinery is called demodulated resonance analysis [47]. The technique involves averaging the signal to reveal

lower frequencies in the envelope of the signal in a similar way to AM radio, where the AE wave acts as a carrier frequency for the lower frequency information, Figure 2.6.
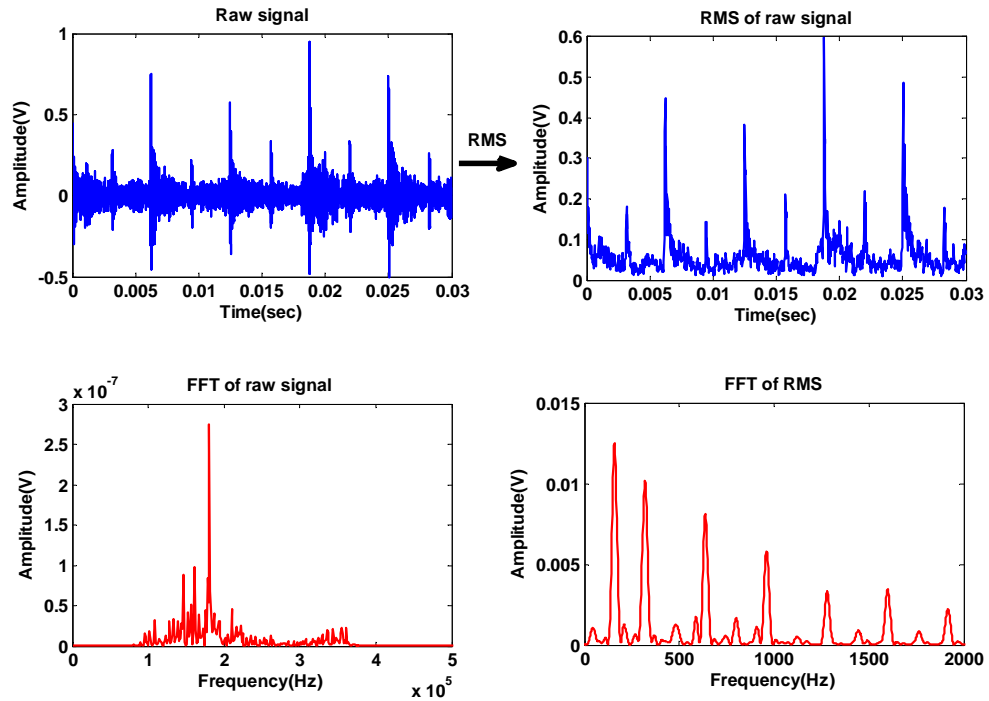
Figure 2. 6: Demodulation of a lower-frequency signal by taking the envelope of the raw AE.

2.3.2. Pattern recognition:

Pattern recognition is "the act of taking in raw data and taking an action based on the category of the pattern"[48]. The sensor type(s), feature extraction mechanism, and classification scheme are the main components of a pattern recognition system, in that the sensors are normally the main source of observations and sensor data is transferred to the feature extraction mechanism to describe the essential elements of the data. The final stage depends on the classification scheme which organizes the features into clusters using a classification algorithm.

The normal statistical approaches to AE analysis are helpful in many cases, but can become unwieldy for complex pattern recognition cases such as for generic or real time monitoring requirements involving large amounts of data and adaptability to new situations. Pattern recognition therefore forms the basis of machine intelligence and AE, with its sensitivity to a wide range of physical phenomena, can clearly play a major role there.

Because of the high sampling rates and consequently high time resolution, AE monitoring normally generates a large set of data. To handle the data, it is therefore

helpful to use some form of data reduction to prepare the variables for further statistical classification and diagnostic algorithms. Principal component analysis (PCA) [49, 50], is one such higher-level statistical analysis technique, involving a mathematical procedure that transforms a number of (possibly) correlated variables into a (smaller) number of uncorrelated variables called *principal components* in order to identify new meaningful underlying variables and to reduce the dimensionality of the data.

An extension of the PCA technique is Independent Component Analysis (ICA), which is also a higher statistical technique mainly used for decomposing a complex dataset into independent sub-parts [51, 52]. In other words, it is a signal isolation technique which works by assuming that the source signals are non-Gaussian, statistically independent and hidden under the main signal. ICA is suitable for many fields, including digital images, document databases, economic indicators and signal processing. It helps provide good representation of multivariate data for reasons of computational and conceptual simplicity.

Fuzzy logic [53] is an approach which simulates the human capability of imprecise reasoning by providing a remarkably simple way to draw definite conclusions from vague, ambiguous or imprecise information. It is very effective for the complex nature of mechanical condition monitoring systems. Fuzzy logic [54] systems usually consist of a fuzzifier, which maps crisp input numbers into fuzzy groups characterized by linguistic variables and membership functions, an inference engine which decides the way in which the fuzzy sets are combined, and a defuzzifier which produces a scholar number into the output of the fuzzy logic system. Fuzzy logic demonstrates a good ability to simulate the human imprecise reasoning [55], but it involves time-consuming processing of the data and so is often combined with other techniques such as expert systems, genetic algorithms, and neural networks to achieve good monitoring and fault diagnostic systems. Neuro-Fuzzy networks accomplish this need by combining fuzzy logic system with neural networks to combine the advantages of fuzzy logic with the learning and adaptation capabilities of neural networks.

An expert system is a computer program, normally categorized as a type of artificial intelligence, which performs functions similarly to a human expert [56, 57]. Building any expert system needs a knowledge engineer or "knowledge base", a coding system to translate how human experts make decisions into a simpler computer programming

language, and the user interface. The declaration of a fault by the coding system is normally done by comparing engine component deviations with predefined thresholds in the knowledge base. There are many types of expert systems such as case-based, modal-based, and rule-based, which is considered the most popular system. Expert systems have been used as a diagnostic tool for many kinds of aero-engines such as the T53 and TF-34 jet engines, and twin engine gas turbines from a helicopter [58, 59]. Doel [60] concluded that expert system technologies were not going to make jet engine diagnostic and maintenance procedures 'smart', but they could add a lot of new capability that will make them more effective and more convenient. A recent development of expert systems is a hybrid version where probability theory, fuzzy logic, and belief functions are used to increase the diagnostic accuracy of the system [61].

An Artificial Neural Network (ANN) is a mathematical model that is inspired by the biological nervous system. Neural networks are structured in layers of interconnecting processing elements (neurons), with the behavior of the network being determined by the weights associated with each connection. These weights can be adaptively trained using example signals to associate a particular input pattern to an output classification. In other words [62] an artificial neural network is actually a massively parallel distributed processor made up of simple processing units (neurons), which have a natural propensity for storing experimental knowledge and making it available for use. Artificial neural networks generally can be classified into two kinds: supervised and unsupervised neural networks. Feed-Forward-Back-Propagation Networks [57] are considered to be the most popular type of supervised neural network where the information propagates from input to output while calculated errors propagate in the opposite direction. In supervised neural networks a set of inputs (x) and outputs (y) are used to build a function that matches the input with the output using iterative training. Next the trained network, with the weights of its neurons adjusted to recognize the output vector, is used to predict the value of the output for any valid new input vector. Normally the training is validated tested against a set of "unseen" training data. Unsupervised neural networks work with an input only to find patterns in data, and classify it into clusters. The most popular learning method for unsupervised neural networks is the competitive method, which consists of two phases, the first of which identifies the winner neurons while the second updates the connection weights of the winner neurons. For engine diagnostics the main unsupervised neural networks used

are; probabilistic neural networks PNN, self-organizing maps SOM, and learning vector quantization LVQ. PNNs [63] classify the training patterns to classes and, when an unknown pattern is input to the network, calculate the Euclidean distances between the stored pattern and input pattern and then convert them, depending on the density function, where the smallest distance has the highest probability and *vice versa*. PNN application is suitable for smooth classification problems. In an SOM [4], the network is like a lattice with the neurons located at its nodes. The statistical features of input patterns and the spatial locations of the neurons determine the tuned neurons. Then these neurons will form a topographic map for the input patterns. The main application of SOMs is for initial pattern clustering to identify similar patterns. LVQ networks [64] consist of Voronoi cells, which are parts of the input space, and Voronoi vectors which define the point to the cells. The learning operation is done by comparing the input vector with the Voronoi vector and, if they do not agree, the Voronoi vector is changed. The application of LVQ is mainly on pattern recognition, multi-class classification and data compression tasks .The main benefits of artificial neural networks [65] comes firstly from their ability to handle a massive amount of data in a short period of time which makes them very useful for real time analysis, and, secondly, their ability to learn and therefore generalize which confers the capability to solve complex problems. These characteristics make ANNs suitable for many applications such as: (a) function approximation, including time series prediction [66], (b) classification, including pattern and sequence recognition [67], (c) data processing including filtering [68], and (d) robotics, including computer numerical control [69].

Not all of the above-mentioned advanced techniques are likely to be suitable for and the particular application in hand. Because of the complexity and non-linearity of AE signals emanating from gas turbines, PCA and ICA are unlikely to be suitable. Fuzzy logic technique would be inappropriate on its own for pattern recognition, unless it is combined with artificial neural networks. The remaining techniques, artificial neural networks and expert systems, are reasonable candidates. Ideally, in this work, we seek a generic technique which does not only carry out straight statistical correlation of data against a condition, but also is informed by mechanical engineering knowledge of gas turbines. This dictates an analysis technique which is effectively a combination between an expert system and an ANN.

2.4. Condition monitoring and diagnostic systems:

Condition monitoring as defined in International Standards as [70] *"Detection and collection of information and data that indicate the state of a machine"*. The application of condition monitoring techniques allows earlier diagnosis and prompt repair of any malfunction and avoidance of breakdown caused by faulty components, which is at its most critical for process plant and machinery. Conventional monitoring and fault diagnosis is based on the experience and background knowledge of operators/technicians and is relatively time-consuming, prone to error and usually results in extended downtime while symptoms are investigated, thus reducing productivity and increasing operational cost. Condition monitoring, performance monitoring, and diagnostics are the key areas of development in modern automated systems offering continuous improvement in machinery reliability. Modern, automated diagnostic systems built on artificial intelligence principles implement intrusive and non-intrusive sensors to provide a range of on-line information including complex time series signals such as accelerations acoustic emission alongside more conventional and less rapidly changing signals, such as temperature, pressure and speed in order to identify the machine condition and process or operating parameters. The main general methods which are established for condition monitoring are performance analysis [1], oil analysis [2], and vibration analysis [3]. The current work complements vibration analysis using AE signals to give diagnostic information over and above that which might be obtained from acceleration.

Wear Debris Analysis (WDA) is a type of oil analysis which involves a careful check of any debris suspended in lubricating oil in order to predict machine condition [5]. To achieve reliable diagnosis of machine condition five features of the debris are usually measured, size, quantity, size distribution, shape, and composition. Each feature has a distinct machine health diagnosis capability. One of the drawbacks of this technique is that it cannot be applied to some machinery, for example electrical machinery and switchgear, although these can be monitored by acoustic emission and ultrasonic techniques. Another disadvantage of WDA is the difficulty of applying it to the monitoring of sealed systems where obtaining a sample for analysis can be difficult and is sometimes not recommended. A further demerit of this analysis is the inability to identify the precise location of the fault and the possibility that debris from several faults may end up in the analysis. The most significant advantage of WDA is the ability

to obtain information not easily gathered by other means, for example on rubbing wear, cutting wear, rolling fatigue, sliding wear and from combined rolling and sliding wear.

Performance analysis is a condition monitoring technique widely used on rotating machines, specifically on gas and steam turbines. The technique is based on the idea that any deterioration in the machine will produce changes in the performance parameters, such as temperature, pressure, rotational speed, and flow rate, from their ideal values. The decrement in performance reflected from these measurements can then be used to detect, isolate, and, in some cases, accommodate faults. Performance analysis can be used in combination with other artificial intelligence techniques to provide information on the severity of any degradation of the machine or its components. One of the limitations of the technique is that its performance is affected substantially by the quality of the measurements, since any measured data can be contaminated by sensor noise, disturbances, instrument degradation, and human error. Initial applications of the technique usually assume that the relationship between the various machine measurable parameter deviations, such as gas path pressures and temperatures, thrust, mass flow rate, and so on, and immeasurable component parameter deviations, such as pressure ratio, flow capacity, and efficiency at each component is linear over certain operating conditions, such as maximum power or cruise. This approach is called the linear model method [71] and is simple, quick and easy to apply, and can help to isolate and quantify faults. On the other hand, it requires the application of several conditions that are difficult to satisfy such as an accurate influence coefficient matrix to describe the engine performance, fault- and noise-free sensors, uncorrelated measurements, and correct choice of measurement locations.

Developments of the performance analysis technique [72], include its combination with genetic algorithms to allow the use of fewer machine measured parameters compared to unknown parameters and non-linear machine behavior. Another successful development of performance analysis has been its combination with artificial neural networks, both supervised and unsupervised. Supervised ANNs (Feed-Forward Back-Propagation) have, for example, been used to filter out measurement noise in order to improve input data quality[73], and unsupervised neural networks as a tool for fault pattern recognition and fault classification [63, 74]. The combination of ANNs with performance analysis does have some limitations, however, such as the inability to perform well when dealing with new data outside the range of training,, a relatively long training time, and the

possibility of the ANN freezing with the consequent need to retrain the network. A further development of performance analysis is as a troubleshooting aid in expert system applications [56, 57] which makes machine diagnostic procedures not only sensor-based but also more effective and convenient.

Vibration analysis [6] is one of the most widely used condition monitoring techniques especially for rotating and reciprocating machines, most commonly using piezo-electric accelerometers because of their wide dynamic range. Acceleration signals are sometimes integrated to produce velocity or even displacement values for some applications. Vibration signal analysis bears quite a lot of resemblance to AE analysis, although the frequency is generally at least an order of magnitude lower involving whole body motion, and techniques like demodulation are appropriate. Generally, vibration analysis starts by drawing a comparison between historical measurements and new values, normally known as trending. A range of features may be trended, including those from the time domain, frequency domain, and the quefrency domain [7], although, obviously these are not totally independent. Time domain analysis refers to the statistical analysis required to extract various features from accelerometer time signals, such as RMS, probability density moments, standard deviation, variance, skewness, and kurtosis. In order to remove any unwanted noise and/or concentrate on specific aspects, the time signal may be filtered using low, high or band pass filters. Frequency domain or vibration signal spectral analysis is probably the most powerful technique particularly for machines that use rolling element bearings where faults are often manifest at characteristic frequencies. The majority of frequency analysis is done using a Fast Fourier Transform (FFT) [40], a special case of the generalized Discrete Fourier Transform which converts the vibration signal from its time domain representation to its equivalent frequency domain representation. Frequency analysis results in frequencies which can reflect the behavior of certain mechanical components, certain malfunctions, or may point to some unexpected source frequencies which may aid the analyst to identify the type and location of the problem and eventually recognize the root cause. A further development of frequency analysis is achieved by combining both frequency and time domain analysis in order to deal with cases where the frequency is changing with time by using Short Time Fourier Transform (STFT) [42]. A recent development of vibration analysis has begun to use wavelet transforms to extract very weak periodic information for which the FFT is ineffective [46, 75]. The wavelet transform results in a scaled, variable resolution in both time and frequency axes. Quefrency is another enhanced

frequency domain technique, defined as the logarithm spectrum of the power spectrum. Quefrency analysis operates in a similar way to spectral analysis except that it highlights periodic components in the frequency domain as opposed to the time domain, i.e. it is the spectrum of the spectrum. Quefrency analysis finds only limited application in condition monitoring, however, it is more widely used for other applications such as speech recognition, echoes and earthquakes.

Visual inspection [76], the simplest, cheapest monitoring technique if done by experienced people, may sometimes provide direct indication of the machine condition. Visual inspection can be enhanced in a number of ways, such as by using lenses, microscopes, endoscopes, borescopes and various dyes and magnetic particles to provide a clearer indication of any cracks, leaks, and/or corrosion occurring on the surface of the machine.

Temperature analysis [76] is considered by some as a kind of visual inspection where the occurrence of any wear and the absence of lubrication will result in temperature increase which may be assessed by the touch of an operator. More technically, temperature analysis of signals from optical pyrometers, thermocouples, thermographs or resistance thermometers can be used in a similar way to other condition monitoring signals, although the relationship between the temperature and its temporal and spatial distribution tends to have rather less discriminatory power in fault type identification.

All the previously mentioned condition monitoring techniques, i.e. performance analysis, oil analysis, visual inspection, borescope inspection, X-ray imaging, vibration monitoring, and lubricant debris monitoring, are indirect in that they measure the changes in some aspect of the machine operation. Furthermore, these approaches are generally unable to give information about the exact location of any changes in the signal. Acoustic Emission (AE) sources include impacts, wear, crack propagation and gas flow, all of which can occur in gas turbine operation and so the signal is potentially more direct in that it is the result of a degradation process, rather than a symptom that degradation has occurred, as might be the case, for example, with an increase in temperature or vibration at a particular frequency. The AE technique has two potential advantages over other techniques which are the earlier identification of any changes happening in the machine and the potential to locate the source of the emission and hence the location of the degradation events.

2.5. Acoustic emission for condition monitoring of turbines and machinery:

Board [10] was among the first to apply AE analysis to a gas turbine in that he mounted AE sensors at two different positions on a bearing housing to detect roller bearing wear of a large industrial gas turbine. He observed that the AE spectrum at one position on a bearing housing had strong indications at 105.8 Hz which he identified as the cage rotational frequency of the roller bearing thus identifying a defect. Board [10] also examined the effect of shaft imbalance in a gas turbine gearbox by recording AE in the normal condition and in two imbalance conditions where eccentric weights had been introduced. He observed that the addition of the imbalance weights led to a modulation of the normal forces between the races and the rolling elements of the bearing supporting the turbine gearbox at a frequency of once per revolution of the imbalanced shaft with the amplitude of the spectral line increasing significantly with increasing imbalance. Mba [9] investigated two faults on the inner and outer races of a test bearing using a range of AE features such as rms amplitude, energy and AE counts. The results showed that the maximum AE amplitude increased with increasing speed, but not with load or defect size. Mba showed a correlation between bearing mechanical integrity and AE counts, an observation also made by other authors i.e. Choudhary and Tandon [77]. Douglas *et al* [78] carried out a preliminary study in which they monitored the operating parameters of a gas turbine using acoustic emission. The experiment was conducted on the same laboratory-scale gas turbine as in the current work, operating under various conditions with AE sensors mounted on different positions on the rig and turbine surface. In all records, the blade passing frequency of the monitored compressor was observed, suggesting that AE is sensitive to processes going on in and around the turbine. Moreover, the frequency analysis of two severities of induced blade fault in the free-power turbine produced a deviation from the normal spectrum suggesting that AE may act as an indicator of individual blade malfunction.
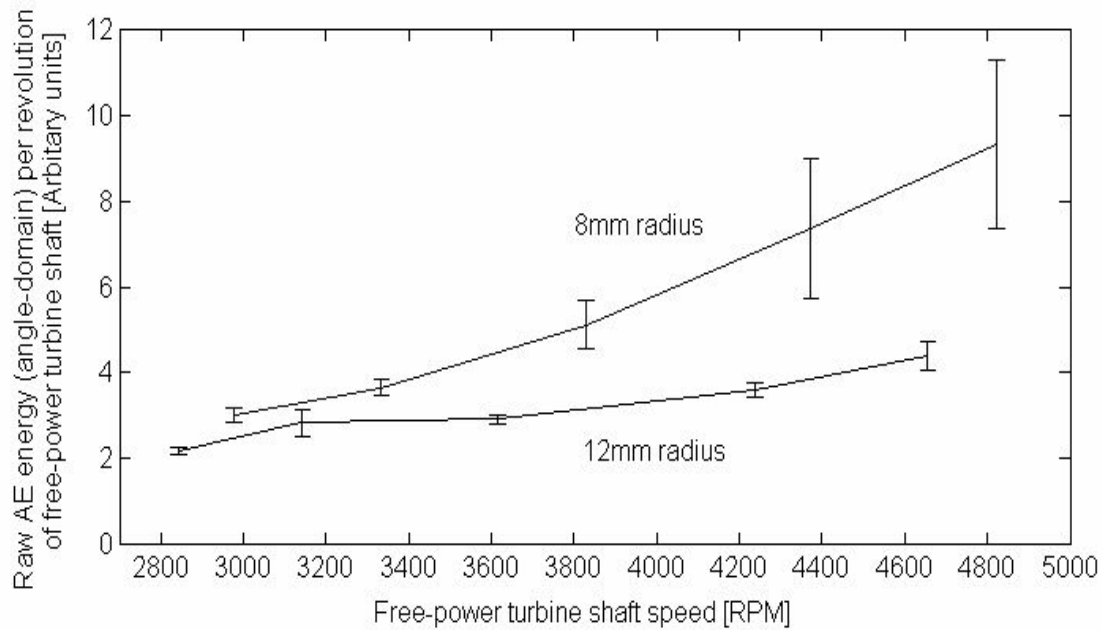
Figure 2. 7: Example of AE energy of simulated damage to blades of free-power turbine (from Douglas *et al*[78]).

Sato [11] was also interested in applying AE to rotating machines to detect rubbing and other damage in bearings. He mounted AE sensors on two turbine journal bearing housings in order to detect metal wipes and bearing tilts, and found a correlation between the AE pulse shapes and the corresponding deformation. Hall and Mba [79] applied acoustic emission to diagnose continuous rotor-stator rubbing on a 500 MW steam turbine operating at full load. They attached AE sensors to two different locations on the bearing and calculated the energy envelope by applying a low order smoothing filter to the RMS data. They found a significant amplitude difference in the AE activity at one position over the other and attributed a modulation of the AE to fluctuations in the rubbing force in response to the shaft whirl orbit. They attributed the higher AE activity at one sensor to the location of the continuous rubbing being extremely close to the sensor, and suggested that it was within 1 m of the bearing. Hall and Mba also studied the transmission of AE waves across such very large-scale turbine rotors [12] and found that it was possible to detect AE sources up to 2 m from the sensor and suggested that the AE technique could be viable for detecting seal and blade rubbing in such machines. Zuluago-Giralda and Mba [80] further investigated shaft-seal rubbing in a 500 MW steam turbine by monitoring the AE activity during run-up and run-down, again placing sensors at two different positions on the journal bearing case. They measured turbine load, turbine speed, and rms AE and concluded that the rms was

effective in identifying the turbine's critical speed during the run-up period, but not during the run-down period.
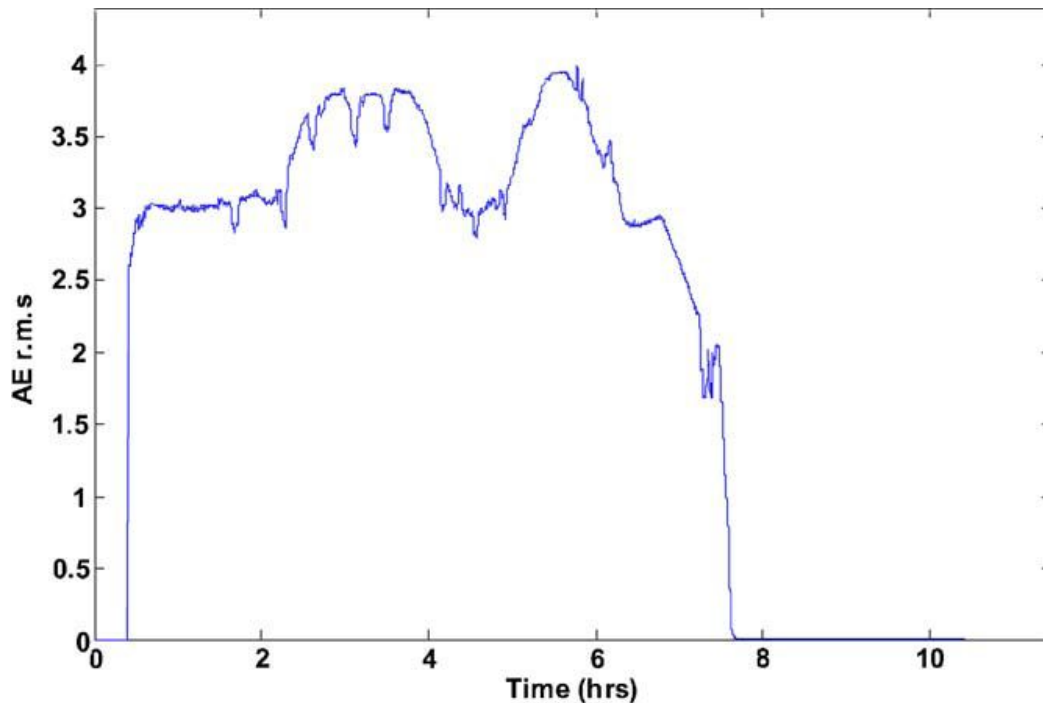
Figure 2. 8: AE r.m.s. (V) activity during run-down of a 500 MW turbine (from Zuluago-Giralda and Mba [80]).

Leahy *et al* [81]investigated the potential capability of the acoustic emission (AE) technology for the detection of seal-to-rotor rubbing in steam turbines. They simulated seal-to-rotor rubbing on rotor with a 4.5 ton, 2 m long, supported at each end by a 7 in (178 mm) hydrodynamic journal bearing. The rotor and bearings were installed within a fully enclosed test chamber with an externally mounted electric motor. Leahy *et al* proved the capability of AE technique to detect simulated rubs from hydrodynamic bearings. Armor and Frank [82] assessed AE for monitoring crack growth emission on the rotor of a steam turbine in a noisy background environment. Attenuation studies demonstrated the importance of having AE signals of fairly large amplitude in order that they could be detected at the bearing position. An experiment on a laboratory test specimen produce a large amplitude signal associated with crack growth which they concluded would probably be detectable at full speed operation taking into account the likely crack growth rate under various conditions.

Wang and Huang [83] used wavelet analysis in their study of AE propagation on a Francis turbine runner to identify its attenuation characteristics. They used a standard

pencil lead break source and the Wavelet Packet Transform technique (WPT) for analysis. They argued that the use of wavelet packet coefficients allowed them to reduce the need for data storage and that the WPT is a feasible technique for monitoring the operating turbine runners.

Many researchers have investigated AE for condition monitoring of pumps. Neill *et al* [17] conducted experiments on both laboratory and industrial scale centrifugal pumps to detect incipient cavitation. By applying both rms and frequency analysis, they were able to detect cavitation earlier than its appearance on the pump's dynamic head and proved the feasibility of incipient cavitation detection using AE in the face of noise from normal running although they did suggest that the nearer the sensor is to the cavitation site the better. Neill *et al* [13] extended their investigation on the AE monitoring of pumps to their rolling bearings, comparing AE-based diagnosis with acceleration monitoring, and concluding that AE rms and characteristics of the demodulation frequency of resonance are good indicators of bearing defects. On the other hand, the acceleration spectra showed a drawback, in that other peaks are present in the spectrum associated with whole body movements of the pump to which AE is not susceptible. Tomaž *et al* [84], working with 2-blade Kaplan turbine model, compared AE and video records in order to explain the relationship between the AE and the visual appearance of cavitation. By running at the minimum operating head with full turbine discharge, Tomaž *et al* initiated the most severe cavitation conditions and concluded that there was a correlation between the AE maximum amplitude and the cavitation number. They found variations in the strength of the acoustic emission as the location of the cavitation on the turbine blades moved around.

AE application to the condition monitoring of diesel engines has attracted much attention due to the potentially high signal to noise ratio which limits the low frequency background noise. This immunity to vibration noise is associated with the high frequency (0.1-1.2 MHz) of AE waves so that they can act like a carrier wave [8], allowing lower frequency information to be extracted from a signal envelope. This has led to successful demonstrations of AE in diagnosing many engine faults such as head gasket leaks [16], injector faults [85], combustion faults [86], and liner scuffing [87], and the development of new processing concepts, such as engine mapping in terms of AE events and spatially-located time-series [88, 89]. Gill *et al* [86] have investigated the fuel delivery process in a four-stroke, high speed direct injection (HSDI) diesel engine

with two induced fault conditions. They concluded that the timing of the increase of fuel line pressure and the time at which the injector needle becomes fully open could be detected using AE and these times advanced while injector discharge pressure reduced. Shuster *et al* [87] carried out an experimental study of piston-ring/cylinder-liner scuffing using AE. The overall results indicated that the detected rms AE signal provided the basis for monitoring the scuffing phenomenon dividing it into three different levels; scuffing initiation, irreversible scuffing and severe scuffing. In particular, the rms AE signal was sensitive to scuffing initiation through its sensitivity to friction coefficient and it was shown that the first peak of spikes in the rms AE signal was associated with the initial iron particles transferring from cylinder liner to piston ring surfaces, confirmed using scanning electron microscopy (SEM). Douglas *et al* [90, 91] have investigated piston ring/cylinder liner interaction on a large two-stroke, slow speed, marine diesel engine under normal operation using AE. The results showed that it was possible to detect sliding contact between the piston rings and the cylinder liner relating them to blow-by or exhaust valve leakage during the compression and expansion strokes. Nivesrangsan *et al* [38, 39, 88, 89] conducted a thorough investigation of the mapping of AE events generated within the cylinder head of a small HSDI diesel engine. In doing so they introduced techniques for the spatial reconstitution [39] and source location [88] of events using multi-sensor arrays. Good results were reported from the reconstitution process, thereby offering more accurate information regarding event timing and amplitude that could be used as the basis of a diagnostic system.

2.6. Artificial neural networks in condition monitoring:

This section describes how ANNs have been used in the enhancement of gas turbine condition monitoring to show how combining ANNs with AE might be used for recognizing the complex patterns of sensor information generated by a gas turbine.

Stephen *et al* [92] employed an ANN system to detect, isolate and assess faults in some of the components of a single spool gas turbine. The ANN was combined with a hierarchical diagnostic methodology and was tested on new data which had not been used for training. They used six measured parameters (shaft speed, fuel flow, total gas pressure and the temperatures of the exhaust and the compressor) of a two-shaft aero-derivative gas turbine with the turbine power as an input to the ANN taking into consideration the deviations of each parameter. They used a probabilistic neural

network (PNN) with an equal number of neurons in the input and output layers. They found that the ANN gave more accurate fault detection compared with other diagnostic techniques such as LGPA and NLGPA using the same input data. Fast *et al* [93, 94] used an ANN for condition monitoring and fault diagnosis of a gas turbine in a combined heat and power plant. The plant comprised a Siemens SGT800 gas turbine with a heat recovery steam generator as well as a bio-fueled boiler and its steam cycle. The artificial neural network models were trained with three months' operating data from the components of the plant. A type of multi-layer feed-forward network, the multi-layer perceptron (MLP), was used consisting of an input layer, one hidden layer and an output layer. The input parameters were the operating mode and the ambient conditions, and the output parameters were the most easily measured features of the turbine such as the output power, compressor pressure, bleed temperature, fuel flow, and exhaust gas flow and temperature. The predicted performance from the ANN model was tested against a number of unseen data patterns to determine the prediction error. The accuracy of ANN modeling of the gas turbine was found to be better with proper training and parameter selection and the study led to a functioning on-line condition monitoring system. Junxia *el al* [95] used a NARMAX time series model, for a gas turbine and analyzed it using the ANN to improve the control of the turbine. The existing PID controller was incapable of managing the whole operating range of the turbine and could not provide a satisfactory response to rapid changes in the dynamic behavior due to the nonlinearities of the engine. A predictive control system using a NARMAX model with a neural network was found to improve the PID and make it capable of representing the engine dynamic throughout its whole operating range. The model was tested in normal and disturbed conditions and continued to show good control performance.

ANNs have also been used to elucidate complex patterns in AE data. . Wilkinson *et al* [18], employed a back-propagation neural network for cutting tool wear prediction using five AE features as input to classify the wear state as light, medium or heavy. The results showed that the ANN could recognize the heavily worn tool state whenever it occurred. The network occasionally misclassified the other states, although it always gave a more pessimistic estimation of tool wear than was actually the case. Grabec *et al* [96] used an ANN for the purposes of identifying the location of continuous AE in one dimension (zone location). An initial set of experiments was used for the learning mode and it contained information from two AE sensors with their coordinates relative to the

source as training data. The cross-correlation function of the signals from the two AE sensors was supplied to the network to train it to the source coordinates. Application of the trained network to new data showed that the technique was able to estimate the zone from which the AE signals are coming.

2.7. Gas turbine faults:

Gas turbines contain thousands of moving and stationary components, the most critical of which are found in the hot environment inside the turbine where they experience high temperatures and pressures, and high, varying stresses resulting from centrifugal loads and aerodynamic forces. Such severe conditions provide some of the biggest challenges in modern materials development and component design. Within the timescale of commissioning to overhaul a number of kinds of faults can develop, including; compressor fouling, blade erosion, blade fatigue, blade creep, corrosion, and seal rubbing.

Compressor fouling [97, 98] is caused by the adhesion of particles bound by oil or water mists to aerofoil and annulus surfaces. The result is an accretion that causes increased surface roughness and, to some degree, changes the shape of the aerofoil or channel and is most commonly encountered in gas turbine compressors. The effect of increased roughness is to increase friction losses although changes of shape can cause more serious operation inefficiencies.

Blade erosion [99, 100] is the abrasive removal of material from the flow path by hard particles impinging on flow surfaces. Solid particle ingestion can be caused by a number of mechanisms, such as vortices generated during landing and take-off, sand storms, volcanic ash, and thrust reverser efflux at low speed which can blow ice and dust into the engine. Erosion damage on turbine blades can be manifested as pitting and chipping of the blade leading and trailing edges and an increase in the blade surface roughness. The overall effects of this erosion are to increase the pressure loss and change the blade geometry. The figure 2.9 shows the aerodynamic zones on a gas turbine blade and identifies the severity of wear per zone.
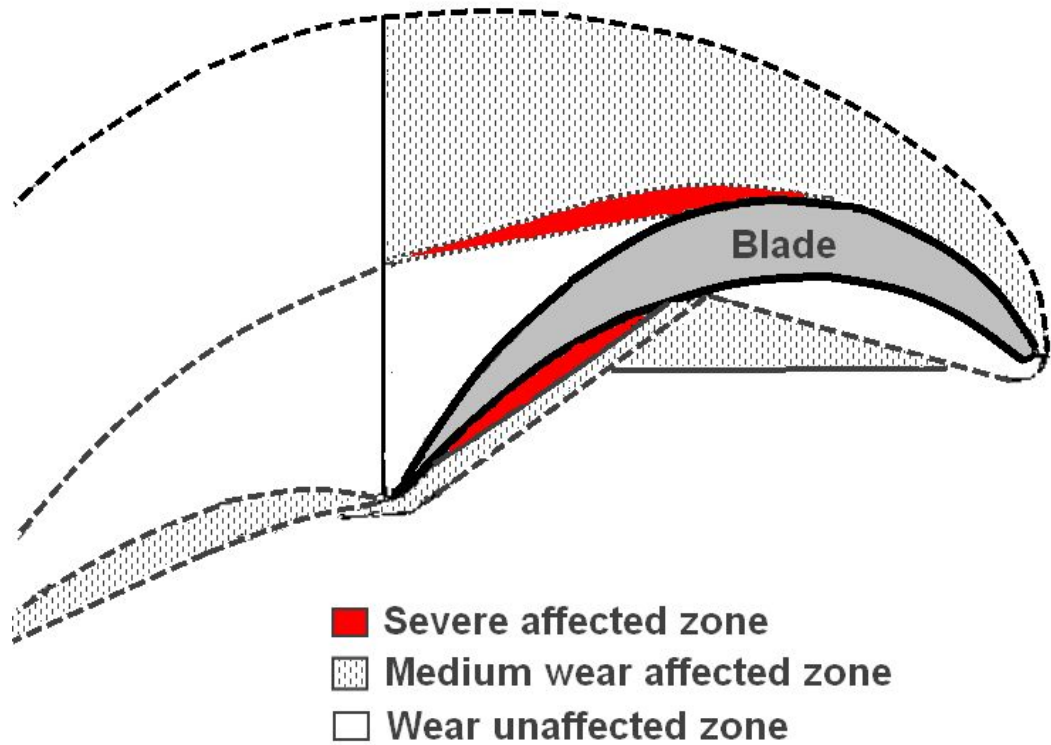
Figure 2. 9: Boundary layer replica of a gas turbine blade.

Any gas turbine engine needs huge amounts of air throughout its operation, which is provided either by sucking it in through the compressor or by ramming due to the forward motion of an aircraft, or both. Foreign object damage (FOD) [101, 102] is caused by debris which can either be hard objects such as stones, hardware and pavement fragments, or soft-bodies such as ice, birds and animals. FOD is typically caused when the rotating blade strikes an object, and the velocity of the blade is usually more significant than the axial velocity of the object. The result of the impact is a localized damage in the form of a notch or dent (typically on, or close to, the leading edge). The overall result of FOD on the gas turbine is a reduction of the fine balance of the system and degradation of the airflow characteristics over the blade aerofoil, leading to aerodynamically-induced vibration or flutter, which initiates fatigue failures excited at rotation or blade passing frequencies.

Blade fatigue failures [103, 104] are most often caused by anomalies in mechanical behavior and/or manufacturing defects. There are two kinds of blade fatigue failure, high cycle fatigue (HCF) and low cycle fatigue (LCF). HCF is rare in turbine blades, unless some form of initiation damage is present, and/or there is excessive bending of the blades for example due to abnormal vibration in the engine. HCF cracks are most likely to be initiated at the surface in the brittle platinum aluminized coating layer and may spend much of the fatigue life very small, accelerating in size with time due to the stress intensification effect and propagating progressively across the thickness of the blades. Once the fatigue crack reaches a critical length it will propagate across the remaining section by fracture leading to other damage in the engine. LCF is related to the much larger stress cycles imposed by starting and stopping operations and constitute the design-limiting fatigue life cycles. The source of these stresses is fairly apparent. When stopped, the disc/blade combination is subjected to loadings mainly due to its self-weight, and is relatively cold. However, in operation the same components are subject to large, though fairly constant loadings from centrifugal forces imposed by the rotational speed, and are at a much higher temperature. The rate of change between these two states is rapid on engine start, inducing high levels of thermal stress, which reach a steady state during operation and then reappear, in reverse, during cool-down. Thus, the number of fatigue cycles is relatively low, although the stress range is high.

Fatigue cracks can appear at a number of locations on the blades, such as; on the aerofoil above the blade root platform near the trailing edge on the concave side of the blade (Figure 2.10, red arrow), on the aerofoil above the blade root platform near the trailing edge on the convex side of the blade (Figure 2.10, white arrow), and on the aerofoil of the blade just above the fillet radius from the trailing edge, Figure 2.11. Fatigue cracks always initiate at the blade surface irrespective of location on the blade and this is because the surface changes temperature more rapidly than the interior, giving it the highest thermal stresses.
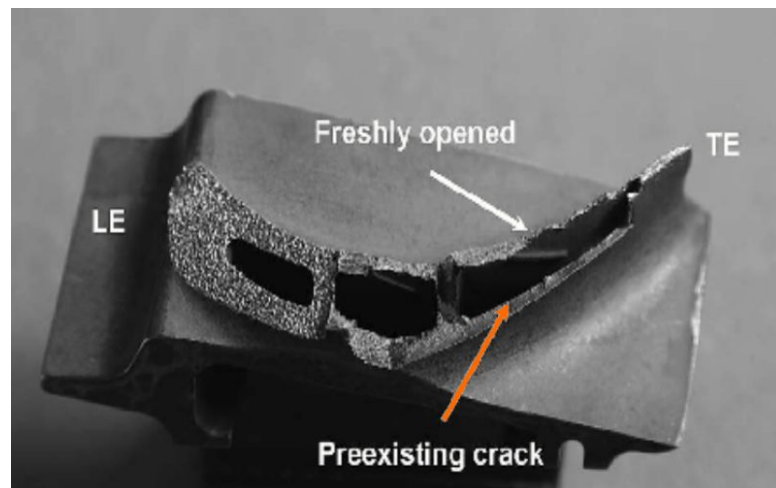
Figure 2. 10: Fracture surface of a blade with fatigue failure on the concave side near trailing edge (TE: trailing edge; LE: leading edge) [103].
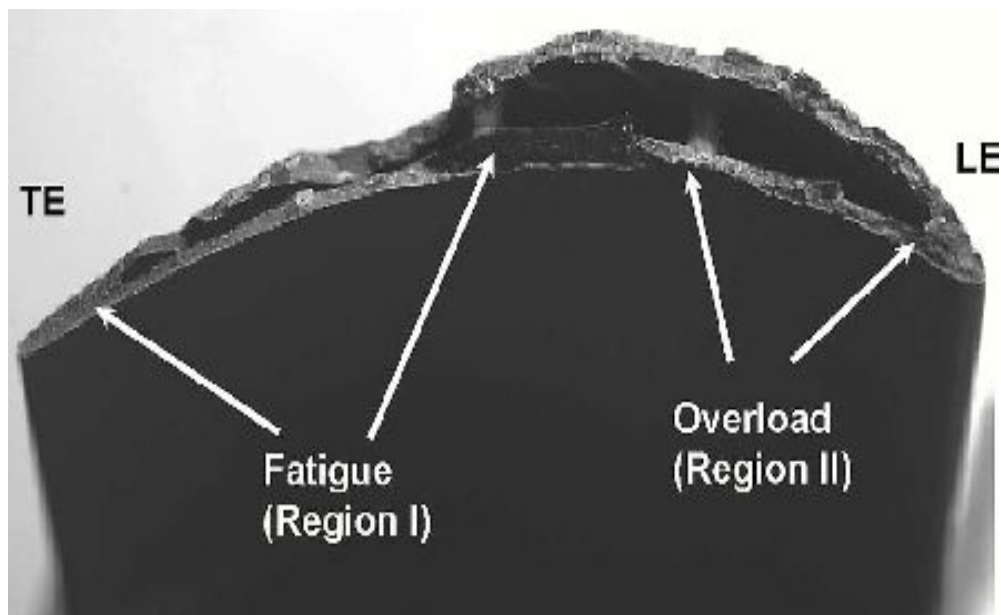
Figure 2. 11: Fracture surface of a blade with fatigue failure on the convex side near trailing edge (TE: trailing edge; LE: leading edge) [103].

Blade creep [105, 106] manifests itself as blade ''stretch'' in which the blade elongates plastically in service under the centrifugal loads. In abnormal conditions and severe situations, this may be sufficient for the blade tip to contact the non-rotating shroud, causing a ''tip rub''. Blades fail by creep when the normal operating temperatures of the engine are exceeded for more than brief periods or when the inspection procedures are not correctly followed.

Hot corrosion [107, 108] is the loss of material from flow path components caused by chemical reactions between the component and certain contaminants, such as Na_2SO_4, NaCl, and V_2O_5 that combine to form molten deposits, which damage the protective surface oxides. There are two kinds of hot corrosion, high temperature hot corrosion (HTHC) and low temperature hot corrosion (LTHC).

HTHC is observed mainly within the temperature range of 850 to 950°C and starts with the condensation of alkali metal salts on the surface of the component. The dominant salt in HTHC is Na_2SO_4 due to its high thermodynamic stability. HTHC can be divided into four progressive stages from initial onset to failure. In stage 1, slight roughening of the surface caused by some growth and localized breakdown of the oxide scale layer is evident. At this stage, neither chromium depletion in the substrate layer nor loss of mechanical integrity is observed. In stage 2, the roughness of the surface is more marked as the oxide layer breakdown continues. While chromium depletion commences at this stage, mechanical integrity is still not affected. In stage 3, oxidation of the base material has penetrated to a significant depth, with an obvious build-up of scale. At this stage, the mechanical integrity has been compromised and the blades are normally removed from service. Progression to stage 4 (catastrophic attack) will occur with or without the continued presence of sodium. In stage 4, the attack penetrates deeply into the blade while forming a large `blister' of scale, and failure is likely to occur due to loss of structural integrity.

LTHC is observed mainly within the temperature range of 650 to 800°C. LTHC produces a characteristic type of pitting, resulting from the formation of low melting temperature (eutectic) mixtures of Na_2SO_4 and $CoSO_4$. The initiation of LTHC is often attributed to failure of the protective oxide layer, which allows the molten salt direct access to the substrate metal. Ultimate failure may result from enhanced erosion,

thermal stresses, erosion-corrosion, and/or chemical reactions. LTHC develops in two stages, the formation of liquid sodium-cobalt sulphate on the surface and the propagation of attack *via* migration of SO_3 and cobalt inward and outward, respectively, through the liquid salt.

Hot corrosion is usually greatest at the hottest point on the pressure (concave) surface of the turbine blades about midway along the length of the blade, and a short distance back from the leading edge. It is more frequently observed in the low-pressure turbine (LPT) than in the high pressure turbine (HPT) due to the lower temperatures involved in the LPT where the corrosive contaminants are more likely to accumulate on the surface in significant amounts and/or for a greater percentage of time**.**

Seal rubbing [109, 110] can occur between the static and rotating components of the turbine. Rubbing in the seal is a secondary phenomenon which results from a primary cause such as high lateral rotor vibrations and high lateral displacement of the rotor centre line due to misalignment. There are two main types of rubbing. The first type is "light partial rubbing" where the contact forces are minimal, and the rotating elements occasionally touch the stationary elements. The second type "continuous rubbing" is more serious because of its influence on the integrity of the machine. This is a full annular rub in which the rotor maintains contact with the seal continuously or almost continuously. Seal rubbing must be avoided as it will ultimately result in wear and an increased leakage flow between the high-pressure and the low-pressure sections which will reduce the efficiency of the gas turbine leading to eventual shut down.

Many of these faults are associated with mechanisms of failure which will generate AE. Some faults produce AE directly such as contact between rotor and stator, damage in bearings, and rotor crack propagation. Other faults such as: abnormal dynamic loading; wear, accretion or corrosion of flow surfaces; misalignment, lubrication degradation, oil starvation, and foreign object damage produce AE indirectly. AE has been found to offer better performance than some other techniques for detecting faults in turbines such as rubbing [12, 79, 111], and damage in bearings [9, 112-114]. For example, vibration monitoring of the bearing pedestals has been studied using accelerometers to identify shaft seal rubbing in turbines and found not to be as effective as AE [115, 116] which can detect faults in the early stages of the rotor-stator rubbing. The high amplitude, high frequency (20KHz-2MHz) AE signatures associated with rubbing [117] can propagate

across the turbine for distances of up to 4 meters, allowing the AE technique to identify the onset and the location of the rubbing in the turbine. However, this success is considered to be dependent on fully understanding the background noise received by the sensor on an operational turbine unit.

2.8. Summary of state of knowledge and thesis identification:

Established condition monitoring techniques for gas turbines such as gas path analysis, oil analysis, and vibration analysis use such parameters as temperature, pressure, speed, accelerometer signals, and oil features to identify the machine condition and to achieve economic performance through increased availability and reduced component replacement costs. However, those techniques are all indirect; they do not provide enough information about degradation in gas turbines at the early stages of fault development and many of them have limited, or no, capacity to locate the sources of faults. The acoustic emission technique addresses these drawbacks by its capability to monitor degradation processes as well as their symptoms inferring an ability to identify changes in the early stages, as well as the capacity to locate the source of any non-continuous AE.

However, the high temperatures in the gas flow areas of gas turbines and the low signal-to-noise ratio has limited the application of AE on industrial machines to studies of bearing defects, rubbing damage, background noise determination and AE propagation characteristics on off-service engines.

A number of the faults that can occur in turbines result in changes to the gas flow over the various operating surfaces and it were decided to address this area of turbine monitoring, as little or no work has been done on this aspect. It was expected that a breakthrough in the application of AE to gas turbines could be achieved by a full understanding of what influences the AE behavior emanating from a gas turbine at various running conditions and differentiating between AE sources resulting from gas flow through the turbine and those resulting from impact or rolling contact in the ancillary mechanical equipment, such as shafts and bearings. This work, therefore, concentrates on establishing the AE signatures of a laboratory-scale gas turbine under normal running conditions and with faults induced in the flow behavior through the free power turbine, by jamming its impeller, removing its power take-off, introducing defects in its blades, and removing the impeller entirely.

Chapter 3 Experimental apparatus and procedures

3.1. Introduction:

This chapter is divided into two parts the first part describes all the requirements and specifications of the apparatus used, and the second part explains all the procedures and arrangements for the research experiments, including calibration. The second part is divided into three sections, the first of which describes the calibration of the AE sensors using simulated sources on a steel block and on the turbine rig and including AE propagation tests on the turbine rig, The second section explains the procedure for the experiments carried out on the turbine under normal running conditions, with the impeller jammed, with the impeller absent, with load and without load. The final section describes the procedure for investigating the effect of impeller damage.

3.2. Apparatus:

A typical AE acquisition system and experimental set-up as used in this work are shown schematically in Figure 3.1. The system generally comprises a test object (here shown as the turbine), an array of AE sensors with their associated pre-amplifiers, a data acquisition card, and a computer with software for controlling the acquisition and storage of data.
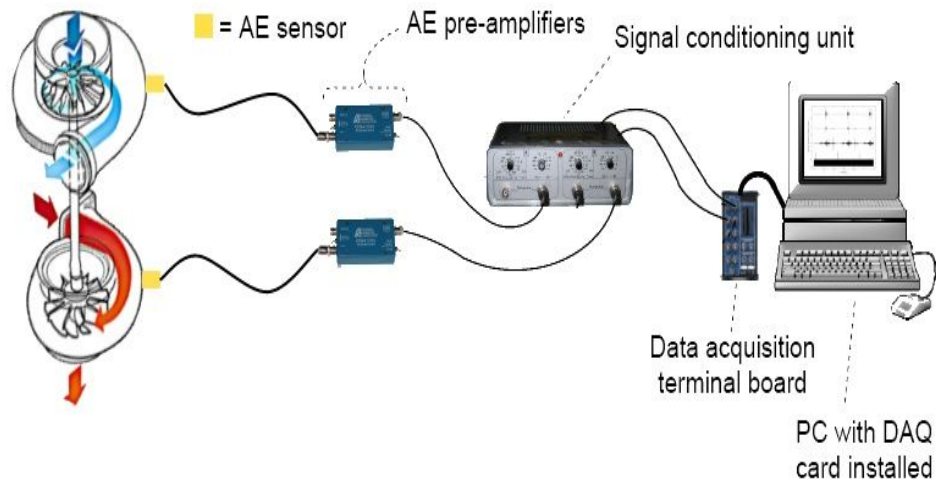
Figure 3.1: Schematic view of turbine rig and acoustic emission system.

The following sub-sections describe each of these component parts of the set-up.

3.2.1. AE sensors and coupling:

Two types of AE sensors were used in this work. The first type is a commercial broadband AE sensor of type Micro-80D (Physical Acoustics, PAC), shown in Figure 3.2, chosen for its versatility and wide use for machinery monitoring tests. The sensor based on lead zirconate titanate (PZT), is omni-directional and produces a relatively flat but resonant frequency response from 175-1000 kHz, over an operating temperature range from -65 to $+177\,^0$C [118]. The sensor is 10 mm in diameter and 12 mm high and was held onto the test object surface using an in-house designed magnetic clamp. In order to obtain good transmission of the AE from the test object to the sensor, the surface was kept smooth and clean and silicone grease was used as couplant to fill any gaps caused by surface roughness and to eliminate any air gaps which might otherwise impair AE transmission. The sensitivity of the sensor at each position was checked using a simulated source by breaking a pencil lead close to it, against expected signal amplitude of around 4-5 volts using the fixed amplifier settings.

Figure 3.2: Micro-80D broad band sensor.

The second AE sensor used was of type S9215, also from PAC and is specially designed for high temperature operation. This AE sensor, shown in Figure 3.3 is also omnidirectional and produces a resonant response from $50-650$ kHz; over an operating temperature range from -200 to $+540\ ^{\circ}\text{C}$. The sensor is 20 mm in diameter and 20 mm high. The lower frequency resonant response required the use of a preamplifier with a lower high-pass filter, passing frequencies above 20 kHz [119]. This kind of sensor offers a good opportunity to acquire AE from positions on hot surfaces close to the likely sources of AE but the lower frequency response causes difficulties with increased noise levels and the possibility that some aspects of the signal will not be captured. The S9215 sensor is used in high temperature nuclear and fossil fuel utility

plants, to monitor leaks and cracks in pipelines and vessels, and in aerospace engine monitoring applications. A high-temperature grease (UCA-HT from Ely chemical) was used as couplant for this sensor.

Figure 3.3: S9215 narrow band, high temperature sensor[119].

3.2.2. Preamplifiers:

The preamplifier (type PAC 1220A) shown in Figure 3.4 was used to amplify the AE signal from the Micro-80D sensor to a level that can be comfortably transmitted and converted by an Analogue to Digital Converter (ADC). These amplifiers have internal band pass filters from 0.1-1.2 MHz and a switchable gain between 40 and 60 dB. The preamplifier is powered by a $+28$ V power supply and used a single BNC connection for both power and signal.

Figure 3.4: Preamplifier type PAC 1220A.

A different preamplifier 0/2/4 from Physical Acoustics corporation was used with the S9215 sensor because of its lower signal to noise ratio. The preamplifier, had a switchable 0/20/40 dB gain and was provided with an internal band pass filter from 0.02-1.2 MHz. As for the D9201A, this amplifier was powered by a +28V power supply and used a single BNC connection for power and signal to and from the sensor.

3.2.3. Signal conditioning unit:

Signal conditioning units were of in-house manufacture and were used to power ($+28$ V) the AE sensors and pre-amplifier as well as amplifying signals. They could also be used to perform analogue RMS processing with amplification capability.

3.2.4. Data acquisition (DAQ) system:

Most of the experiments in this research focused on acquiring raw AE signals in the bandwidth 0.1 to 1MHz and required a high performance data acquisition system. The system was based on an in-house built desktop PC with a 12 bit, National Instruments (NI), PCI-6115 board as seen in Figure 3.5. This board can be used to acquire simultaneously the raw AE signal at up to 10M samples/s for up to four channels with a total on board memory of 32 MB. The board is a multifunction analogue, digital and timing device without on-board switches or jumpers so that it can be configured and calibrated by software. The software-programmable gain can be set to 0.2, 0.5, 1, 2, 5, 10 or 50 and covers an input range from ± 200 mV to ± 42 V. The board supports only differential input configuration and has an over-voltage protection at ± 42 V. A LabVIEW programme was used to control a sampling frequency, a number of acquired

data per channel, a number of records, an input range, pre-trigger data, a trigger channel and a trigger level.
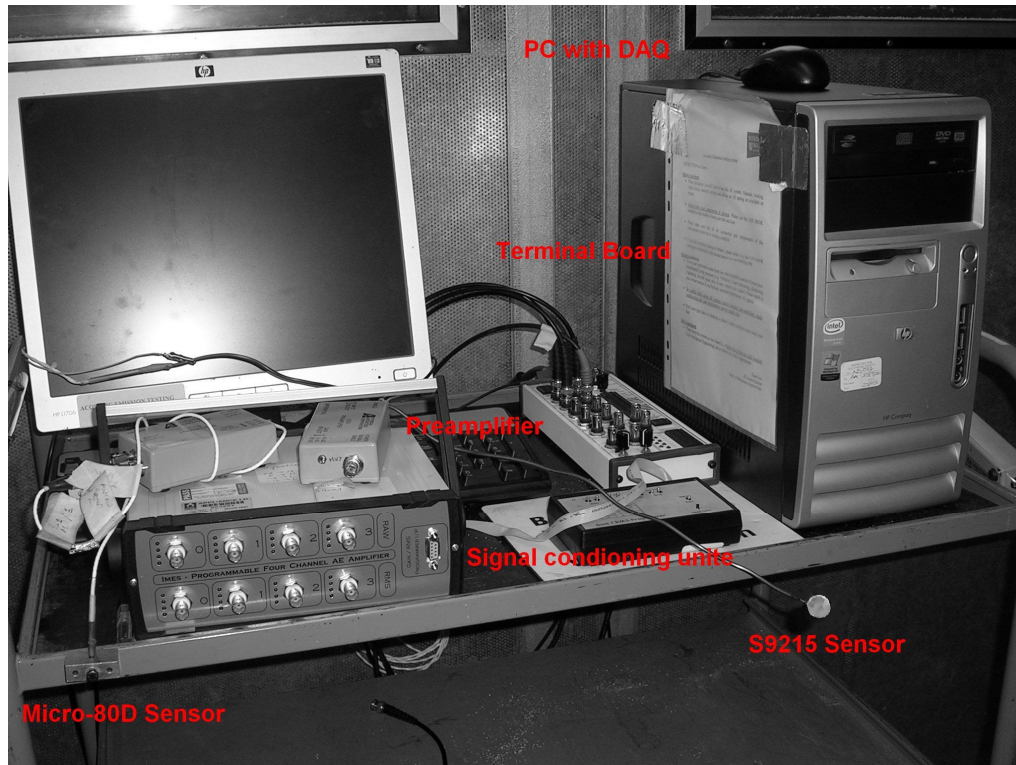
Figure 3.5: Data acquisition system with accessories.

3.2.5. Simulated source for calibration and attenuation:

A commercial mechanical propelling pencil with an in-house machined guide ring was used to generate simulated AE sources by breaking a 2H pencil lead, the so-called Hsu-Nielsen source. A standard guide ring (Nielsen shoe, Figure 3.6(a)) [120] is normally used to aid in breaking the lead consistently but its collar ring deforms very easily under the breaking forces and also becomes mis-shapen when used for many tests. Higo and Inaba [121]have suggested a modified guide ring with increased stiffness of the collar to improve the reproducibility of AE production, the design of which is shown in Figure 3.6(b), and this was used in the current experiments. The ASTM standard, E976–99 [120] recommends that the pencil lead should be the same type (0.3 or 0.5 mm diameter, HB or 2H pencil lead) with a length of 2-3 mm and so a 2H, 0.5 mm diameter lead was used here to generate simulated AE sources. The lead was broken under the same conditions, i.e. at the same position on the test surface, using the same angle and the same orientation of the pencil for all repeat tests.

Diameter	GT (± 0.05 mm)
0.3 mm	0.84 mm
0.5 mm	0.92 mm

References:
1. ASTM Standards E 976 - 99
2. Higo, Y. and Inoba, H., ASTM STP 1077, 1991.

(a) Standard guide ring (Nielsen shoe)

GUIDE RING

TEFLON
DIMENSIONS GIVEN IN mm.
TOLERENCE ± 0.1 mm.

(b) Modified guide ring
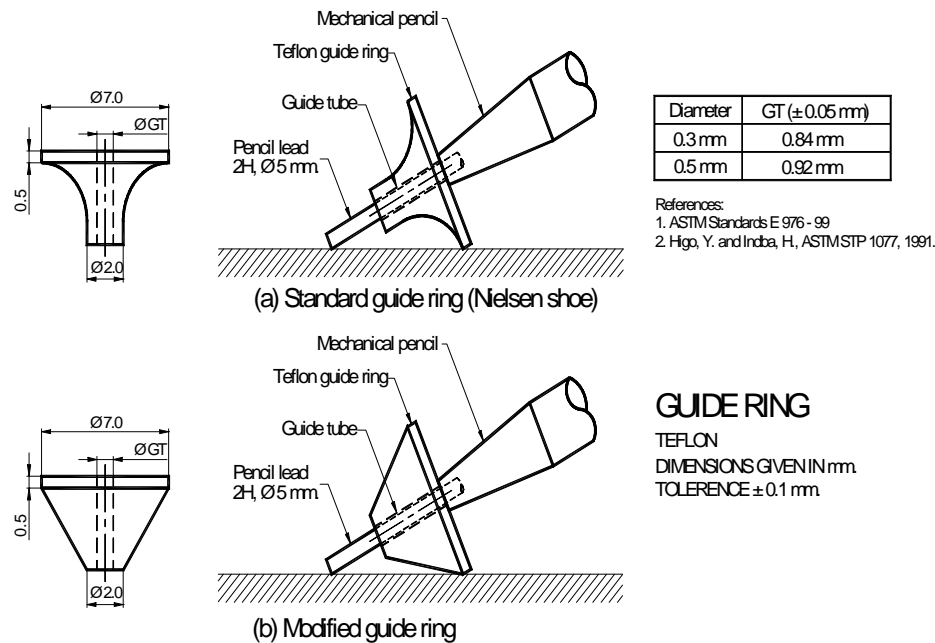
Figure 3.6: Drawings and dimensions of standard (a) and modified (b) guide rings[120, 121] .

3.2.6. Gas Turbine Rig:

The gas turbine used was a P.9000 gas turbine [122] unit manufactured by Cussons Ltd., shown schematically in Figure 3.7. The gas turbine consists of two stages. The first stage is gas generator which is a compressor and turbine mounted back to back on a short shaft supported in a journal bearing. The second stage is the free power turbine which is a single stage radial turbine operating over the range 170 to 600 rps and developing a maximum power of approximately 4 kW. The free power turbine is connected with an alternator which generates electricity that could be dissipated through heat lamps or made available from normal plug sockets. The change in the excitation voltage applied to the alternator field coils allows the power loading on the alternator (and hence the turbine) to be easily variable over the required operating range. The efficiency of the converted power between free power turbine and alternator could reach 85%.

The turbine was fuelled by propane, delivered from standard gas take-off bottles. Consumption was approximately 3.2 g/s at full load and about 1.1 g/s idling with no loading. Cooling was *via* an oil/water heat exchanger at about 10 liters per minute and the oil temperature was automatically controlled by a thermostat and solenoid valve

which admits water to the oil cooler. The lubricating system is a continuous circulation one with separately driven pump, filter and heat exchanger. The capacity is approximately 5 liters and the oil undergoes little deterioration and is normally changed only if the system has to be dismantled for any reason. A high energy ignition system is used for starting purposes only. This system is energised from the AC supply and the circuit includes a pilot lamp that serves also as a ballast resistance. The starting system is effected by closing a valve at the normal air inlet and blowing air through the compressor inlet from a separate centrifugal blower unit. The manufacturer-supplied instrumentation consists of a manometer for measuring the inlet air flow, a flow meter for measuring the consumption of propane, sensitive pressure gauges for measuring fuel supply pressure, combustion chamber pressure and outlet pressure, pressure gauges for indicating gas bottle pressure and lubricating oil pressure, an oil temperature gauge, a sensitive jet pipe pyrometer and a tachometer.

A waveguide was welded to the exhaust pipe giving a temperature at its end low enough for the application of the Micro-80D sensor. The temperature of the exhaust surface was around 400°C, so the required length of the waveguide was estimated to be 300mm. After careful welding of the waveguide to the turbine exhaust pipe, testing showed the surface temperature at the sensor-mounting platform to be less than 177^0C. The positions of the two AE sensors used for monitoring the turbine are shown in Figure 3.8. The tachometer shown in Figure 3.9 was designed and manufactured to record shaft speed on the free power turbine. The slotted disc is composed of 34 teeth of circumferential extent 5° and one of 15° to obtain a characteristic pattern for every cycle allowing shaft speed and rotational position to be determined alongside the AE, should this be necessary.

Figure 3.7: Schematic diagram of turbine rig showing positions of temperature and pressure sensors.

Figure 3.8: Photograph of turbine rig showing AE sensor positions.
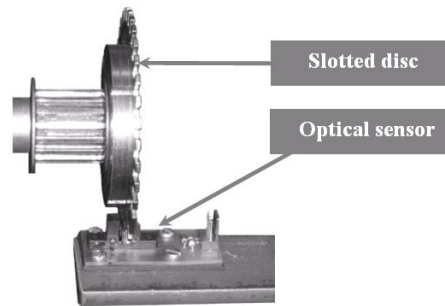
Figure 3.9: Timing signal system

3.3. Experimental procedure:

Three types of experiments were done; tests with the turbine running normally with and without power being taken off, tests with the impeller jammed and absent and, finally, tests with simulated blade defects. The rationale behind these experiments is described below. Essentially, the objective was first to determine what the sources of AE are in a turbine and then to determine whether these sources might give useful diagnostic information under normal operating conditions and/or fault conditions.

3.3.1. Turbine running tests:

The purpose of this set of tests was to find the AE characteristics associated with the processes going on in the running turbine. To do this, the two calibrated sensors and positions were used, and the turbine run in a variety of conditions including normal running with and without load, and in two conditions where the behavior was simplified by jamming the impeller so that it did not rotate and with the impeller removed from the free power turbine. The turbine shaft speed of the gas generator was varied between 30000 and 70000 rpm which, accordingly, changes the free power turbine speed (if the impeller is operating normally). Figure 3.10 shows the general arrangement for the turbine running tests.
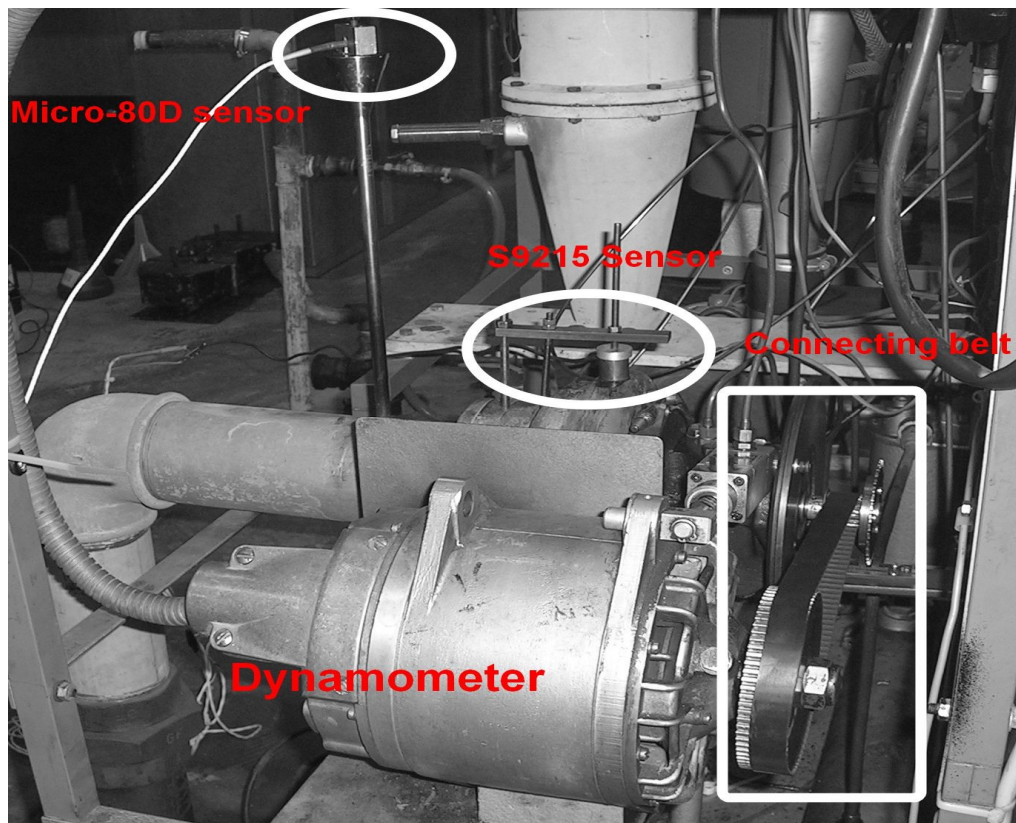
Figure 3.10: Running test arrangement showing free power turbine with AE sensors and power take-off belt.

3.3.1.1. Turbine running test with jammed impeller and without impeller:

For this experiment, the impeller of the free power turbine was either jammed by connecting the turbine belt to a fully loaded alternator, or entirely removed from the turbine. When the impeller was removed, it was necessary to replace it with a dummy piece (Figure 3.11) which allowed free passage of gas through the shroud but prevented gas leakage from the free power turbine to the lubrication system. Three, nominally identical tests were run for each of the jammed impeller and absent impeller configurations. Each test consisted of acquiring data over a range of incrementally increased gas generator shaft speeds between 500-1150 RPS achieved by means of changing the fuel flow. At each operating condition, fuel flow, air flow, and gas pressure and temperature of both the compressor and turbine were recorded as these were not precisely reproducible between tests. At each operating condition, raw AE was recorded for 0.03 sec and 20 records were obtained at each operating condition.
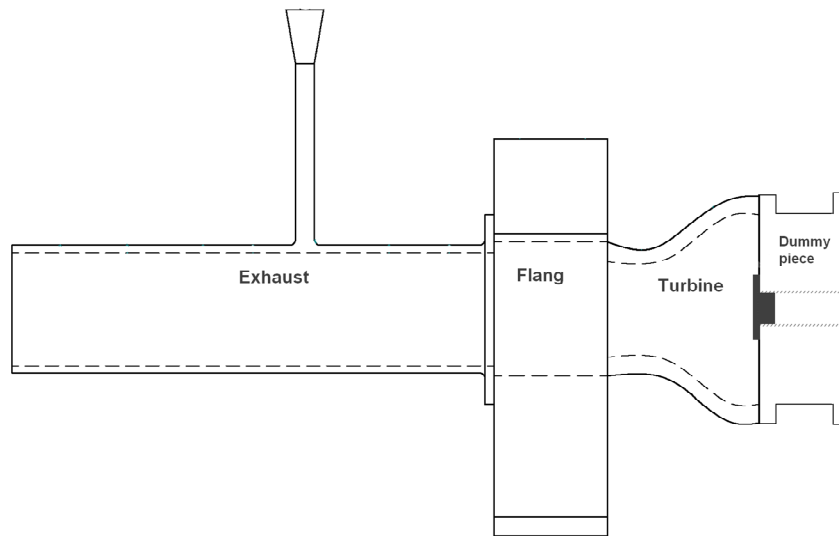
Figure 3.11: Schematic of dummy piece used to replace the impeller.

3.3.1.2. Turbine normal running test with and without load:

In this series of experiments, AE was acquired over a range of free power turbine speeds while the machine was under load and not under load. For the loaded condition, the speed of the gas generator was kept constant, and the speed change in the free power turbine was achieved by changing the alternator load. For the no-load (idling) condition, the connecting belt between the free power turbine and the alternator was removed and the turbine speed changed by changing the fuel flow incrementally which, accordingly, resulted in changes in both the gas generator and free power turbine speeds. The speed of the free power turbine was measured by means of the optical sensor connected to the slotted disc at the end of free power turbine shaft, and other operating parameters such as the gas generator speed fuel flow, air flow, and gas pressure and temperature of both the compressor and turbine, were recorded as for the other tests.

For each of the two conditions, with and without load, the speed was varied between 120 RPS and 380 RPS and 20 records of raw AE of length 0.03 sec acquired at each

speed. Each experiment (i.e. range of speeds with or without load) was again repeated a total of three times to check for consistency.

3.3.2. Damaged impeller tests:

This set of tests was carried out under the same conditions as the unloaded normal running tests to examine the effect of a series of induced faults on the AE signature. Blade damage was simulated in the 10-blade free-power turbine impeller by grinding off about 20mm from the tips of opposing blades. The choice of damaging opposing blades was made primarily for safety reasons, but also because it minimises the introduction of radial imbalance which might otherwise have an independent effect on the AE signature. In the first experiments, two opposing blades were damaged and, in the second, four opposing blades were damaged. In the second test, the blade damage was deliberately not made circumferentially symmetrical. Figures 3.12 and 3.13 show the impeller with two and four damaged blades, respectively. As for the normal no-load test, the connecting belt between the free power turbine and the alternator was removed and the speed of the turbine was changed between 100 RPS and 400 RPS by means of changing the fuel flow, which was recorded along with other thermodynamic aspects of the turbine rig. Again, as before, 20 records of length 0.03 sec were taken at each speed for each of the degrees of damage and each test was repeated three times.
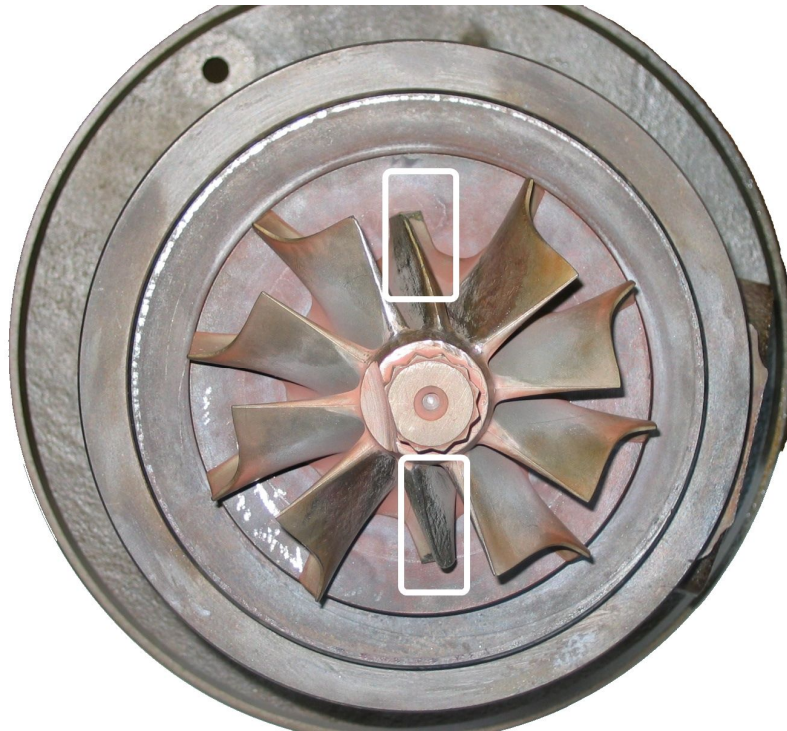
Figure 3.12: Free power turbine impeller with two damaged blades.
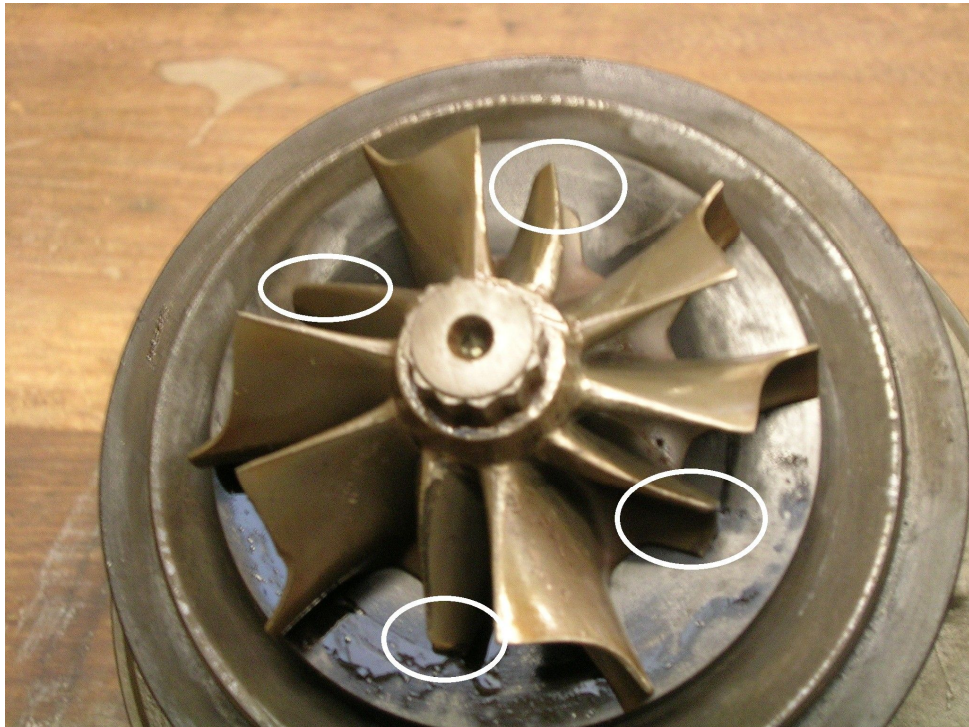
Figure 3.13: Free power turbine impeller with four damaged blades.

3.4. AE transmission and calibration tests:

Before carrying out any experiments, it was first necessary to calibrate the AE sensors and assess the transmission between various parts of the turbine and the sensor positions. Calibration tests were carried out on a steel block and on the turbine in order to check the response of the AE sensors and note any changes with temperature or time. It was also necessary to check the degree of reproducibility that could be expected after removing and replacing a sensor (i.e. the reproducibility of coupling). Finally, it was also necessary to know the relative sensitivity of the two different sensors used.

The transmission experiments were carried out to establish the characteristics of AE wave propagation through and over the surface of the gas turbine, including the waveguide. Attenuation of AE energy and changes to frequency content were measured for a variety of sensor source positions.

All calibration and transmission experiments used a pencil lead break as the AE source and AE energy as the main quantitative feature of the signal. All lead breaks were recorded at 5MHz for duration of 0.015 sec.

3.4.1. Calibration tests on steel block:

A large cylindrical steel block of dimensions 307mm diameter and 166mm height was used to calibrate sensors back-to-back. Pencil leads were broken on the centre of the top surface of the block typically with an array of three AE sensors mounted at the same radial distance, 62.5 mm from the source (Figure 3.14). The aims of this calibration were: to provide a means of calibrating the sensors before and after each test, to assess the variation of recorded AE due to individual pencil lead breaks and with individual installations (effect of coupling variation), and to compare the sensitivity and frequency response of the two types of sensors used. To investigate these effects, three Micro80D sensors were used at four sensor positions separated circumferentially by 90°. With the three sensors in each position 10 pencil lead breaks were recorded and the sensors removed and replaced in the same positions and another 10 breaks recorded. This process was repeated for a total of ten times so that 100 breaks were recorded for each sensor at each position. Next, the sensors were moved to another position and the entire process repeated.

(a)   **(b)**
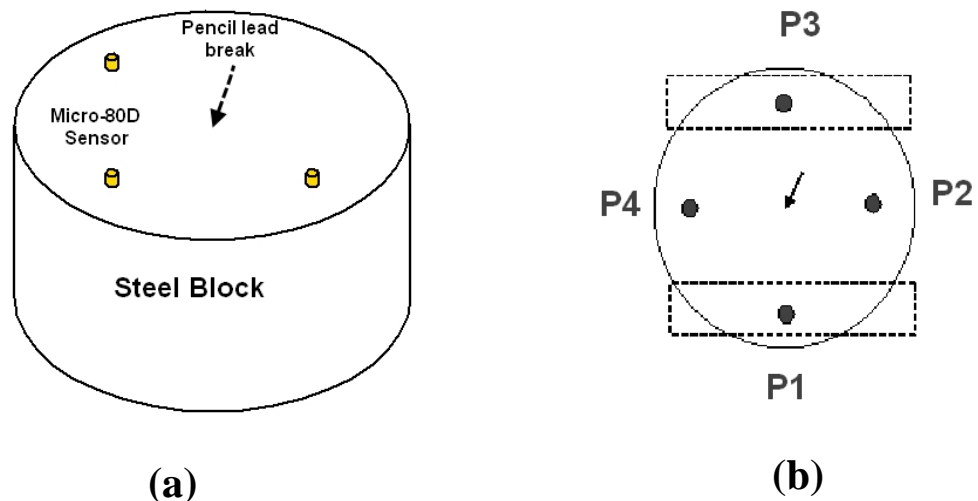
Figure 3.14: (a) Overall schematic and (b) plan view of sensor positions on steel calibration block.

Figure 3.15 summarises the recorded AE energy for the pencil lead breaks for all sensors at all positions. The wave arrival was identified by the time at which the signal level first exceeds a threshold of 1.5 times the maximum amplitude of the noise recorded in the first 180 µs. The energy was calculated by integrating the square of the amplitude for the duration between the first and the last threshold crossing. It is clear from Figure 3.15 that there is some variation between sensors and positions, but also that there is considerable variation for a given sensor in a given position. In order to analyse the data more systematically, a single factor analysis of variance was carried out grouping the data in a range of ways.

Figure 3.16 shows sensor 1 energy distribution at the four positions and the 10 removal-replacements at each position. Grouping the individual placements at a given position, the variance between placements (variation in coupling) can be compared with the variance within a given placement (variation in pencil lead breaks). The indicator F_{value} is compared with F_{crit} (1.98 for the degrees of freedom involved and at the 95% confidence level) and, as can be seen in Figure 3.16, F_{value} is always greater than F_{crit} indicating that the effect of removal and replacement of the sensor is more important than the variation in pencil lead breaks at all positions. Table 3.1 shows the value of F_{value} for all sensors at all positions and, confirming the same findings for all sensors.
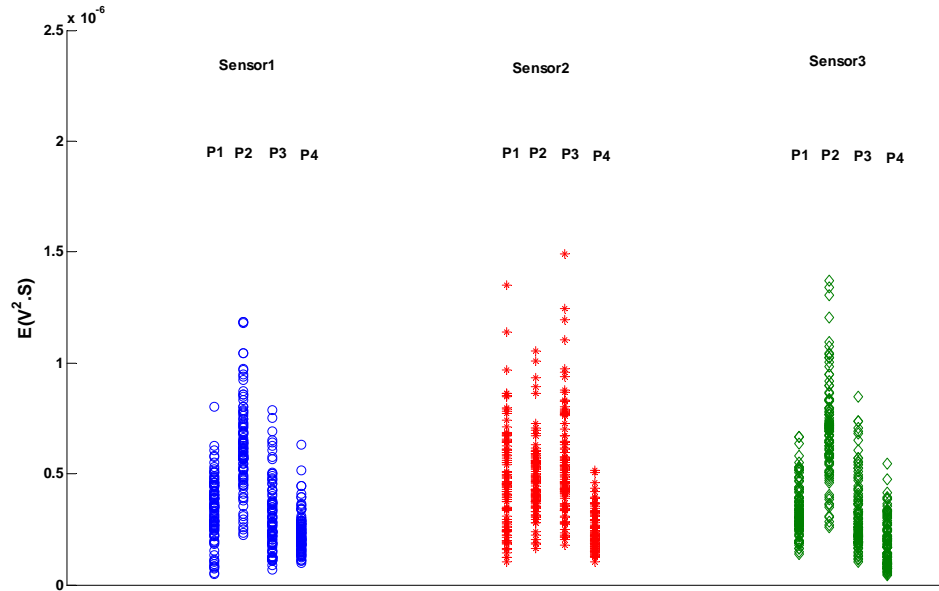
Figure 3.15: AE energy recorded at the three sensors on the steel block at four positions.
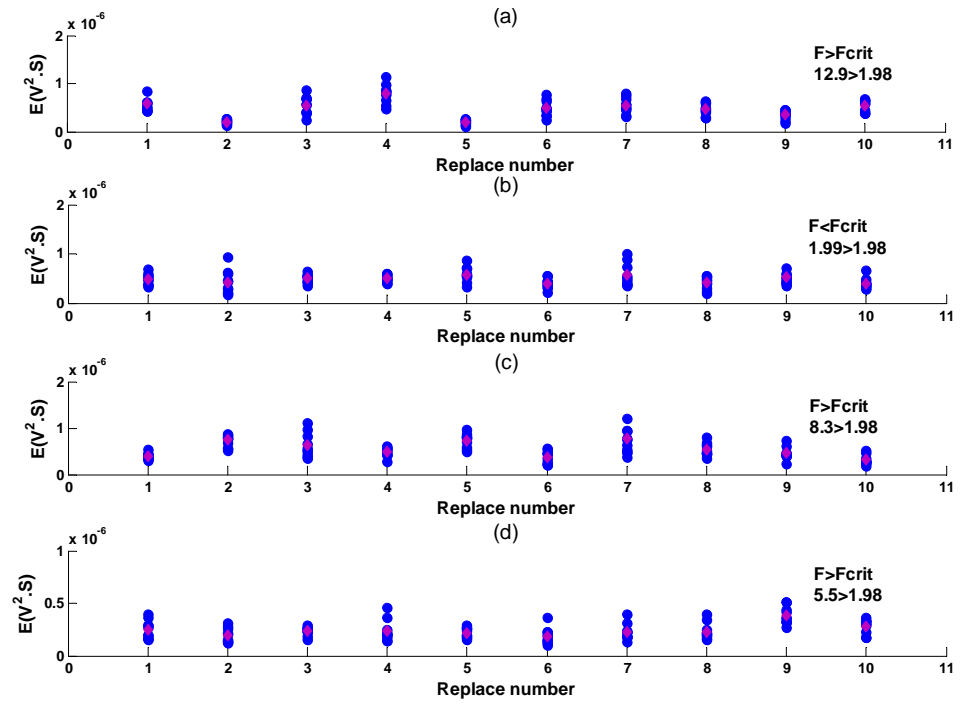
Figure 3.16: Sensor 1 energy distribution for 10 placements at four positions; (a) position 1, (b) position 2, (c) position 3, (d) position 4.

Sensor	Position	F Value
1	1	12.9696
1	2	1.9978
1	3	8.3188
1	4	5.5898
2	1	8.5964
2	2	2.3407
2	3	13.9594
2	4	3.4022
3	1	2.8630
3	2	1.9942
3	3	11.2764
3	4	17.6060

Table 3.1: Summary of Anova results comparing effects of variation in source with variation in coupling for each sensor at each position.

The data for each position for all three sensors has been grouped to analyse the variance between positions and within positions. This will compare the effect of position with the effect of lead break, sensor and coupling. Table 3.2 shows that F_{value} is always greater than F_{crit} (3.026 for the degrees of freedom involved and at the 95% confidence level) which indicates that the effect of changing position is more important than the variation in pencil lead breaks, sensor and coupling. Finally the data for each sensor at all four position has been grouped to analyse the variance between sensors with variance from lead break, position and coupling. The F_{value} is again greater than F_{crit} which indicates that the effect of changing sensor is significant and led to the use of the same sensor for all experiments.

Position	F Value
1	27.9
2	140.2
3	14.6
4	131.8

Table 3.2: Summary of Anova results comparing effects of variation in position with variation in lead break, sensor and coupling at each position.

Next, the S9215 sensor and the selected Micro-80D sensor were calibrated back-to-back on the steel block. The two sensors were mounted at the same radial distance, 62.5 mm from the source, and 100 pencil lead breaks acquired without moving or removing either sensor. The objective of this calibration was to identify the variation in sensitivity between sensors. The average AE energy of both sensors was calculated using equation 2.4 and it was found that the Micro-80D sensor gave AE energy 80-140 times higher than the S9215 sensor using the same gain settings as in the experiment. Figure 3.17 shows the raw AE spectra for both sensors on steel block, reflecting the narrow bandwidth of the S9215 sensor (50-250 kHz) compared with the Micro-80D sensor (100-400 kHz). Appendix A contains sensitivity calibration certificates for AE transducers S9215, and Micro-80D.
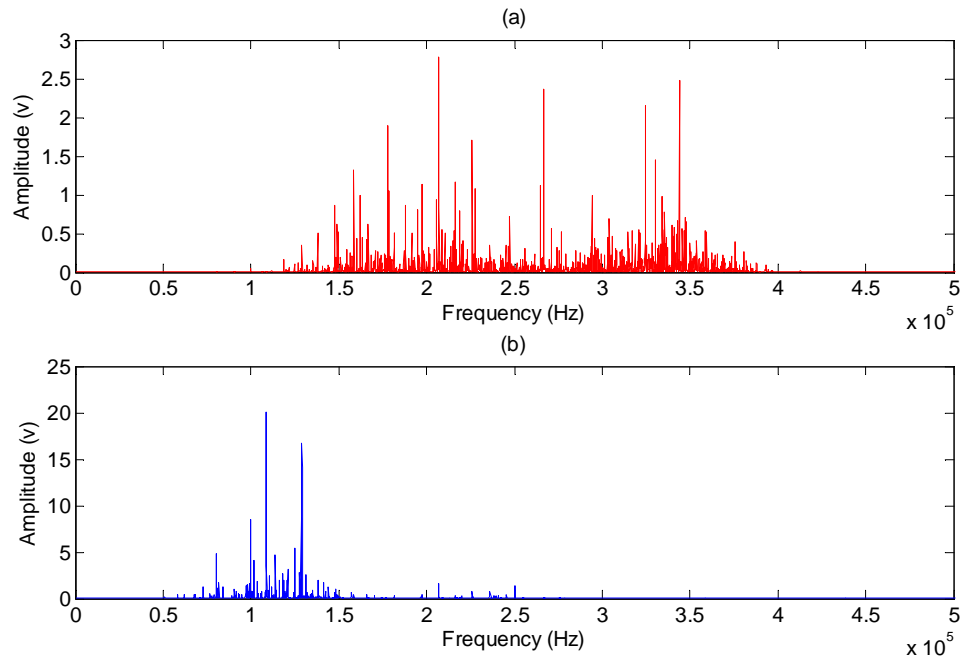
Figure 3.17: Frequency domain of two AE sensor on steel block (a) Micro-80D (exhaust) sensor, (b) S9215 (shroud) sensor.

3.4.2. Calibration test on gas turbine:

This calibration was carried out to identify any changes and/or deterioration in sensor sensitivity associated with mounting onto the turbine surface. The S9215 was mounted on the free power turbine shroud using an in-house manufactured clamp. A flat contact surface of diameter equal to that of the sensor and depth 2mm was machined onto the free power turbine shroud. The Micro-80D sensor was mounted onto the waveguide using a magnetic clamp. Figure 3.18 shows a schematic of the free power turbine with the sensor positions. A total of 50 pencil lead breaks with the source either mid-way along the exhaust or on the turbine shroud were acquired for each sensor in each of three conditions; before an experiment with the turbine cold, immediately after an experiment with the turbine hot, and some time after an experiment when the turbine was cold.
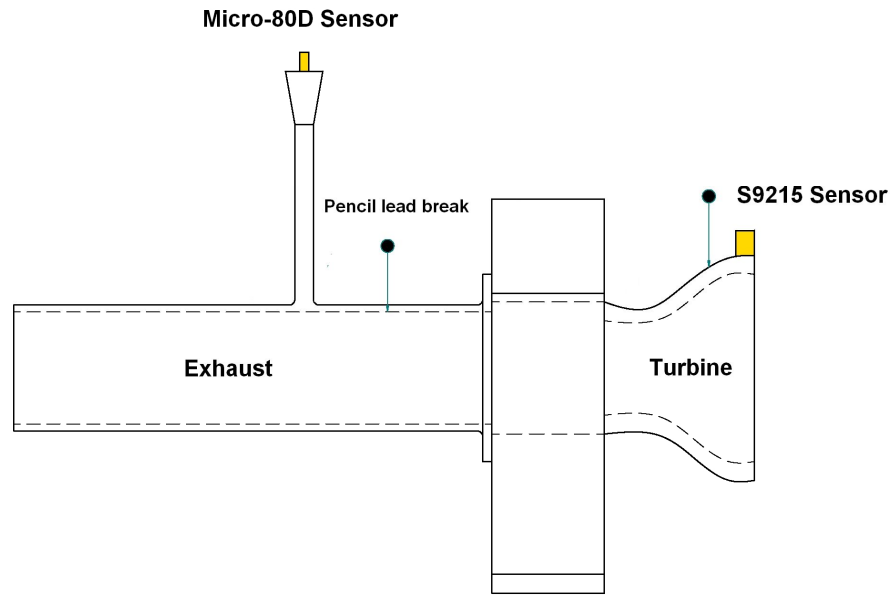
Figure 3.18: Turbine sensor calibration arrangement showing sensor and AE source positions.

Figure 3.19 shows how the AE energy of pencil lead breaks as recorded by the S9215 sensor varies before and after turbine operation and Figure 3.20 shows the same data plotted as histograms. Comparing the three responses using Anova gave an F_{value} of 75 compared with F_{crit} of 3.05, and comparing the values between hot and cold experiments after testing, F_{value} was found to be 6.4 compared with an F_{crit} of 3.98. Thus, the S9215 sensor is significantly more sensitive at higher temperatures although the variation is significantly greater after running the turbine, even when cold.
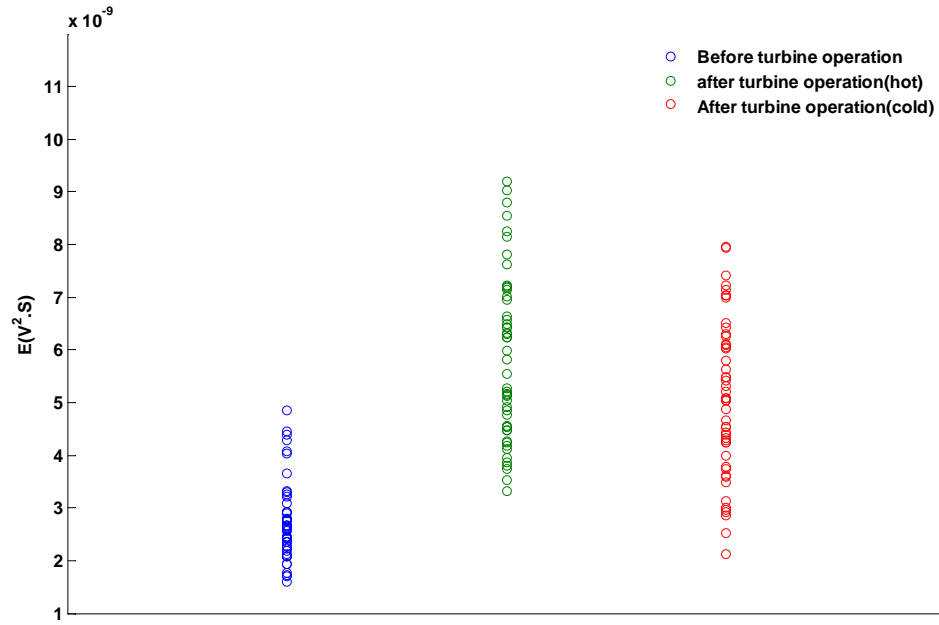
Figure 3.19: AE energy calibration of S9215 sensor on turbine rig.
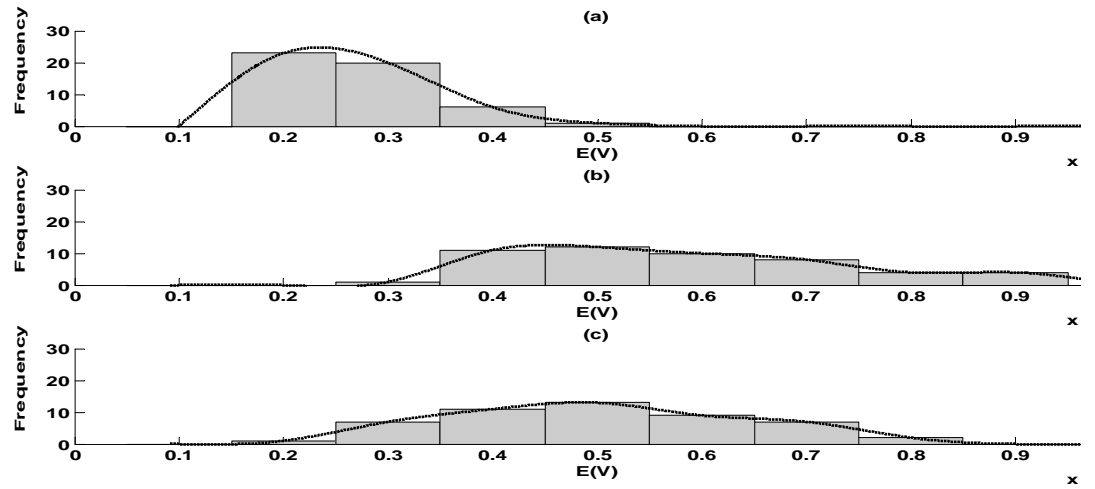
Figure 3.20: Histogram of AE energy for S9215 sensor calibration on turbine rig, (a) before turbine operation, (b) after turbine operation (hot), (c) after turbine operation (cold).

Figures 3.21 and 3.22 show the AE energy and histograms for the Micro-80D sensor for the turbine calibration experiment. Carrying out Anova among the three conditions gave a value of F_{value} of 55.3 compared with F_{crit} of 3.98, and comparing the hot and cold

values before and after testing gave F_{value} of 4.58 against an F_{crit} again of 3.98. Thus, the Micro-80D sensitivity goes down when the turbine is hot, even though it should be within its normal operating temperature range. Once the temperature returns to normal, the response is practically the same as it was before the test.
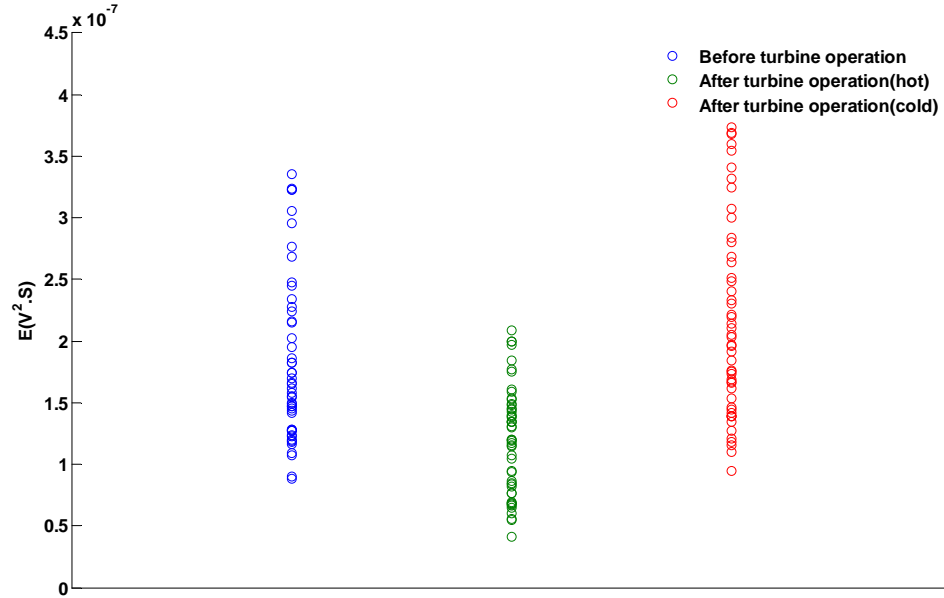
Figure 3. 21: AE energy calibration of Micro-80D sensor on turbine rig.
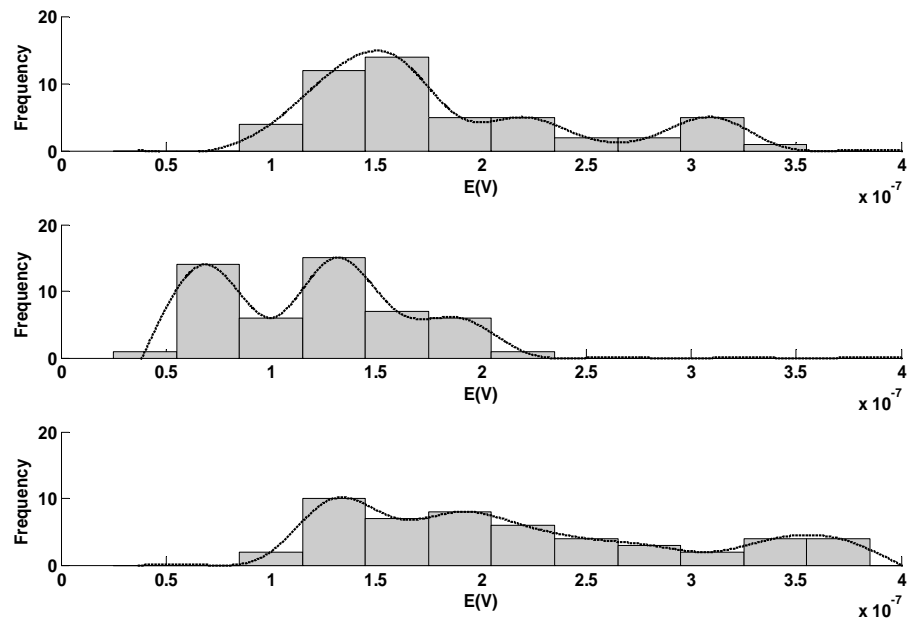
Figure 3. 22: Histogram of AE energy for Micro- 80D sensor calibration on turbine rig, (a) before turbine operation, (b) after turbine operation (hot), (c) after turbine operation (cold).

3.4.3. AE propagation on gas turbine:

These tests were carried out to investigate the attenuation and frequency distortion of sources at various positions on the free power turbine as recorded by the two different AE sensors at the two different positions (turbine shroud and turbine waveguide). Thus, the effects not only of source-sensor distance, but also aspects of the geometry of the turbine such as discontinuities, webs and non-uniform cross section could be studied for potential sources resulting from gas flow through the turbine blades and exhaust, oil lubrication, and bearings in addition to unwanted sources such rubbing of mountings due to vibration. In this test three AE sensors were used, two Micro-80D sensors and one S9215 sensor. One Micro-80D sensor was positioned on the waveguide (as used in the experiments) and another on the turbine shroud adjacent to the S9215 sensor in order to assess the relative effects of sensor type. The source position was moved along the free power turbine starting at the shroud and ending at the exhaust with ten repeat breaks being recorded for each sensor at each position. Figure 3.23 shows the sensors and source positions.
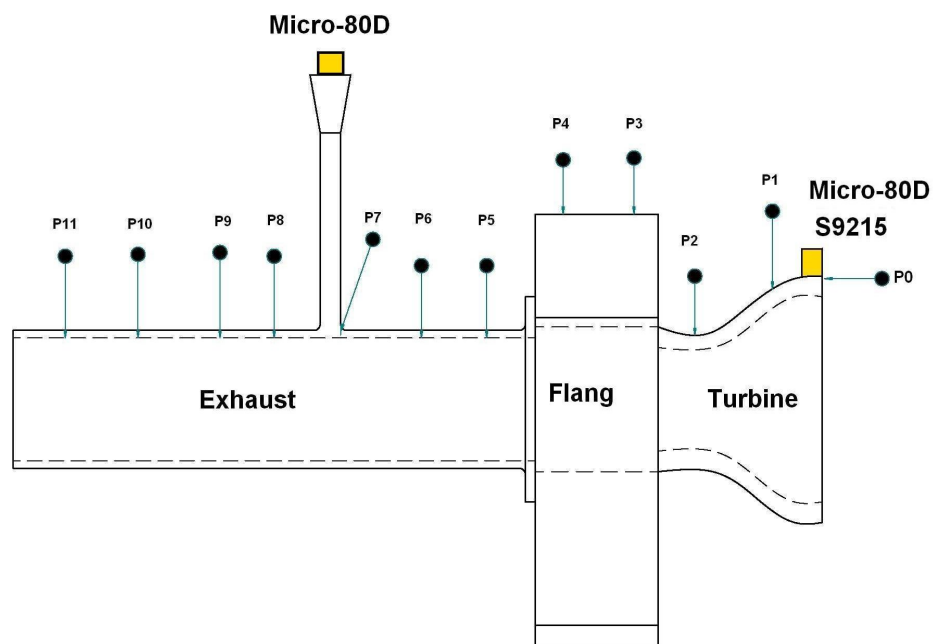
Figure 3.23: Turbine propagation test arrangement showing sensors and AE source positions.

The energy, calculated as for the calibration tests, was plotted as a function of source-sensor distances and the best-fit exponential decay curve, according to equation (2.4), used to determine an attenuation coefficient. Figures 3.24 and 3.25 show the energy plots with the best-fit exponential decay curves for the S9215 sensor and Micro-80D sensor, respectively, mounted on the turbine shroud. Both figures exhibit high variability of AE energy in the region close to the sensor position, i.e. on the turbine shroud. Such an effect has been attributed [27, 32, 123] to the complicated near-field waves compared with reflected waves. Both graphs also show a marked reduction in energy following major discontinuities in the structure, illustrated as vertical dotted lines.
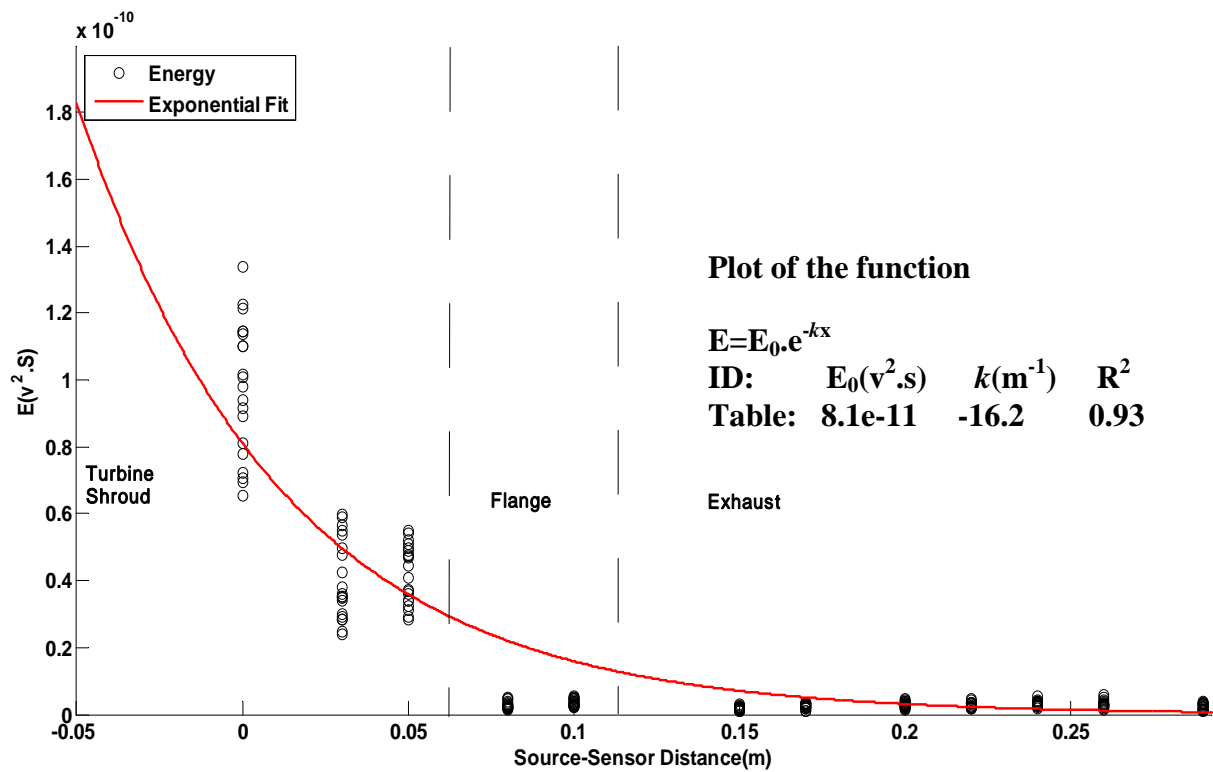
Figure 3.24: AE energy versus source-sensor distance with best-fit exponential decay curve for S9215 sensor mounted on turbine shroud.
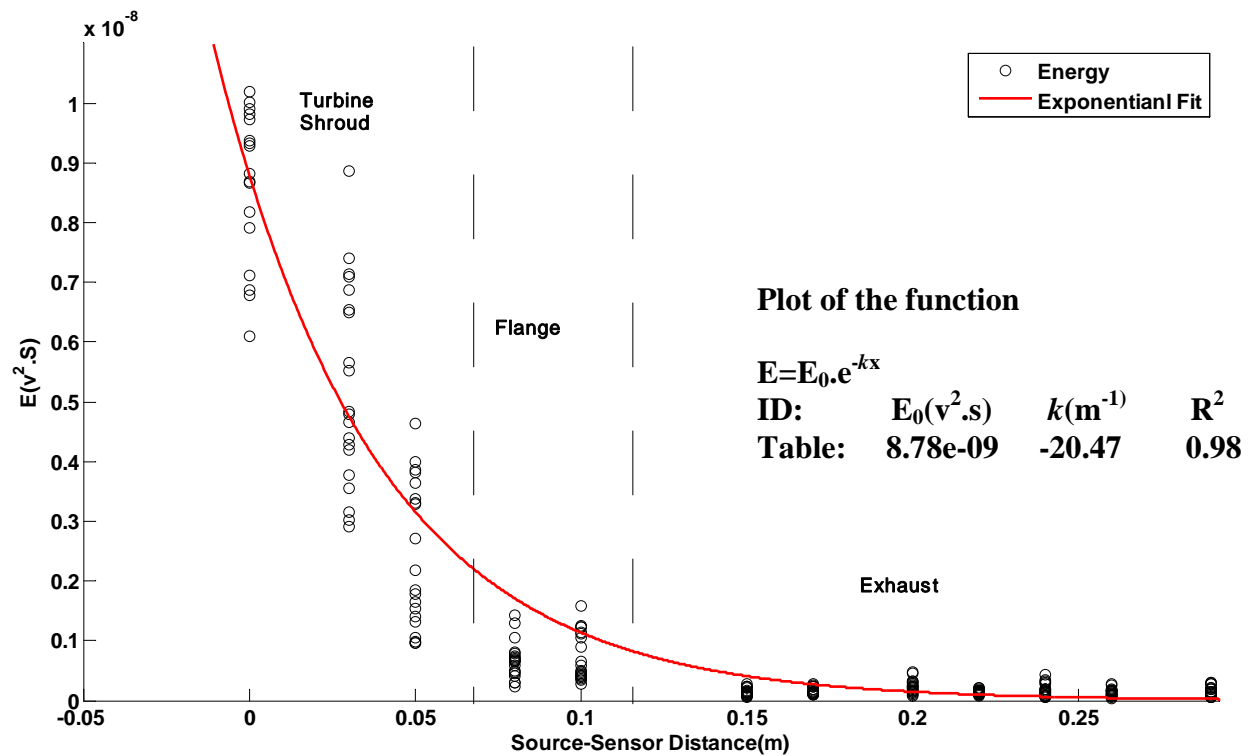
Figure 3.25: AE energy versus source-sensor distance with best-fit exponential decay curve for Micro-80D sensor mounted on turbine shroud.

Figure 3.26 shows the AE energy plot with best-fit exponential decay for the Micro-80D sensor mounted on the waveguide, where the source-sensor distance is measured to the bottom of the waveguide. Compared with the other two curves, the attenuation curve is rather steeper and the scatter in the area close to the sensors is considerably greater. It is unlikely that the reason for this scatter is associated with the near field as the sensor is actually quite distant from the root of the waveguide, although it is quite likely that the amount of AE being transmitted up the waveguide is sensitive to this field.
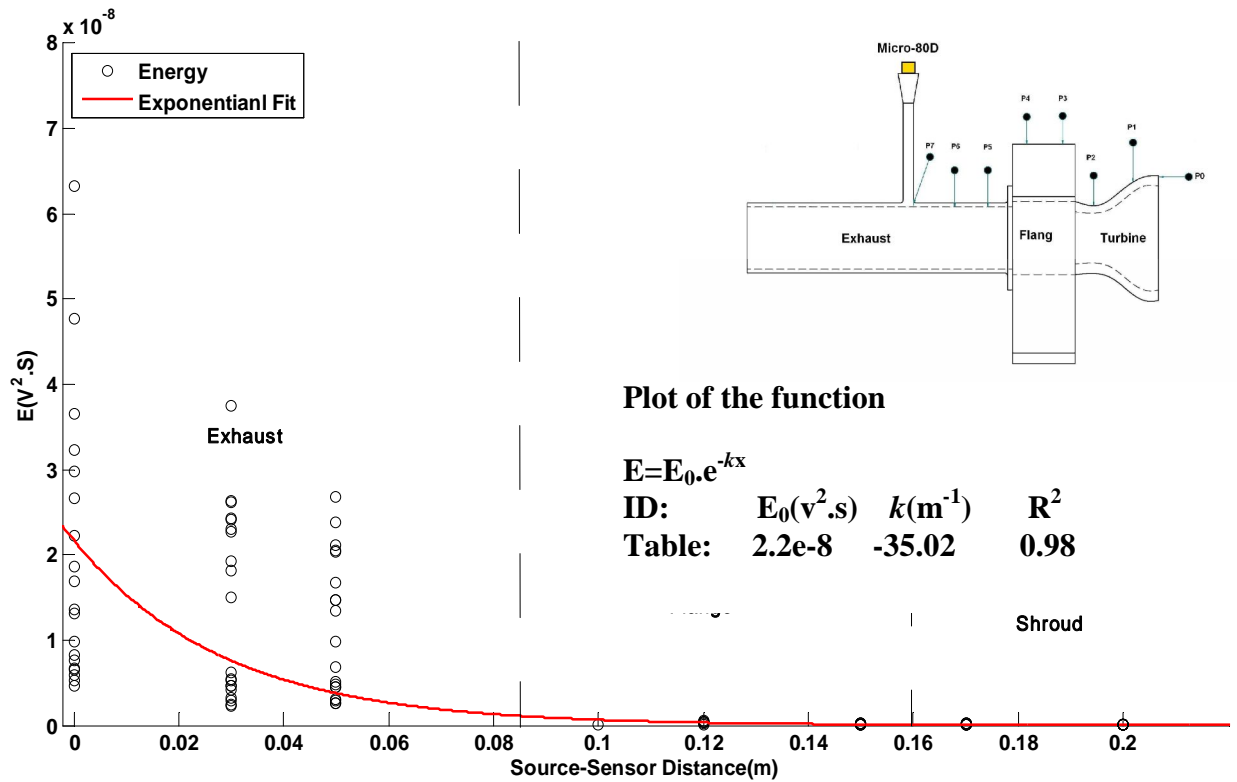
Figure 3.26: AE energy versus source-sensor distance with best-fit exponential decay curve for Micro-80D sensor on waveguide.

To illustrate the detectability by each of the sensors of an AE source with respect to source position in the turbine figure 3.27 shows the logarithmic attenuation using equation (2.2) [22, 27, 29] data plotted against position on the turbine. The reference source in this analysis was position P0 for the S9215 sensor and P7 for the Micro-80D sensor and the average value of the maximum amplitude of ten pencil lead breaks was used to produce each data point. As before, the vertical dotted lines represent discontinuities in the surface. Figure 3.27 demonstrates that the S9215 sensor is clearly sensitive to sources in the turbine and the flange, but that the Micro-80D sensor on the waveguide also detects such sources since the attenuation decreases as the source is moved towards the sensor although there is a distance between the sensor and the turbine. There seems to be very little attenuation for either sensor for positions along the exhaust. When monitoring the turbine operation it is important to note that sources in the turbine will be weaker ranging between 30 and 15dB as seen by the Micro 80D sensor and sources at the exhaust weaker by about 30dB as seen by the S9215 sensor.
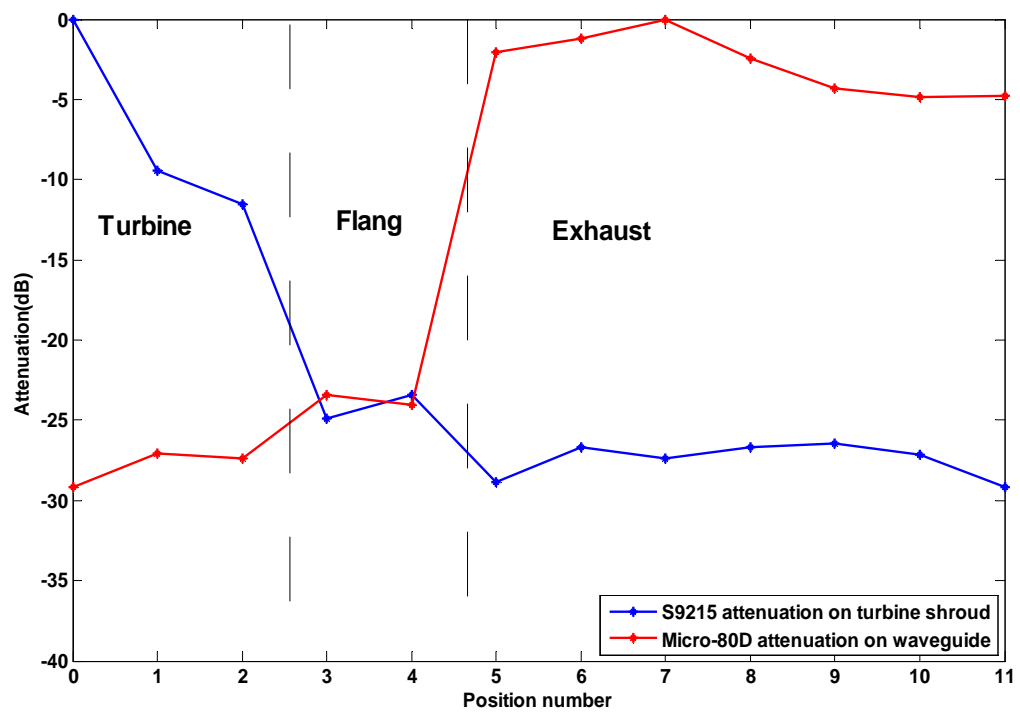
Figure 3.27: Micro-80D & S9215 sensor attenuation characteristics for sources on the turbine surface.

Chapter 4 Results: normal running tests and tests without functioning impeller

This chapter summarises the results of the tests with the turbine running normally, either idling with the speed being controlled by fuel and air flow, or under load at fixed fuel and air flow with the speed being controlled by the amount of load applied. The results of the two abnormal running tests are also presented here, i.e. those in which the impeller was either prevented from rotation or removed entirely. Together, these experiments provide a range of conditions of gas flow through the turbine, from the simplest cases with no impeller and with a stationary impeller, through idling and, finally, with the impeller being used to extract power from the gas.

The analysis in this chapter is confined to simple time- and frequency-domain processing, with higher level analysis and discussion of the results being deferred to Chapter 5.

4.1. Turbine operation test without impeller

This configuration is the simplest of those studied for turbine operation, where the impeller had been removed and replaced by a non-rotating disc which essentially acts as a simple baffle in the free power turbine. As with all non-rotating tests, the principal experimental variable is the gas generator speed.

Figures 4.1 and 4.2 show samples of normalized AE signals recorded, respectively, from the Micro-80D sensor on the waveguide attached to the turbine exhaust and the S9215 sensor mounted directly onto the turbine shroud. Each AE signal was normalized as a proportion of the maximum amplitude in the AE record in order to avoid distortion by the varying total energy. Records at nine different gas generator speeds are shown, both in raw form and with the associated signal envelopes, obtained by taking the RMS with an averaging time of 0.03 ms. The averaging time value has been chosen to make balance between processing time, which would high if we use shorter averaging time, and the expense of information loss, which would to much if use longer averaging time. The Micro80D (exhaust) signals exhibit some higher amplitude bursts of approximate duration 1ms, and these seem to be more prevalent as the gas generator speed increases. These bursts appear to be aperiodic in nature and are set on an apparently continuous background. The S9215 (turbine shroud) sensor does not show such obvious bursts and

the AE activity appears continuous at all gas generator speeds. Table 4.1 shows the running speed of gas generator turbine of without impeller test.

Without impeller test speed	Gas generator speed (RPS)
S1	500
S2	600
S3	700
S4	850
S5	900
S6	934
S7	1017
S8	1133
S9	1167

Table 4. 1: Gas generator speed of without impeller test.
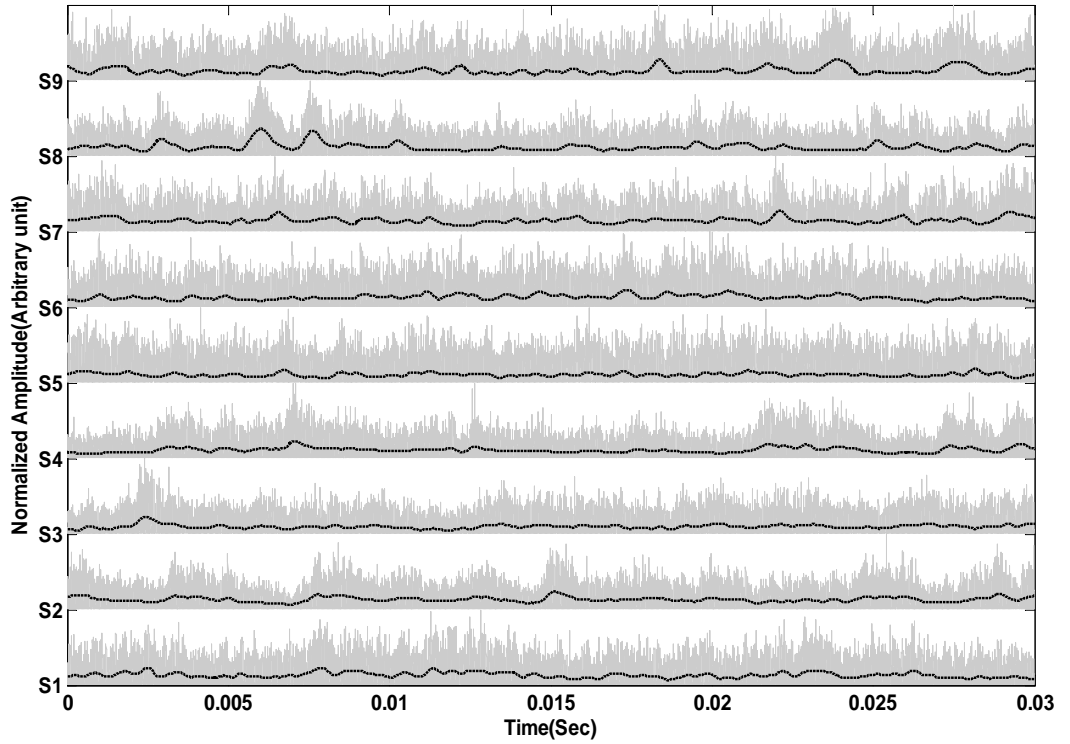
Figure 4.1: Typical Micro-80D AE signatures (exhaust) for test without impeller. Gas generator speed increases from bottom to top, with S1 recorded at 500 RPS and S9 recorded at 1170 RPS.
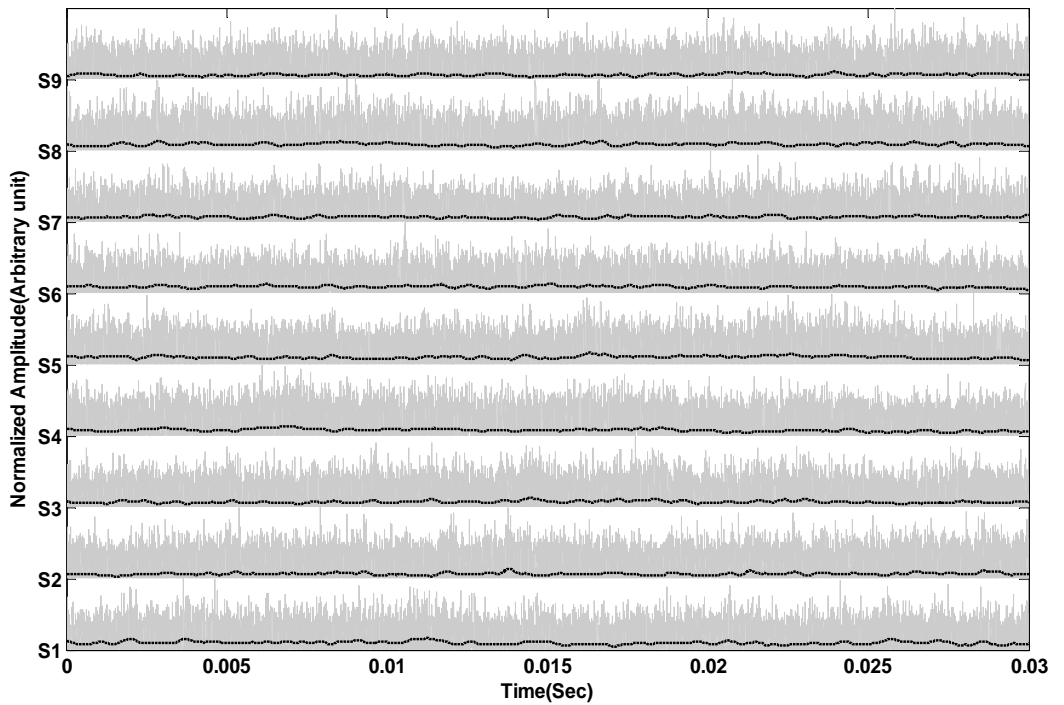
Figure 4.2: Typical S9215 AE signatures (shroud) for test without impeller. Gas generator speed increases from bottom to top, with S1 recorded at 500 RPS and S9 recorded at 1170 RPS.

Figures 4.3 and 4.4 show the evolution of AE energy with gas generator speed for the exhaust and turbine shroud sensors, respectively. Each point represents the energy content of the record using equation 2.4 and all 20 values are shown at each speed for each of the two tests. As can be seen, the AE energy at a given speed seems consistent between the records (each of which accounts for typically 15-33 revolutions of the machine) but there is a marked variation in the level of energy between the two tests for the exhaust-mounted sensor, not reflected in the record for the shroud-mounted sensor. Given that the surface of the shroud is hot, it is possible that this variation was due to some degradation of the coupling between the two tests. Notwithstanding this, both sensors indicate an increase in AE energy with a speed of an increasing slope, fitted here using an exponential growth function. It might also be noted that the energy recorded on the shroud is a factor of 50-100 lower than that recorded at the exhaust, which is approximately the same as the ratio of the sensitivities of the two sensors when both are mounted on the turbine shroud (cold) and on the steel block.

Figures 4.5 (a) and (b) show typical raw AE spectra for the nine speeds for the Micro-80D and S9215 sensors, respectively. These spectra have been normalized across the relevant filter bandwidth so that the effect of the absolute energy does not mask the frequency content. The effect of the different analogue filters and sensor bandwidths is immediately apparent in the two sensor responses, with significant energy being shown by the S2915 sensor in the 0.05 to 0.1MHz range, just below the analogue filter cut-off for the Micro-80D sensor. Despite this, both the Micro-80D and S2915 sensors show a very strong peak at around 7.5kHz at some speeds which must be very strong indeed to be able to penetrate the filter. Within its bandwidth, the Micro-80D shows a general narrowing of the frequency content of the signal toward the bottom end of the filter band-pass, and this probably indicates a shift to frequencies below 0.1MHz. Conversely, the S9210 sensor shows a (less marked) migration of the frequency content towards a band between 80 and 100kHz.
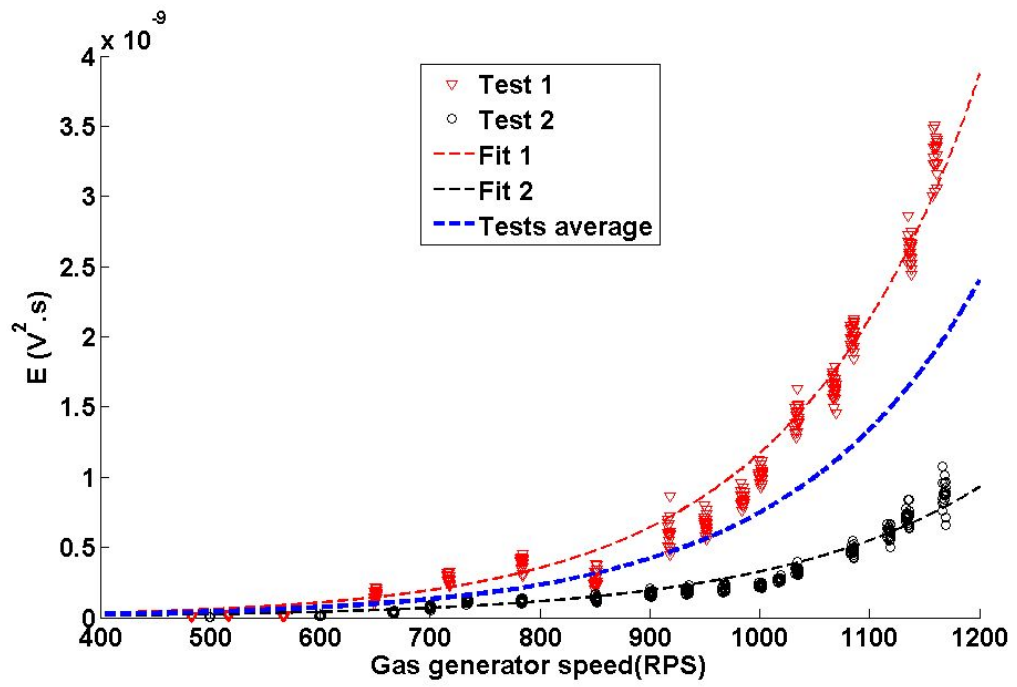
Figure 4.3: Micro-80D (exhaust) sensor AE energy *vs.* gas generator speed for tests without impeller.
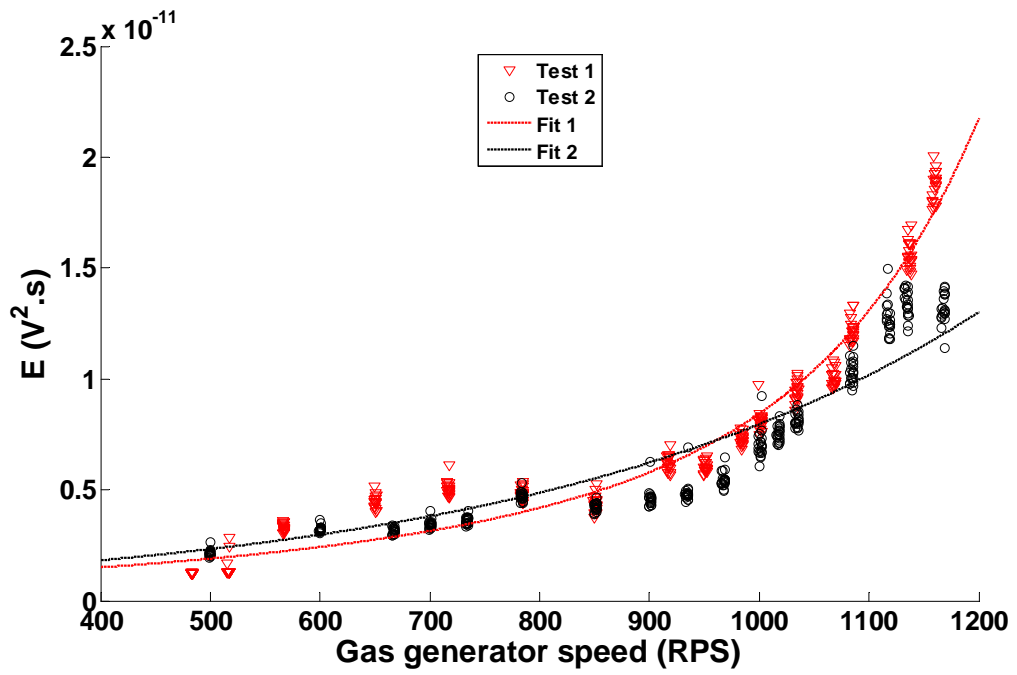
Figure 4.4: S9215 (shroud) sensor AE energy *vs.* gas generator speed for tests without impeller.
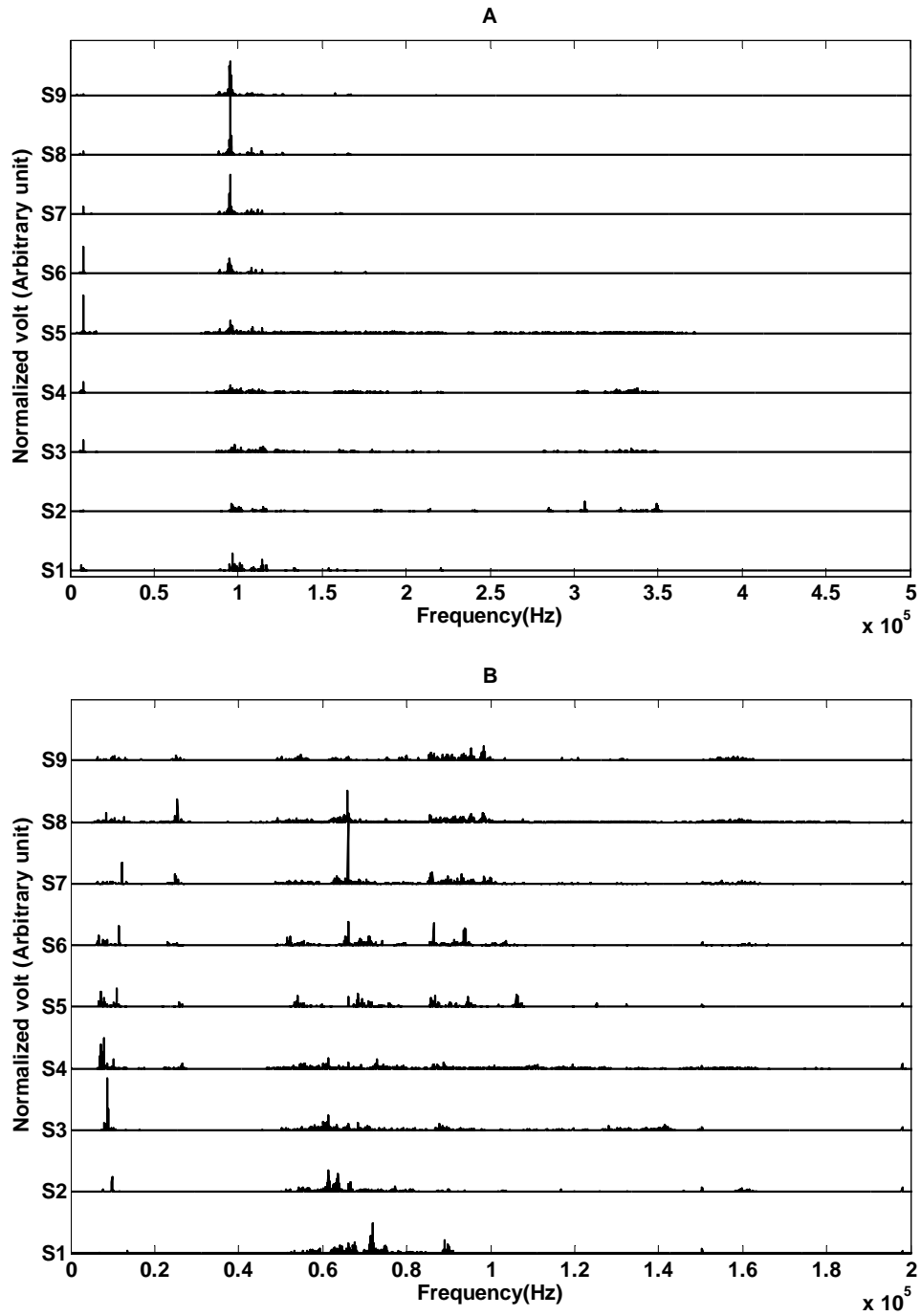
Figure 4.5: Typical raw AE spectra for test without impeller: (a) Micro-80D sensor, (b) S9215 sensor. Gas generator speed increases from bottom to top, with S1 recorded at 500 RPS and S9 recorded at 1170 RPS.

Demodulated frequency analysis was also applied to the signals by RMS averaging them over 150 points, making an effective sampling rate of 33333 Hz. Transforming the resulting signals into the frequency domain shows pulsatile information at frequencies up to 1kHz and samples of such spectra are shown in Figures 4.6 and 4.7 (the spectra have been normalized). The Micro-80D sensor on the turbine exhaust shows a peak whose frequency increases with the gas generator speed, varying from 300 Hz at 490 rps to 700 Hz at 1170 rps. These frequencies are absent in the records of the S9215

sensor mounted on the turbine shroud. Table 4.2 shows the running speed of gas generator turbine of without impeller test.

Without impeller test speed	Gas generator speed (RPS)
S1	500
S2	600
S3	667
S4	700
S5	734
S6	784
S7	850
S8	900
S9	934
S10	967
S11	1000
S12	1017
S13	1034
S14	1083
S15	1117
S16	1133
S17	1167

Table 4. 2: Gas generator speed of without impeller test1.
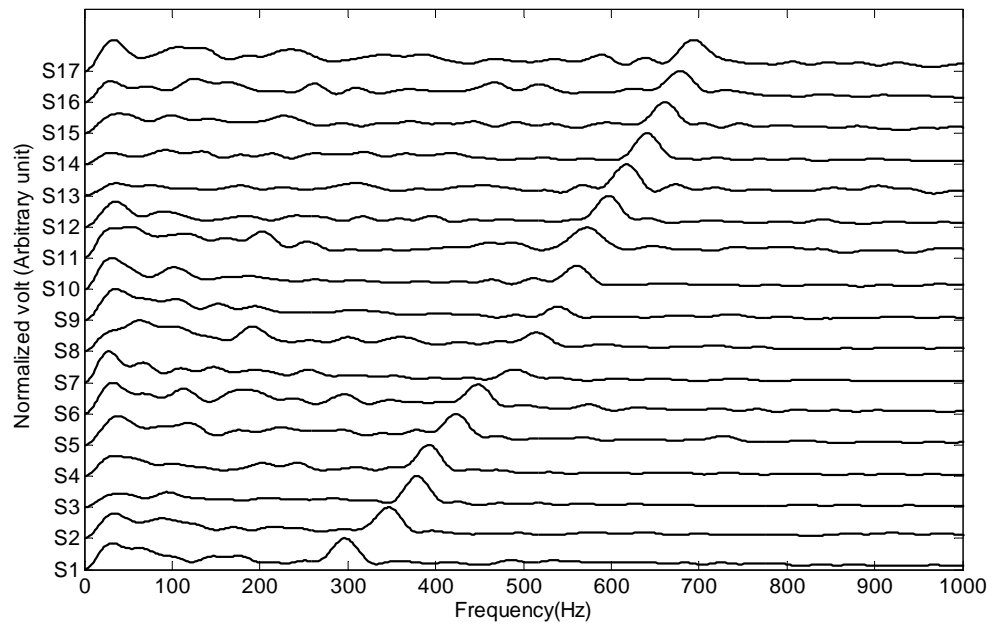
Figure 4.6: Typical demodulated AE spectra for test without impeller with Micro-80D sensor. Gas generator speed increases from bottom to top, with S1 recorded at 500 RPS and S17 recorded at 1170 RPS.

Figure 4.7: Typical demodulated AE spectra for test without impeller with S9215 sensor. Gas generator speed increases from bottom to top, with S1 recorded at 500 RPS and S17 recorded at 1170 RPS.

4.2. Test with jammed impeller

Figures 4.8 and 4.9 again show samples of raw and enveloped normalized AE signals for the two sensors at nine speeds of the gas generator turbine. As for the test with the absent impeller, the signals for the sensor mounted on the exhaust show apparently aperiodic pulses whose occurrence becomes more frequent as the gas generator speed increases. In this case, however, the pulses are of rather longer duration, typically around 5ms. The S9215 sensor shows much shorter bursts (typically less than 1ms) and the occurrence of the bursts does not seem to depend on running speed. Table 4.3 shows the running speed of gas generator turbine of jammed impeller test.

Jammed impeller test speeds	Gas generator speed (RPS)
S1	550
S2	567
S3	592
S4	617
S5	667
S6	683
S7	733
S8	783
S9	817

Table 4. 3: Gas generator speed of jammed impeller test.
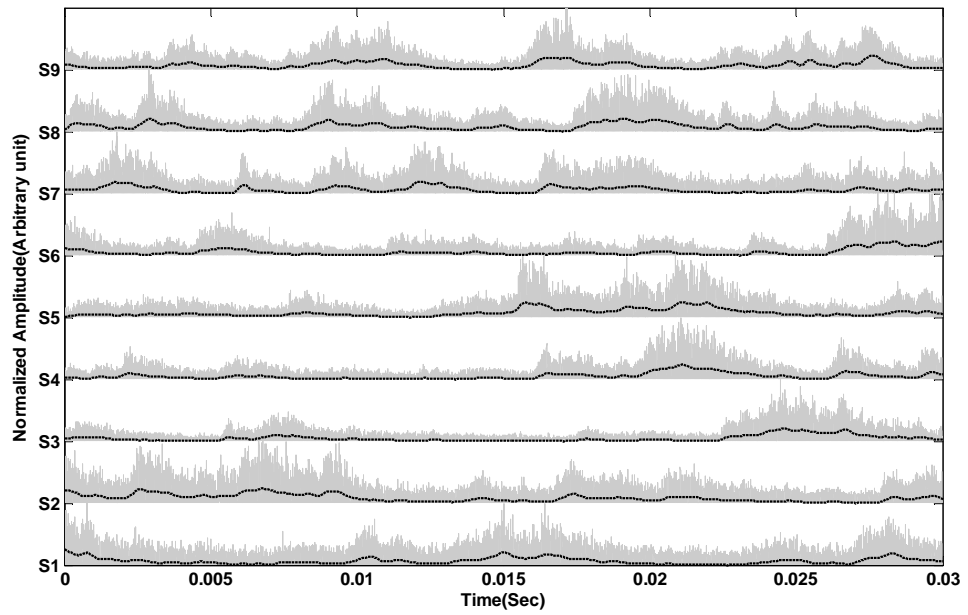
Figure 4.8: Typical Micro-80D AE signatures for jammed impeller test. Gas generator speed increases from bottom to top, with S1 recorded at 500 RPS and S9 recorded at 850 RPS.
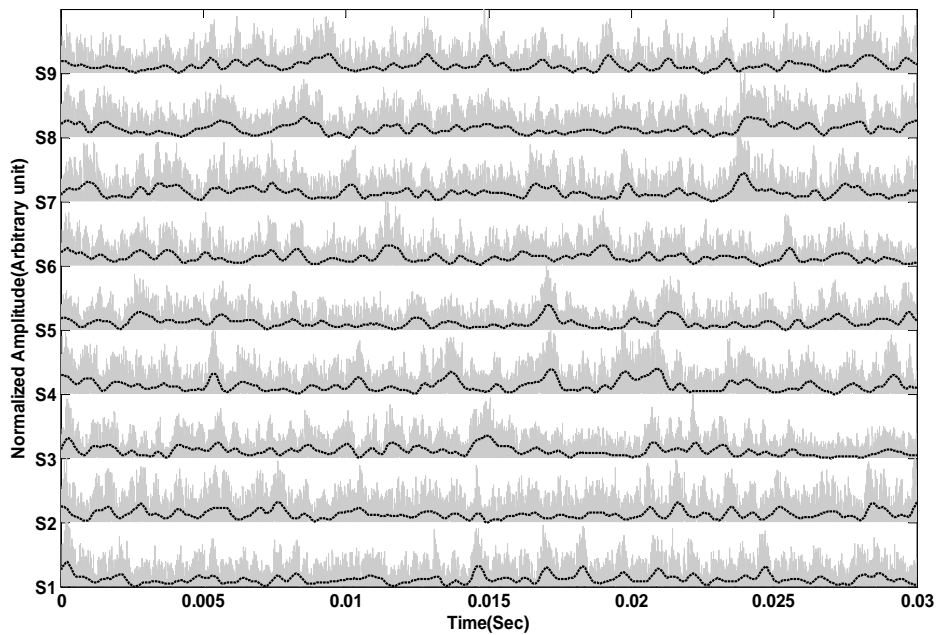
Figure 4.9: Typical S9215 AE signatures for jammed impeller test. Gas generator speed increases from bottom to top, with S1 recorded at 500 RPS and S9 recorded at 850 RPS.

Figures 4.10 and 4.11 show the evolution of AE energy with gas generator speed for the two AE sensors. The two tests give repeatable results and, as for the test with the impeller absent, there is a monotonic increase in energy with gas generator speed. Unlike the test with the impeller absent, the energy recorded at the two sensors is of

approximately the same magnitude indicating a shift in the total energy of the source away from the exhaust towards the shroud.
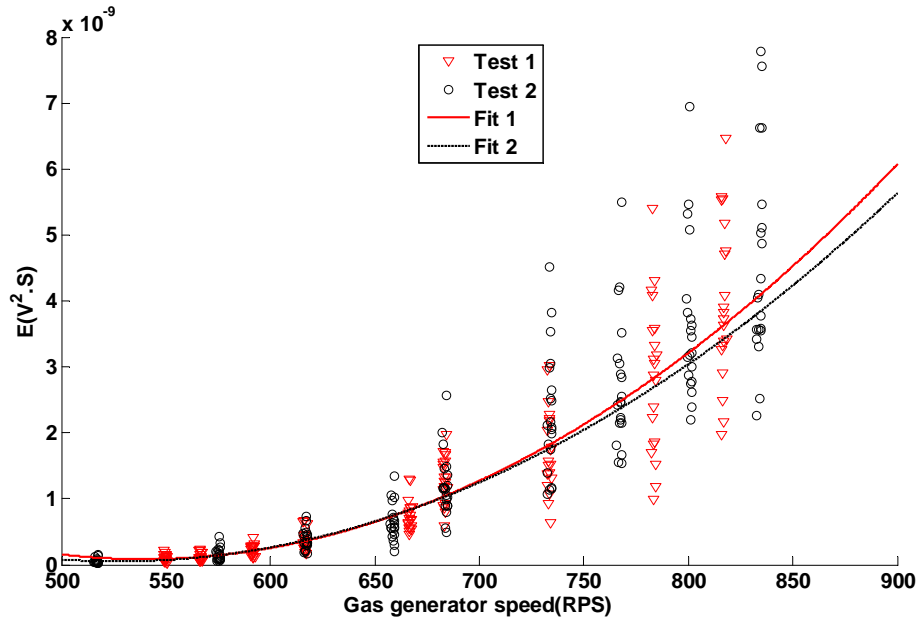
Figure 4.10: Micro-80D (exhaust) sensor AE energy *vs.* gas generator speed for tests jammed impeller.

.
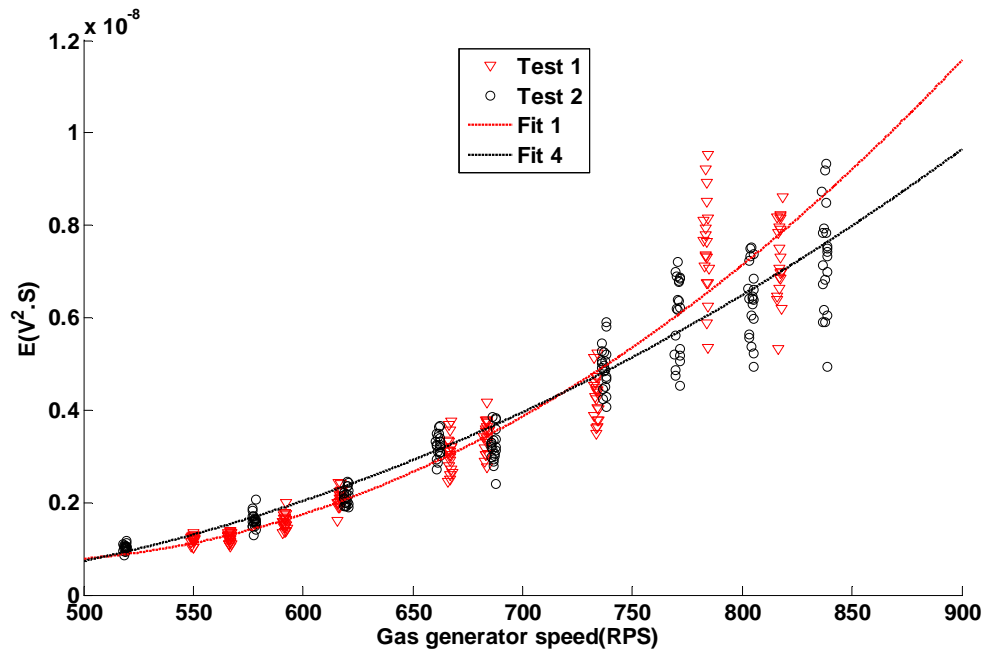
Figure 4.11: S9215 (shroud) sensor AE energy *vs*. gas generator speed for tests jammed impeller.

Figure 4.12 shows samples of the normalised raw AE spectra across the relevant filter bandwidth for nine speeds of the gas generator turbine for both sensors. Unlike the case for the absent impeller, there is a systematic shift in AE energy towards the higher end

of the frequency band at around 350kHz. The energy recorded by the S9215 sensor is focused in a narrow band around 27kHz and this does not appear to change much with gas generator speed.
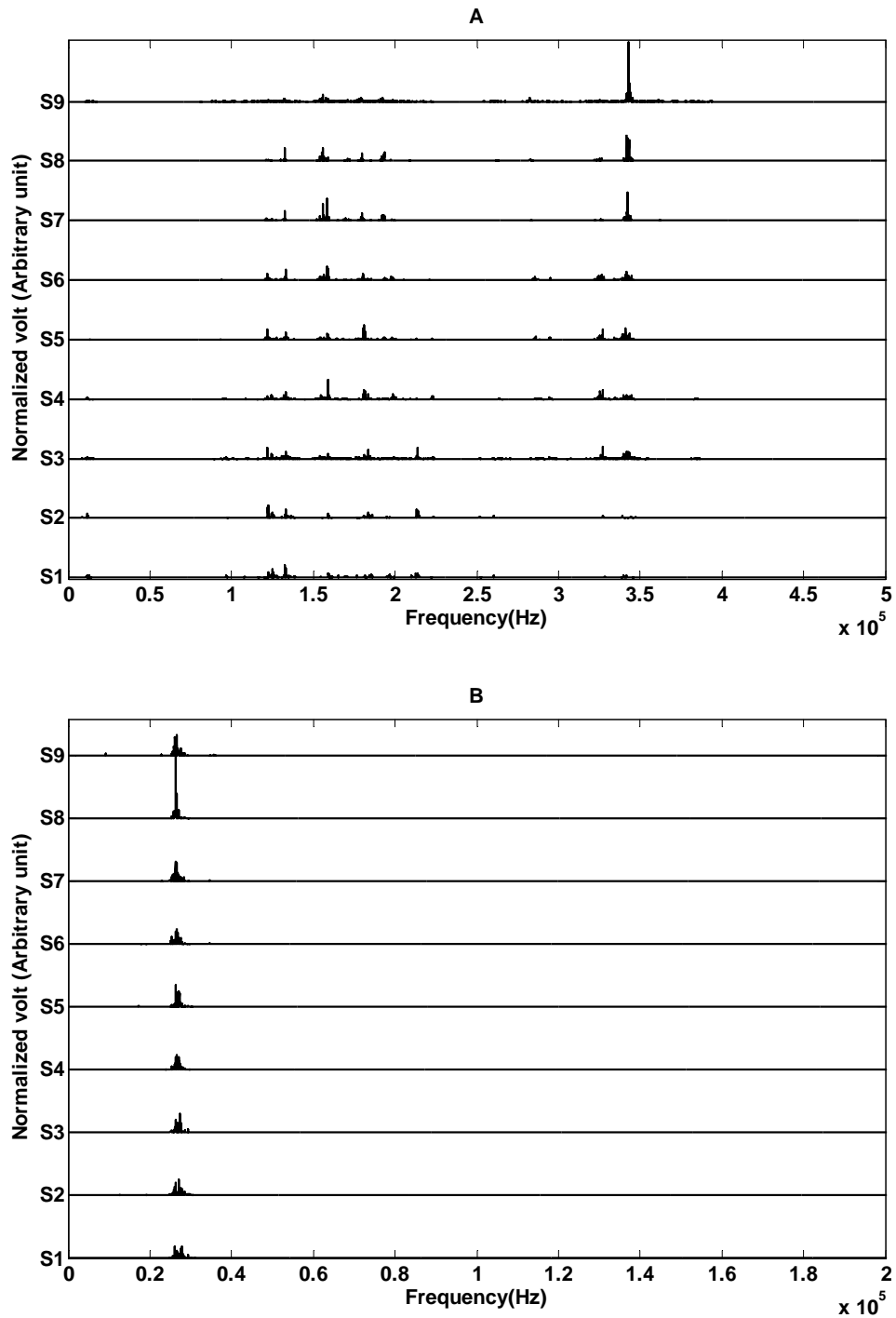
Figure 4.12: Typical raw AE spectra for test jammed impeller: (a) Micro-80D sensor, (b) S9215 sensor. Gas generator speed increases from bottom to top, with S1 recorded at 500 RPS and S9 recorded at 850 RPS.

The demodulated frequency analysis (Figures 4.13 and 4.14) does not show any particular features in the range up to 1500Hz.
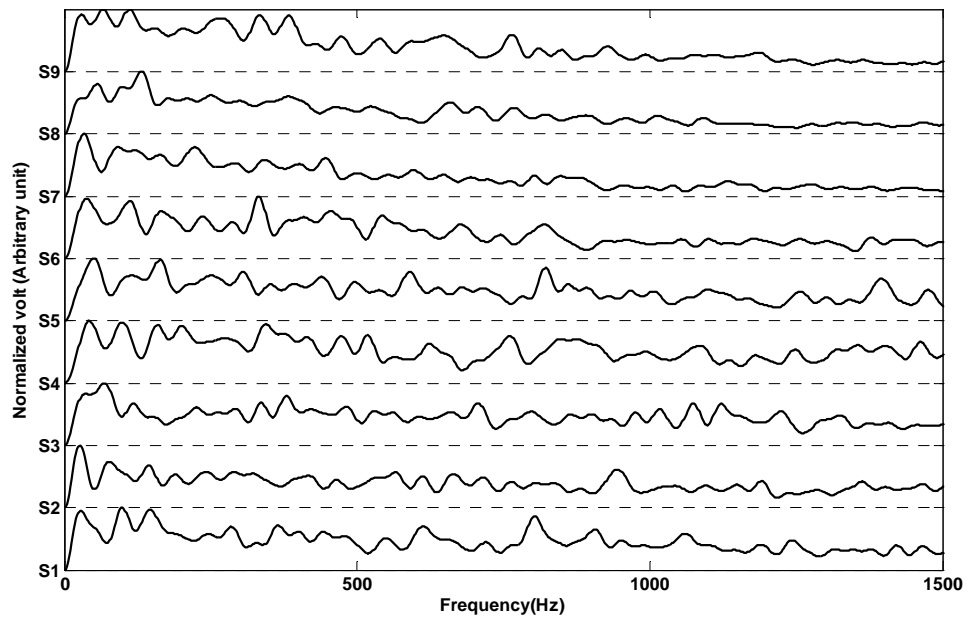
Figure 4.13: Typical demodulated AE spectra for test with jammed impeller with Micro-80D sensor. Gas generator speed increases from bottom to top, with S1 recorded at 500 RPS and S9 recorded at 850 RPS.
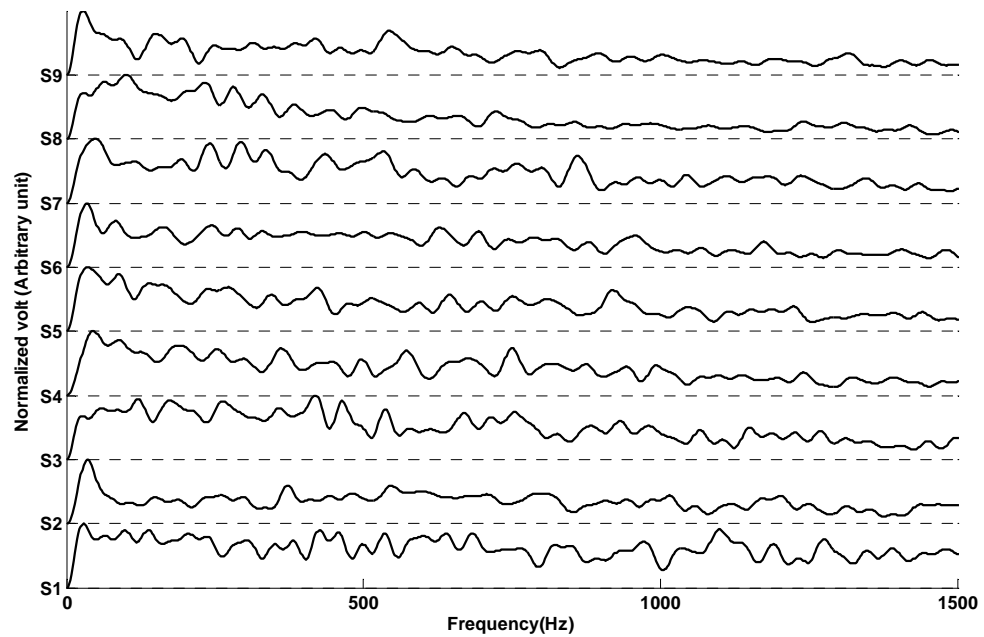
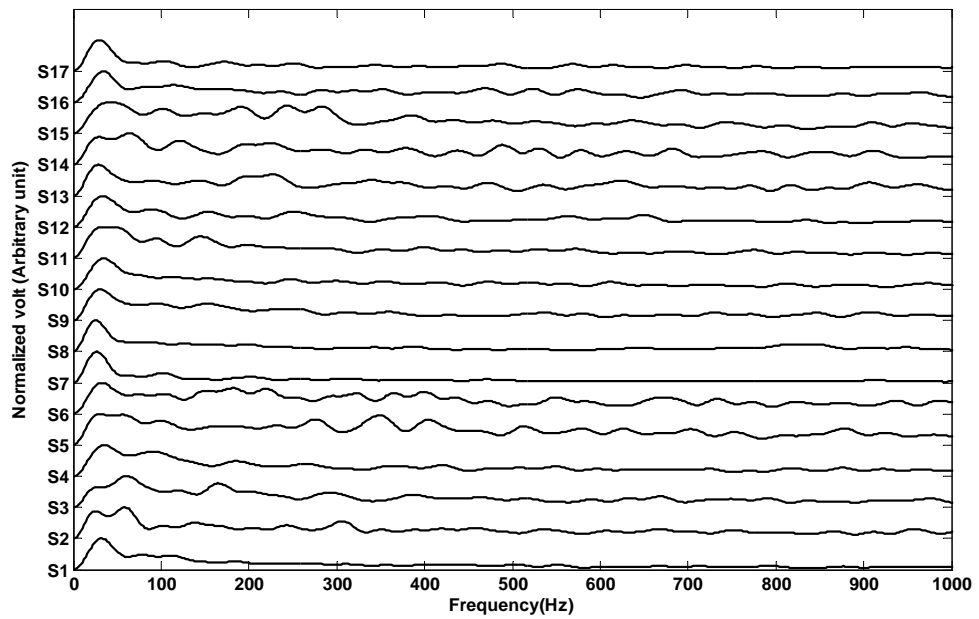Figure 4.14: Typical demodulated AE spectra for test with jammed impeller with S9215 sensor. Gas generator speed increases from bottom to top, with S1 recorded at 500 RPS and S9 recorded at 850 RPS.

4.3. Turbine operation test without load

In this series of tests, both the gas generator turbine and the free power turbine were rotating, so the results are expressed here in terms of the speed of the free power turbine. To assist comparison with the two previous series of tests, Figure 4.15 shows the relationships between FPT and GGT speeds for each of the three tests. Figures 4.16 and 4.17 again show samples of the normalized AE signals recorded by the two sensors. The Micro-80D sensor on the turbine exhaust again exhibits pulse-like events, although these are generally longer and with steeper rise than in the other two tests. Also, at higher speeds of the free power turbine, the individual pulses appear to coalesce so that the signal becomes continuous. As was the case with the jammed impeller, the S9215 record exhibits relatively short pulse, although these, if anything,, become less frequent as the FPT speed increases. Figures 4.18 and 4.19 show the evolution of AE energy with free power turbine speed for the two sensors. For the Micro-80D sensor the general trend curves are similar in shape for each of the three tests and are also similar in shape and magnitude to the jammed impeller tests. In contrast to the jammed impeller tests the measurements on the shroud are about a factor of two higher than those measured at the exhaust. Also, for both sensors, the most striking difference in the idling tests compared with the jammed impeller tests is the considerable degree of increased scatter and the introduction of what appear to be peaks in the energy evolution with FPT speed. Table 4.4 shows the running speed of free power turbine of idling test.

Idling test speeds	Free power turbine speed (RPS)
S1	199
S2	224
S3	243
S4	261
S5	267
S6	292
S7	309
S8	323
S9	339

Table 4. 4: Free power turbine speed of idling test.
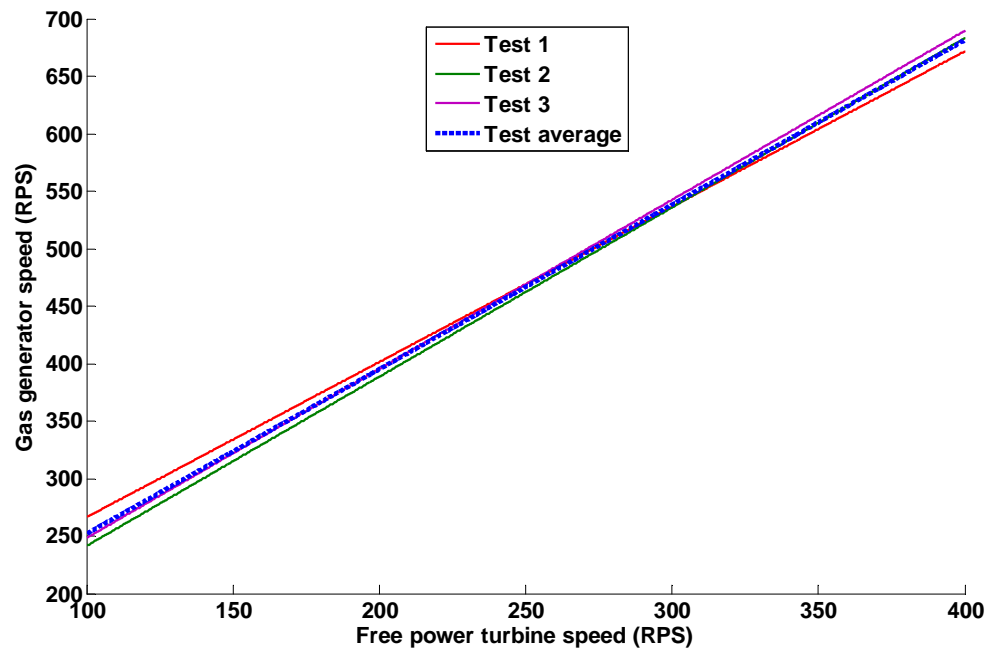
Figure 4.15: Relationship between free power turbine speed and. gas generator speed for idling test.

Figure 4.16: Typical Micro-80D AE signatures (exhaust) for test without load. Free power turbine speed increases from bottom to top, with S1 recorded at 140 RPS and S9 recorded at 345 RPS.

Figure 4.17: Typical S9215 AE signatures (shroud) for test without load. Free power turbine speed increases from bottom to top, with S1 recorded at 140 RPS and S9 recorded at 345 RPS.

.
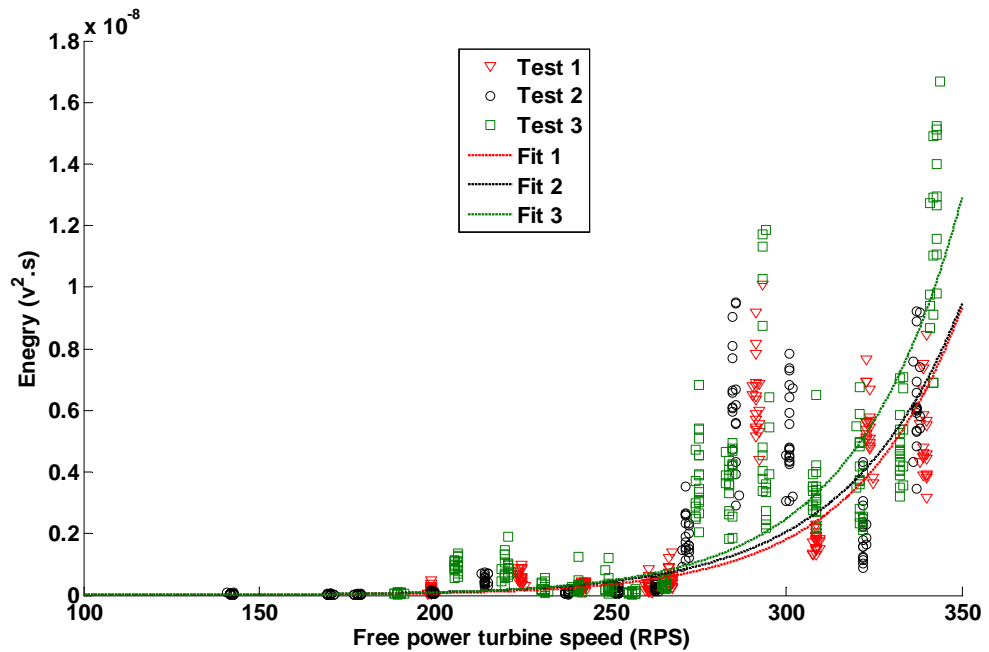
Figure 4.18: Micro-80D (exhaust) sensor AE energy *vs.* free power turbine speed for tests without load.

Figure 4.19: S9215 (shroud) sensor AE energy *vs*. free power turbine speed for tests without load.

Figure 4.20 shows a sample of raw AE spectra for the idling tests, with the Micro-80D showing a gradual shift towards lower frequencies, and the S9215 sensor again showing a narrow frequency range at around 35kHz with a slight tendency towards lower frequencies at higher FPT speeds. Records from the turbine shroud show a similar behavior at several points, i.e. S6, S8, and S9.

Figure 4.20: Typical raw AE spectra for test without load: (a) Micro-80D sensor, (b) S9215 sensor. Free power turbine speed increases from bottom to top, with S1 recorded at 140 RPS and S9 recorded at 345 RPS.

.

Figures 4.21 and 4.22 show the demodulated spectra at a range of running speeds. Both sensors exhibit considerable complexity in the spectra, but share a common feature, which is a peak of running speed which increases with FPT running speed. However, the strength of this peak is not consistent, and the observed energy is obviously carried in a number of other frequencies as well as the running speed.

Figure 4.21: Typical demodulated AE spectra for test without load with Micro-80D sensor. Free power turbine speed increases from bottom to top, with S1 recorded at 140 RPS and S9 recorded at 345 RPS.

Figure 4.22: Typical demodulated AE spectra for test without load with S9215 sensor. Free power turbine speed increases from bottom to top, with S1 recorded at 140 RPS and S9 recorded at 345 RPS.

4.4. Turbine operation test with load

This test involved adding a dynamic device i.e. the alternator, to the turbine rig in order to study the changes in the AE behaviour when the FPT was subjected to an external load, increased load being reflected in a reduced speed of the FPT. In this respect, the signals were expected to be the most complex of the tests studied, but also those of most relevance to real operations. A hint of this complexity is seen in Figures 4.23 and 4.24 where the examples of raw AE signals from two AE sensors show them all to contain pulses, but with little obvious pattern in time or between running speeds. Table 4.5 shows the running speed of free power turbine of load test.

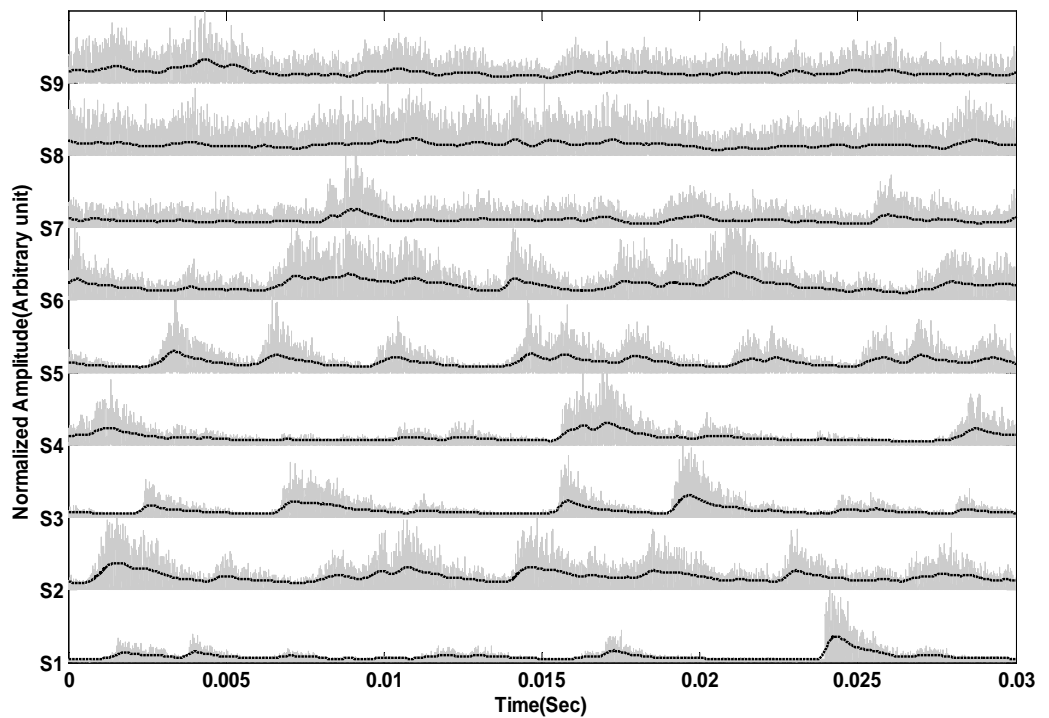| Load test speeds	Free power turbine speed (RPS)
S1	184
S2	206
S3	216
S4	231
S5	263
S6	275
S7	284
S8	301
S9	320

Table 4. 5: Free power turbine speed of load test.
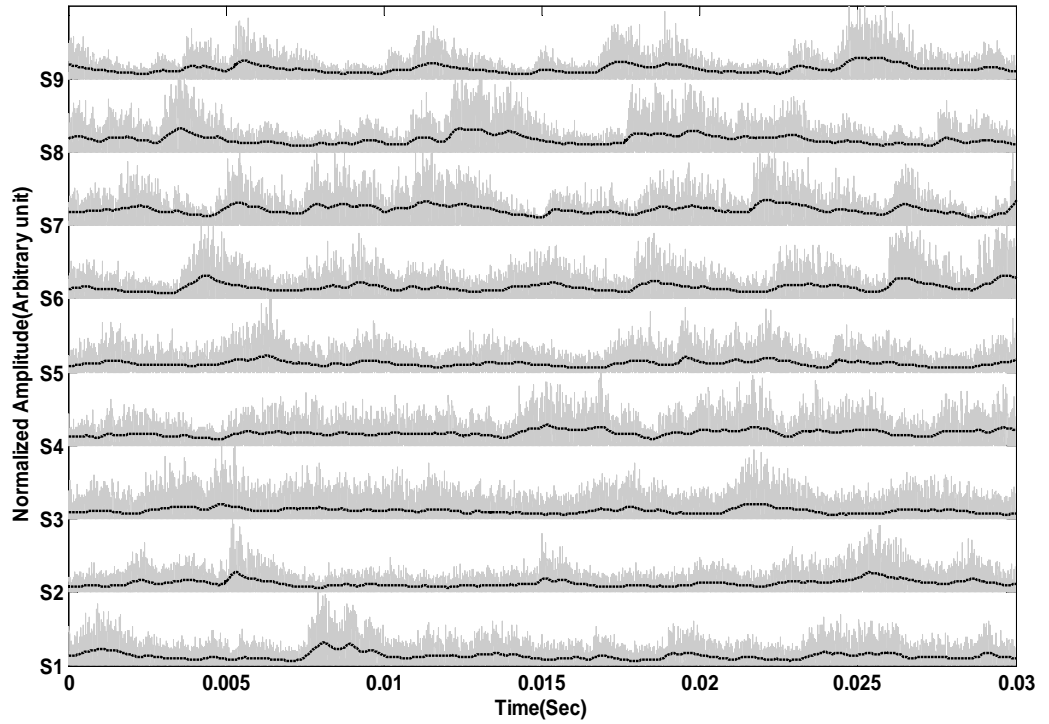
Figure 4.23: Typical Micro-80D AE signatures (exhaust) for test with load. Free power turbine speed increases from bottom to top, with S1 recorded at 150 RPS and S9 recorded at 360 RPS.
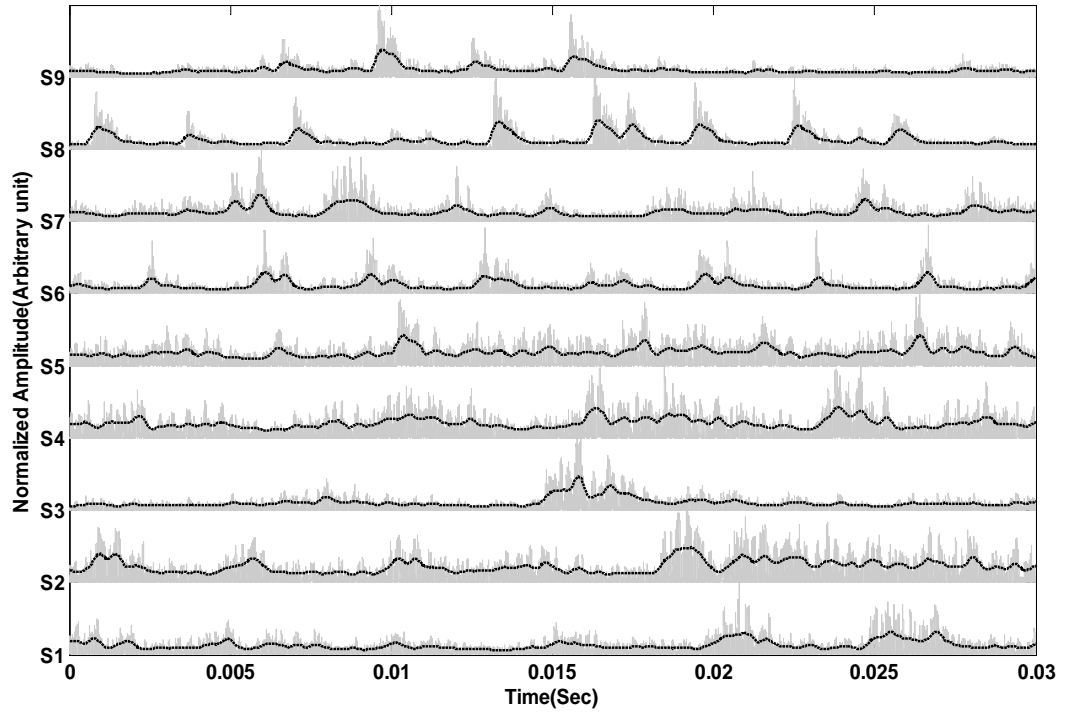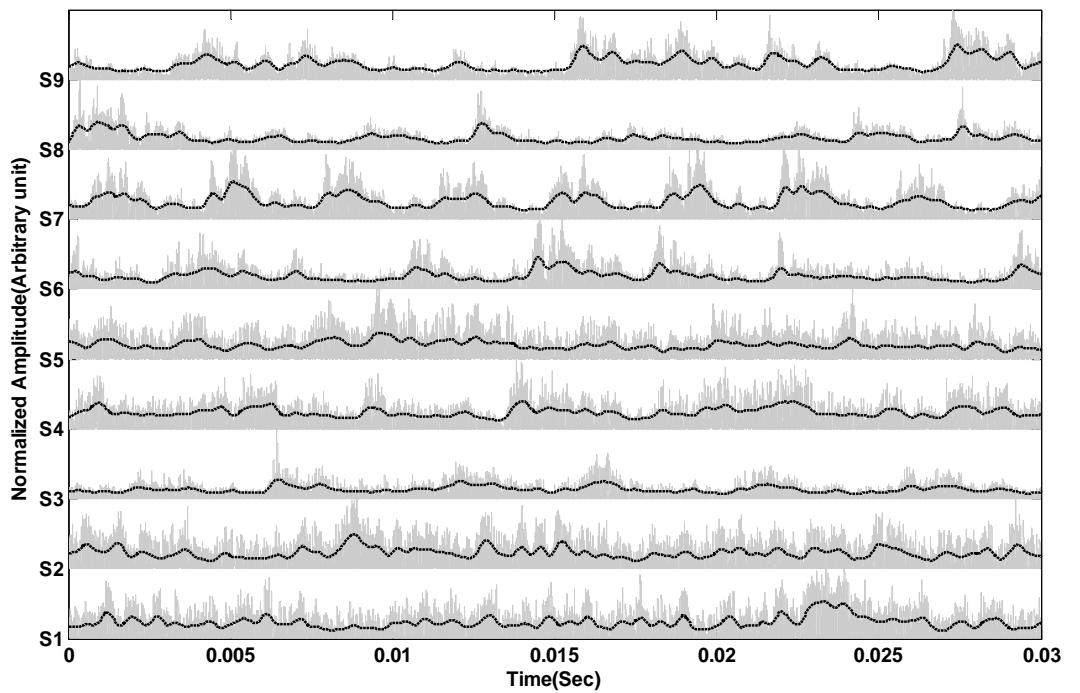

Figure 4.24: Typical S9215 AE signatures (shroud) for test with load. Free power turbine speed increases from bottom to top, with S1 recorded at 150 RPS and S9 recorded at 360 RPS.

Figures 4.25 and 4.26 show the variation in AE energy with FPT speed for the two sensors. The most striking features of these two curves are that they are up to two orders of magnitude higher than the equivalent idling curves and that the curves are no longer monotonic, with peaks in AE energy across the range of speed studied, the speeds at which the peaks occur varying between the three individual tests. The energy levels recorded at the shroud are generally an order of magnitude lower than those recorded at the exhaust.
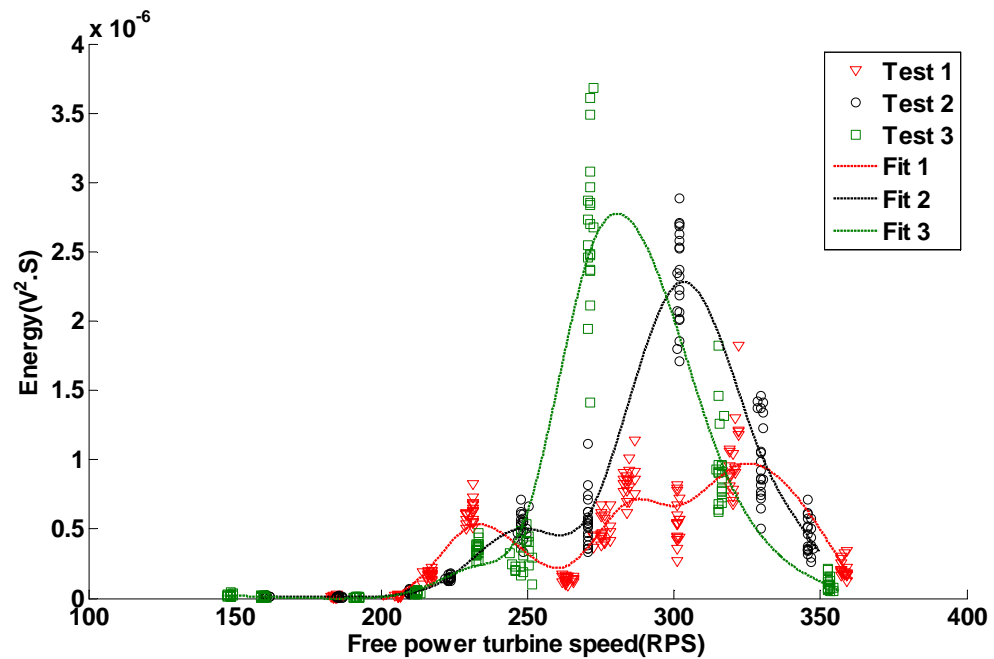
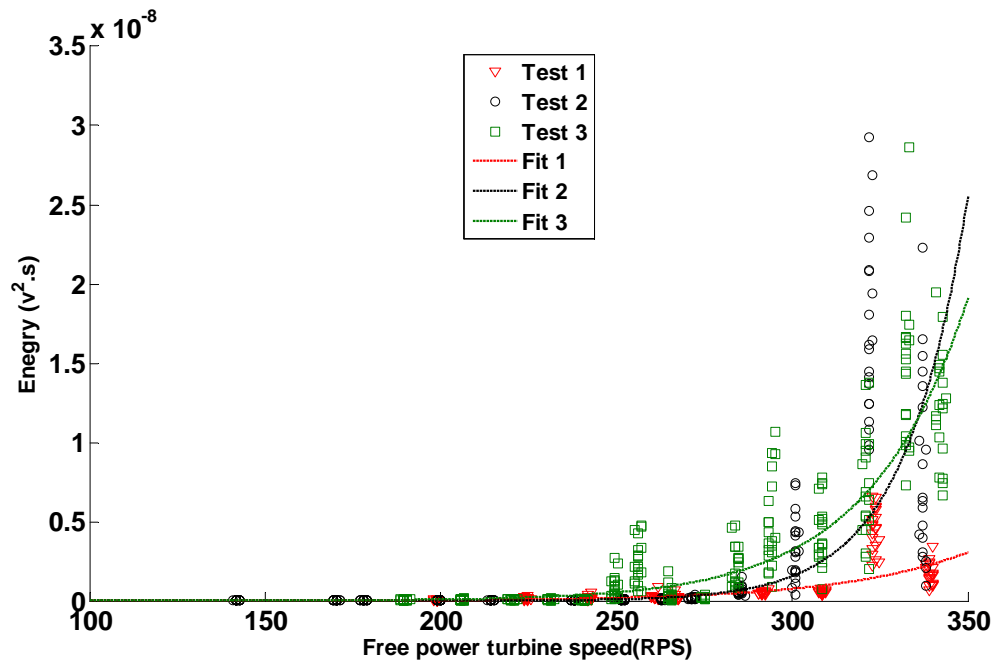Figure 4.25: Micro-80D (exhaust) sensor AE energy *vs*. free power turbine speed for tests with load.
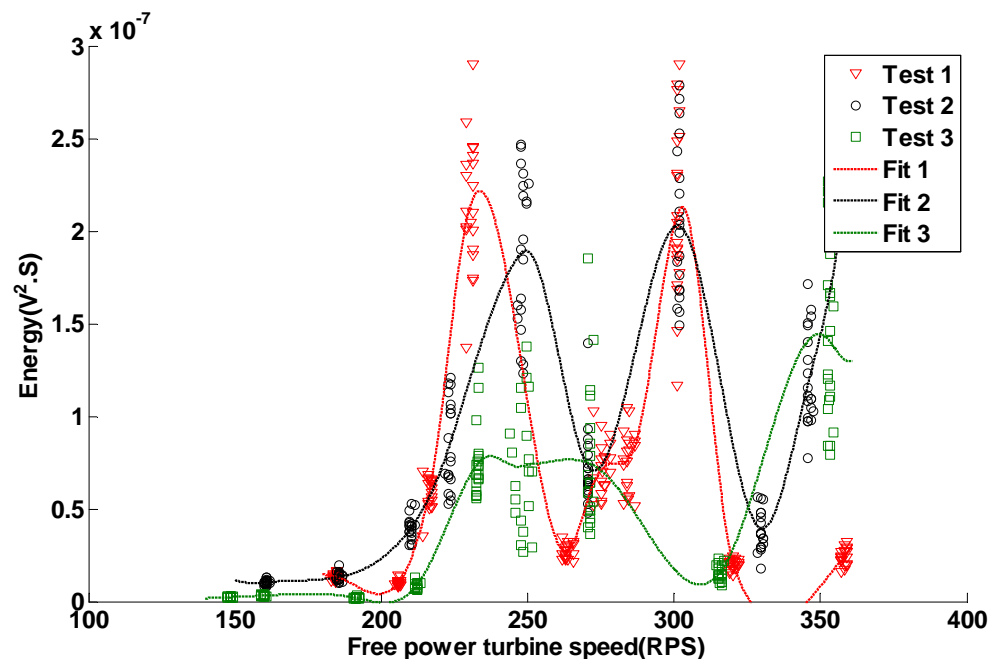
Figure 4.26: S9215 (shroud) sensor AE energy *vs*. free power turbine speed for tests with load.

Figure 4.27 shows sample raw AE spectra, those for the exhaust again showing a tendency to drift towards the bottom of the analogue filter bandwidth as the speed increases. The S9215 spectra show one peak at around 25kHz, which slowly moves towards 20kHz as the speed increase with other peaks which appear and disappear with speed.
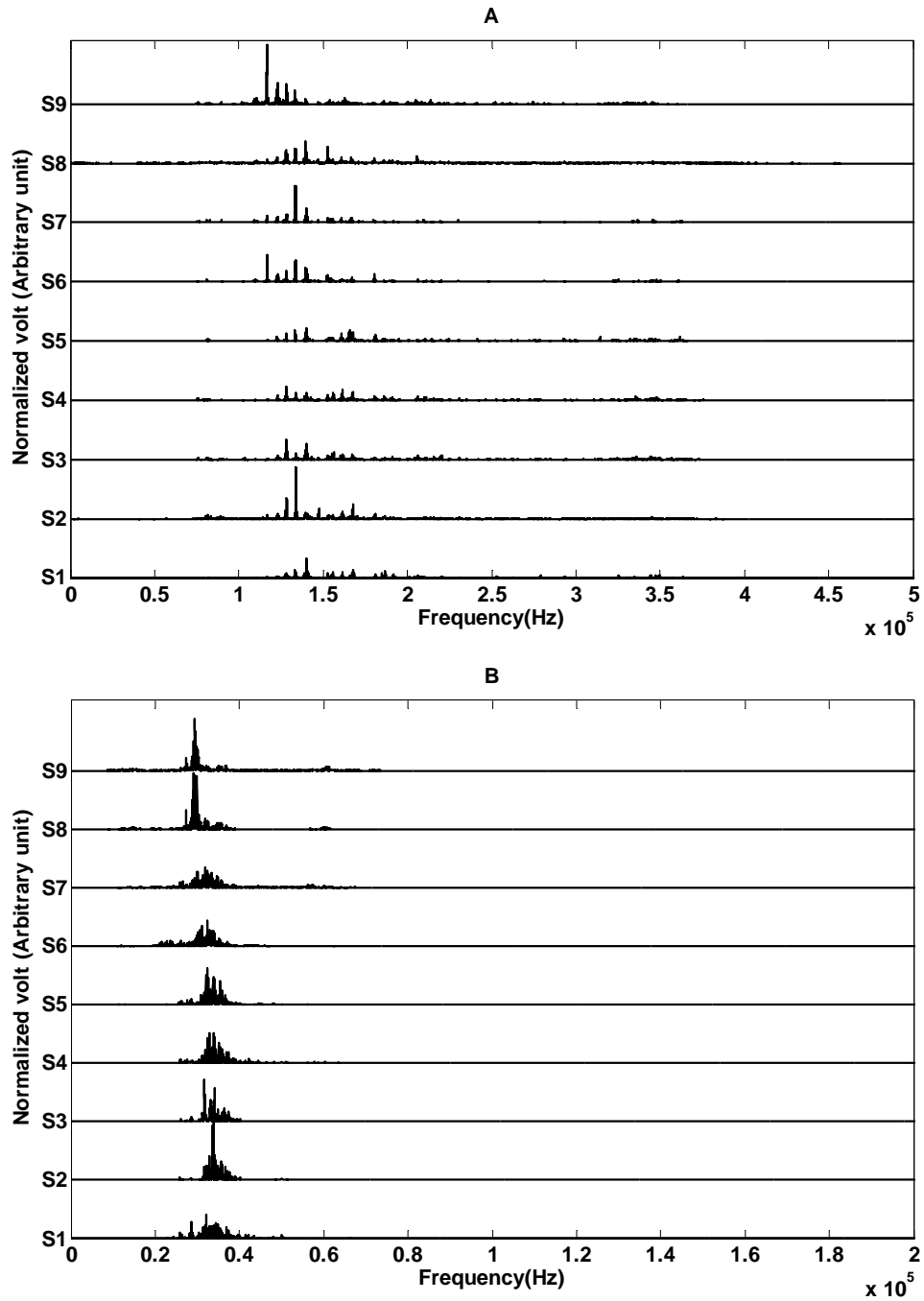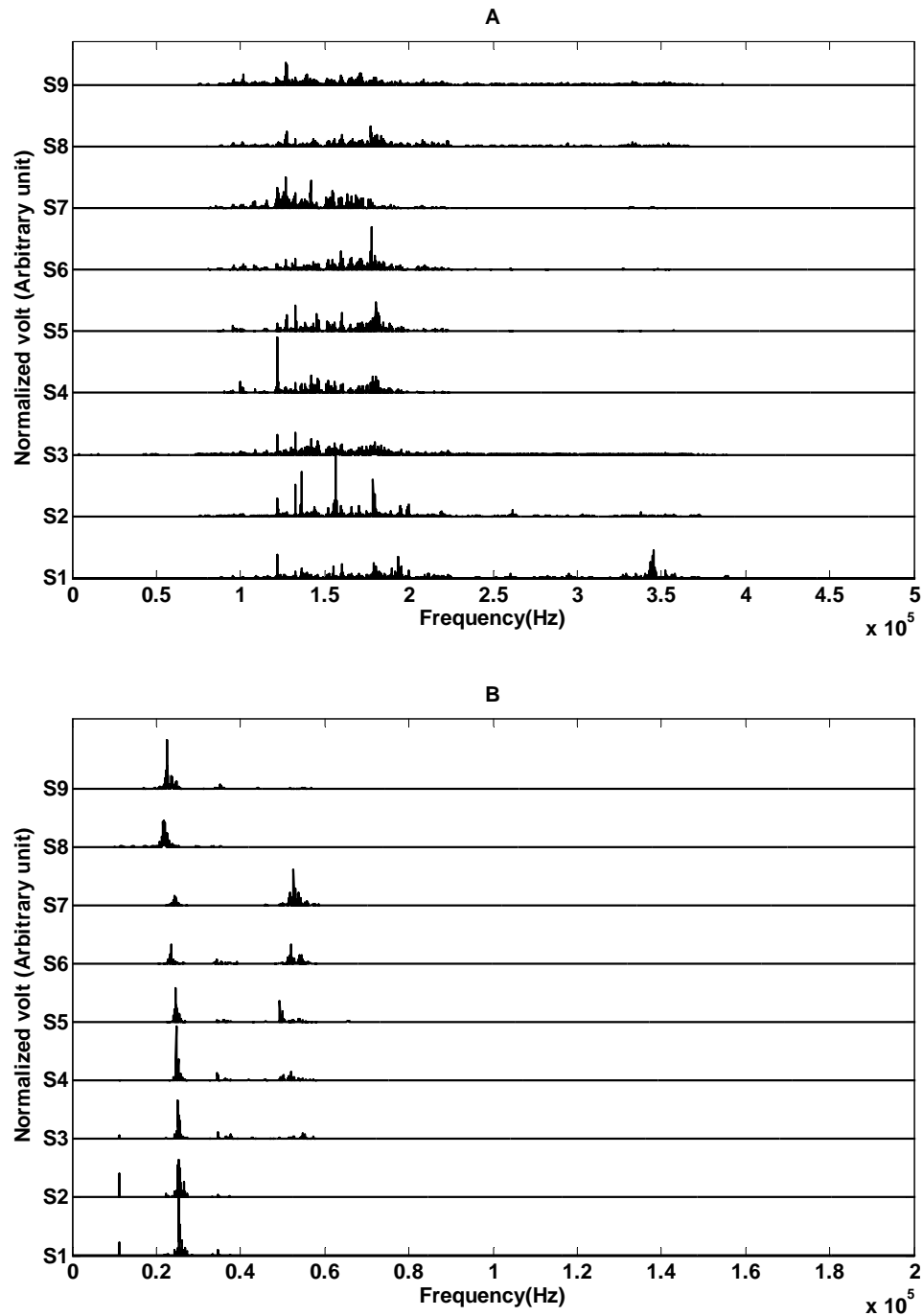

Figure 4.27: Typical raw AE spectra for test with load: (a) Micro-80D sensor, (b) S9215 sensor. Free power turbine speed increases from bottom to top, with S1 recorded at 150 RPS and S9 recorded at 360 RPS.

The demodulated frequency spectra in figures 4.28 and 4.29 both show a strong series of peaks at the running speed frequency and its harmonics. Nevertheless, the strength of these is again not consistent and a number of other, sometimes equally strong, peaks are present.
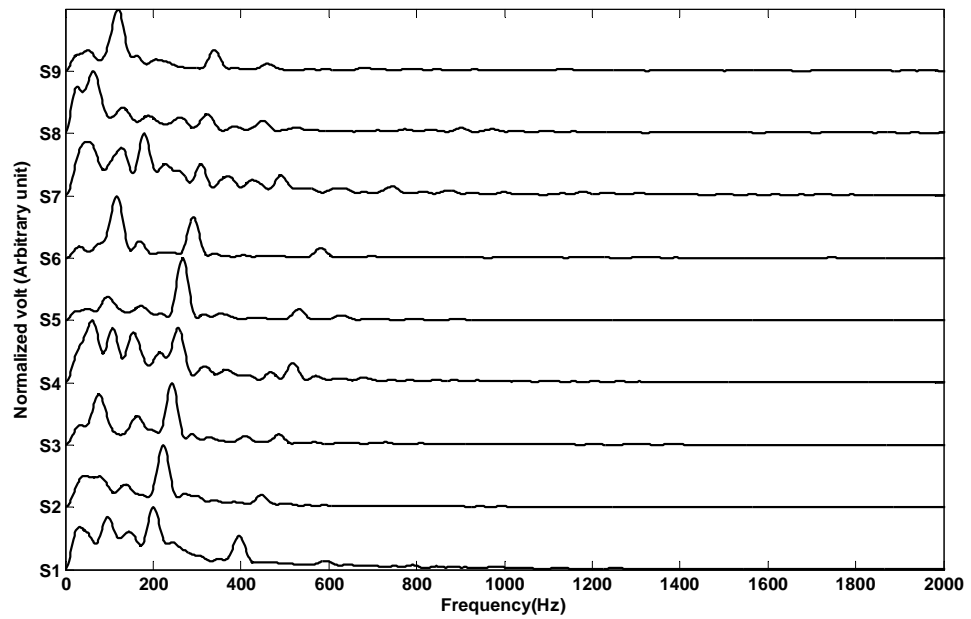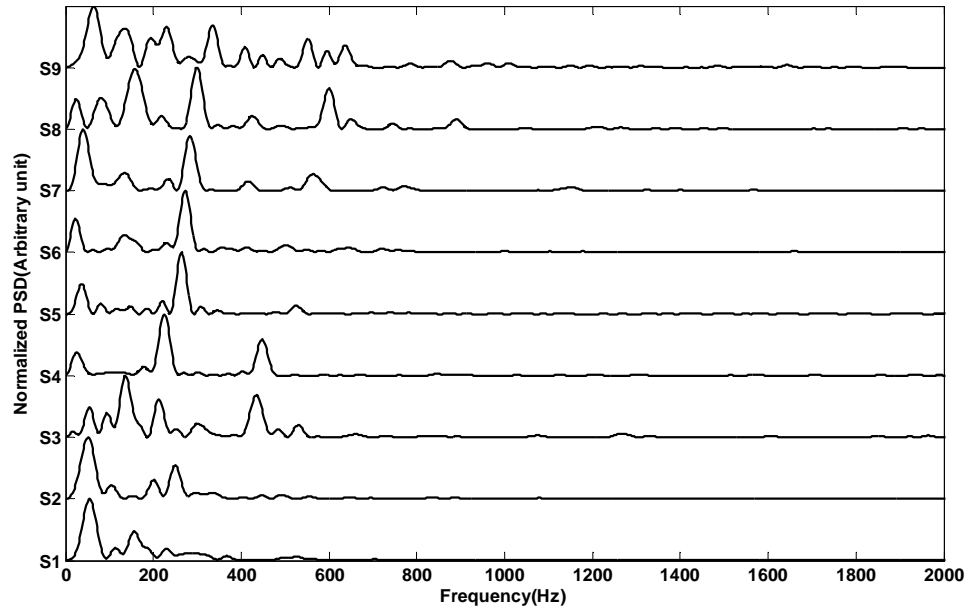

Figure 4.28: Typical demodulated AE spectra for test with load with Micro-80D sensor. Free power turbine speed increases from bottom to top, with S1 recorded at 150 RPS and S9 recorded at 360 RPS.
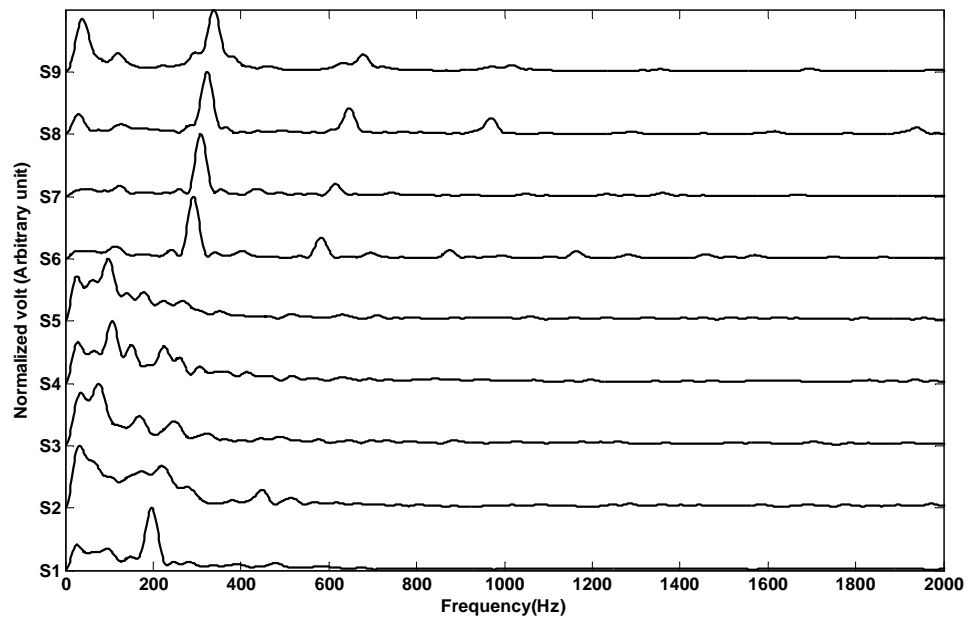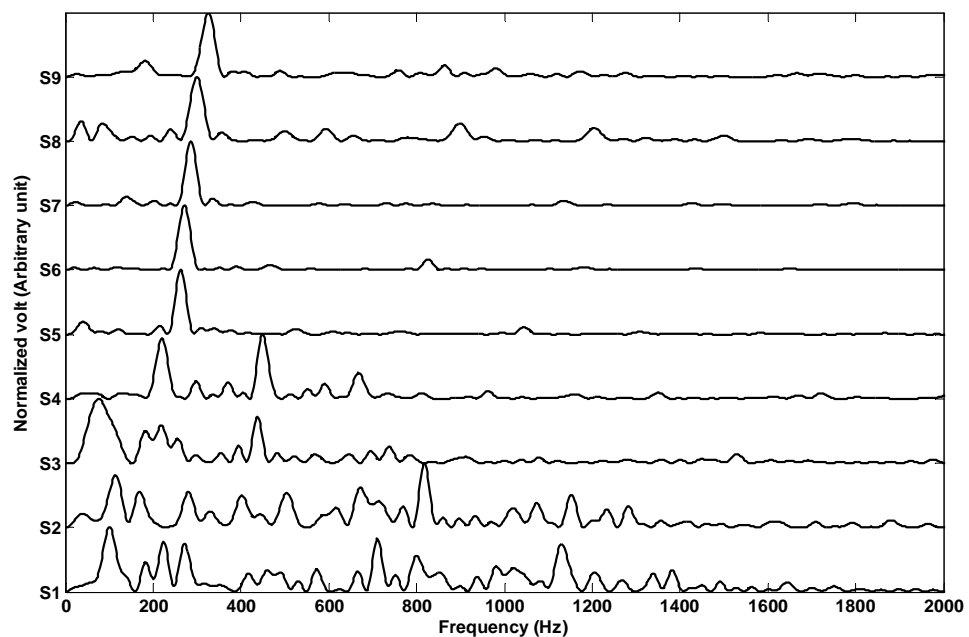

Figure 4.29: Typical demodulated AE spectra for test with load with S9215 sensor. Free power turbine speed increases from bottom to top, with S1 recorded at 150 RPS and S9 recorded at 360 RPS.

4.5. Summary

The initial analysis of the results in this section indicate that the complexity of the AE signals increases with the complexity of the fluid-mechanics occurring within the free power turbine and its exhaust, with both sensors yielding information which changes with speed whilst each clearly is sensitive to different phenomena. The experiments with the impeller stationary are the least complex and contain the least AE energy at a given speed, indicating that much of the complexity and AE energy is associated with the rotation of the FPT impeller. The fact that the signals are not wholly continuous indicates a dynamic effect which potentially contains information over and above the mean energy level. Table 4.6 shows AE energy average for all four tests. It is clear from the table and the pervious energy graphs that the mean energy level is a poor indicator of operating conditions when the turbine is under load and this is clearly associated with the presence of pulses with frequencies in the range of a few tens to a few hundreds of Hz. In view of the complex nature of the AE patterns, the next chapter will examine the signals in more detail with the aid of an ANN algorithm.

Idling tests									Load tests								
Test1			Test2			Test3			Test2			Test2			Test3		
Energy (V².S)		Speed (RPS)	Energy (V².S)		Speed (RPS)	Energy (V².S)		Speed (RPS)	Energy (V².S)		Speed (RPS)	Energy (V².S)		Speed (RPS)	Energy (V².S)		Speed (RPS)
S9215	Micro-80D		S9215	Micro-80D		S9215	Micro-80D		S9215	Micro-80D		S9215	Micro-80D		S9215	Micro-80D	
4.7E-11	1.7E-10	199	5.3E-12	4.6E-11	142	5.9E-11	6.3E-11	190	1.3E-08	1.2E-08	184	1.1E-08	1.5E-08	161	2.4E-09	2.1E-08	149
1.5E-10	6.0E-10	224	6.1E-12	2.7E-11	170	6.5E-11	9.7E-10	206	1.0E-08	1.8E-08	206	1.3E-08	9.4E-09	186	3.2E-09	1.2E-08	160
1.6E-10	3.4E-10	243	1.0E-11	1.2E-11	178	7.2E-11	9.0E-10	220	5.9E-08	1.7E-07	217	4.0E-08	4.3E-08	210	2.0E-09	6.0E-09	192
2.4E-10	2.8E-10	261	3.8E-11	8.5E-11	200	8.0E-11	2.3E-10	231	2.2E-07	6.2E-07	231	8.4E-08	1.5E-07	223	8.2E-09	4.3E-08	212
2.1E-10	5.7E-10	267	1.2E-11	4.9E-10	214	6.3E-11	2.9E-10	241	2.7E-08	1.4E-07	263	1.9E-07	5.2E-07	248	7.5E-08	3.5E-07	233
5.2E-10	6.5E-09	292	2.7E-11	9.2E-11	238	8.1E-10	3.2E-10	250	7.3E-08	4.9E-07	276	7.2E-08	5.6E-07	270	7.3E-08	3.1E-07	248
5.3E-10	1.7E-09	309	6.9E-11	1.4E-10	252	2.5E-09	8.7E-11	256	7.6E-08	8.4E-07	284	2.0E-07	2.3E-06	302	7.5E-08	2.7E-06	271
4.4E-09	5.5E-09	323	9.8E-11	3.6E-10	263	3.9E-10	3.6E-10	265	2.1E-07	5.5E-07	301	3.8E-08	1.0E-06	330	1.5E-08	9.5E-07	316
1.7E-09	5.2E-09	339	1.7E-10	1.9E-09	272	2.0E-10	3.8E-09	275	2.0E-08	1.0E-06	320	1.2E-07	4.5E-07	346	1.4E-07	1.0E-07	353
-	-	-	6.4E-10	6.1E-09	285	2.2E-09	3.7E-09	284	2.4E-08	2.1E-07	358	-	-	-	-	-	-
-	-	-	3.3E-09	5.2E-09	301	4.8E-09	5.5E-09	294	-	-	-	-	-	-	-	-	-
-	-	-	1.7E-08	2.1E-09	322	4.3E-09	3.4E-09	308	-	-	-	-	-	-	-	-	-
-	-	-	8.3E-09	6.3E-09	337	7.2E-09	3.8E-09	321	-	-	-	-	-	-	-	-	-
-	-	-	-	-	-	1.5E-08	4.8E-09	333	-	-	-	-	-	-	-	-	-
-	-	-	-	-	-	1.2E-08	1.2E-08	342	-	-	-	-	-	-	-	-	-

Table 4. 6: Average AE energy for both exhaust and shroud sensors of idling and load tests.

Chapter 5 Analysis and discussion of normal running tests

The foregoing chapter has shown that the evolution of AE energy with turbine running speed is relatively simple when the gas flow is simple, but that the energy evolutions become non-monotonic when the impeller is rotating and more so when the turbine is under load.

This chapter focuses on a more detailed analysis of the two tests with a rotating impeller, idling and with the FPT under load. Because the AE patterns are complex, a pattern recognition approach has been taken based on the observations made in chapter 4. Also, because the requirement is to understand the changing characteristics of the AE with normal running operating conditions the focus of the pattern recognition has been the turbine running speed.

The analysis is divided into three parts, time domain processing, frequency domain processing and, finally, an approach that combines features from both time and frequency domains

5.1. Time domain analysis

As observed in chapter 4 the AE time series signals at various speeds both with and without load are not obviously periodic but exhibit pulses on a background continuous signal. Therefore a processing approach was devised, based on a categorisation of pulse shape, and this was applied to the idling tests. Next, a more statistical approach was taken, whereby a wide range of time-based features was extracted and these were tested using an ANN.

5.1.1. Pulse shape categorisation

Here the aim was to categorise the bursts and to describe their temporal distribution to examine if this was characteristic of the running conditions. To this end, AE signals were examined visually in the time domain and four distinct shapes of envelope were identified for each of the sensors/positions, Figures 5.1 and 5.2.
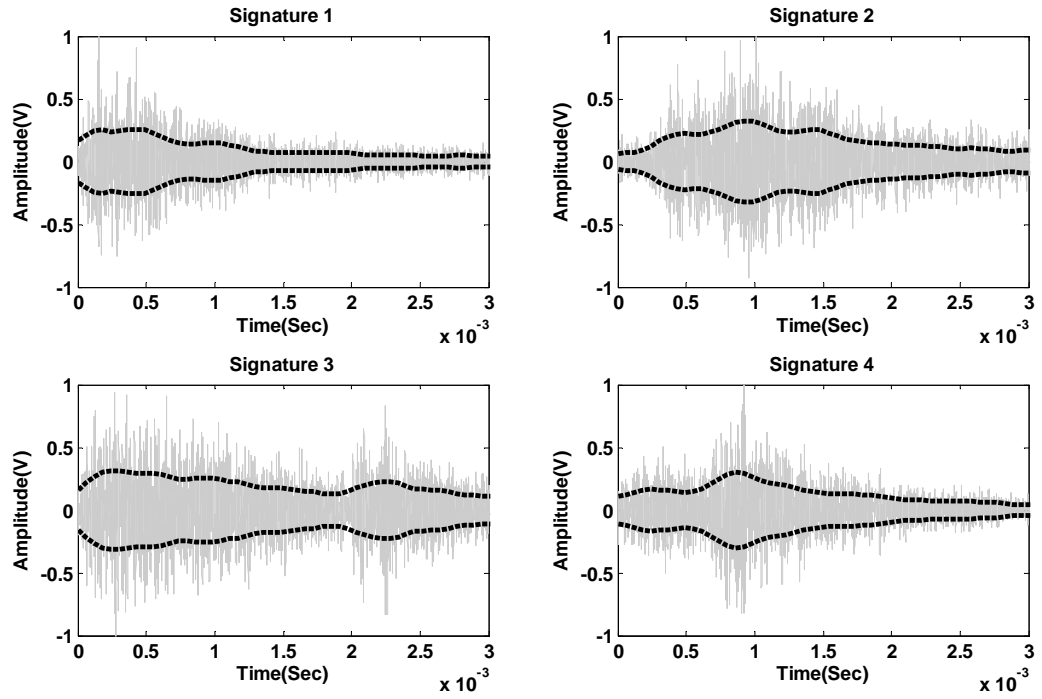
Figure 5.1: The four characteristic pulse signatures identified from Micro-80D signals.
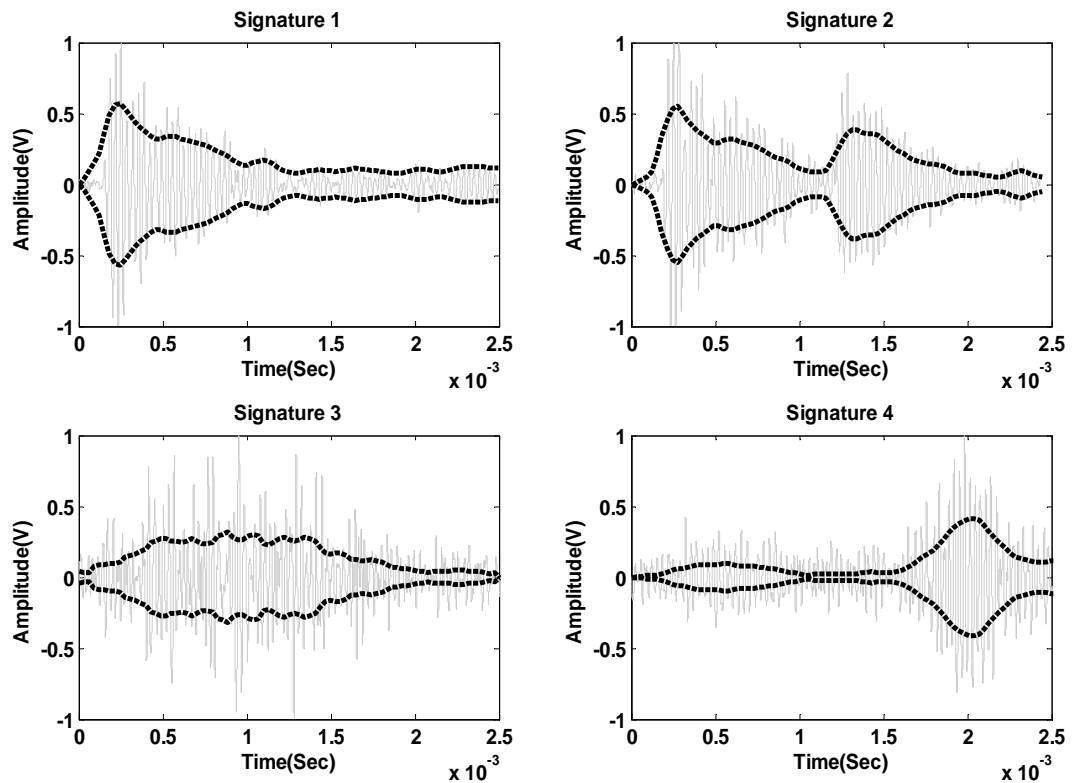
Figure 5.2: The four characteristic pulse signatures identified from S9215 signals.

A total of 20 examples of the positive envelope of each shape was used to train a two-layer, log-sigmoid/log-sigmoid ANN, Figure 5.3. The first hidden layer had 40 neurons,

found to give consistently good training performance. The network was trained to produce an output structure that is a series of 4 digits containing 0 or 1, the position of the 1 indicating which of the four pulse types has been recognised. For example if an AE signature of the first kind mentioned previously is recognised, the output will be "1 0 0 0", if the second type is recognised the output will be "0 1 0 0", and so on.
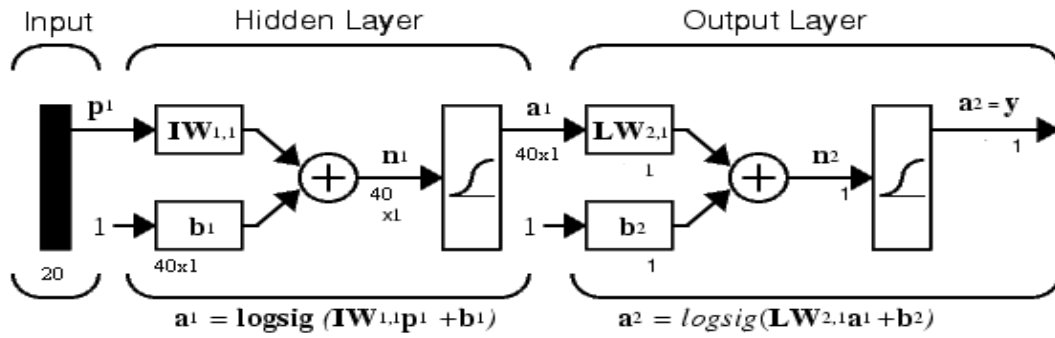
Figure 5.3: Artificial neural network structure for pulse shape recognition.

After training, the ANN was tested with 20 unseen signatures of each kind and figure 5.4 shows an example of the recognition performance. Figure 5.5 shows an example segment of AE signal after being processed by the first ANN to give a pulse sequence code " 3 4 2 1", so the output code actually is describing the pattern of AE bursts at each speed, then the mission of next ANN is to find out whether each running condition is associated with a specific pulse pattern.
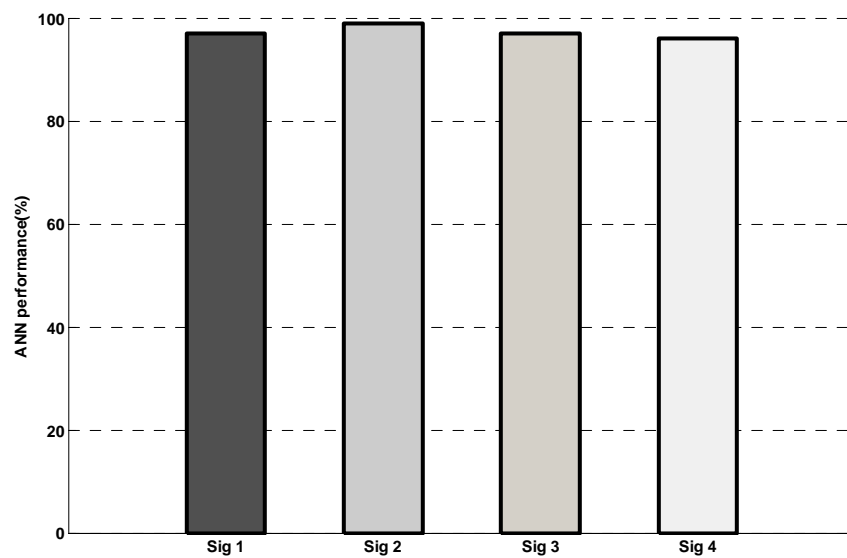
Figure 5.4: Example ANN recognition performance for AE signatures of Micro-80D (exhaust) for unseen signatures from idling test.
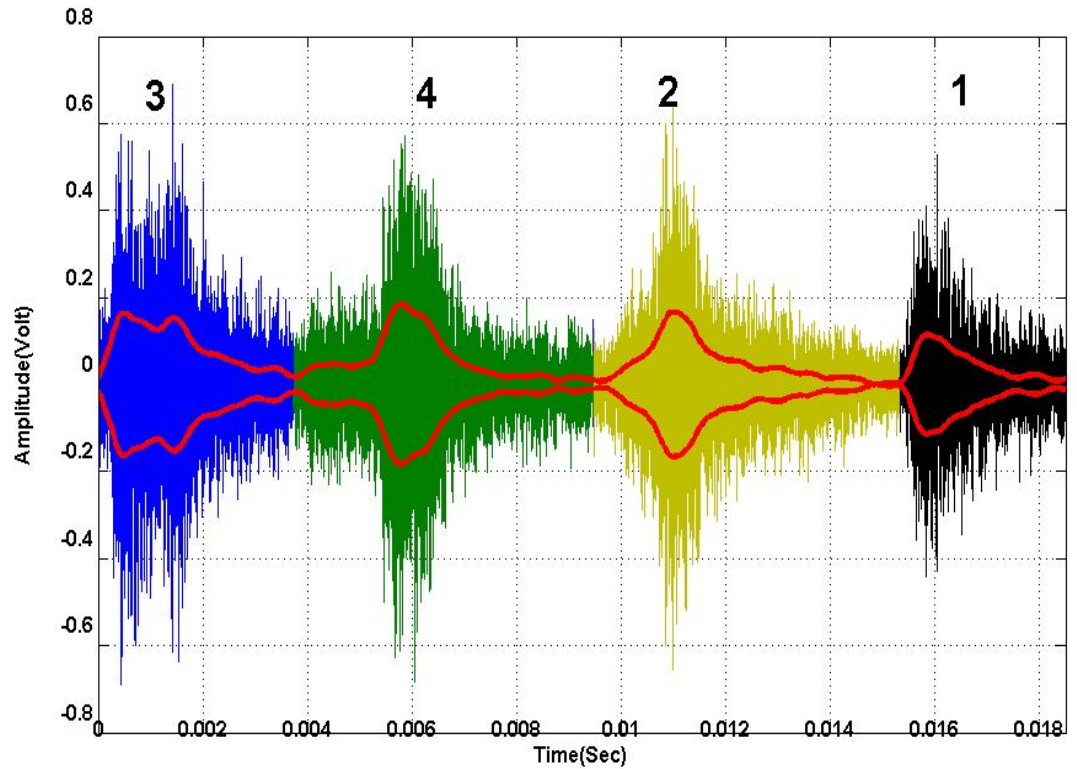
Figure 5.5: Sample coded signal for pulse shape recognition of Micro-80D (exhaust) sensor for idling test.

The number of pulses in each record will change depending on the turbine speed; for instance, each record contains 5 pulses at a speed of 150 RPS and 8 pulses at a speed of 300 RPS. The longer records were truncated to the first 5 pulses to build a suitable input to the ANN. The resulting data for both sensors for each speed of the idling test were divided into two equal parts, one for training and one for testing, as input to a second neural network whose output was the running speed. This was a feed-forward, back-propagation ANN with two-layers. The hidden layer again used 40 neurons and a log-sigmoid transfer function. The transfer function for the output layer was also a log-sigmoid and the number of neurons in this layer was equal to the number of speeds to which the network was to be trained. Figures 5.6 and 5.7 show the resulting performance, as percentage speed correct classification, for each sensor, and for the three individual tests and for the three tests collectively.
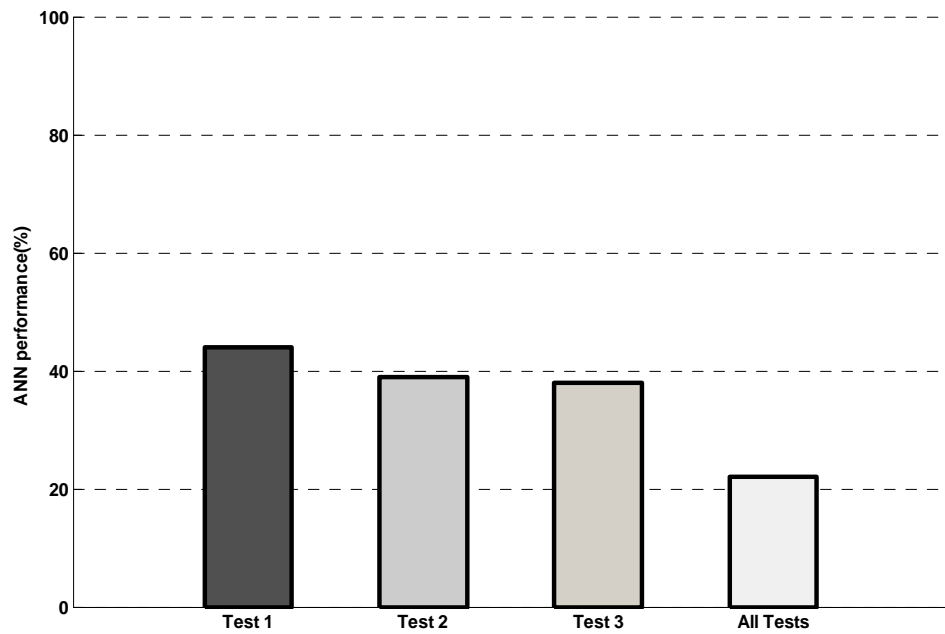
Figure 5.6: Pulse shape recognition ANN performance for Micro-80D (exhaust) data from idling tests.
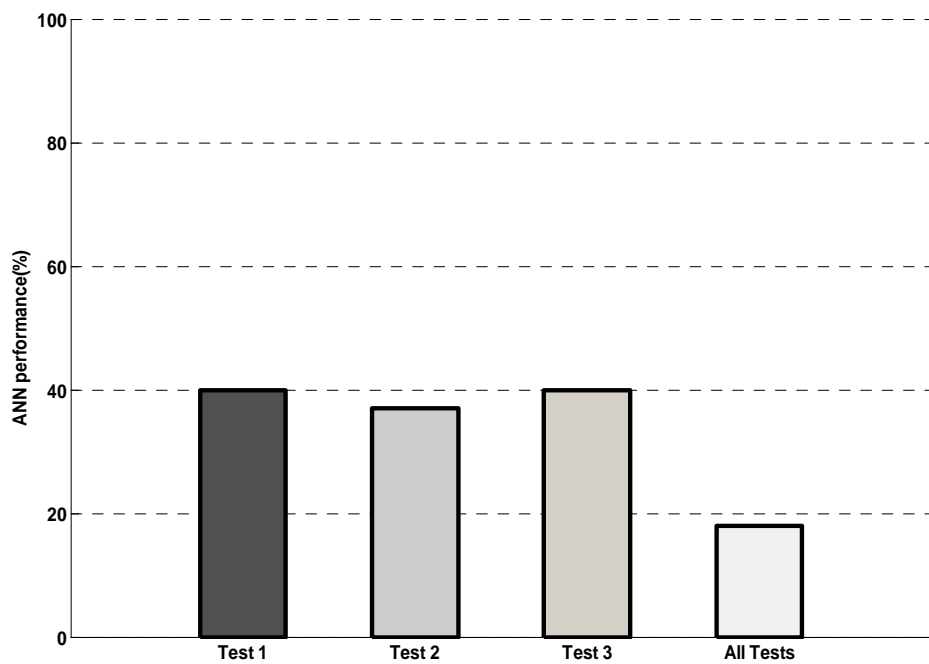
Figure 5.7: Pulse shape recognition ANN performance for S9215 (shroud) data from idling tests.

As can be seen, the performance of the pulse shape network was poor, so the input was improved by adding information about the time between pulses. The input codes were modified to include the time differences between each pulse and the network was

trained and tested again with the new input data. Figures 5.8 and 5.9 show that there was a general improvement in the performance of the updated network, but this is still relatively poor at around 60% correct speed classification for the individual tests and around 40% for the tests grouped together.
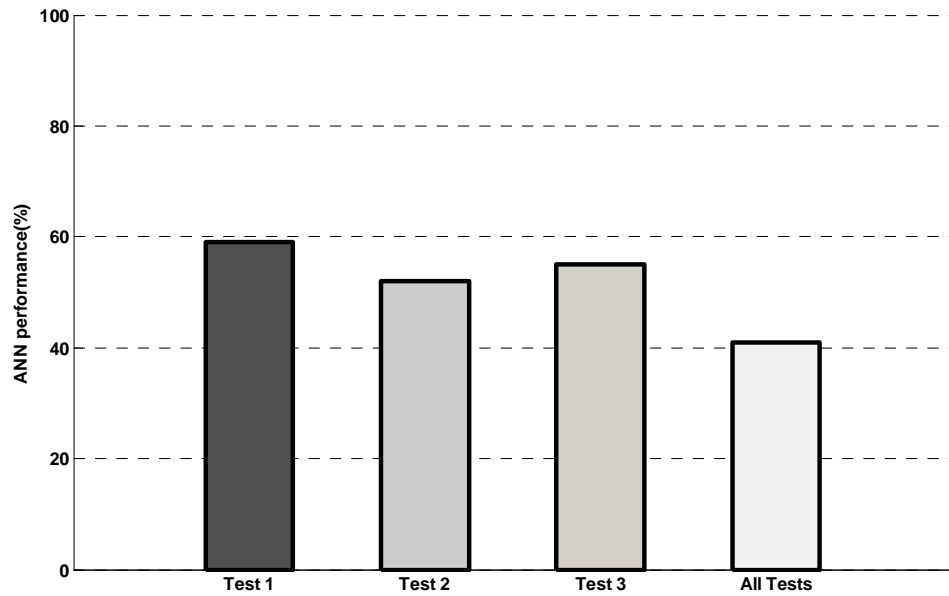
Figure 5.8: Improved pulse shape recognition ANN performance for Micro-80D (exhaust) data from idling tests.
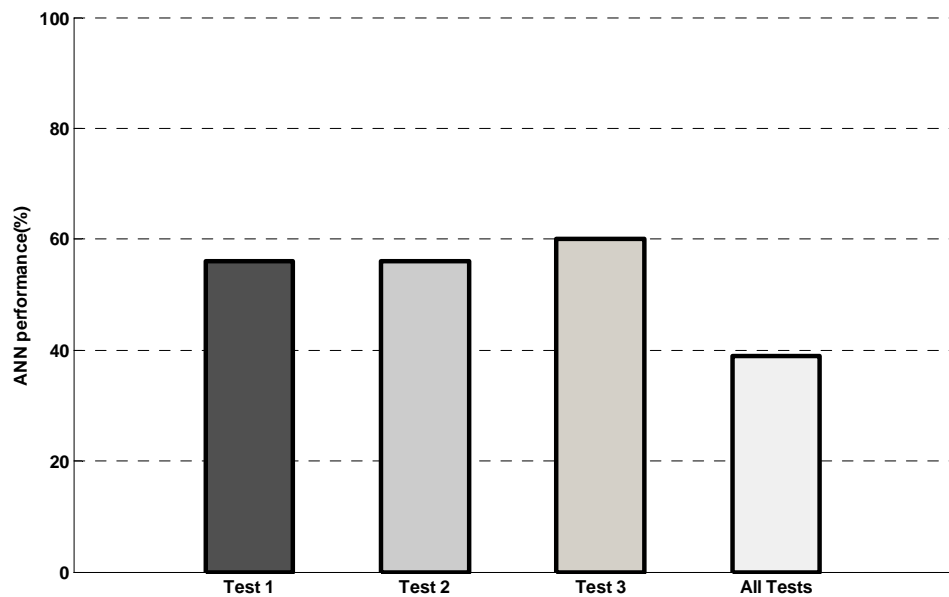
Figure 5.9: improved pulse shape recognition ANN performance for S9215 (shroud) data from idling tests.

5.1.2. Statistical time feature classification

In view of the poor performance of the pulse recognition techniques, it was decided to extract the maximum possible amount of information from the time domain. To this end a range of features; energy, maximum amplitude, counts, RMS, mean, standard deviation, skew, and kurtosis, were generated from the time series in the interest of describing the signals as fully as possible. Also, the static neural network, where the output is calculated directly from the input through feed-forward connections, was replaced with a dynamic network. The output of a dynamic network depends not only on the current input but also on previous inputs, outputs, or states of the network, i.e. it has a memory and its response at any given time depends not only on the current input but also on the history of the input sequence. The implementation used consisted of one log-sigmoid layer with 20 neurons with a feed-forward, back-propagation learning algorithm again with the output consisting of the running speed, one node being allocated to each speed used. As before, half of the data set was used to train the network to the measured running speed. The network was then tested, delivering weights to the output nodes from which a speed classification could be obtained (most highly weighted output node) and an estimate of running speed (weighted mean of all output nodes). Figure 5.10 shows the resulting ANN performance with time domain features for each of the sensor records acquired on the running turbine with and without load. As before, the ANN was applied to the data from the three individual tests and again on data from the three tests mixed together. The performance figure is the percentage of times that a test speed is correctly classified.
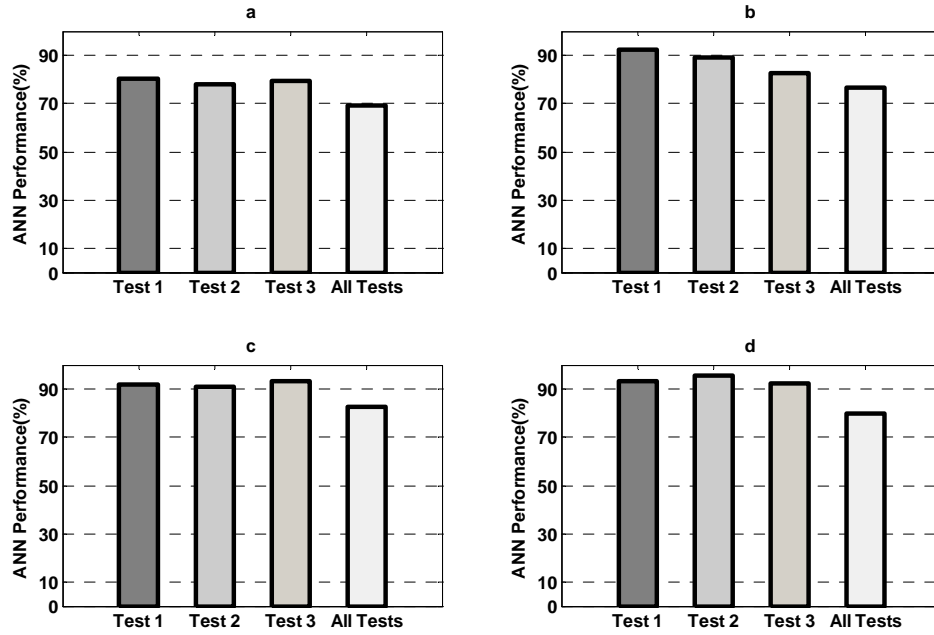
Figure 5.10: ANN classification performance using all statistical time features: (a) S9215 sensor, idling tests, (b) Micro-80D sensor, idling tests, (c) S9215 sensor, load tests, (d) Micro-80D sensor, load tests.

Figure 5.10 shows good performance for the individual tests, but poorer performance for the collected data. Figures 5.11 to 5.13 show the weighted output of the ANN compared with the measured turbine speed. The weighted output provides an estimate of the speed which takes account of the weights of each output neuron (as opposed to the value at maximum weight, i.e. the classification). The red points on the graphs represent the actual running speed whereas the blue points represent the estimated running speed. Presentation of the data in this form allows a number of additional observations, such as the generally higher level of certainty in the load tests and the tendency to over-estimate the actual speed when all tests are grouped.
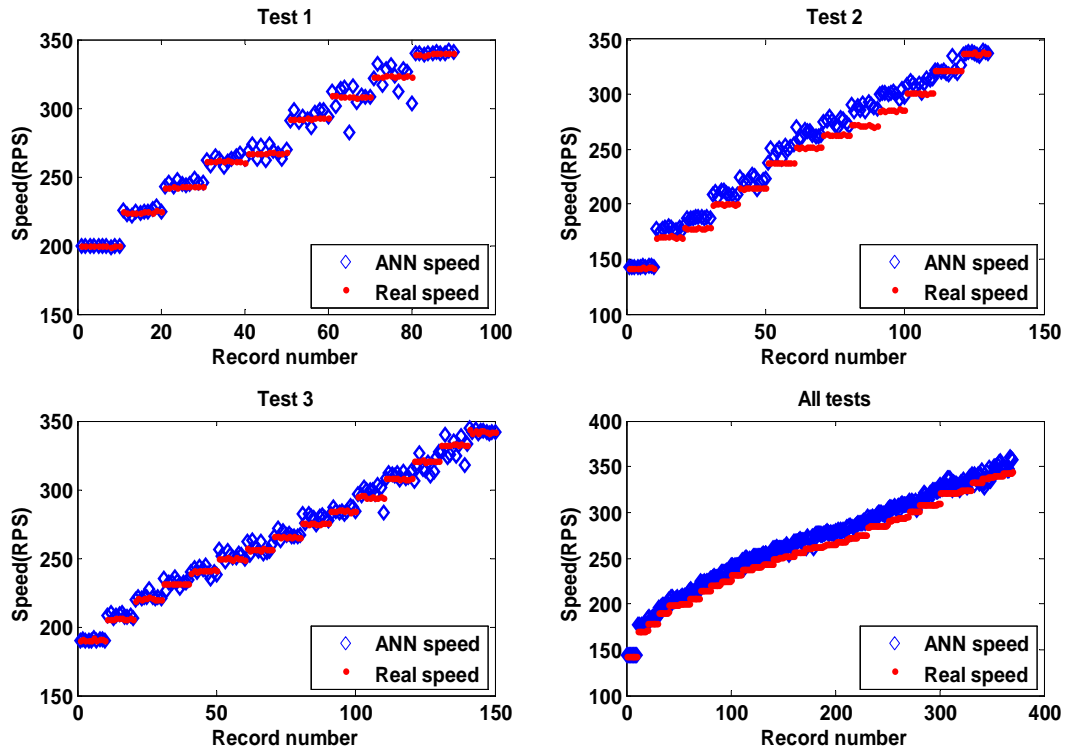
Figure 5.11: ANN speed estimate error for S9215 sensor idling test.
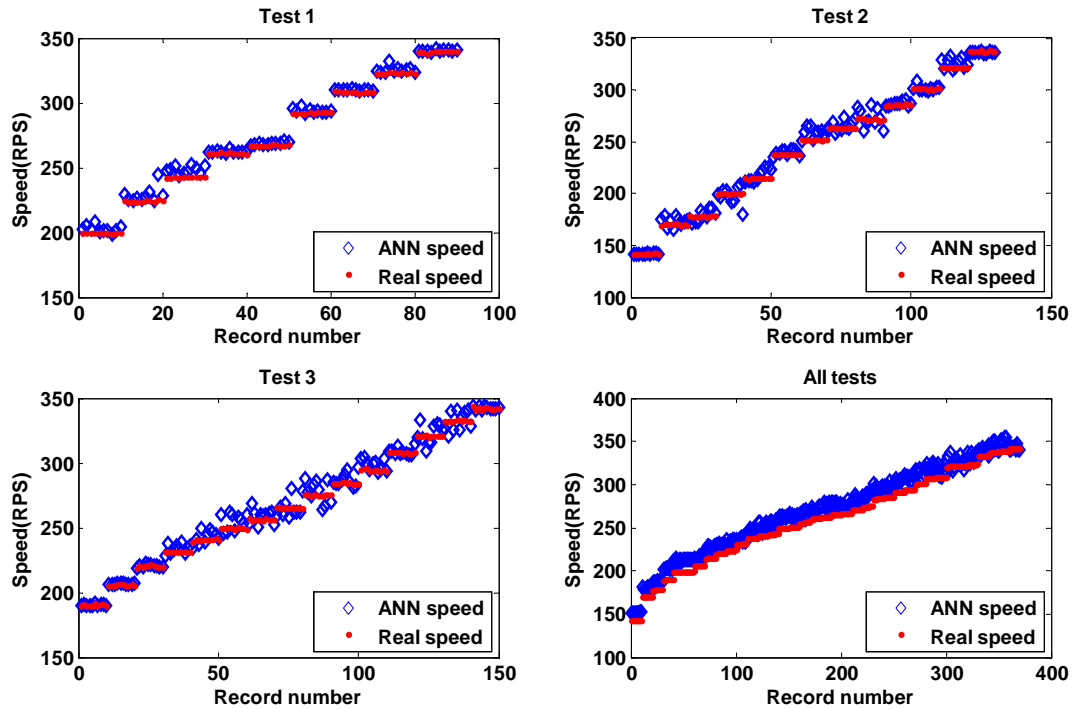
Figure 5.12: ANN speed estimate error for Micro-80D sensor on idling test.
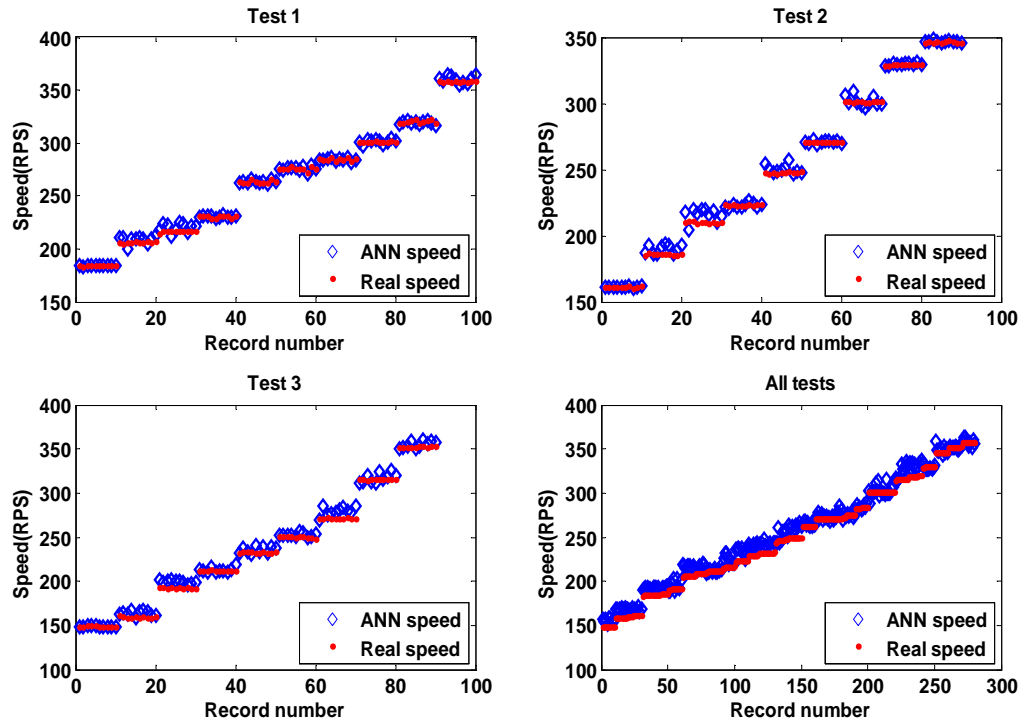
Figure 5.13: ANN speed estimate error for S9215 sensor on load test.
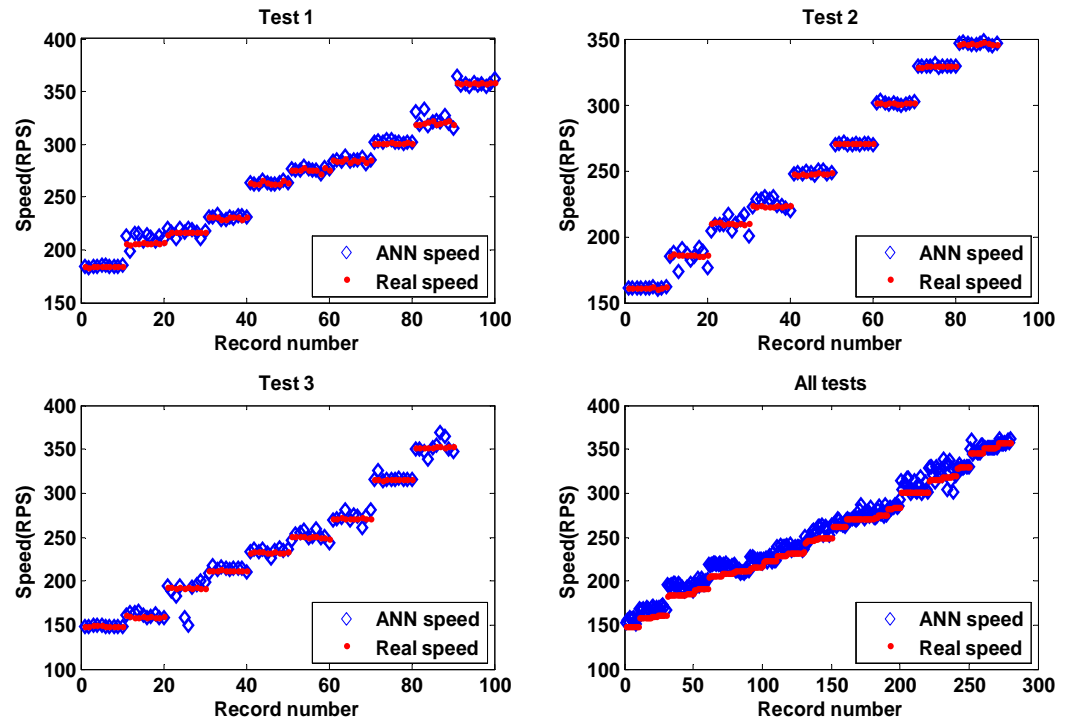
Figure 5.14: ANN speed estimate error for Micro-80D sensor on load test.

Although the ANN performance for individual tests with all time features was over 75%, the features driving that performance were not yet known. Accordingly, the ANN

was trained and tested with each individual time feature in order to identify the most efficient time features in pattern recognition. Figures 5.15 and 5.16 show the resulting ANN performance and show two clear groups, those with high discriminating power (STD, RMS, Max amp, Counts, and Energy), and those with low discriminating power group (Skew, Kurtosis and Mean).
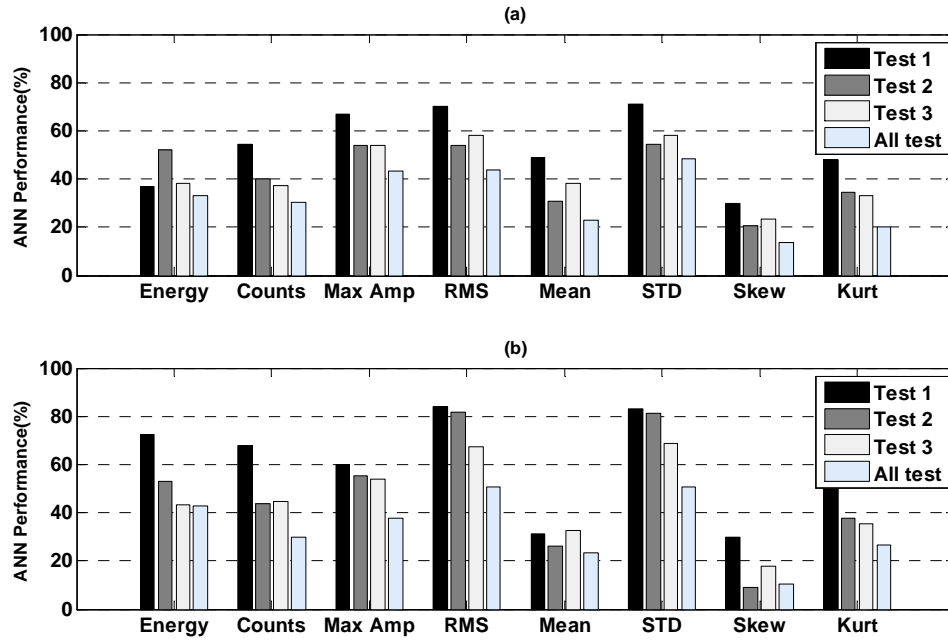
Figure 5.15: ANN performance for individual time features derived from idling test: (a) S9215 sensor,(b) Micro-80D sensor.
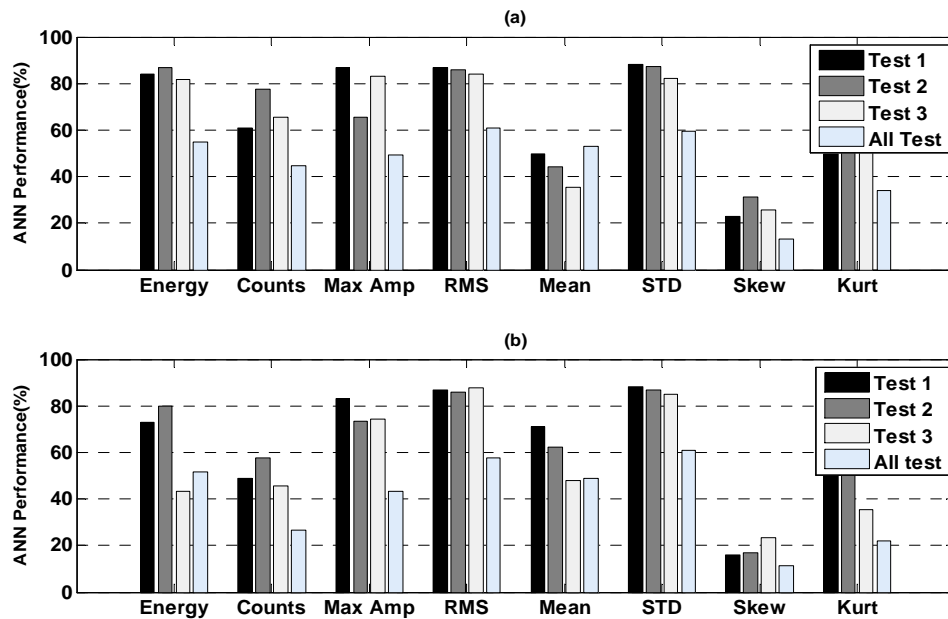
Figure 5.16: ANN performance for individual time features derived from without load test: (a) S9215 sensor,(b) Micro-80D sensor.

Figures 5.17 and 5.18 show the cumulative effect on ANN performance of time features, sorted in order of strongest discriminating power for each sensor at each test. The features of the strongest discriminating power, i.e. STD and RMS, appear in figures 5.17 and 5.18 as features 1 and 2. On the other hand, the features of less discriminating power, i.e. Max amp, Counts, or Energy appear as 3, 4 or 5 in figures 5.17 and 5.18. Finally, features of the least discriminating power, i.e. Skew, Kurtosis and Mean appear as 6, 7, or 8 in figures 5.17 and 5.18. For the individual tests, improvement is slow with added features, and sometimes deteriorates. For the collective tests, steady improvement is obtained, at least up to six features.
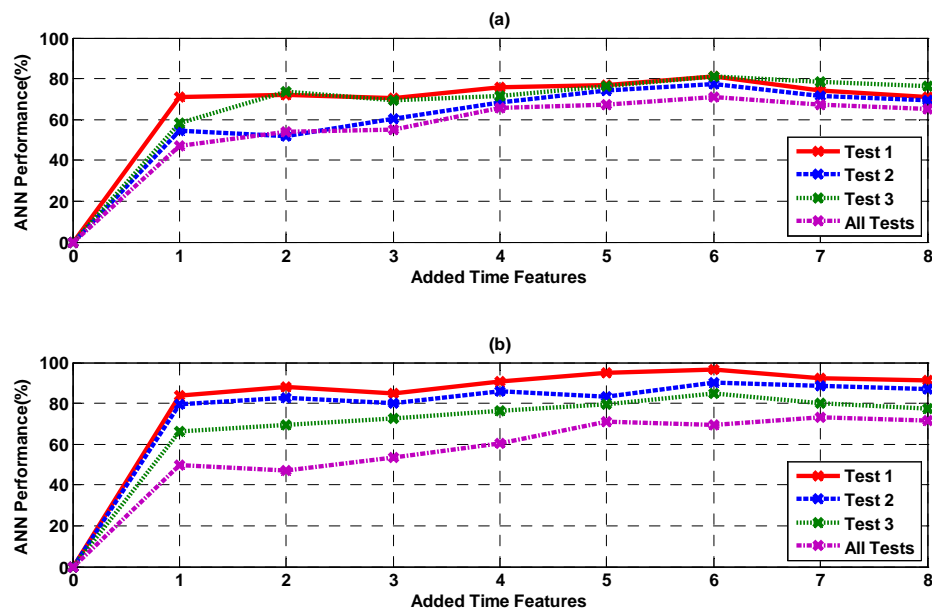
Figure 5.17: Cumulative ANN performance for time features in idling test: (a) S9215 sensor, (b) Micro-80D sensor.
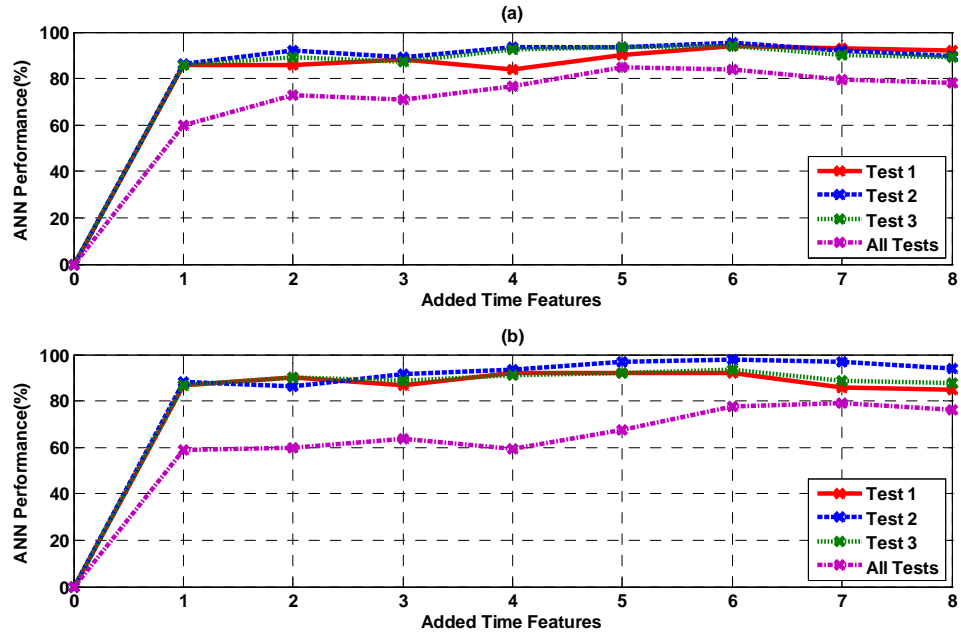
Figure 5.18: Cumulative ANN performance for time features in load test: (a) S9215 sensor, (b) Micro-80D sensor.

5.2. Frequency domain analysis

In chapter 4, it was seen that few systematic changes in raw AE frequency content could be discerned in the data set as a whole. Also, a number of characteristic frequencies (including the turbine running speed) were visible in the demodulated spectra. It was therefore expected that the demodulated spectra would be more likely to produce information indicative of operating conditions of the turbine, although the raw spectra were also subjected to some initial pattern-recognition analysis.

5.2.1. Raw frequency classification

On the basis of an examination of figures 4.19 and 4.26, five features were extracted from the raw frequency domain: (a) the ratio of the energies in a low frequency band (100-200 kHz) to a high frequency band (300-450kHz), (b) the standard deviation of the spectrum, (c) the maximum amplitude of the spectrum, (d) the frequency at maximum amplitude, and (e) the frequency skewness. Values of these frequency features from the idling tests were split into two equal parts, as before, and the network trained to recognize the running speed, performance being measured by the proportion of correct classifications in the test set. Figure 5.19 shows the classification performance for both the Micro-80D and S9215 sensors. As expected, this shows a relatively poor classification for both sensors.
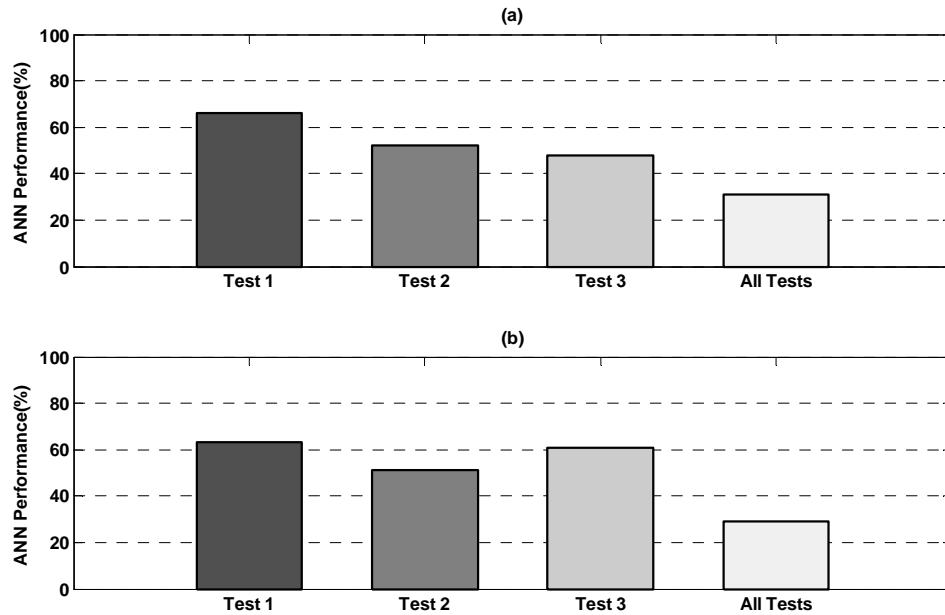
Figure 5.19: ANN performance for without load tests of frequency features (a) Micro-80D sensor performance (b) S9215 sensor performance.

5.2.2. Demodulated frequency spectra

Figures 5.20 and 5.21 show all of the demodulated spectra recorded in the idling tests for the exhaust-mounted sensor and the shroud-mounted sensor, respectively. All spectra were normalised to the energy content to facilitate comparison and averaging and avoid the complication of including the energy or amplitude of the signal which is the subject of the analysis in the previous section. Each of the independent sample spectra are shown in blue and the averaged spectra are shown as heavy red dotted lines.

As can be seen, many of the averaged spectra show a clear peak at the running speed (arrowed in Figures 5.20 and 5.21), and, less often, the first harmonic of the running speed. However, the running speed is rarely the dominant peak in the spectrum and, in cases where its peak is weak or absent, the individual spectra which make up the average often contain strong peaks at a very wide range of frequencies. Many of the exhaust spectra contain a strong peak at around 110Hz, sometimes associated with peaks either side at around 40Hz and 165Hz. The 110Hz peak tends to be more strongly exhibited at the exhaust, whereas the running speed peaks tend to be more strongly exhibited at the shroud.
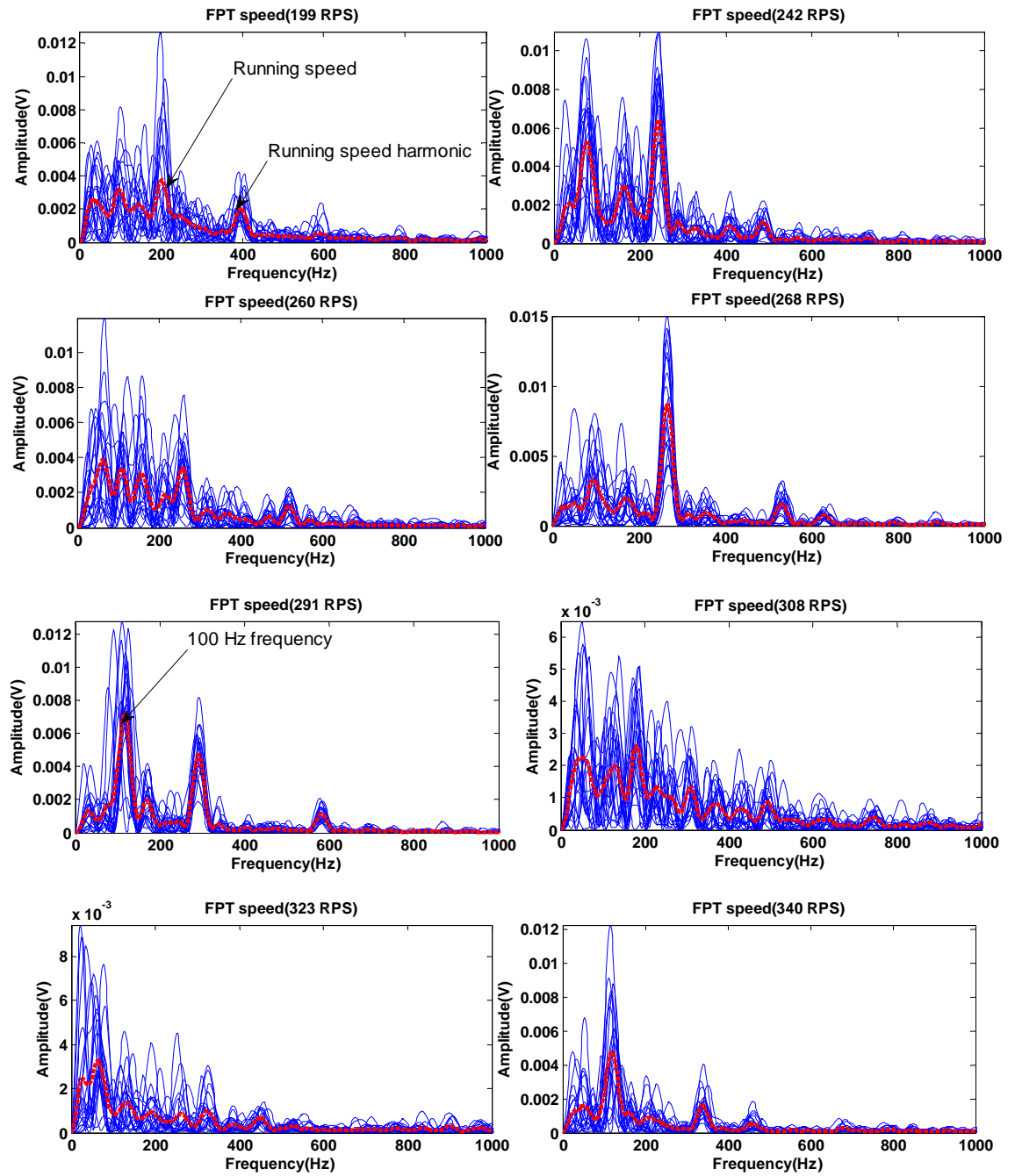
Figure 5.20: Demodulated spectra for idling test with Micro-80D sensor at 8 different speeds of FPT. Individual spectra shown in blue and averaged spectra shown in red.
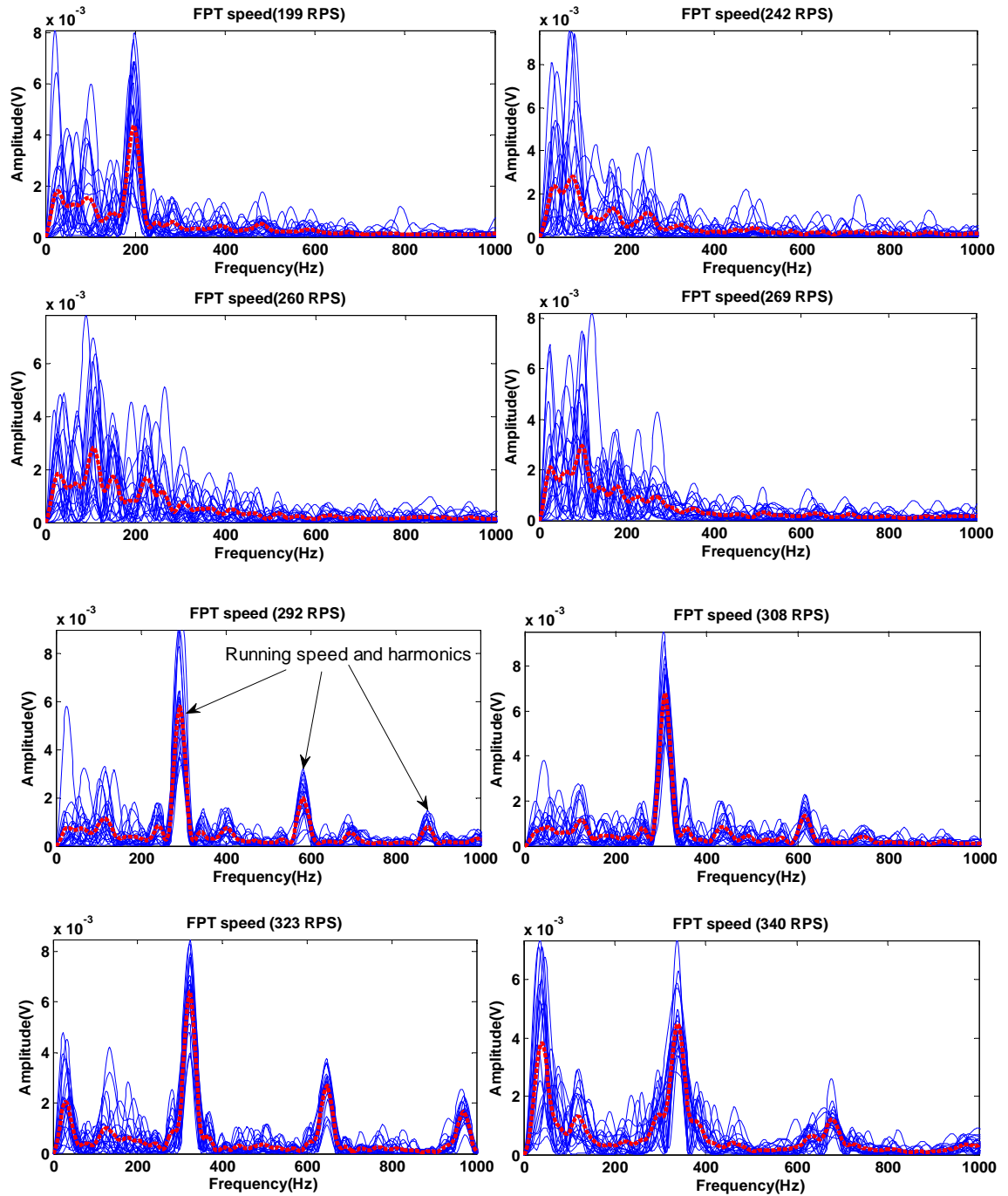
Figure 5.21:Demodulated spectra for idling test with S9215 sensor at 8 different speeds of FPT. Individual spectra shown in blue and averaged spectra shown in red.

Figures 5.22 and 5.23 show the demodulated frequency spectra for the Micro-80D sensor and the S2910 sensor for the load tests. As for the idling tests, the running speed is not always present in the spectrum, although it is generally more strongly represented in the load tests than in the idling tests. In the cases where the running speed cannot be discerned, it is possibly obscured by broad-band noise at the lower end of the spectrum which affects both the exhaust and the shroud sensors at the lowest and the highest speeds. The 100Hz peak observed in the idling tests does not seem to be present in the

load tests. It is also clear that the high AE energy of exhaust sensor at speeds 230, and 263 rps "figure 4.25 test 1" is associated with more spectral peaks of running speed. The same observation has been noticed with shroud sensor at speeds 230, 263,286,and 300 rps "figure 4.26 test1".
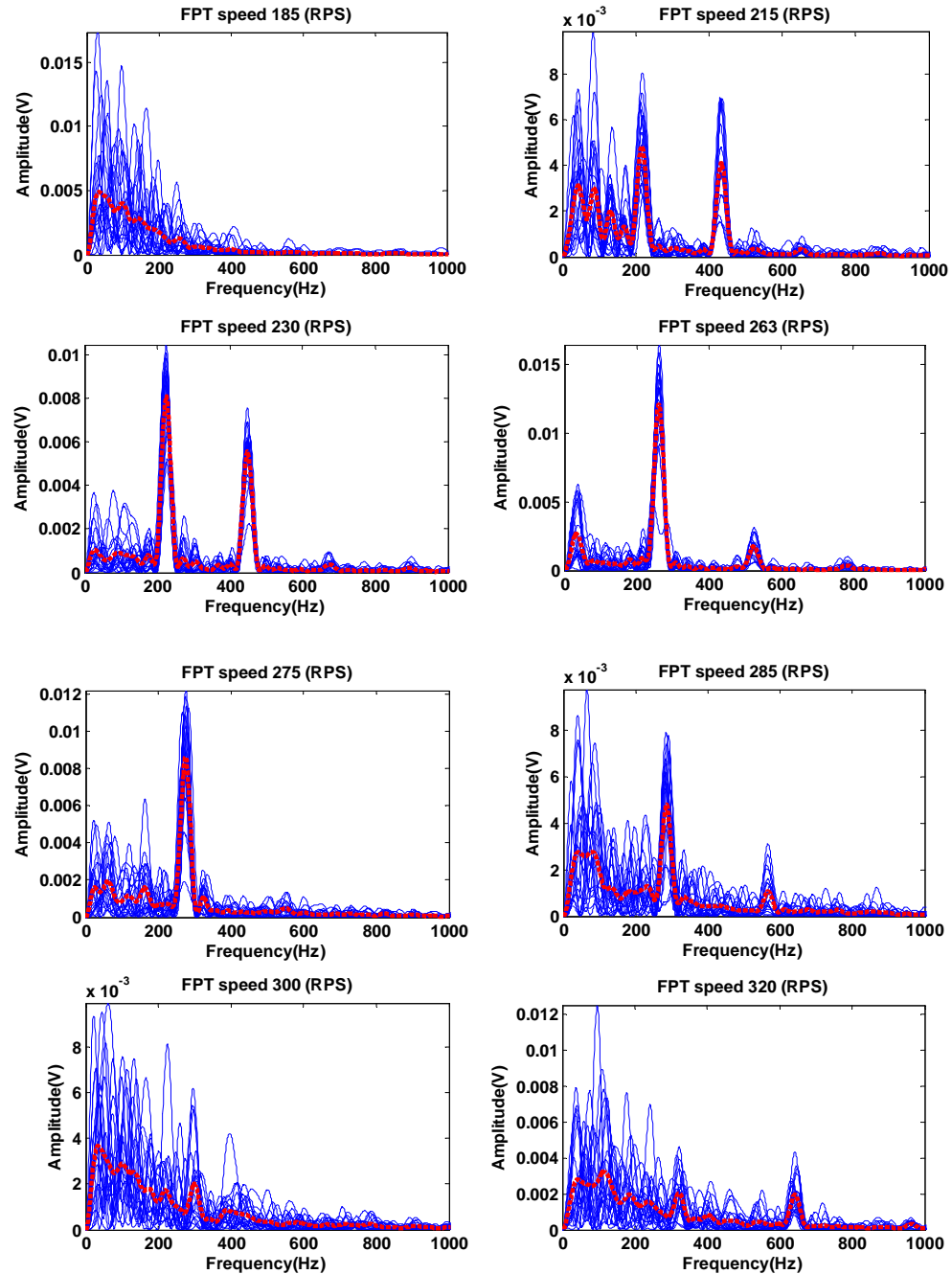
Figure 5.22: Demodulated spectra for load test with Micro-80D sensor at 8 different speeds of FPT. Individual spectra shown in blue and averaged spectra shown in red.
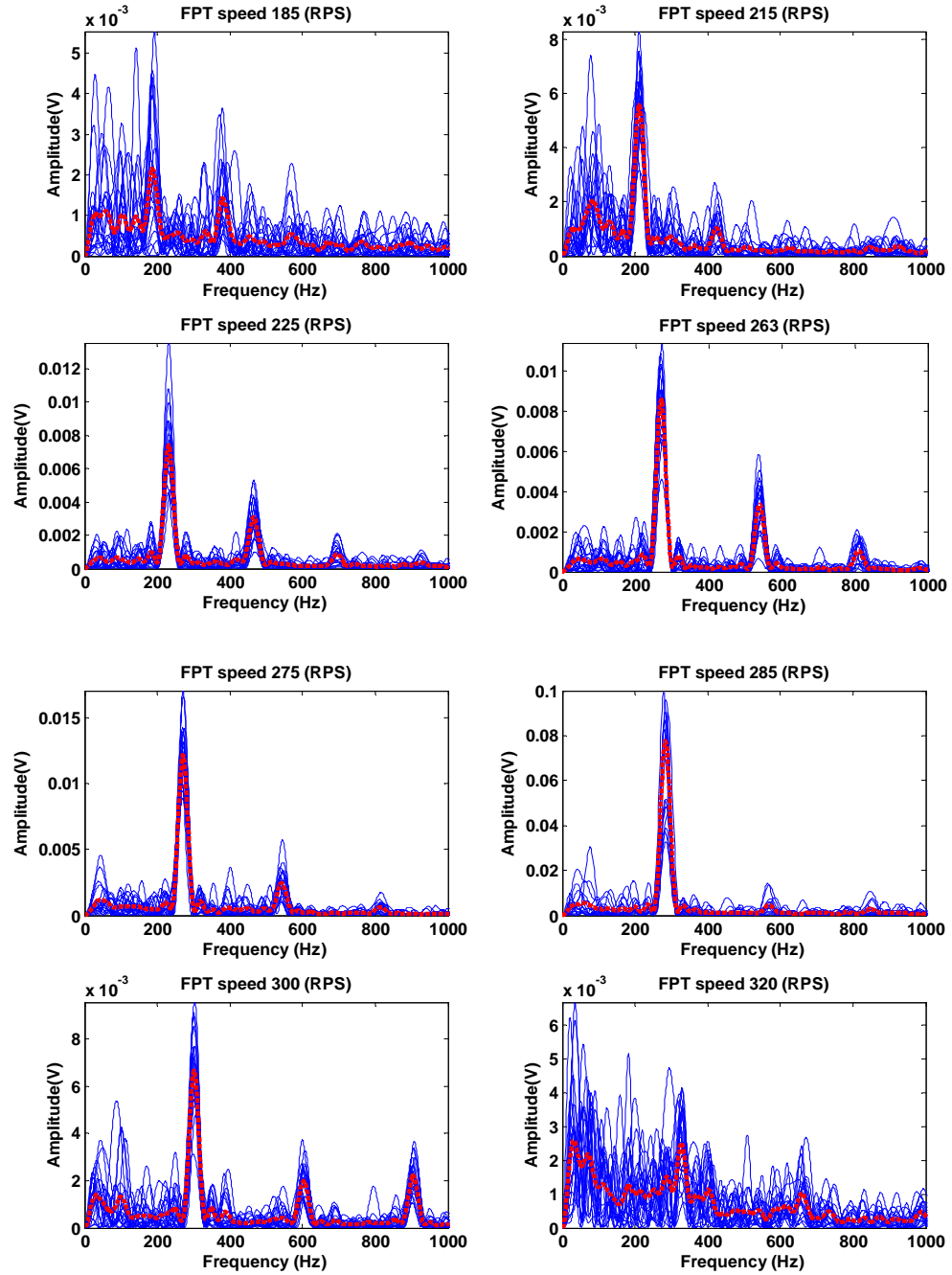
Figure 5.23: Demodulated spectra for load test with S9215 sensor at 8 different speeds of FPT. Individual spectra shown in blue and averaged spectra shown in red.

5.2.3. Demodulated frequency domain feature classification

To provide a complementary analysis to that presented in section 5.1.2, a set of features were generated from the demodulated frequency analysis as input to an ANN with the same specification as for the analysis based on time features. The features were selected to employ as much of the information seen in Figures 5.20 to 5.23 as possible without the computational burden of using the entire spectrum as input to the ANN. Across the 20 records at each speed in each experiment the ten highest amplitude

frequencies were first identified and the energies and the frequencies of the five commonest frequencies used as input to the ANN. As before, half of the data set was used to train the network to the measured running speed and the network was then tested, delivering weights to the output nodes from which a speed classification and an estimate of running speed could be obtained. Figure 5.24 shows the ANN classification performance to be superior to that using time-based features (Figure 5.10) with classification being better than 90% for all individual tests and over 80% for the grouped data. Figures 5.25 to 5.28 show the ANN speed error which, compared with the time-based assessment, exhibits a very high level of certainty for most of the classifications, the performance of the Micro-80D sensor being generally better than the S2910. The relatively poor performance on the grouped data for the S92105 sensor on the load tests can be seen to be confined to a few records where the speed estimate is well away from the actual.

Figure 5. 24: (a) S9215 without load tests, (b) Micro-80D sensor without load tests, (c) S9215 sensor with load tests, (d) Micro-80D sensor with load tests.
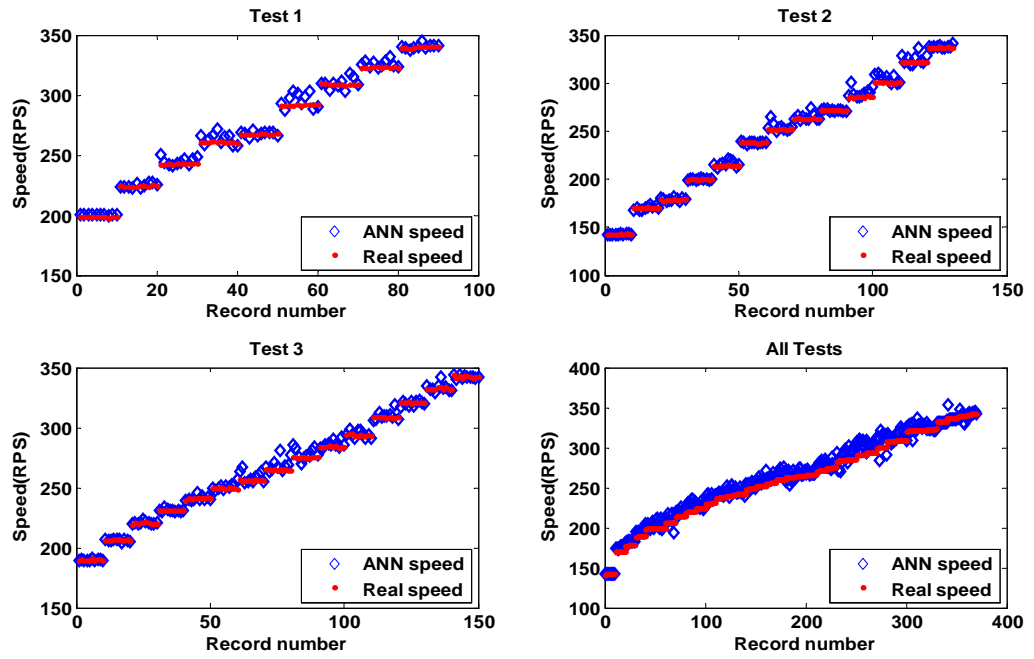
Figure 5.25: ANN speed estimate error for S9215 sensor on idling test.
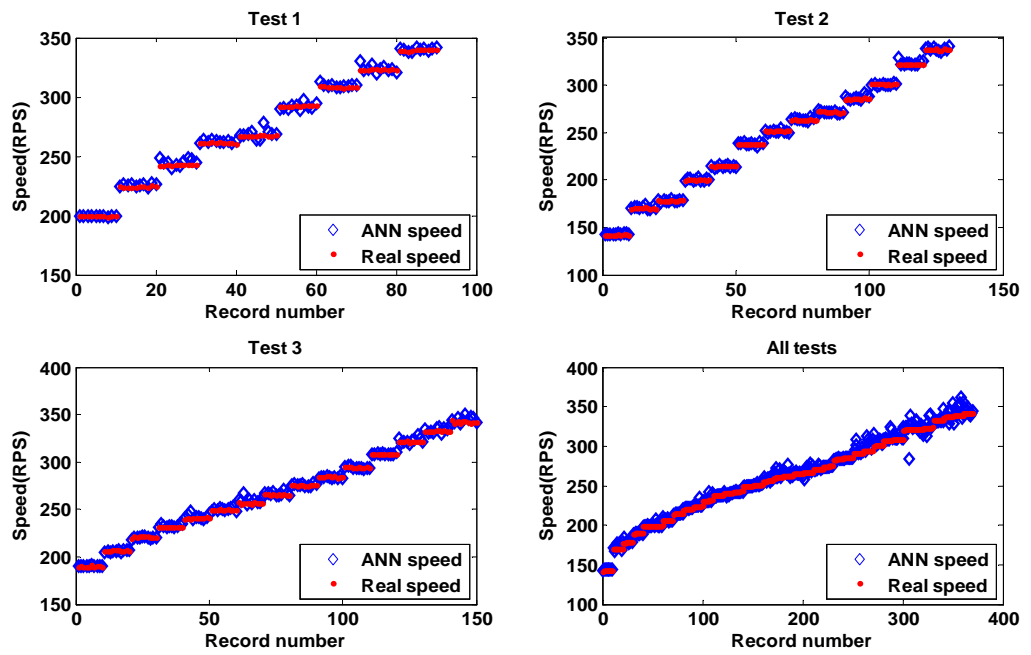
Figure 5.26: ANN speed estimate error for Micro-80D sensor on idling test.
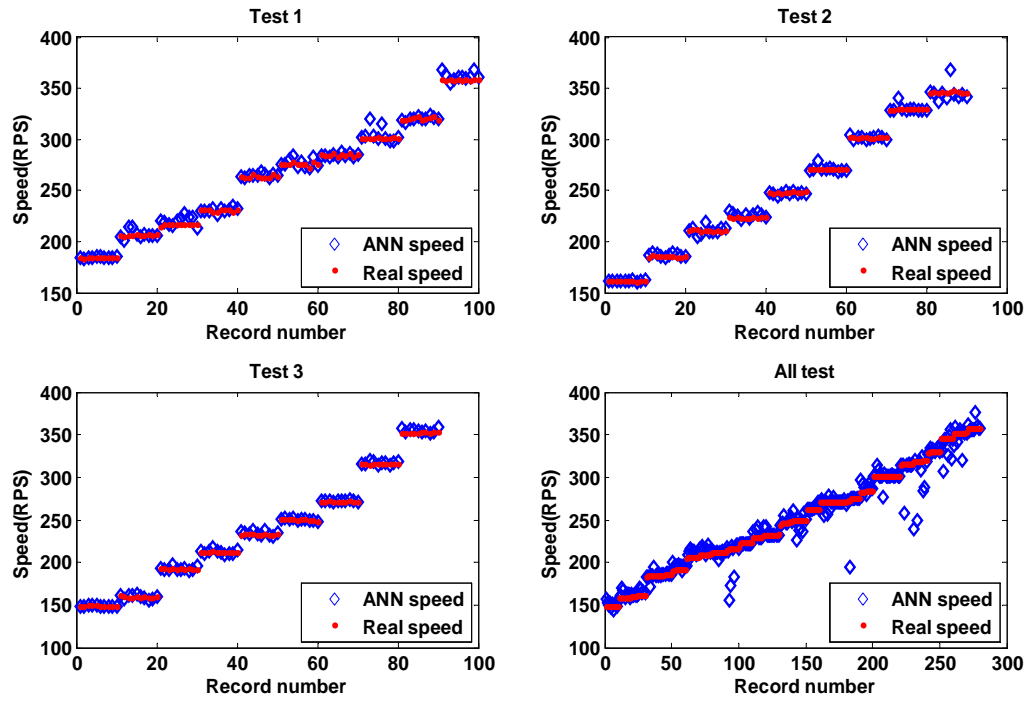
Figure 5.27 : ANN speed estimate error for S9215 sensor on load test.
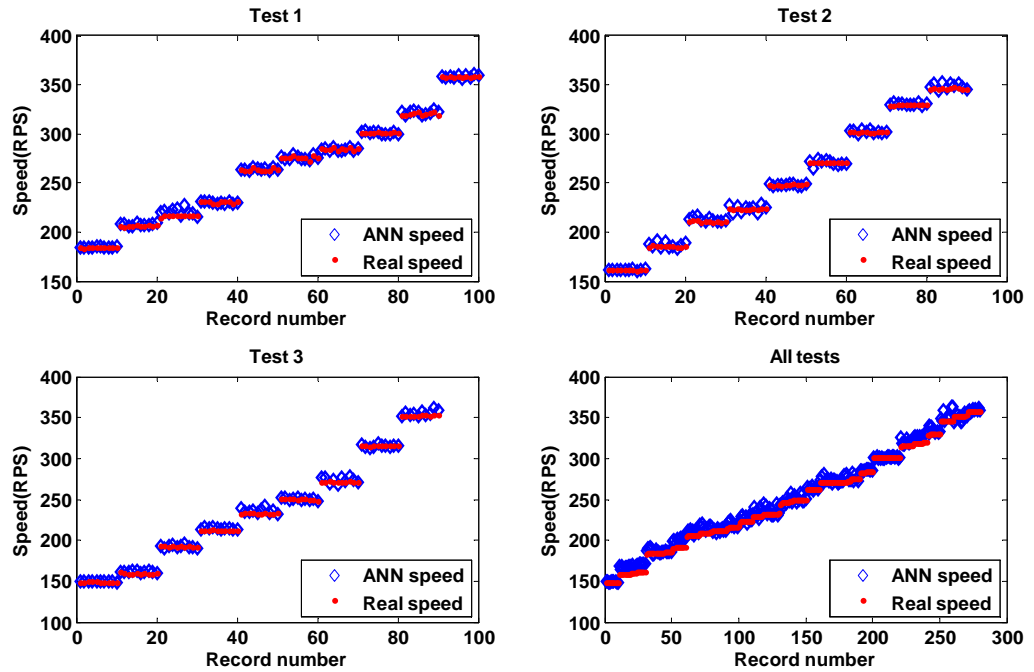
Figure 5.28: ANN speed estimate error for Micro-80D sensor on load test.

5.3. Analysis combining time features and demodulated frequency features

Because it relies on the energy of the signal, the statistical time-based analysis suffers from two potential drawbacks. Firstly, calibration of the sensors is required on every application as the energy will depend on many factors not related to the running condition, not the least of them being the source-sensor distance and the quality of the coupling. Secondly, the statistical time-based ANN is probably doing little more than a multi-point fit to curves such as in figure 4.25, and this is why it is susceptible to changes in the positions of peaks in the repeat tests. On the other hand, although the frequency-based analysis can clearly identify instabilities in the same evolutions, it is not able to detect the clear (albeit weaker) trends in stable regimes, such as that shown in figure 4.10.

Therefore, this section seeks to combine the strengths of the time-based analysis with the frequency-based analysis to obtain a better understanding of the sources of AE in the tests and how these might be used to produce a model for normal running of the turbine.

5.3.1. Pulse shape recognition combined with frequency features

The pulse shape recognition network, although it shows poor performance, has the potential advantage over the statistical one in that it is not amplitude-dependent and the pulse-space approach also encodes some non-periodic frequency information. Figure 5.29 shows the effect of combining the pulse shape recognitions with raw AE features and, clearly, the performance is only marginally better than the pulse shape recognition alone, and poorer than the raw AE feature performance. The pulse-space approach achieves its best performance when it is combined with demodulated frequency approach to perform up to 90% for both sensors (figure 5.30).
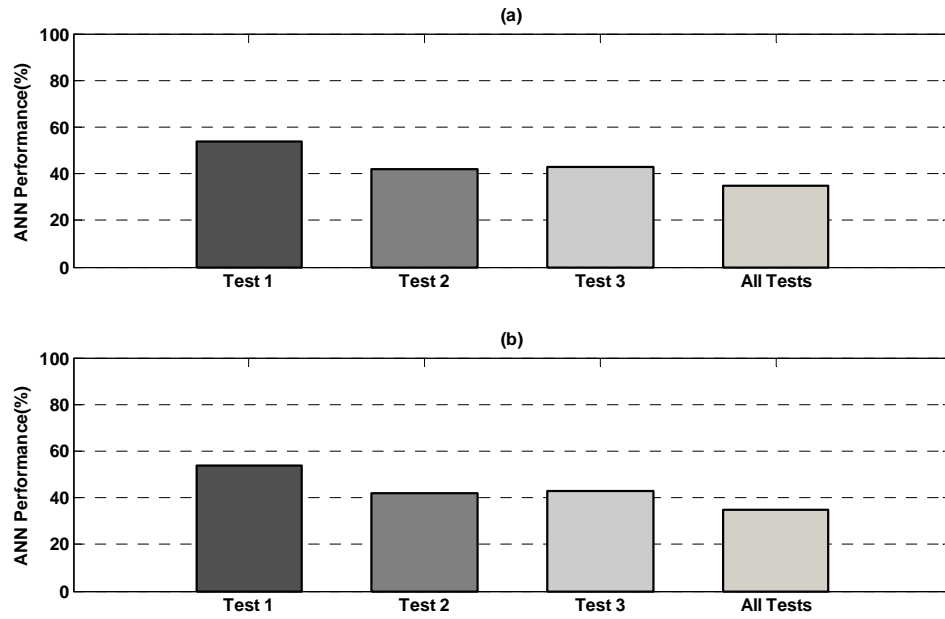
Figure 5.29: Pulse shape recognition ANN performance for idling tests including raw frequency features (a) Micro-80D sensor performance (b) S9215 sensor performance.
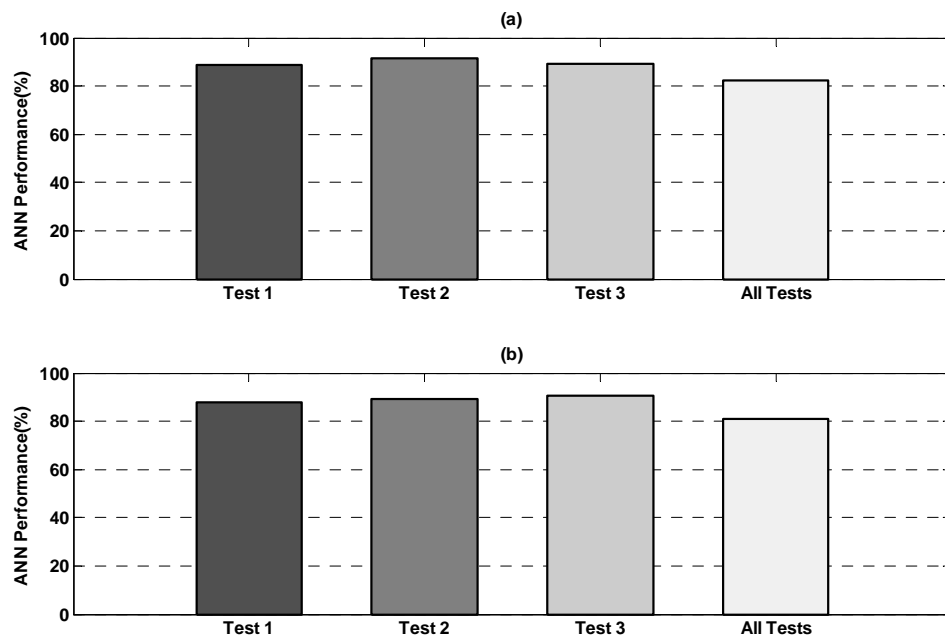
Figure 5. 30: Pulse shape recognition ANN performance for idling tests including demodulated frequency features (a) Micro-80D sensor performance (b) S9215 sensor performance.

5.3.2. Statistical time features combined with demodulated frequency features

As can be seen from figures 5.10 and 5.24, speed classification based on statistical time features and demodulated frequency features both give good performance (75%-90% classification success) for both sensors in the idling and load tests, when the tests are considered separately. However, for both feature sets, the performance drops to between 70% and 80% when the tests are grouped together, suggesting that the network is training to a particular curve shape rather than particular behaviour reflected in the AE signal. Figure 5.31 shows the ANN performance for the running turbine with and without load when both the statistical time features and the demodulated frequency features are used together. As can be seen, the success for the individual tests has improved to almost 100% and the success when the tests are treated as a group has risen to around 90%. Figures 5.32 to 5.35 show the corresponding ANN error and, again, it can be seen that the confidence of classification is very high and the predicted speed is very close to the actual speed in all records except for three in the grouped load tests for the S9215 sensor.
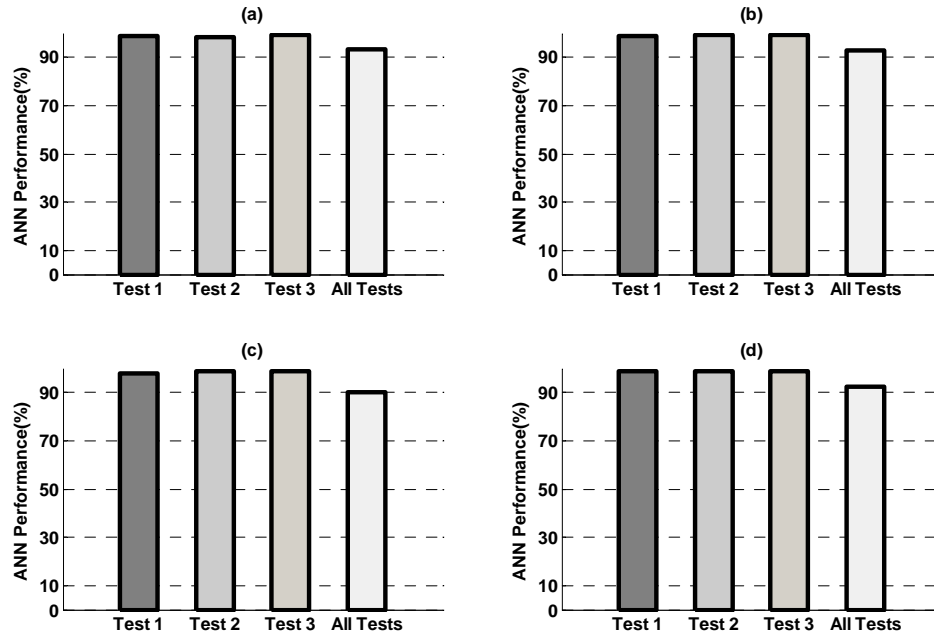
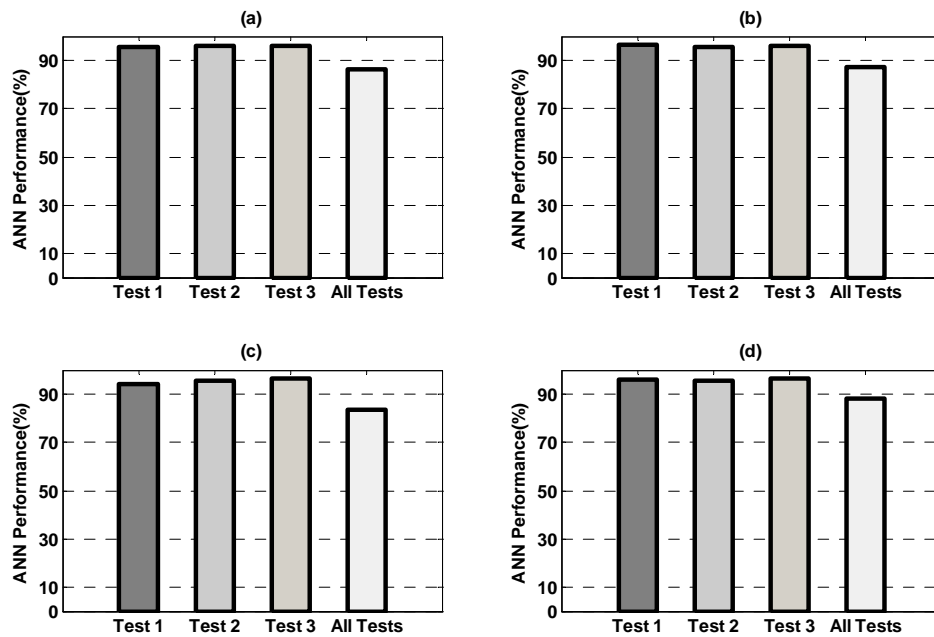Figure 5.31: ANN performance with time and frequency features: (a) S9215 sensor without load tests, (b) Micro-80D sensor without load tests, (c) S9215 sensor with load tests, (d) Micro-80D sensor with load tests.
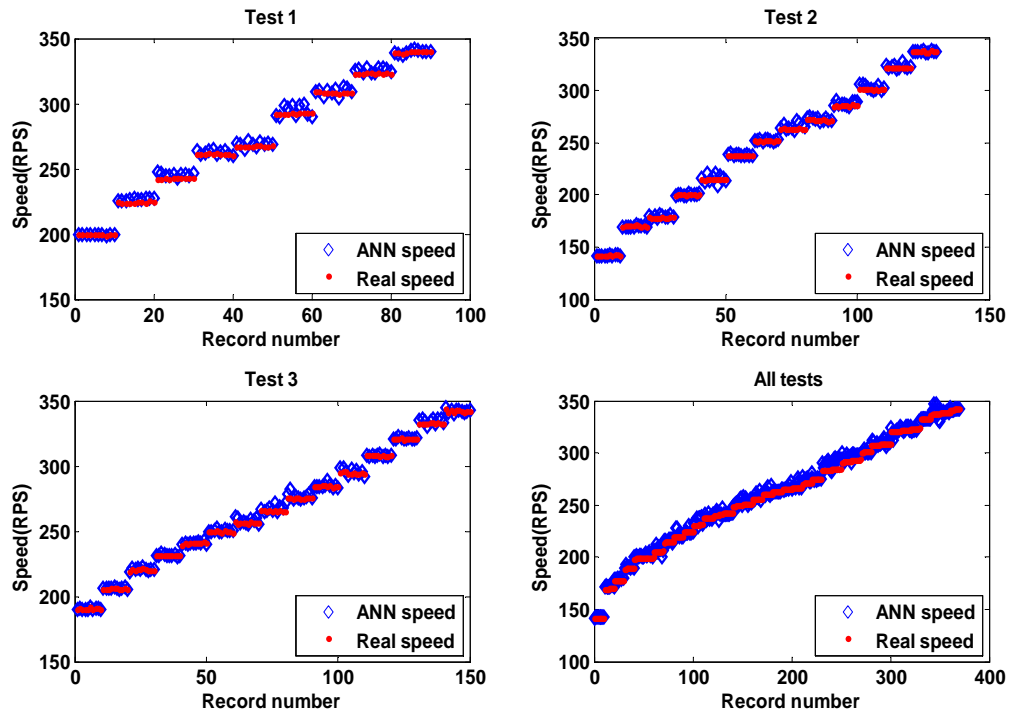
Figure 5.32: ANN error for S9215 sensor during without load test.
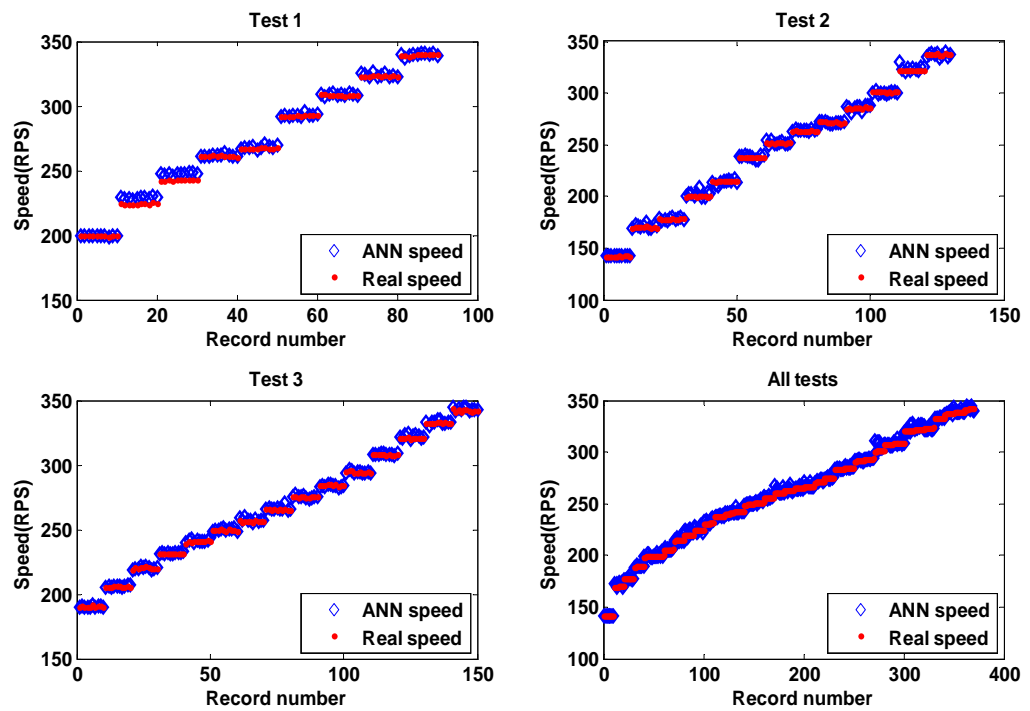
Figure 5.33: ANN error for Micro-80D sensor during without load test.
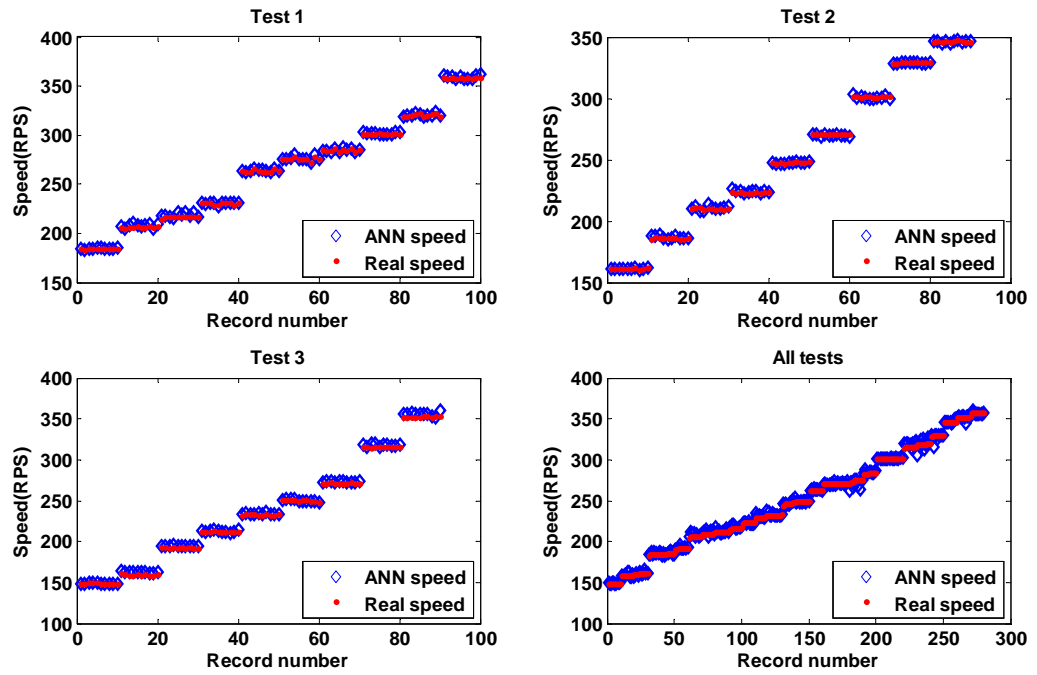
Figure 5.34: ANN error for S9215 sensor during with load test.
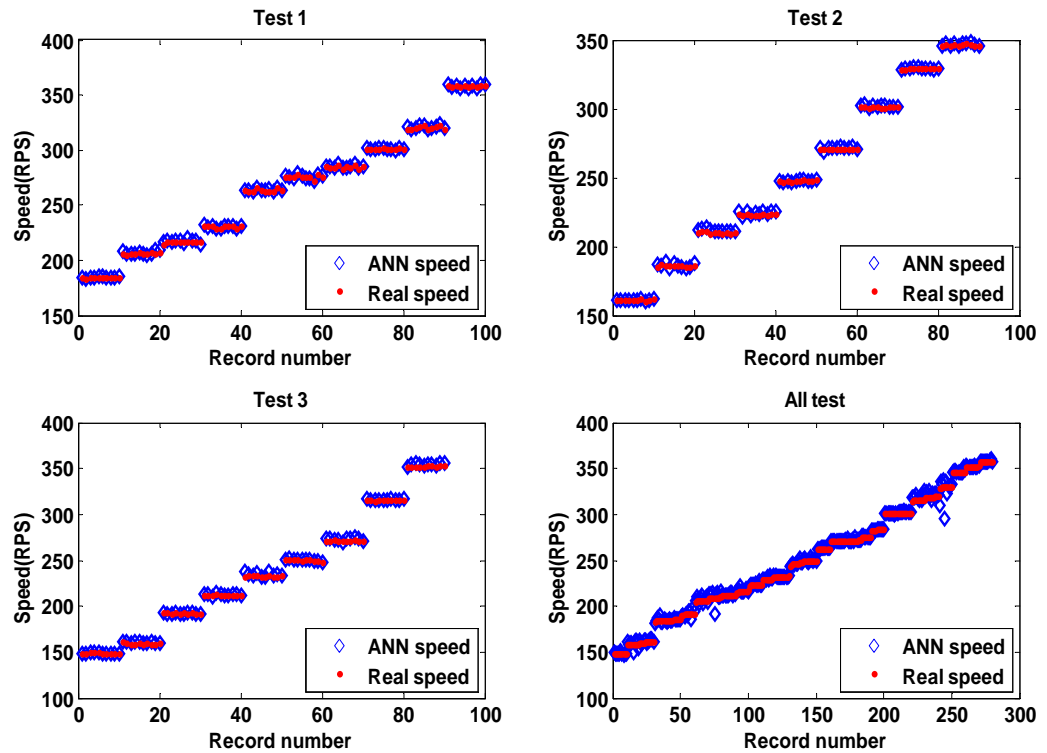
Figure 5.35: ANN error for Micro-80D sensor during with load test.

5.4. Discussion of AE sources in the running turbine

Chapter 4 illustrated that the AE generated in a gas turbine has two components; a background broad band source, probably due to the turbulent gas flow through various parts of the turbine, plus some peaks whose speed position varies a bit between tests, and which are associated with peaks in the demodulated frequency spectrum.

The background AE energy increases smoothly with speed and, on the basis of other work on flow in confined spaces in machinery, it would be expected that the energy of such a source would depend on the nature of the fluid, the flow rate and the size(s) of any orifice(s) in the flow [124, 125]. Also, it would be expected that such sources, if localized, would be able to be traced to certain zones within the machine [17, 126].

The analysis in Chapter 5 has shown that this background energy associated with gas flow begins to become modulated when the impeller is rotating and, at higher speeds, there are a number of spectral peaks in the 20-1000Hz range. These spectral peaks disrupt the smooth evolution of energy *vs* running speed and the peaks in the energy curve, as well as the speed at which certain spectral peaks appear, are not precisely reproducible in repeat tests. However, as shown by the ANN analysis, the behavior of the turbine can be characterized by a combination of the energy within those spectral peaks bands and the overall energy. Potential sources of the spectral peaks are; the combustion chamber, the impeller, the exhaust, and feedback between the alternator and the impeller under load. For the same running speed, the AE signature for the loaded and idling conditions is different and, for the same test, the behaviour recorded at the exhaust-mounted and shroud-mounted sensors is different. This section is devoted to trying to understand these patterns in terms of the sources of AE within the turbine.

The first stage is to separate the two components of the signal in a systematic way. The "spectral peaks energy" in each record, identified as the total energy in the five highest peaks of the demodulated frequency spectrum (which typically accounts for 80% of spectral peaks energy) was subtracted from the total energy to leave the background. Figures 5.36 to 5.38 show the spectral peaks energy removal for each of the repeats of each of the tests. In each figure, the black curves in the first three graphs show the best exponential fit to the energy after removing the spectral peaks energy for each repeat

and the last graph shows the best fit lines for the three tests for each sensor location with
and without load.
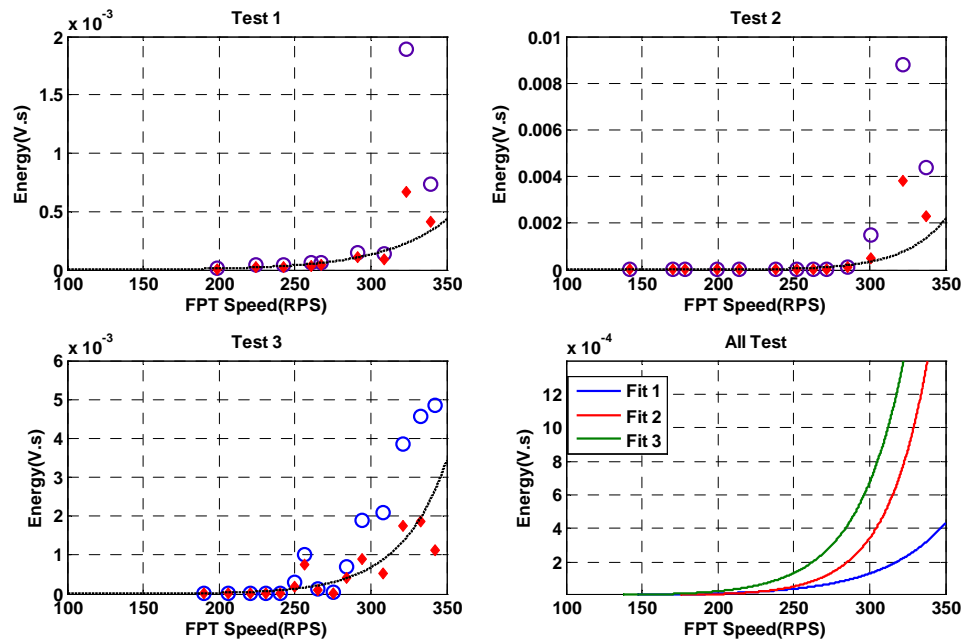
Figure 5.36: Shroud sensor spectral peaks energy removal for idling tests. (Blue points
before removing energy and the red points after)
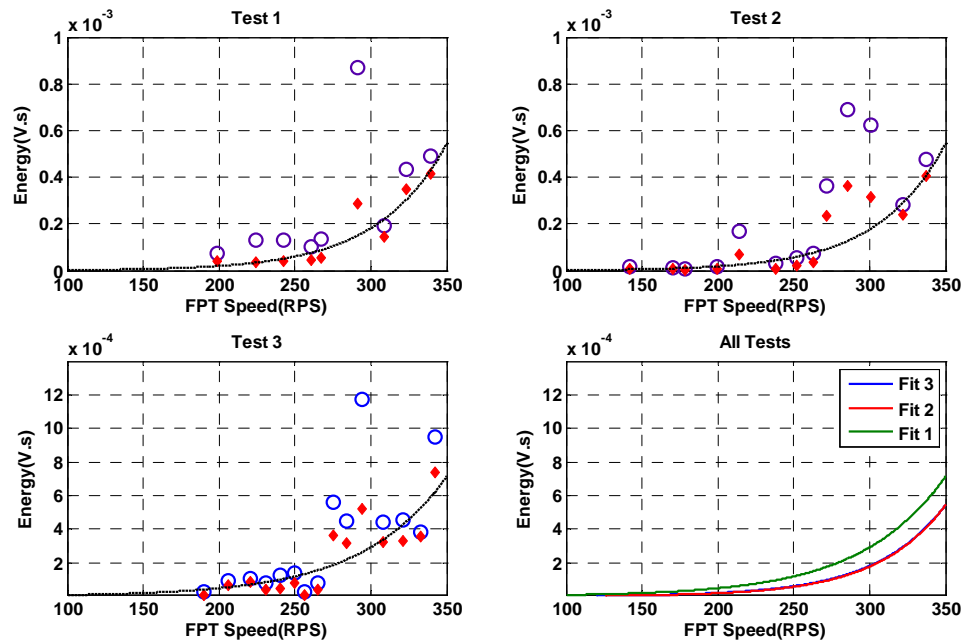
Figure 5.37: Exhaust sensor spectral peaks energy removal idling tests. (Blue points
before removing energy and the red points after)
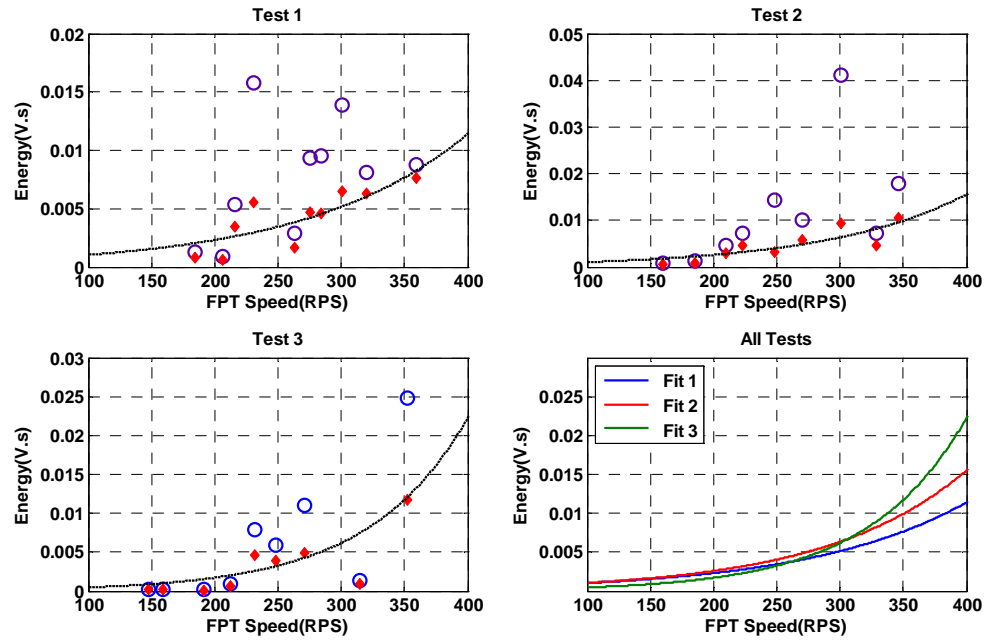
Figure 5.38: Shroud sensor spectral peaks removal load tests. (Blue points before removing energy and the red points after)
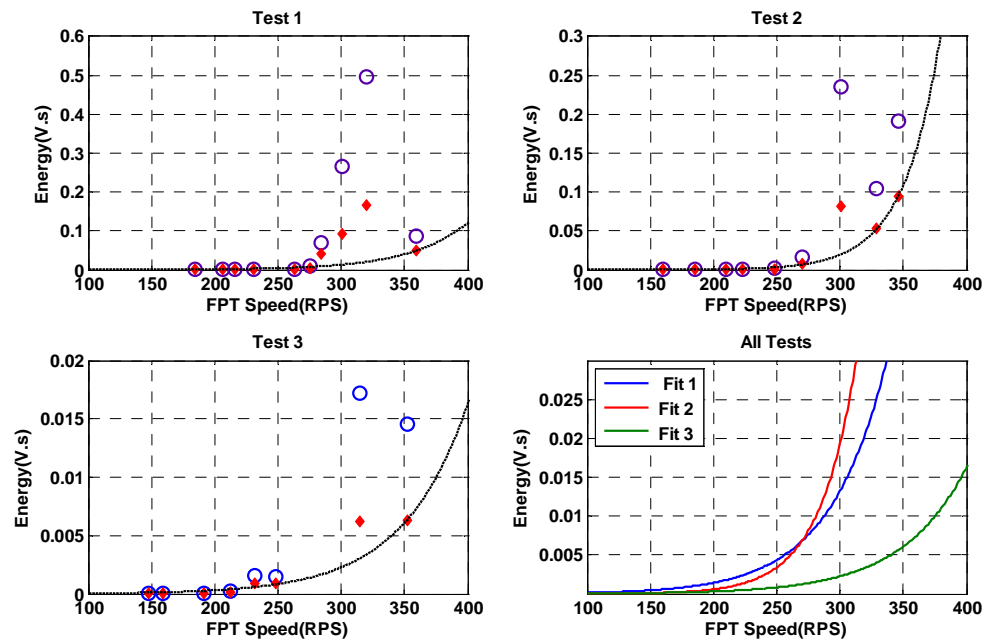
Figure 5.39: Exhaust sensor spectral peaks removal load tests. (Blue points before removing energy and the red points after)

The background AE energy thus obtained from the idling test is compared with the background energy for the static impeller tests (jammed impeller, without impeller) in Figures 5.40 and 5.41, re-plotted against the combustion gas flow rate through the turbine. It is clear that the AE energy is mainly correlated with gas flow resistance, where it is lowest for the test without an impeller where the resistance to gas flow

through the turbine shroud is at its lowest, becomes higher for the jammed impeller tests where the gas has to pass through the orifices represented by the blades and vanes, and is at its highest when the gas flow passes through the rotating blades. It might be noted that, for a given gas flow rate, the differences between the AE energies associated with the three configurations are larger for the shroud sensor than for the exhaust sensor.
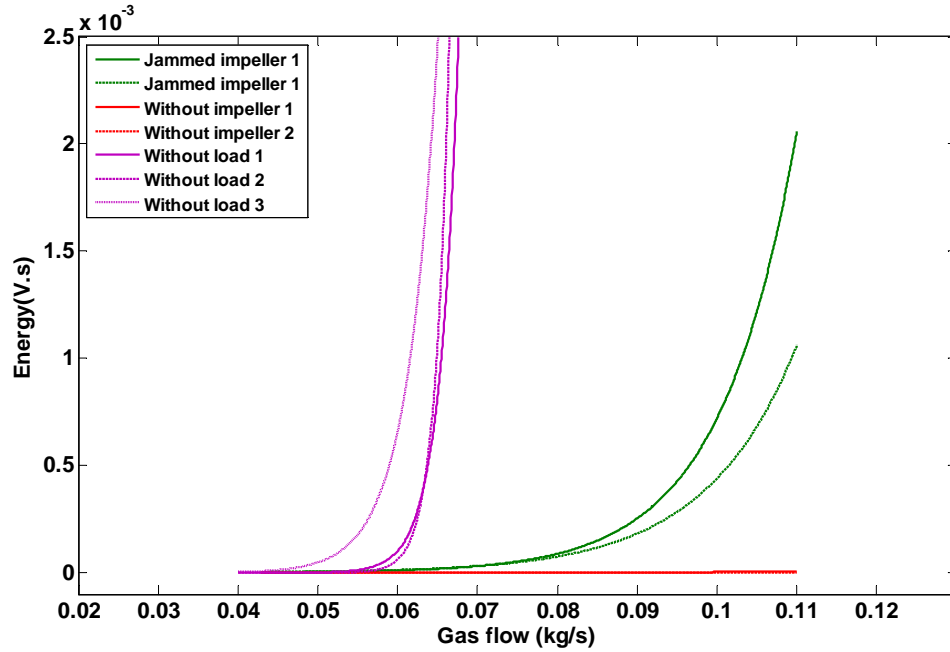
Figure 5. 40: Shroud sensor background AE energy for idling, jammed, without impeller tests.
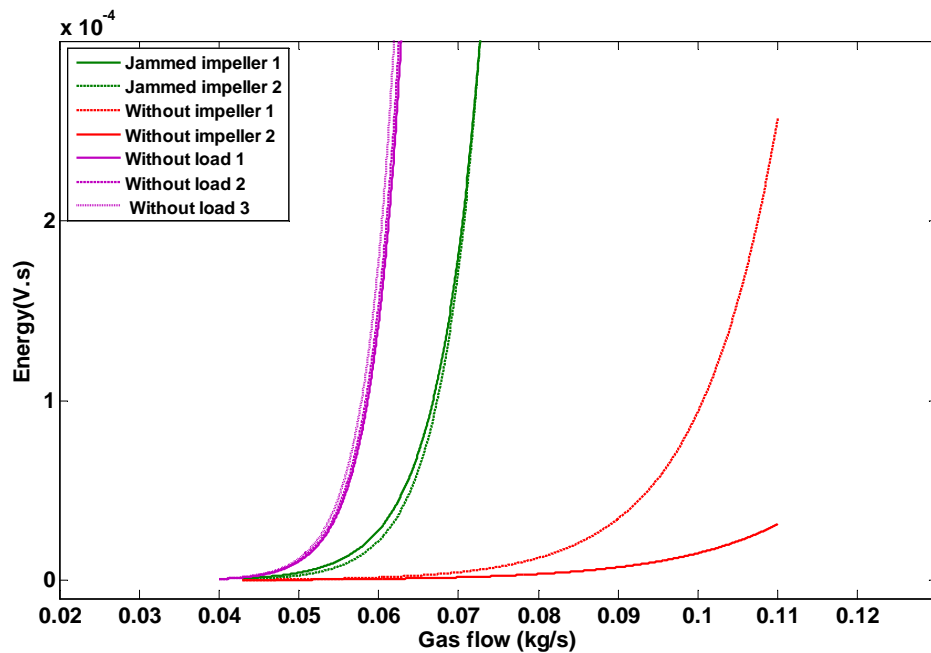
Figure 5.41: Exhaust sensor background AE energy for idling, jammed, without impeller tests.

The background AE energy for the idling test is compared with the background energy for the load test in Figures 5.42 and 5.43, in this case plotted against free power turbine speed. At a given speed, the load test contains more background AE energy only for the exhaust sensor; for the shroud sensor the background is, if anything higher for the idling test. At a given FPT speed, this suggests that loading results in a reduced background flow noise associated with the blades, and an increased flow noise associated with the exhaust.
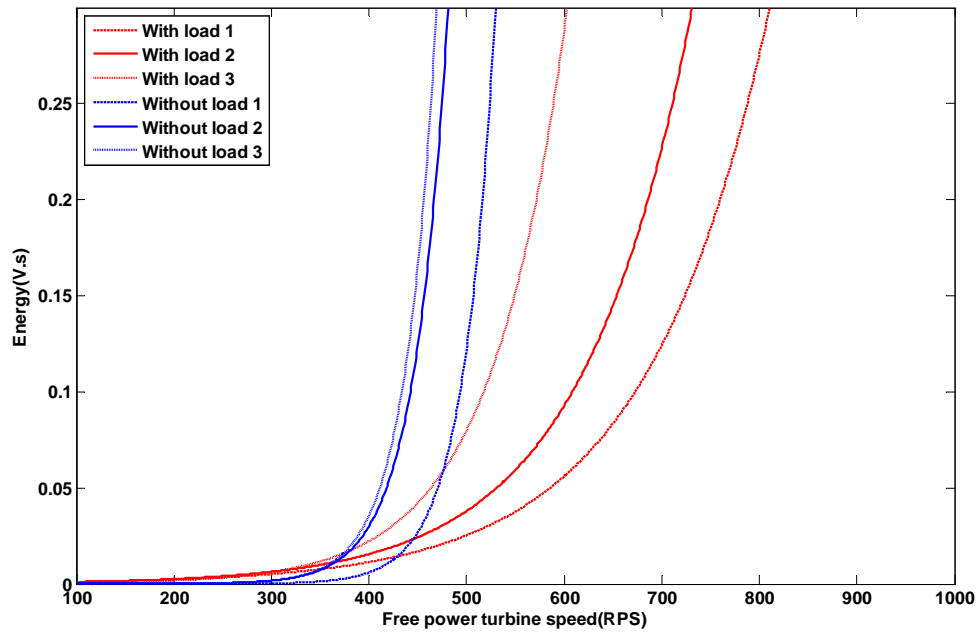
Figure 5.42: Shroud sensor background AE energy for idling and load tests.
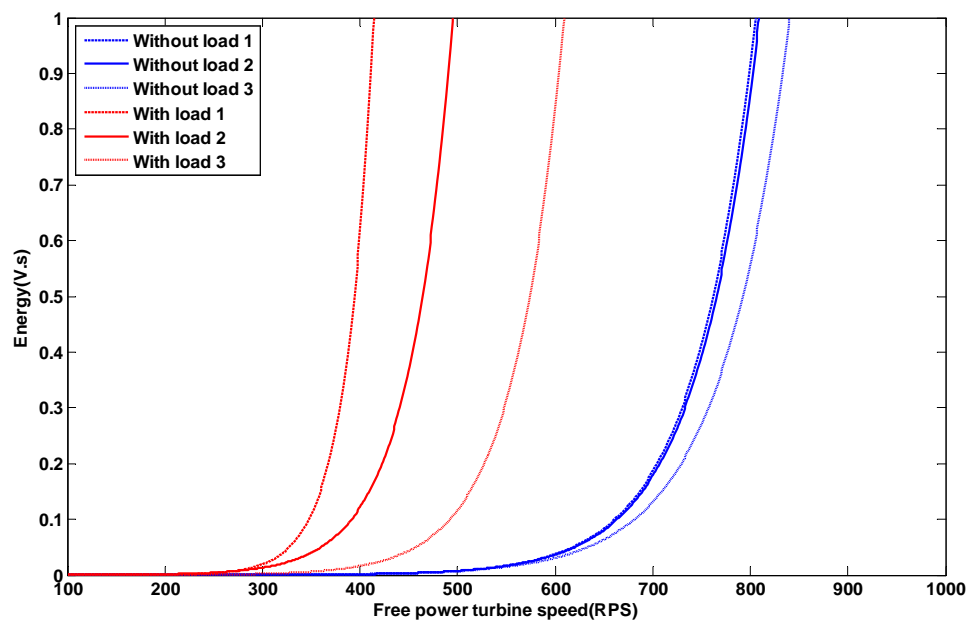
Figure 5.43: Exhaust sensor background AE energy for idling and load tests.

In order to identify the energy not accounted for in Figures 5.42 and 5.43, the five highest energy spectral peaks frequencies were classified into five categories; the band from 20-100 Hz, the band from 100-200 Hz, the frequency corresponding to the running speed, the first harmonic of the running speed, and a frequency corresponding to 0.65-0.7 times the gas generator running speed. Figures 5.44 to 5.46 show the fraction of the total spectral peaks energy in each category for the shroud sensor for the idling tests. It can be seen here that none of the fractions change monotonically with turbine speed and that the energy fraction at the running speed frequency is almost always the highest. The 20-100 Hz and 100-200 Hz bands occupy a significant proportion of the total spectral energy at all turbine speeds.
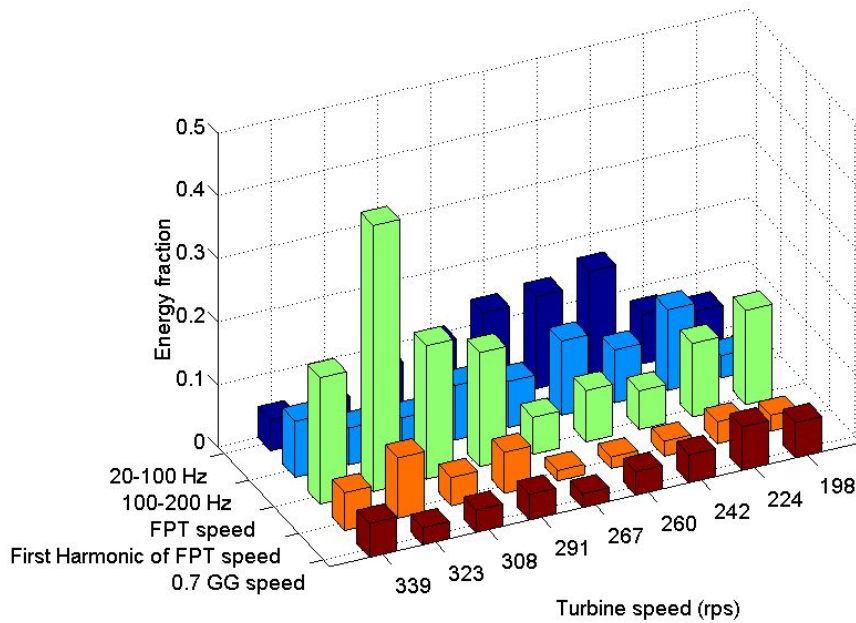
Figure 5.44: Shroud sensor energy fraction of spectral peaks frequencies for idling test1.
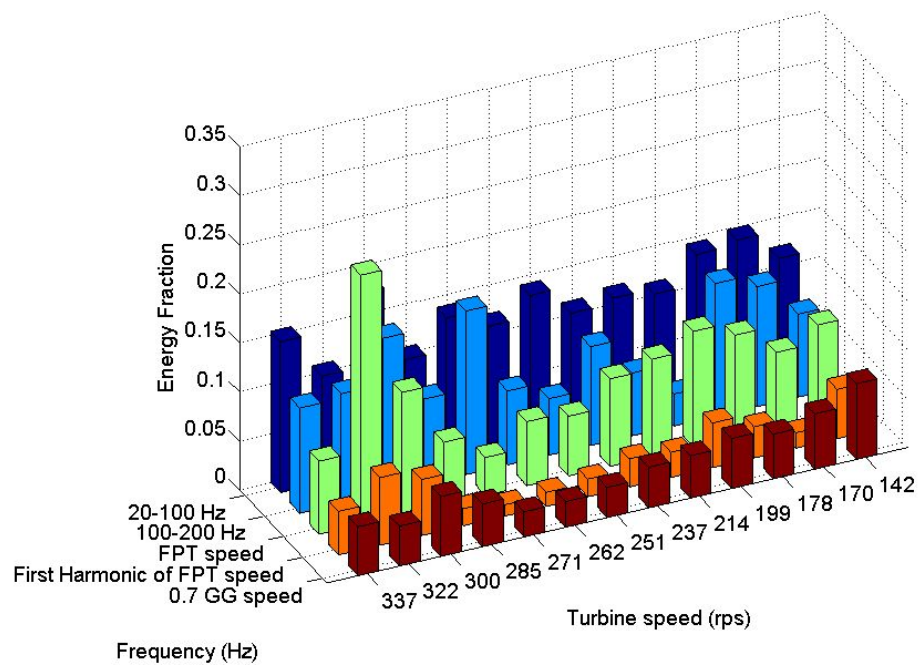
Figure 5.45: Shroud sensor energy fraction of spectral peaks frequencies of idling test2.
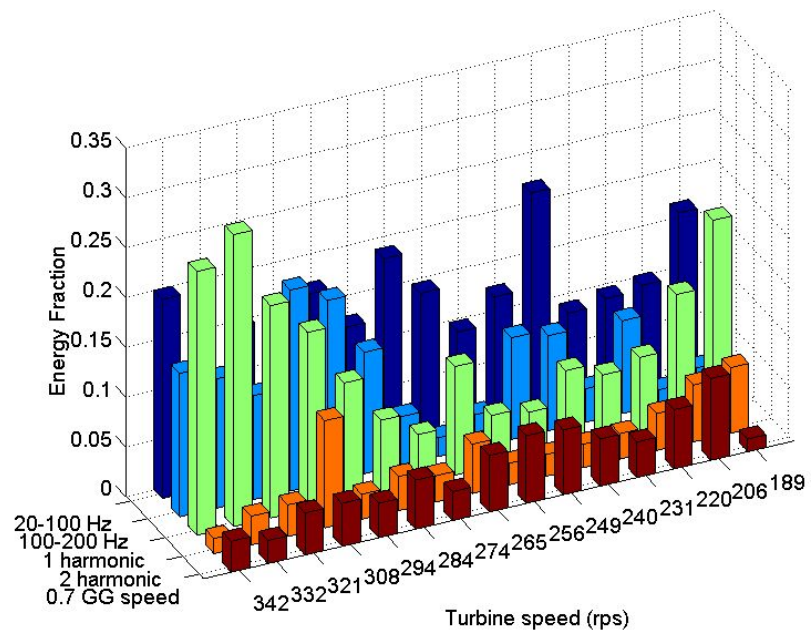
Figure 5.46: Shroud sensor energy fraction of spectral peaks frequencies of idling test3.

Figures 5.47 to 5.49 show the energy fractions for the exhaust sensor for the idling tests. The running speed frequency still has the highest proportion of spectral energy at all turbine speeds and the 20-100 Hz and 100-200 Hz bands seem to be higher than those for the shroud sensor for idling tests. 0.7 GG frequency has higher proportion of energy at lower speed of gas turbine than that of higher turbine speeds.
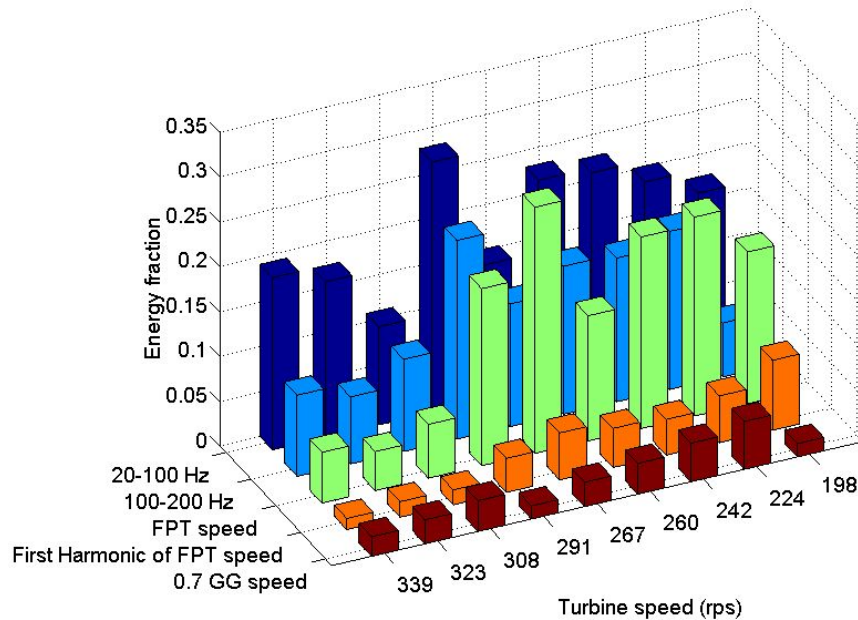
Figure 5.47: Exhaust sensor energy fraction of spectral peaks frequencies of idling test1.
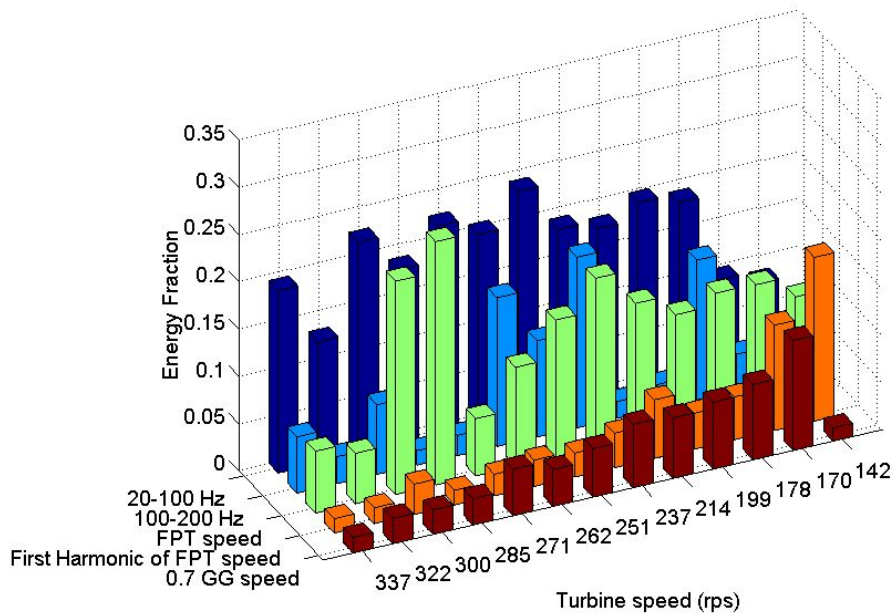
Figure 5.48: Exhaust sensor energy fraction of spectral peaks frequencies of idling test2.
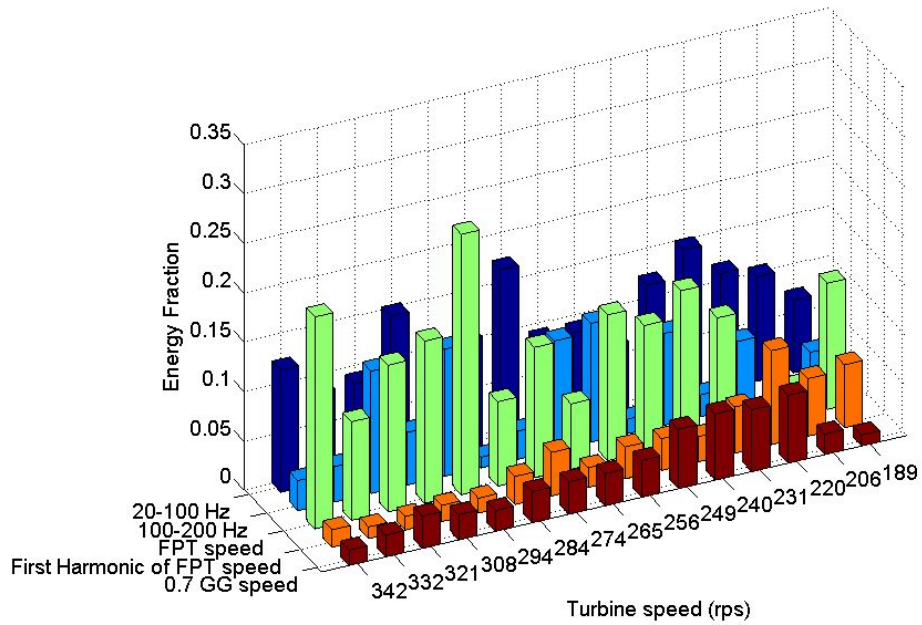
Figure 5.49: Exhaust sensor energy fraction of spectral peaks frequencies of idling test3.

Figure 5.50 to 5.55 show the energy fraction of spectral peaks frequencies of both shroud and exhaust sensors for the load tests. The observations are similar to those for the idling tests for both sensors with the running speed frequency having the highest energy proportion and the 20 -100 Hz and 100-200 Hz bands being stronger and higher with the exhaust sensor than the shroud sensor. In the load tests the running speed frequency and its harmonics are generally stronger than that in the idling tests for both sensors and the 0.7 GG frequency is absent amongst the five highest energy bands.
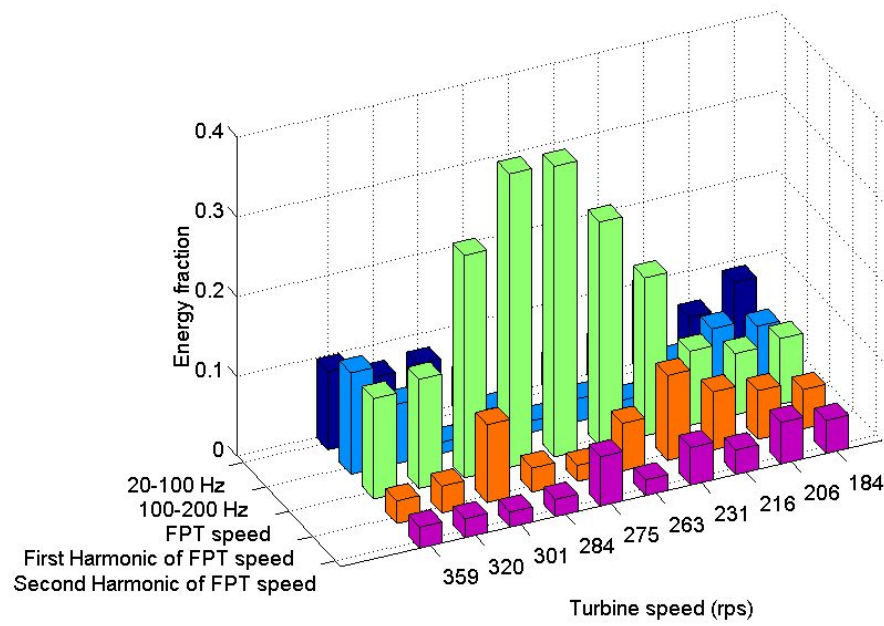
Figure 5.50: Shroud sensor energy fraction of spectral peaks frequencies for load test1.
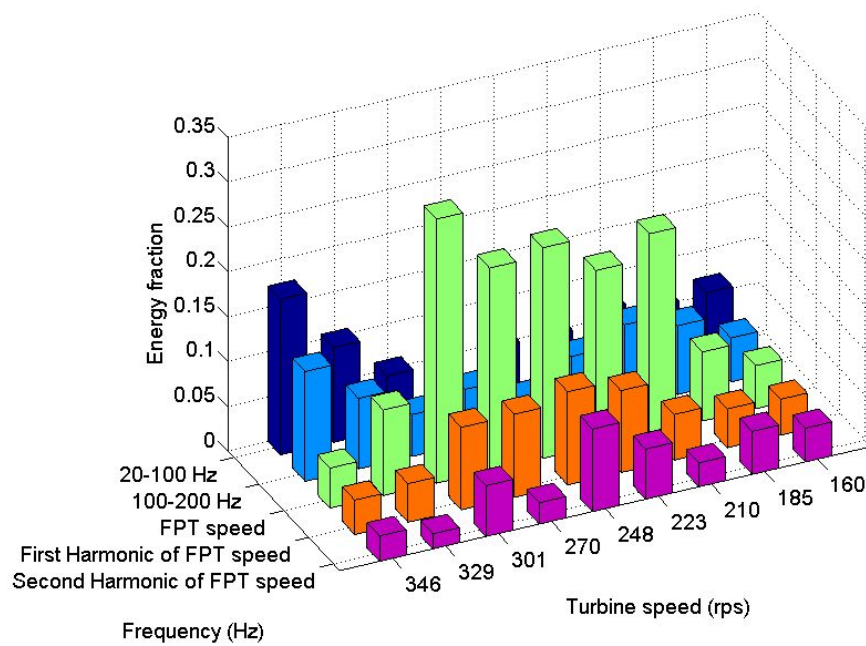
Figure 5.51: Shroud sensor energy fraction of spectral peaks frequencies for load test2.
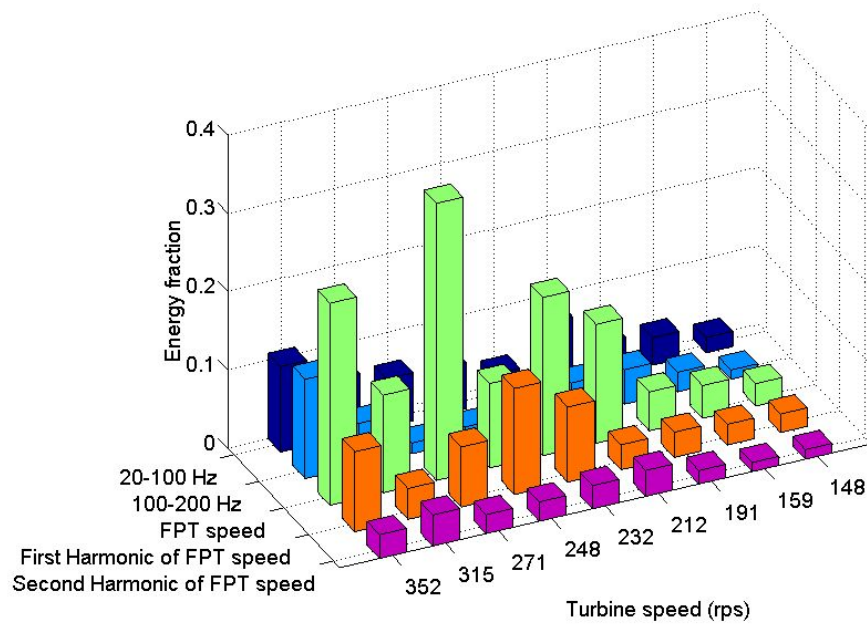
Figure 5.52: Shroud sensor energy fraction of spectral peaks frequencies for load test3.
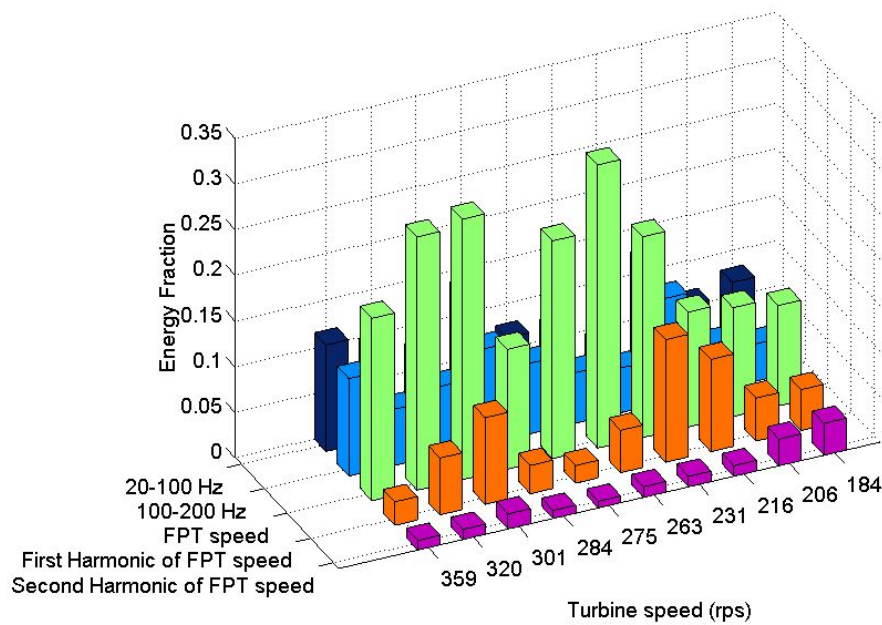
Figure 5.53: Exhaust sensor energy fraction of spectral peaks frequencies for load test1.
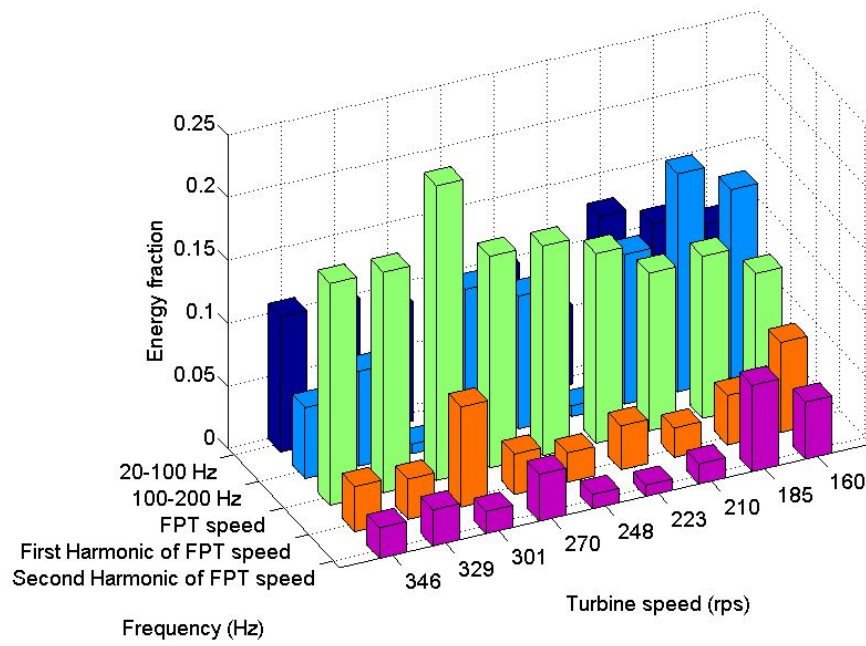
Figure 5.54: Exhaust sensor energy fraction of spectral peaks frequencies for load test2.
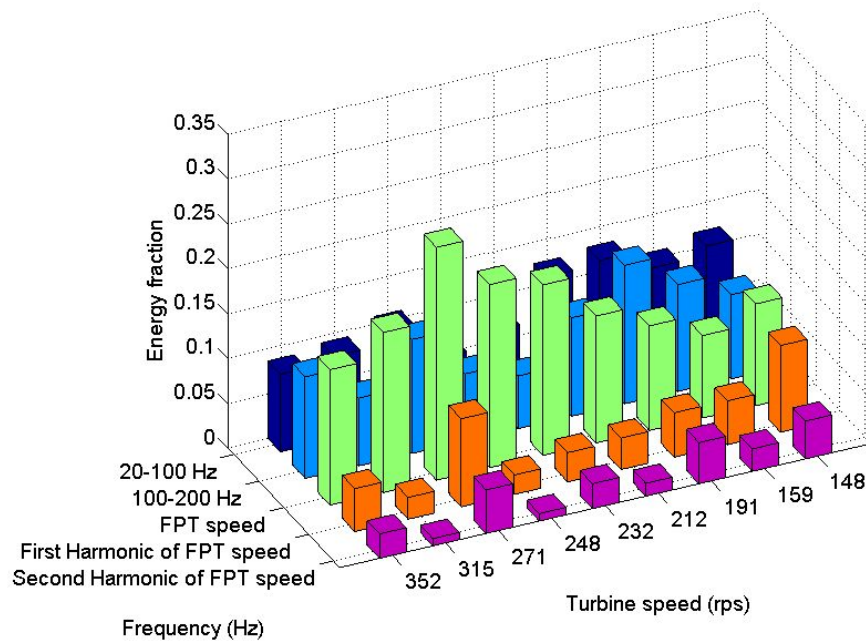
Figure 5.55: Exhaust sensor energy fraction of spectral peaks frequencies for load test3.
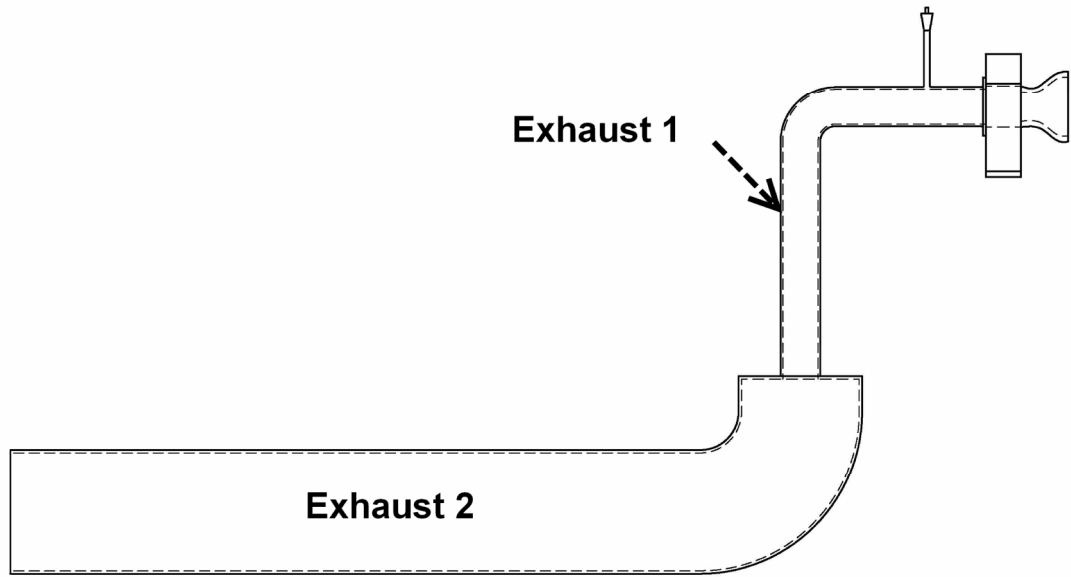
Figure 5.56: Schematic of gas turbine exhaust system.

Figure 5.56 shows a schematic diagram of the turbine exhaust, which consists of two pipes of 100 mm and 300 mm diameter and length1.69 m and 4.15 m, respectively. The temperature of the exhaust gases varies between 400 and 530°C for the load and idling tests, respectively, and the speed of sound, c (ms^{-1}), in each tube can be calculated from:

$$c = \sqrt{\frac{\gamma RT}{M}}$$ (5.1)

where

γ is the adiabatic index of the gas

R is the molar gas constant (Jmol^{-1}K^{-1}).

T is the absolute temperature (K)

M is the molar mass (kgmol^{-1})

The reverberation frequency, f (Hz), in the tube can be estimated from:

$$f = \frac{c}{2L}N$$ (5.2)

where

$N = 1,2,3,.....$

L is the length of the tube (m)

From equation 5.2 the reverberation frequency in the smaller diameter pipe can be estimated to be between 100 and 200 Hz, and, in the larger diameter pipe between 20

and 100 Hz. This suggests that the energy in the 20-100 Hz and 100-200 Hz bands are associated with exhaust reverberations and explains why these are expressed more strongly in the exhaust sensor than the shroud sensor for both load and idling tests.

For the idling tests, the running speed frequency and its harmonics seem to be more strongly expressed at specific turbine speeds and examination of these speeds has shown them to be coincident with the first harmonic of the reverberation frequency of the small diameter exhaust pipe, suggesting that the reverberation frequency is powering the running speed frequency in the turbine. On the other hand the higher energy associated with the running speed frequency and its harmonics in the load tests indicates that the spectral peaks here are dominated by feedback between the turbine impeller and alternator. Table 5.1 and table 5.2 show running speeds, exhaust temperatures, and reverberation frequencies of exhaust1 and exhaust 2.

Idling test				
Turbine speed (RPS)	Exhaust temperature(C^0)	Exhaust sound speed (m/s)	Exhaust1 frequency(HZ)	Exhaust2 frequency(HZ)
190	420	521	156.0	63.5
206	430	525	157.1	64.0
220	435	526	157.6	64.2
231	440	528	158.1	64.4
241	445	530	158.6	64.6
250	450	530	158.6	64.6
256	455	531	159.1	64.8
265	460	535	160.2	65.2
275	465	535	160.2	65.2
284	470	535	160.1	65.2
294	475	537	160.7	65.4
308	480	537	160.6	65.4
321	485	538	161.2	65.6
333	495	538	161.2	65.6
342	505	541	162.1	66.0

Table 5. 1: Thermo features of idling test.

Load test				
Turbine speed (RPS)	Exhaust temperature(C^0)	Exhaust sound speed (m/s)	Exhaust1 frequency(HZ)	Exhaust2 frequency(HZ)
184	520	555	164.1	66.8
206	520	555	164.1	66.8
216	520	555	164.1	66.8
231	520	555	164.1	66.8
263	520	555	164.1	66.8
275	520	555	164.1	66.8
284	520	555	164.1	66.8
301	520	555	164.1	66.8
320	520	555	164.1	66.8
359	520	555	164.1	66.8

Table 5. 2: Thermo features of load test.

Chapter 6: Faulty impeller condition monitoring tests

This chapter describes, analyses and discusses the results of the tests carried out on the turbine with an impeller which had been damaged by removal of the tips of some of the vanes. The tests were carried out with the same sensor positioning as the load tests whose results were described in chapter 4 and analysed in chapter 5. The defective impeller tests were also carried out in the same way, i.e. the speed being varied by gas and air flow.

The results are first described for each of the degrees of damage (two damaged blades and four damaged blades) in comparison with the tests with undamaged blades. Finally the results are analysed against the background of the findings of chapter 5 to assess how impeller damage in the FPT can be detected against the already complex pattern of AE generated in normal operation.

6.1. Results of tests with two damaged blades

Figures 6.1 to 6.9 show the results in a form that can be compared to figures 4.16-4.22. Figures 6.1 and 6.2 show samples of scaled AE signals from the two sensors at nine different speeds of the FPT along the corresponding signal envelopes. Compared with the corresponding examples in figures 4.16 and 4.17 these signals show a much higher density of sharp rise-time pulses, especially for the shroud-mounted sensor, indicating a significant effect in the FPT. The most striking difference, however, is that the signal recorded at the shroud becomes distinctly periodic at higher speeds.
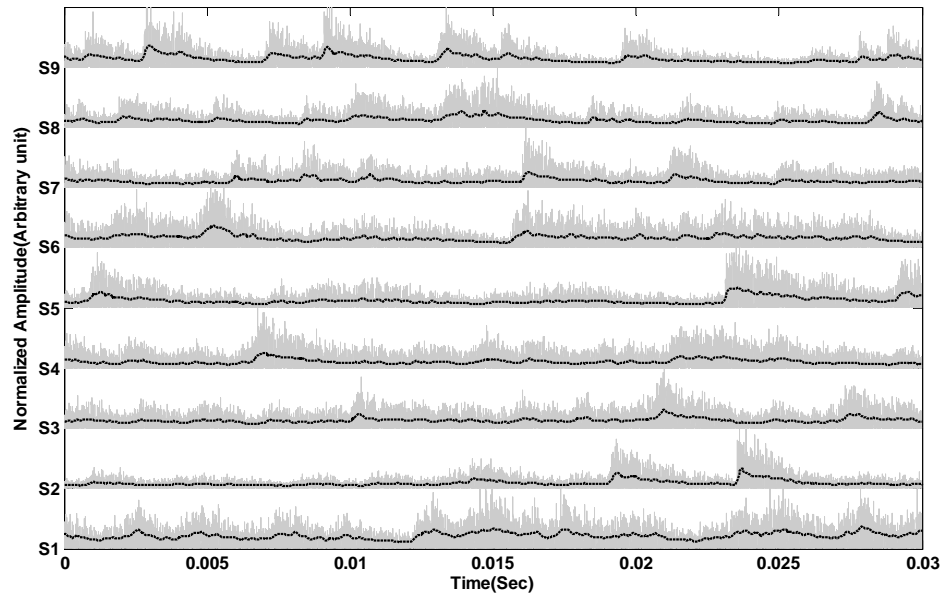
Figure 6.1: Typical Micro-80D AE signatures (exhaust) for test with two damaged blades. Free power turbine speed increases from bottom to top, with S1 recorded at 95 RPS and S9 recorded at 325 RPS.
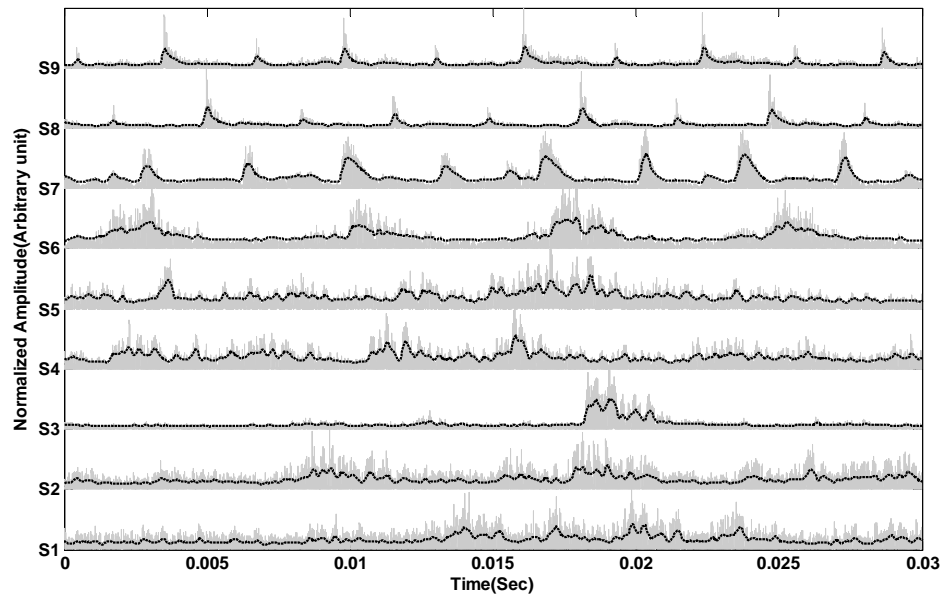
Figure 6.2: Typical S9215 AE signatures (shroud) for test with two damaged blades. Free power turbine speed increases from bottom to top, with S1 recorded at 95 RPS and S9 recorded at 325 RPS.
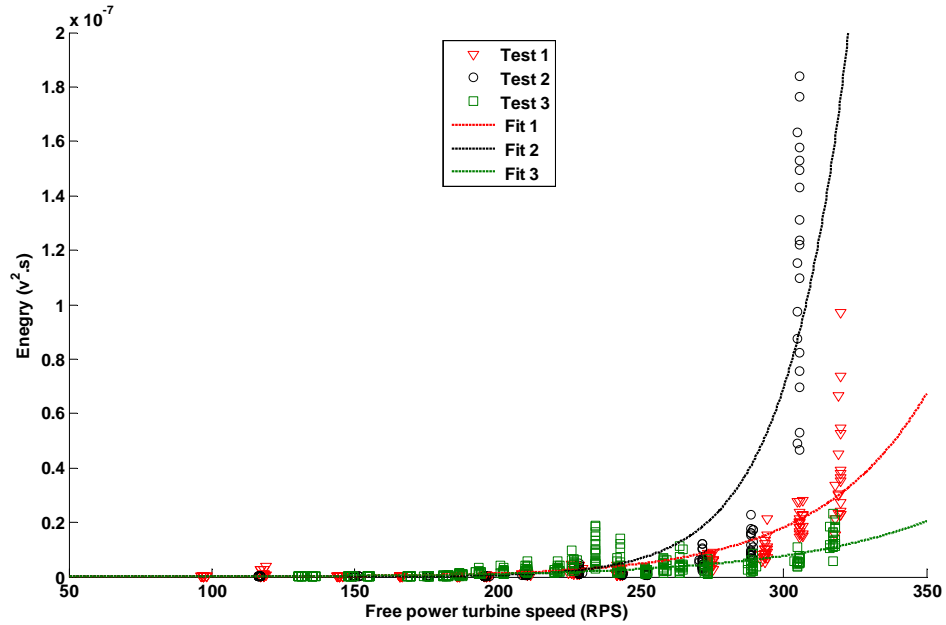
Figure 6.3: Micro-80D (exhaust) sensor AE energy *vs*. free power turbine speed for test with two damaged blades.

Figure 6.3 shows the AE energy evolution with speed for the exhaust-mounted sensor compared with the corresponding evolution for the normal running condition. The AE energy level is around a factor of 10 times higher for the damaged impeller. Furthermore, the exhaust-mounted sensor records a monotonic increase in AE energy with speed, although the highest speed points begin to show the characteristics of energy variability of the signal. Figure 6.4 shows energy recorded at the shroud-mounted sensor to be about 100 times higher than that of the equivalent normal running test.
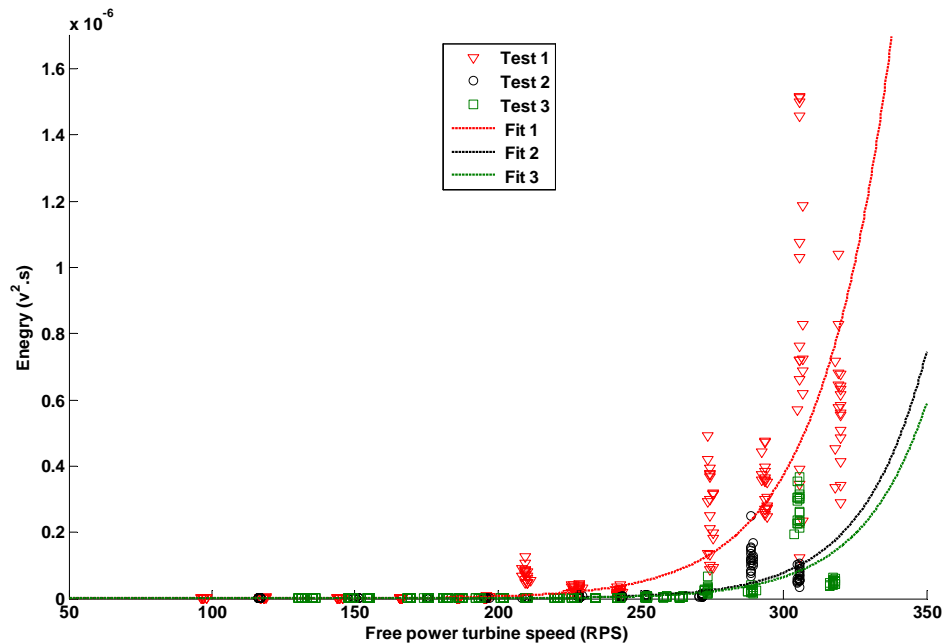
Figure 6.4: S9215 (shroud) sensor AE energy *vs*. free power turbine speed for test with two damaged blades.

Figure 6.5 shows raw AE spectra at nine different speeds for the impeller with two damaged blades. Figure 6.5 (a) shows no change in the raw AE spectrum with running speed for the exhaust-mounted sensor, not dissimilar to the situation for the normal running condition. Also, there is little apparent difference between the normal condition and condition with the defective impeller. For the shroud-mounted sensor, the main 30kHz activity reduces gradually in frequency as the speed increases, as is the case for the undamaged impeller (Figure 4.20). There is a distinct change in the raw AE spectrum at the two highest speeds, with some lower frequency (around 10-20kHz) activity appearing, and some activity at around 50kHz at some intermediate speeds. These secondary bands do not present in the normal running condition (Figure 4.20), although in neither case is there a clear pattern associated with these frequencies. It seems, therefore that the raw AE spectrum is not likely to be a strong indicator of impeller damage.
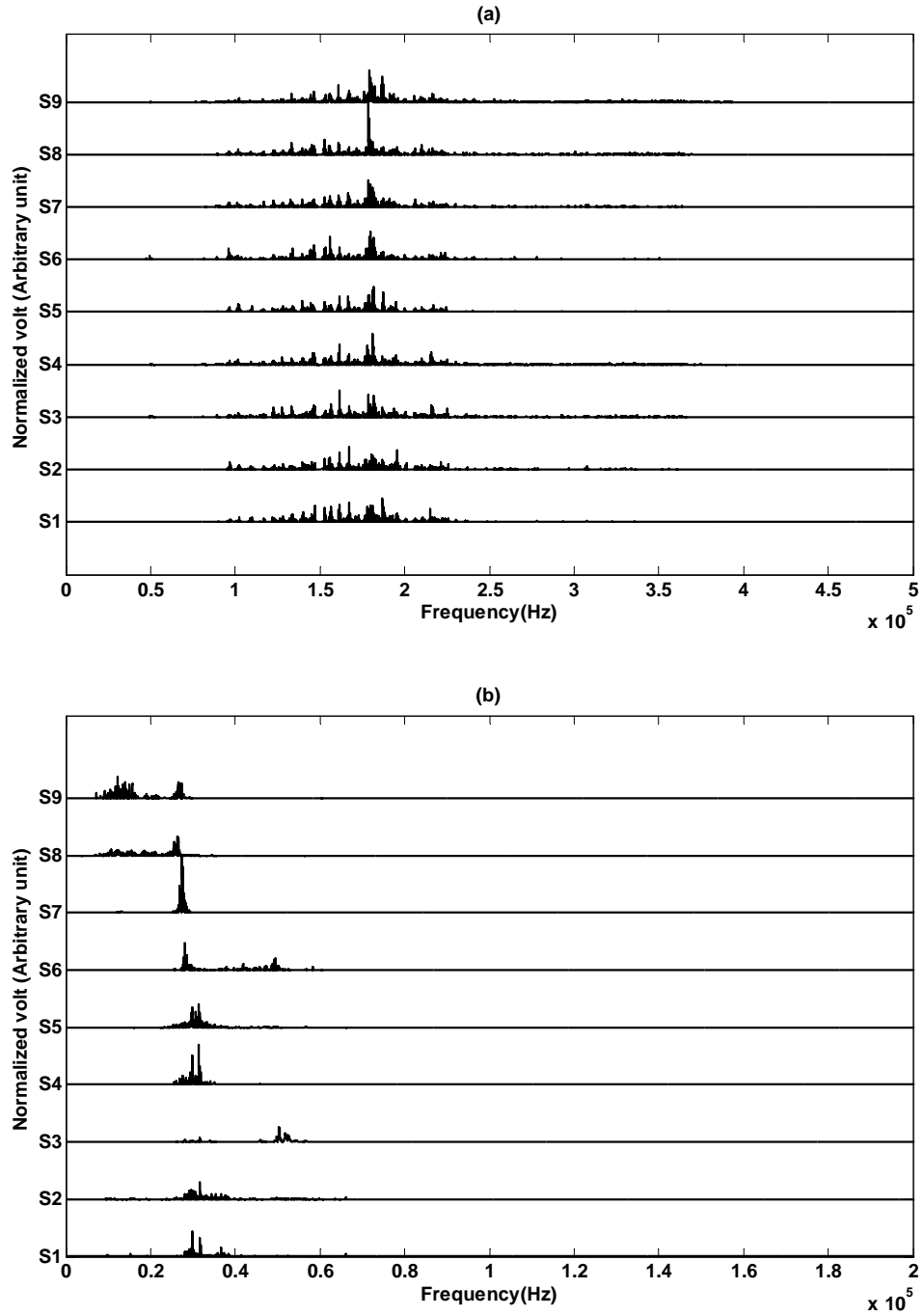
Figure 6.5: Typical raw AE spectra for test with two damaged blades: (a) Micro-80D sensor, (b) S9215 sensor. Free power turbine speed increases from bottom to top, with S1 recorded at 95 RPS and S9 recorded at 325 RPS.

Figure 6.6 shows the demodulated frequency analysis for the exhaust-mounted sensor, and these clearly lack the strong spectral peaks observed at low speed for the normal running condition (Figure 5.20). At higher speeds, however, spectral peaks at multiples of half the running speed begin to appear.
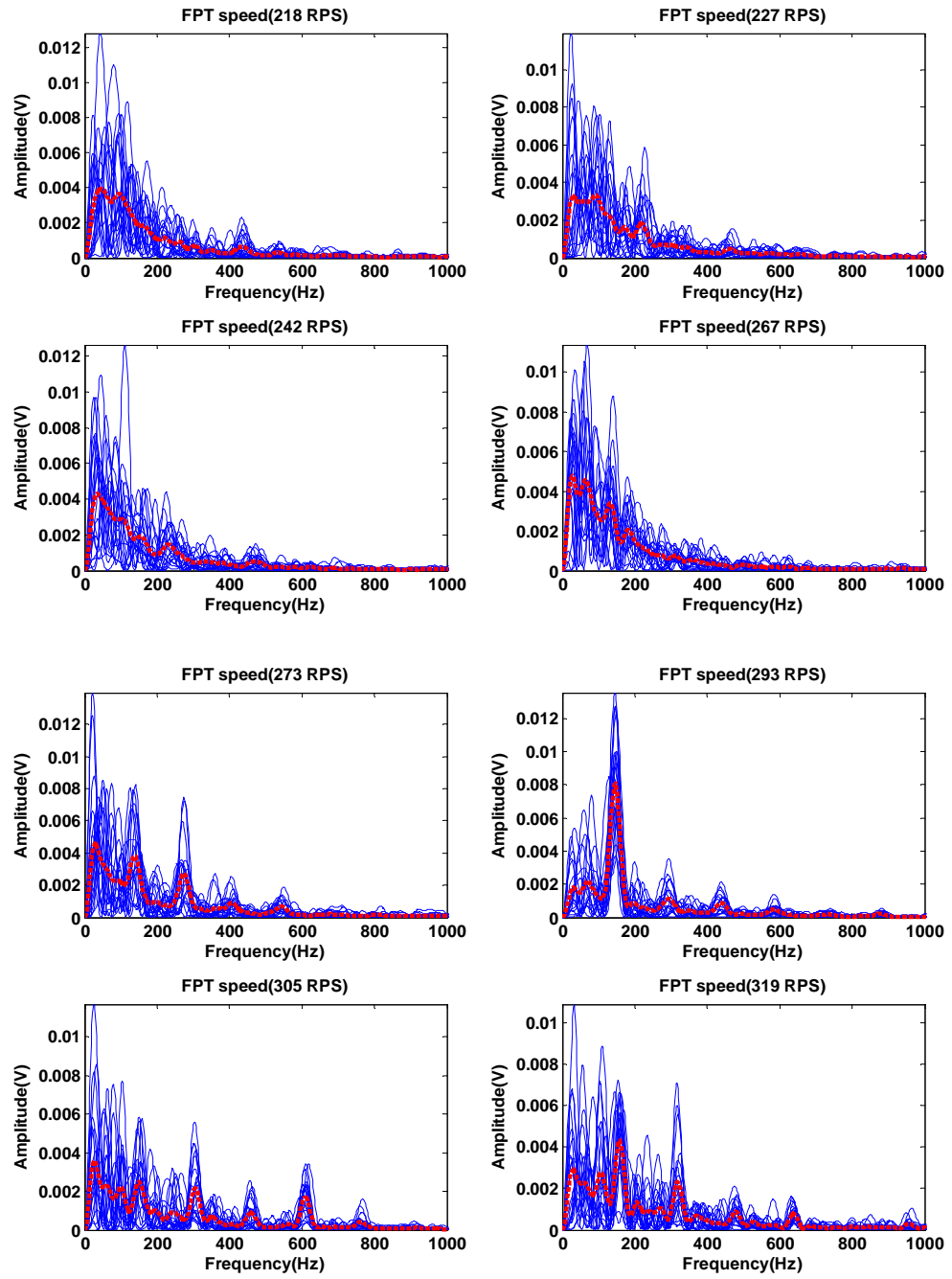
Figure 6.6: Demodulated spectra for test with two damaged blades with Micro-80D sensor at 8 different speeds of FPT.
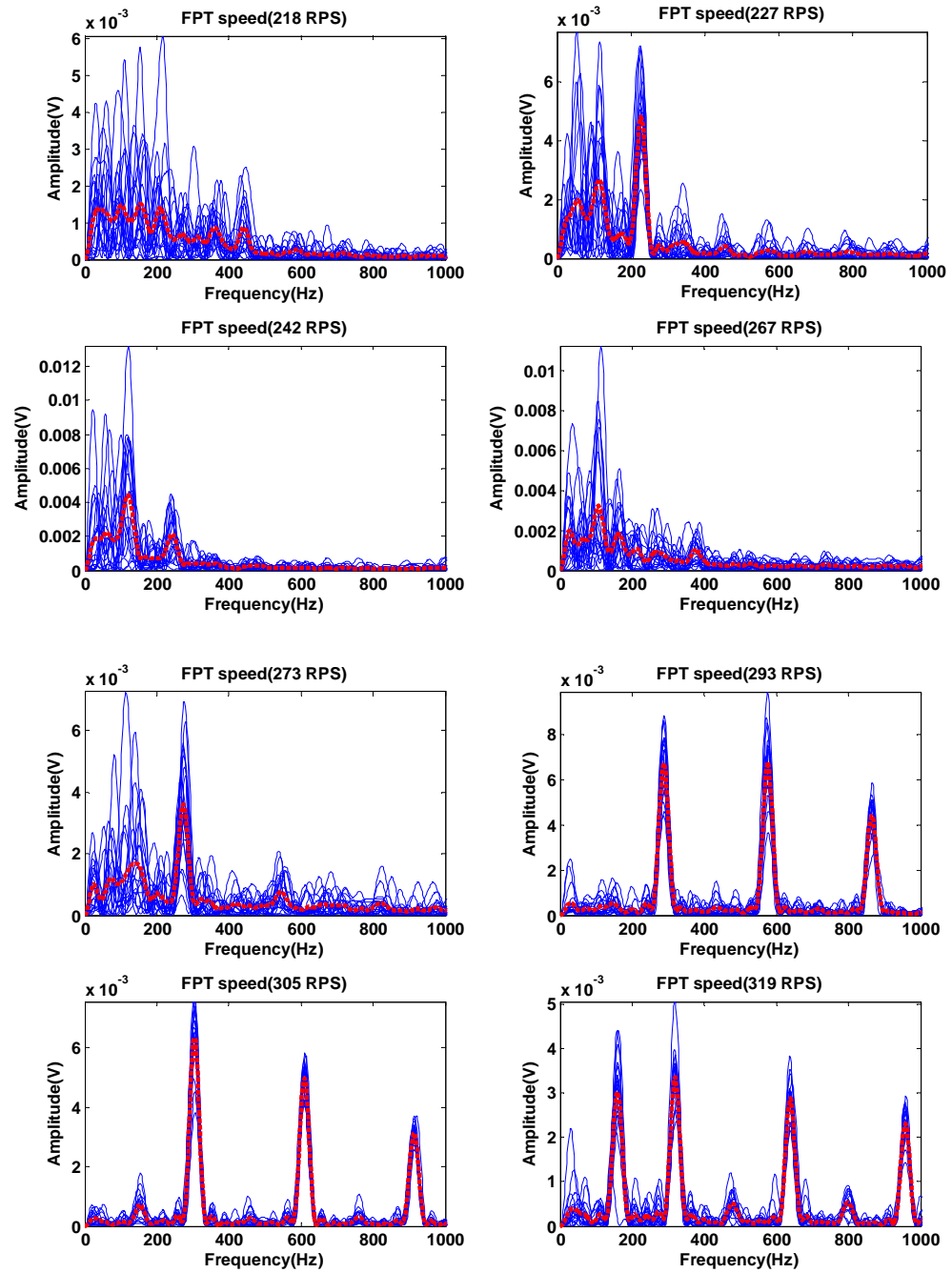
Figure 6.7 : Demodulated spectra for test with two damaged blades with S9215 sensor at 8 different speeds of FPT.

Figure 6.7 shows the demodulated frequency analysis of the shroud-mounted sensor. As for the normal running condition (Figure 5.21), strong spectral peaks are present at the running speed in many instances but, unlike the normal condition, very strong harmonics of the running speed are present and, in some cases, harmonics at half the running speeds are displayed.

6.2. Results of tests with four damaged blades

Figures 6.8, 9, 10 and 11 to 6.13 show a summary of the energy and demodulated frequency analyses for the test with four damaged blades and can be compared directly with Figures 6.3, 6.4, 6.5 and 6.7.
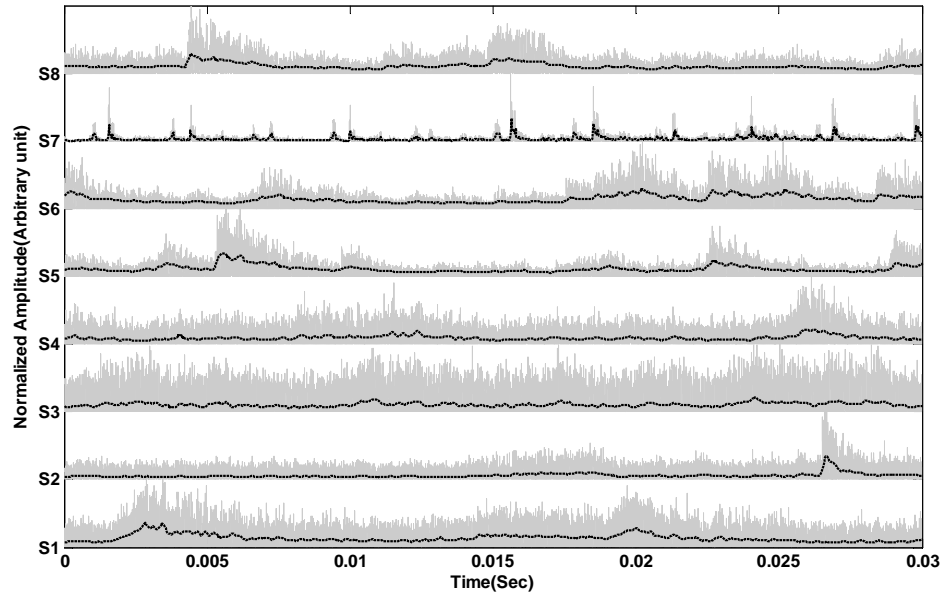
Figure 6.8: Typical Micro-80D AE signatures (exhaust) for test with four damaged blades. Free power turbine speed increases from bottom to top, with S1 recorded at 110 RPS and S8 recorded at 385 RPS.

Comparing figures 6.9 and 6.3 shows the AE energy recorded at the exhaust-mounted sensor to be about a factor of two less than that of the test with two damaged blades. The test with four damaged blades, however, shows variability in AE energy between 300 and 350 rps, which is absent in the test with two damaged blades. The shroud-mounted sensor, on the other hand (Figure 6.10) records a rather similar level and evolution of energy to the tests with two damaged blades (Figure 6.4).
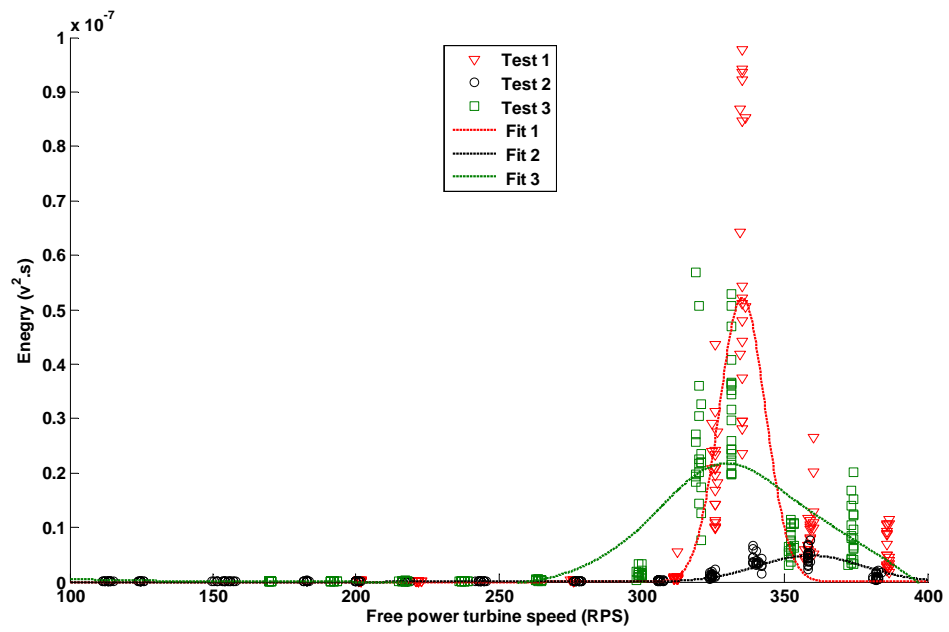
Figure 6.9: Micro-80D (exhaust) sensor AE energy *vs.* free power turbine speed for test with four damaged blades.
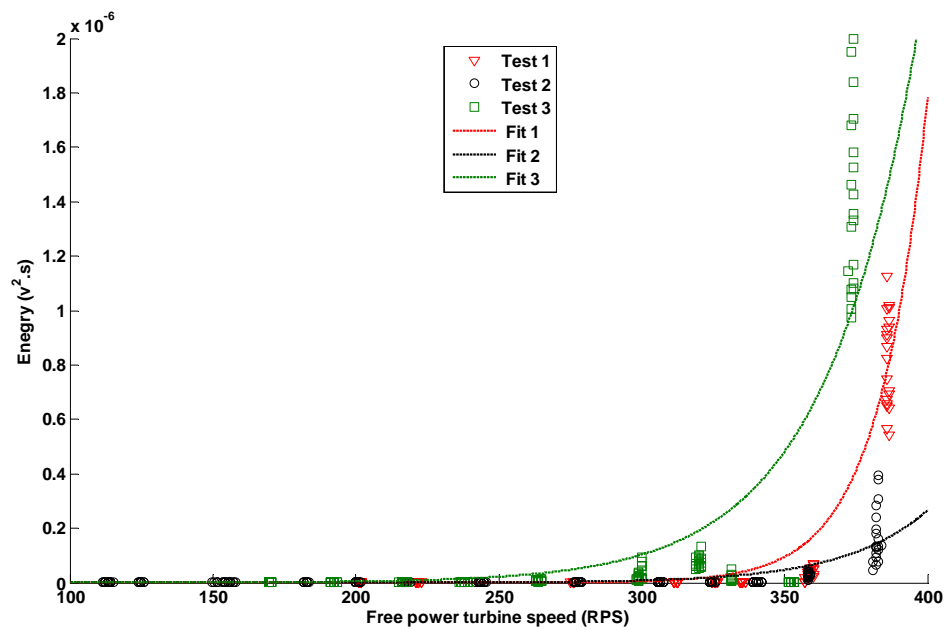
Figure 6.10: S9215 (shroud) sensor AE energy *vs.* free power turbine speed for test with four damaged blades.
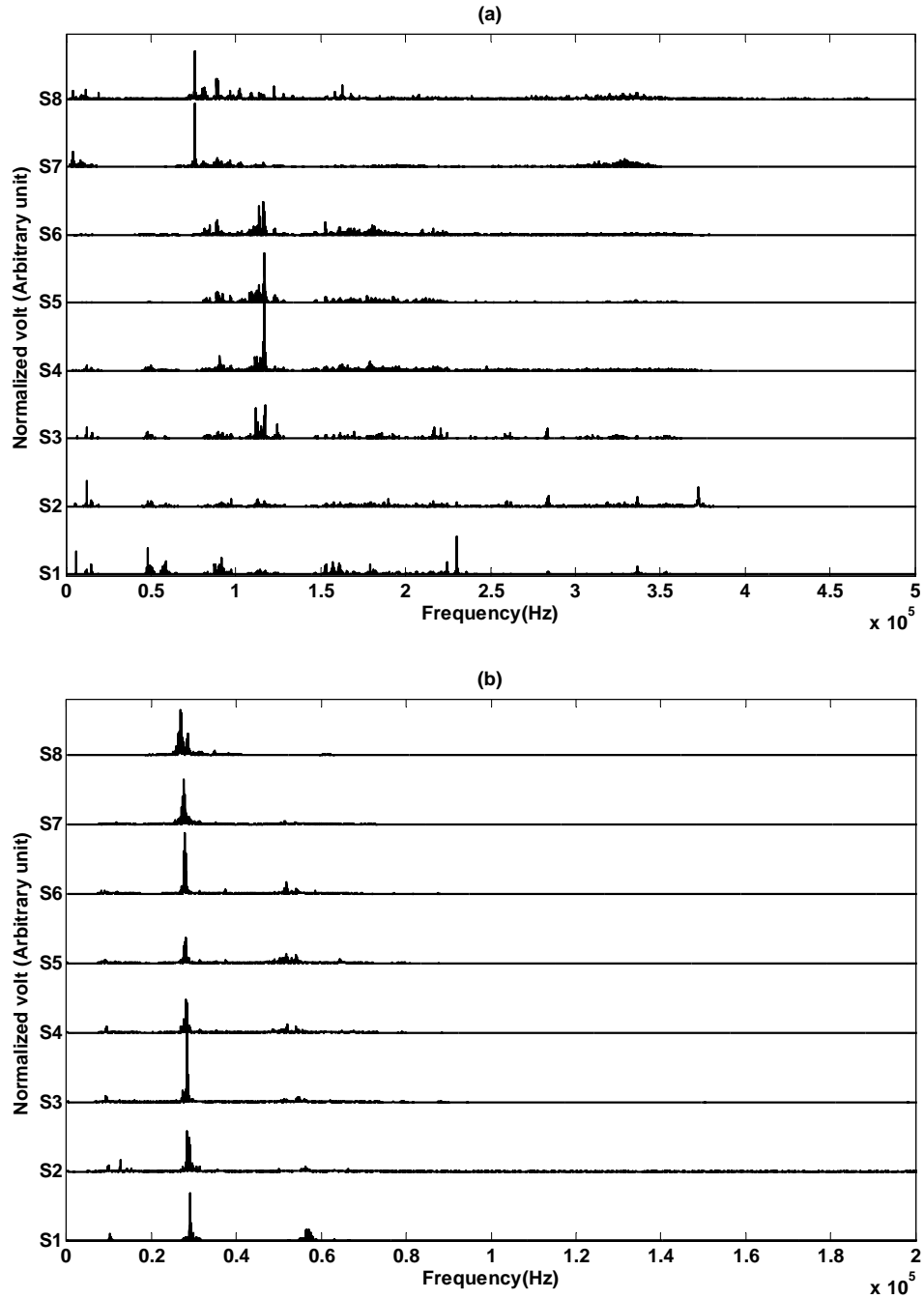
Figure 6.11: Typical raw AE spectra for test with four damaged blades: (a) Micro-80D sensor, (b) S9215 sensor. Free power turbine speed increases from bottom to top, with S1 recorded at 110 RPS and S8 recorded at 385 RPS.

Figure 6.12, like figure 6.6, exhibits a fairly broad demodulated frequency spectrum at most running speeds. The energy at 358 rps is associated with peaks at the running speed and at its harmonics, with odd harmonics (1, 3, 5) being significantly stronger than even ones. This is in contrast to the patterns recorded at higher speeds on the exhaust with the two damaged blades where the spectrum is considerably less sharp, and contains harmonics at half the running speed. The shroud-mounted sensor (Figure 6.13) shows a similar demodulated spectrum pattern to the exhaust-mounted sensor for

the four damaged blades (Figure 6.12) and again contrasts with the equivalent for the two damaged blades (Figure 6.7) in not exhibiting harmonics at half the running speed.
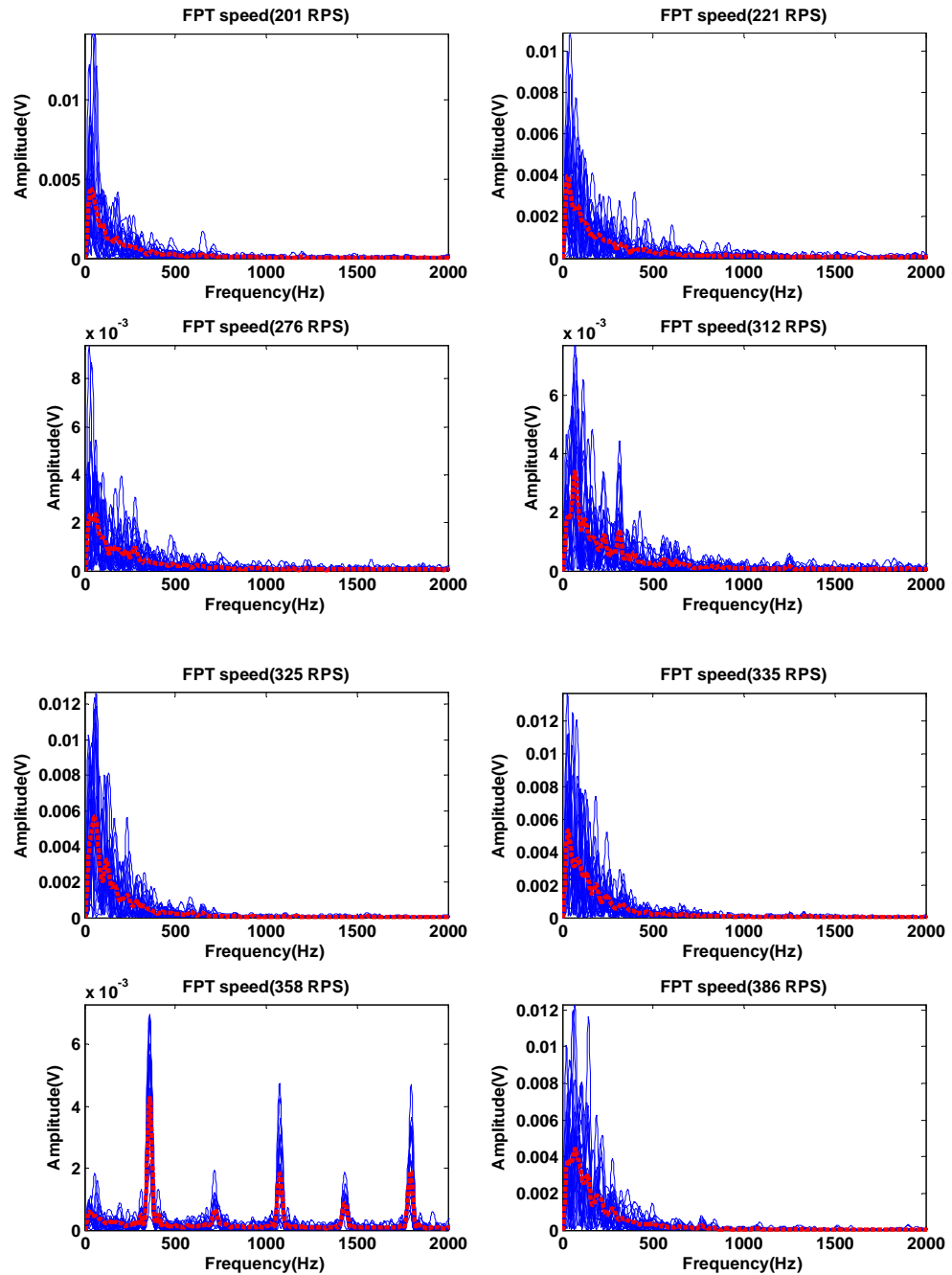
Figure 6.12: Demodulated spectra for test with four damaged blades with Micro-80D sensor at 8 different speeds of FPT.
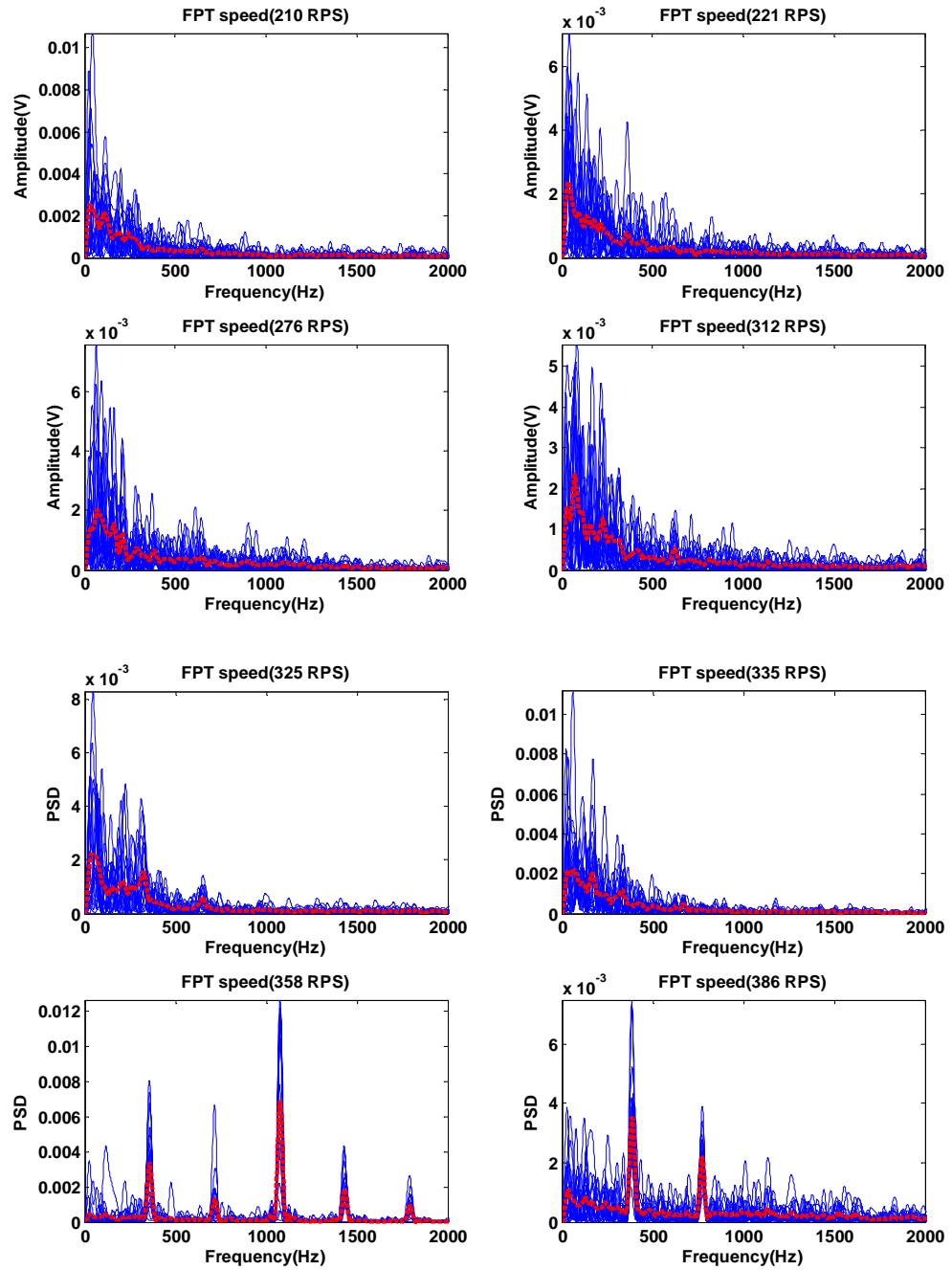
Figure 6.13: Demodulated spectra for test with four damaged blades with S9215 sensor at 8 different speeds of FPT.

6.3. Discussion of damaged impeller tests

The previous sections confirm that damaged blades produce characteristic AE patterns at some speeds, visible in the demodulated frequency domain. These patterns could form the basis of a diagnostic system involving running the turbine through a range of speeds to observe whether the pattern is excited. An example of such "tuning" can be seen in figure 6.7, where, as the turbine speed goes towards the maximum of 320rps, the spectral peaks pattern approaches its full expression. The corresponding effect occurs over a narrower range of about 350rps for the impeller with four damaged blades.

Figure 6.14 shows an AE signature recorded on the shroud during the test where the impeller has two damaged blades. The record has been chosen as one where the characteristic spectral peaks are excited and, as well as the raw signal, the RMS (averaging time of 0.03 ms) is shown along with the shaft encoder signal. As can be seen, the time series exhibits a series of pulses, one per cycle, and the intensity of these pulses alternates between cycles of the turbine. Figure 6.15 shows the corresponding demodulated frequency analysis which exhibits two harmonic series, one at the running speed and one at half the running speed. Such a pattern is typical of a train with two unequally-sized, but symmetrically distributed, pulses per cycle Thakkar *et al* [127] and the two-cycle repeat time of the pulse pair explains why a harmonic series at half the running speed occurs.
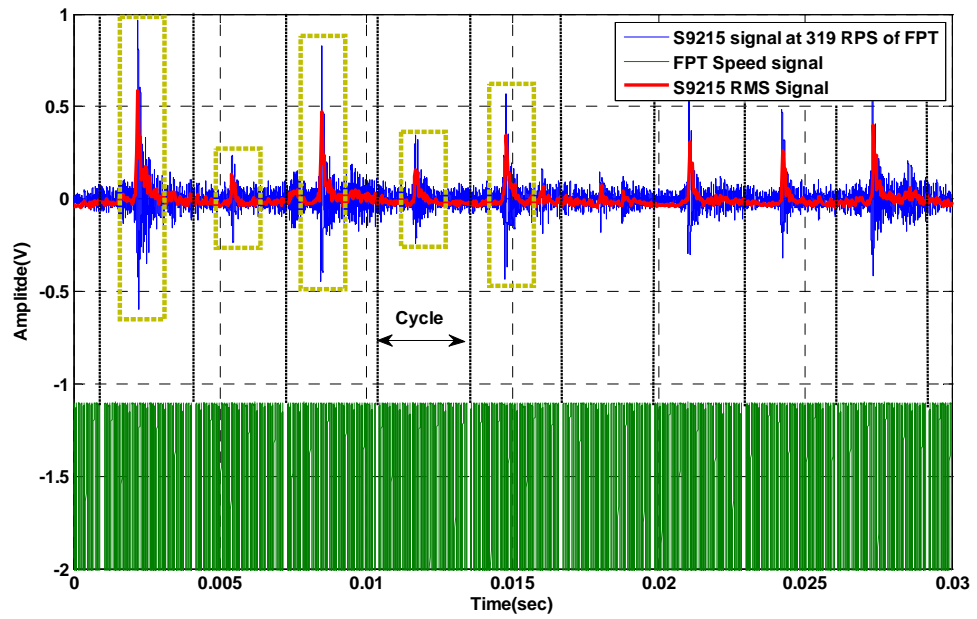
Figure 6. 14: AE signature recorded on shroud for test with two damaged blades.
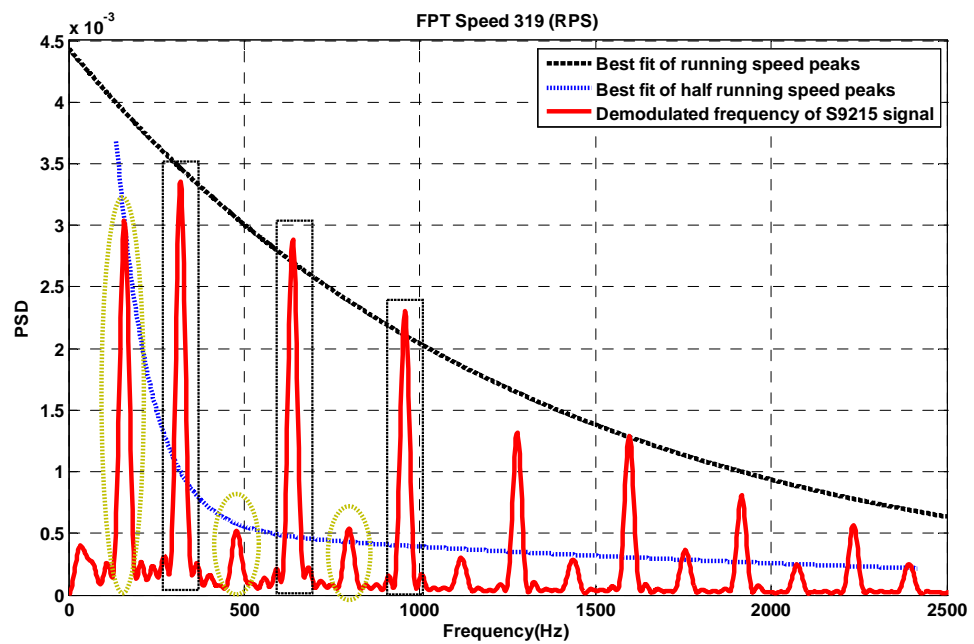
Figure 6.15: Demodulated frequency graph from shroud AE signature for test with two damaged blades.

Figure 6.16 shows the AE signature of the impeller with four damaged blades, again at a speed where the characteristic spectral peaks pattern is exhibited, but this time for the exhaust-mounted sensor. Like the signal with two damaged blades the signal is pulsatile, although this time there are two pulses per cycle and these are of approximately the same height within and between cycles. Furthermore, the pulses are unequally spaced. The pattern is also a little less clear than in figure 6.14. Figure 6.17 shows the corresponding demodulated frequency analysis with the dashed line tracing the heights of the harmonics of the running speed, which can be seen to be roughly sinusoidal in its shape. Again, such patterns are predictable Thakkar *et al* [127] and an appropriate spectral analysis can therefore yield information on the pulse distribution.
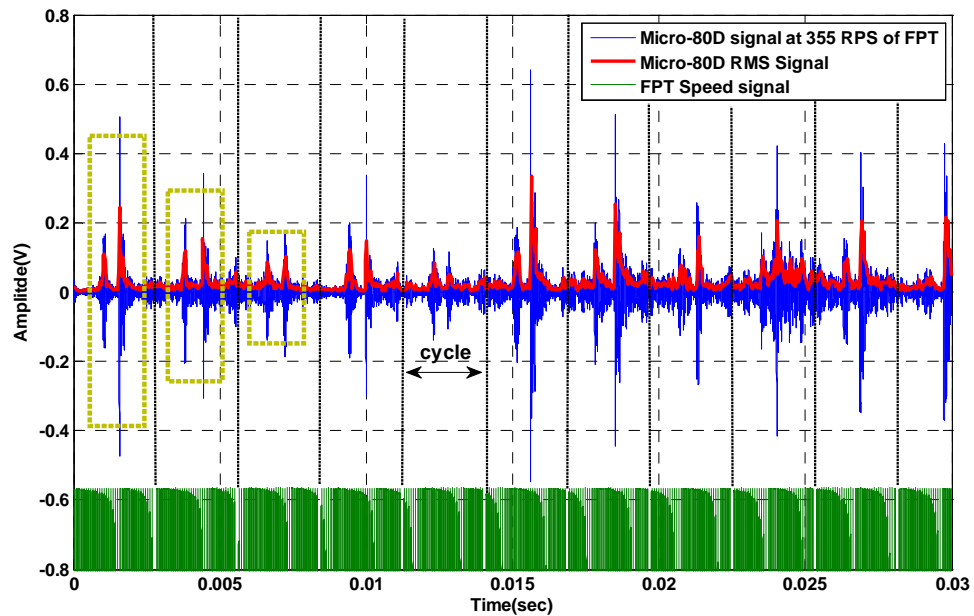
Figure 6.16: AE signature recorded on exhaust for test with four damaged blades.
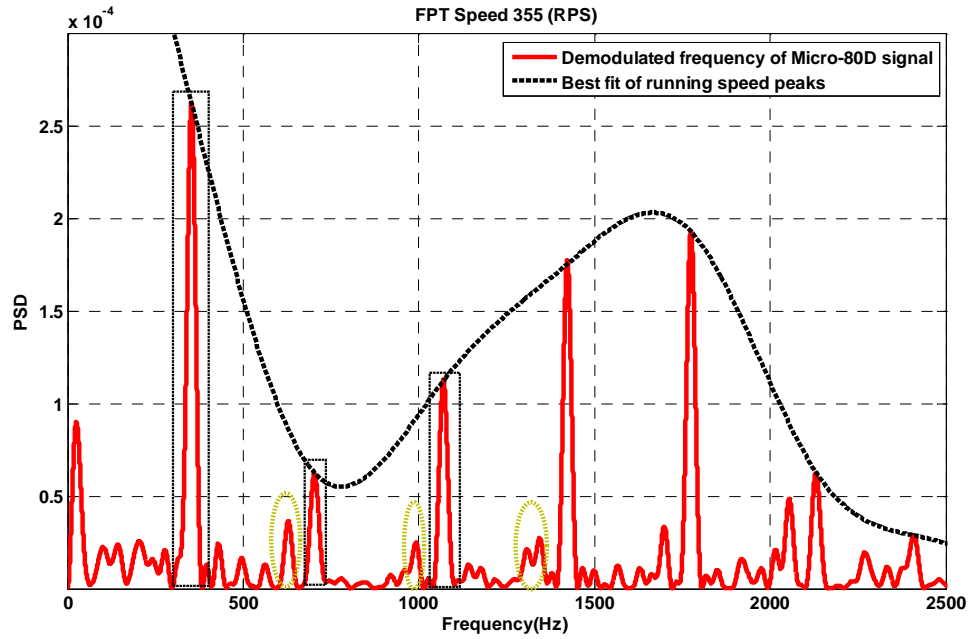
Figure 6.17: Demodulated frequency graph for exhaust AE signature for test with four damaged blades.

What remains to be understood is why the particular defects yield such characteristic patterns, but this is not a matter that can simply be resolved with the measurements that have been made here. A systematic study would require a range of defects of different sizes and distributions to be studied.

Chapter 7 Conclusion and future work

In this work three types of experiments have been conducted, AE propagation and calibration tests, AE monitoring of a healthy gas turbine under various operating conditions, and AE diagnosis of a gas turbine with simulated impeller faults. The AE propagation and calibration studies were essentially enabling tests to determine the characteristics of AE propagation on the experimental gas turbine although they have some generic value in assessing possible monitoring strategies for industrial scale machines. The most significant contributions come from the understanding of how AE is generated in gas turbines and how it might be used to monitor operating conditions and detect blade faults. The main conclusions of the research are listed below, followed by recommendations for future work.

7.1. Conclusions:

Sensor calibration:

1. The remounting and the repositioning of the AE sensors result in a variation in the recorded AE energy for a pencil lead break source in a range of 10-45% and, on a simple steel block, there is no other significant source of variation.
2. The turbine surface temperature affects the response of both AE sensors used; the S9215 sensor on the turbine shroud is more sensitive at higher temperatures, whereas the Micro-80D is less sensitive at higher temperatures.
3. Both of these findings have practical implications for sensor placement on industrial turbines and, importantly, indicate that trending using amplitude-based features will be difficult.

Propagation on gas turbine

1. In many parts of the machine, AE energy can be described as decaying exponentially with increasing source-sensor distance.
2. Structural details and complications such as geometrical boundaries, webs, and discontinuities have a considerable effect on the AE propagation causing a step change in transmitted AE energy, attributed to leakage and reflection.
3. The AE energy in a field close to the source position (up to 0.04 m) has a high variability due to the complex nature of near-field waves.

4. As expected, the shroud mounted sensor monitors AE emanating from the turbine impeller better than the exhaust mounted sensor and *vice versa*.

Configuration tests:

1. The experiments without an impeller and with the jammed impeller demonstrated a smooth evolution of AE energy with GGT speed. On the other hand the experiments with a rotating impeller with and without load exhibited complex AE energy against running speed and much higher levels of AE energy. Thus the rotation of the turbine impeller has a significant influence on the AE generated.

2. The general AE energy level increases with gas flow rate and with the complexity of flow in turbine shroud, being lowest when the impeller is absent and highest for the turbine running under load.

3. Whereas the AE energy level increases with turbine speed and can be curve-fit reasonably reproducibly, this does not, in itself, provide an explanation for the AE sources.

4. The AE records contain structural information such as pulses in the time series and information in the frequency domain, but the patterns with running speed are too complex to be elucidated by inspection.

Identification of operating condition in normal running.

1. Artificial neural networks can be used with time domain features to recognize the complex AE pattern associated with gas turbine running speed. Using eight time features the percentage of correct speed classification was 70-80%, and two of the time features, the RMS and the standard deviation of the raw AE gave performance at the 65-85% level on their own.

2. Artificial neural network performance using only demodulated frequency features was better than that of the time features alone, but the combination of frequency features and time features results in the best ANN recognition performance, up to 99%.

3. Using pulse-shape recognition features in combination with demodulated frequency features gave a performance of around 90%. Whereas this is not the

best performance, features of this type are not prone to shifts in calibration as they are not amplitude-dependent.

4. On the basis of the analysis, two types of AE source were recognized in the gas turbine. The first is a continuous background associated with gas flow through the turbine which increased in intensity with turbine speed. The second source is a pattern of spectral peaks emanating from different zones in the gas turbine and identified as gas reverberation in the exhaust, and feedback between the impeller and alternator.

Faulty impeller tests.

1. At specific ranges of running speed, the two kinds of damaged blades have clearly different AE signatures and could be distinguished from normal running in their general energy level and the pattern of spectral peaks in the demodulated signal.

2. The impeller with two damaged blades produced one pulse per revolution in the RMS record whose amplitude alternated between high and low in consecutive cycles. The impeller with four damaged blades produced two similar pulses per cycle.

3. Demodulated frequency analysis of the damaged impeller tests provided some insight into how the two defects might be detected in practice. The demodulated frequency domain of the impeller with two damaged blades contains two harmonic series, one with FPT speed as its fundamental, the harmonics decreasing smoothly with frequency. The other series has half of the running speed as its fundamental frequency with the amplitude of the harmonics decreasing sharply with frequency. The spectrum for four damaged blades contains harmonics of the FPT speed plus some other peaks. The amplitude of the FPT harmonics changed with frequency in a more complex (sinusoidal) way than with two damaged blades.

4. The demodulated spectra are as would be expected for the observed pulse trains, and so could potentially be used to identify the presence of particular pulse patterns in a running machine. The reasons for the particular pulse patterns are yet to be understood.

7.2. Future work:

Further work could usefully be done in the following directions.

1. Introducing a wider range of severity of blade damage to assess the detection threshold.

2. Studying the AE signature of other kinds and severity of blade damage to understand the cause of the pulses observed in the AE signal.

3. Developing zone location techniques more to identify the sources of AE and reject noise.

4. Application to industrial-scale turbines to assess the degree to which the findings of the work are generic.

References

1. Rao, B.K.N., *Handbook of condition monitoring* 1st ed. 1996: Elsevier Science.

2. Hunt, T.M., Evans, J. S., *Oil analysis handbook* 2008: Coxmoor Publishing Co.

3. Taylor, J.I., *The Vibration Analysis Handbook*. 2nd ed. 2003: VCI.

4. Li, Y.G., *Performance-analysis-based gas turbine diagnostics: a review*. Power and Energy, IMechE, 2002. **216**.

5. Hunt, T.M., *Handbook of wear debris analysis and particle detection in liquids* 1st ed. 1993: Springer.

6. Wowk, V., *Machinery vibration: measurement and analysis*. 1st ed. 1991: McGraw-Hill Professional.

7. Goldman, S., *Vibration Spectrum Analysis* 2nd ed. 1999: Industrial Press, Inc.

8. Reuben, R.L., *The role of acoustic emission in industrial condition monitoring*. International Journal of COMADEM, 1998. **1**(4): p. 35-46.

9. Morhain. A, M.D., *Bearing defect diagnosis and acoustic emission* Proceedings of IMech, Journal of Engineering Tribology, 2003. **217**(4).

10. Board, D., *Stress wave analysis of turbine engine faults.* IEEE Aerospace Conference Proceedings, 2000. **6**: p. 79-93.

11. Sato, I., *Rotating machinery diagnosis with acoustic emission techniques.* Electrical Engineering in Japan, 1990. **100**(2): p. 115-127.

12. Mba, D., Hall, L. D., *The transmission of acoustic emission across large scale turbine rotors.* NDT & E International, 2002. **35**(8): p. 529-539.

13. Neill, G.D., Benzie, S., Gill, J. D., Sandford, P. M., Brown, E. R., Steel, J. A., and Reuben, R. L. *"The relative merits of acoustic emission and acceleration monitoring for the detection of bearing defects"* in *Proceeding of the 11th International Conference on Condition Monitoring and Diagnostic Engineering Management, COMADEM, . (*1998. Australia.

14. Miller, R.K., and McIntire, P.,, *Nondestructive testing handbook, Acoustic emission testing*. 2 ed. Vol. 5. 1987: American Society for Nondestructive

15. Miller, R.K., Pollock, A. A., Watts, D. J., Carlyle, J. M., Tafuri, A. N., and and J.J. YezziJr, *A reference standard for the development of acoustic emission pipeline leak detection techniques.* NDT & E International, 1999. **32**(1): p. 1-8.

16. El-Ghamry, M.H., Reuben, R. L., and Steel, J. A., *The development of automated pattern recognition and statistical feature isolation techniques for the*

diagnosis of reciprocating machinery faults using acoustic emission. Mechanical Systems and Signal Processing, 2003. **17**(4): p. 805-823.

17. Neill, G.D., Reuben, R. L., Sandford, P. M., Brown, E. R., and Steel, J. A., *Detection of incipient cavitation in pumps using acoustic emission.* Proceedings of the Institution of Mechanical Engineers, Part E: Journal of Process Mechanical Engineering, 1997. **211**(4): p. 267-277.

18. Wilkinson, P., Reuben, R. L., Jones, J. D. C., Barton, J. S., Hand, D. P., Carolan,T. A., and Kidd, S. R., *Tool wear prediction from acoustic emission and surface characteristics via an artificial neural network.* Mechanical Systems and Signal Processing, 1999. **13**(6): p. 955-966.

19. Rogers, L., *Structural and engineering monitoring by acoustic emission methods -fundamentals and applications.* September 2001, Lloyd's Register Technical Investigations Department Report.

20. Lim, T., Niverangsan, P. Corney, J. R., Steel, J. A., and Reuben, R. L., *Predicting AE attenuation within solids by Geometric Analysis*, in *International conference on shape modeling and application SMI-05*. 2005: MIT, USA.

21. Gorman, M.R., *Plate wave acoustic emission.* Journal of the Acoustical Society of America, 1991. **90**(1): p. 358-364.

22. Pollock, A.A., *Classical wave theory in practical AE testing*, in *Progress in Acoustic Emission III - JAP Society of Non-Destructive Testing*. 1986.

23. Scruby, C.B., *An introduction to acoustic emission.* Instrument science and technology, 1987. **20**: p. 946-953.

24. Vallen, D.I.H., *AE Testing Fundamentals, Equipment, Applications*. 2002: Munich.

25. Matthews, J.R., *Acoustic Emission*. Vol. 2. 1983: Gordon and Breach, Science Publishers,Inc.

26. Scott, I.G., *Basic acoustic emission*. Vol. 6. 1991, New York: Gordon and Breach.

27. Holford, K.M., and Carter, D. C., *Acoustic emission source location.* Key Engineering Materials, 1999. **167**: p. 162-171.

28. Maji, K.A., Satpathi, D., and Kratochvil, T., *Acoustic emission source location using Lamb wave modes.* Journal of Engineering Mechanics, 1997. **123**(2): p. 154-161.

29.   Graham, L.J., and Alers, G. A, *Acoustic emission in the frequency domain.* Monitoring Integrity by Acoustic Emission, ASTM STP-571, American Society for Testing Materials, 1975: p. 11-39.

30.   Prosser, W.H., *Advanced AE techniques in composite material research.* Journal of Acoustic Emission,, 1996. **14**(3-4): p. 1-11.

31.   Shehadeh, M., Steel., J. A., and Reuben, R., L., *Acoustic emission source location for steel pipe and pipeline applications: the role of arrival time estimation.* Proceedings of the Institute of the Mechanical Engineers. Part E: Journal of Process and Mechanical Engineering, 2006. **220**(2): p. 121-133.

32.   Hsu, N.N., Simmons, J. A. and Hardy, S. C. , *An approach to acoustic emission signal analysis – theory and experiment.* Materials Evaluation, 1977. **35**(10): p. 100-106.

33.   Brown, E.R., Reuben, R. L., Neill, G. D. and Steel, J. A, *Acoustic emission source discrimination using a piezopolymer based sensor.* Materials Evaluation, 1998. **57**(5): p. 515-520.

34.   Vallen, H., *AE testing, fundamentals, equipment, applications [online], NDT.net*. 2002, 7(9, available at: http://www.ndt.net/article/az/ae_idx.htm).

35.   Hsu, N.N., and Breckenbridge, F. R, *Characterisation and calibration of acoustic emission sensors.* Materials Evaluation,, 1981. **39**(1): p. 60-68.

36.   Esward. T. J , T.P.D., Dowson. S. P and Preston. R. C, *An investigation into the establishment and assessment of a test facility for the calibration of acoustic emission sensors*. 2002, Centre for Mechanical and Acoustical Metrology, National Physical Laboratory.

37.   Kolsky, H., *Stress Wave in Solids*. 1963, New York, USA: Dover.

38.   Nivesrangsan, P., Steel, J. A. and Reuben, R. L, *AE mapping of engines for spatially located time series.* Mechanical Systems and Signal Processing, 2005. **19**(5): p. 1034-1054.

39.   Nivesrangsan, P., Steel, J. A. and Reuben, R. L, *Acoustic emission mapping of diesel engines for spatially located time series – Part II: Spatial reconstitution.* Mechanical Systems and Signal Processing, 2007. **21**(2): p. 084-1102.

40.   Cochran, W.T., Cooley, J. W., Favin, D. L., Helms, H. D., Kaenel, R. A., Lang, W. W., Maling, G. C., Nelson, D. E., Rader, C. M., and Welch, P. D., *What is Fast Fourier Transform.* IEEE Transactions on Audio and Electroacoustics, 1967. **15**(2): p. 45-55.

41. Welch, P.D., *The use of fast fourier transform for the estimation of power spectra: a method based on time averaging over short, modified periodograms.* IEEE Transactions Audio Electroacoustics, 1967. **AU-15**: p. 70-73.

42. Qian, S., Chen, D., *Joint Time Frequency Analysis: Methods and Application.* 1996, New Jersey, USA: Prentice-Hall.

43. Ding, Y., Reuben, R. L. and Steel, J. A, *A new method for waveform analysis for estimating AE wave arrival times using wavelet decomposition.* NDT&E International, 2004. **37**(4): p. 279-290.

44. Jeong, H., and Jang, Y. S., *Wavelet analysis of plate wave propagation in composite laminates.* Composite Structures, 2000. **49**(4): p. 443-450.

45. Peng, Z.K., Chu, F. L., , *Application of the wavelet transform in machine condition monitoring and fault diagnostics: a review with bibliography.* Mechanical Systems and Signal Processing, 2004. **18**(2): p. 199-221.

46. Rioul, O., and Vetterli, M.,, *Wavelets and signal processing.* IEEE Signal Processing Magazine, 1991. **8**(4): p. 14-38.

47. Mcfadden P. D, S.J.D., *Vibration monitoring of rolling element bearings by the high-frequency resonance technique. A review.* Tribology international 1984. **17**(1): p. 3-10.

48. Fukunaga, K., *Introduction to statistical pattern recognition* 2nd ed. 1990: Academic Press.

49. Jolliffe, I.T., *Principal component analysis.* 2nd ed. 2002 Springer Series ln Statistics.

50. Dunteman, G.H., *Principal components analysis.* 1989: Sage Publications, Inc.

51. Comon, P., *Independent component analysis-a new concept?* Signal Processing, 1994. **36**: p. 287-314.

52. Hyvarinen. A; Karhunen. J, a.O.E., *Independent Component Analysis.* 2001, New York: Wiley.

53. Tanaka, K., Niimura, T., *An Introduction to fuzzy Logic for practical applications* 1st ed. 1996: Springer.

54. Ross, T.J., *Fuzzy Logic with Engineering Application.* 1995, USA: McGraw-Hill, Inc.

55. Ganguli, R., *Data rectification and detection of trend shifts in jet engine gas path measurements using median filters and fuzzy logic*, in *ASME 2001-GT-0014, ASME TURBO EXPO 2001*. June 2001: New Orleans, Louisiana.

56. David, L., Doel, L.R., *Diagnostic expert systems for gas turbine engines - Status and prospects* in *Joint Propulsion Conference, 25th.* 1989, AIAA: Monterey, CA,.

57. Torella, G., *Expert systems and neural networks for fault isolation in gas turbines*, in *International Symposium on Air Breathing Engines, 13th.* 1997: Chattanooga, TN; UNITED STATES.

58. Hamilton, T.P., *HELIX: A helicopter diagnostic system based on qualitative physics.* Artif. Intell. Eng, 1988. **2**(2): p. 141–150.

59. Winston, H., Sirag, D., Hamilton, T., Smith, H., Simmons, D. and Ma, P, *Integrating numeric and symbolic processing for gas path maintenance.* AIAA, 1991. **91-0501**.

60. Doel, D.L., *The role for expert systems in commercial gas turbine engine monitoring*, in *The Gas Turbine and Aeroengine Congress and Exposition.* June 1990, ASME Paper 90-GT-374: Brussels, Belgium.

61. Meher-Homji, C.B., Boyce,M. P., Lakshminarasimha, A.N., Whitten, J. and Meher-Homji, F. J. , *Condition monitoring and diagnostic approaches for advanced gas turbines.* ASME COGEN-TURBO, September 1993. **IGTI 8**: p. 347–354.

62. R. Beale, T.J., *Neural Computing: An Introduction.* 1st ed. 1990: CRC Press; .

63. Romessis, A., Stamatis, A. and Mathioudakis, K., *A parametric investigation of the diagnostic ability of probabilisticneural networks on turbofan engines*, in *ASME 2001-GT-0011, ASME Turbo Expo 2001*: New Orleans, Louisiana.

64. Eustace, R., *Neural network fault diagnosis of a turbofan engine.* ISABE, 1993. **XI**.

65. Haykin, S., *Neural Networks: A Comprehensive Foundation.* 2nd ed. July 16, 1998: Prentice Hall.

66. Cichocki, A., Unbehauen, R., *Neural networks for optimization and signal processing* 1st ed. 1993: Wiley.

67. Bishop, C.M., *Neural networks for pattern recognition.* 1st ed. 1996: Oxford University Press, USA.

68. Hu, Y.H., Hwang, J. N. , *Handbook of neural network signal processing.* 1st ed. 2001: CRC Press.

69. Haykin, S., *Neural networks and learning machines.* 3 ed. 2008: Prentice Hall

70. BSI, *"Condition monitoring and diagnostics of machines - Vocabulary"*, in *British Standard.* 2004, BS ISO 13372:2004.

71. Urban, L.A., *Parameters selection for multiple fault diagnostics of gas turbine engines.* AGARD-CP- 165 ASME paper 74-GT-62, 1975: p. 225-230.

72. Mathioudakis. K, K.P., Stamatis. A, *Gas turbine component fault detection from a limited number of measurements.* Proceedings of the Institution of Mechanical Engineers, Part A: Journal of Power and Energy, 2004. **218**(8): p. 609-618.

73. Torella, G., Lombardo, G., *Neural Networks for the diagnostics of gas turbine engines.* ASME 96-TA-39, 1996: p. 1-11.

74. Patel, V.C., Kadirkamanathan, V., Kulikov, G. G., Arkov, V. Y. and Breikin, T. V. , *Gas turbine engine condition monitoring using statistical and neural network methods*, in *Colloquium-IEE*. September 1996: Leicester.

75. Hamstad, M.A., O'Gallagher, A., and Gary, J.,, *A wavelet transform applied to acoustic emission signals, Part 1: Source identification.* Journal of Acoustic Emission, 2002. **20**: p. 39-61.

76. Davies, A., *Handbook of condition monitoring - techniques and methodology.* 1st ed. 1997: Springer.

77. Choudhury. A, T.N., *Application of acoustic emission technique for the detection of defects in rolling element bearings.* Tribology International, 2000. **33**: p. 39-45.

78. Douglas, M., Beugné, S., Jenkins, M. D., Frances, A. K., Steel, J. A., Reuben, R. L, and Kew, P. A. *Monitoring of gas turbine operating parameters using acoustic emission* in *EWGAE, DGZfP-Proceedings BB 90-CD*. (2004.

79. Hall. L. D. and Mba. D, *Diagnosis of continuous rotor-stator rubbing in large scale turbine units using acoustic emissions.* Ultrasonics, 2004. **41**(9): p. 765-773.

80. Zuluaga-Giraldo. C.; Mba. D.; and Smart. M, *Acoustic emission during run-up and run-down of a power generation turbine.* Tribology International,, 2004. **37**(5): p. 415-422.

81. Leahy, M., Mba. D., Cooper. P., Montgomery. A., and Owen. D,, *Experimental investigation into the capabilities of acoustic emission for the detection of shaft-to-seal rubbing in large power generation turbines: a case study.* IMechE, Journal of Engineering Tribology, 2006. **220**: p. 607-615.

82. Armor, A.F., Graham, L. J., and Frank, R. L. , *Acoustic emission monitoring of steam turbine*, in *Power generation conference* 4-8 October , (1981: Missouri.

83. Wang. X. H; Zhu. C. M; Mao. H. L; Huang. Z. F, *Wavelet packet analysis for the propagation of acoustic emission signals across turbine runners.* NDT&E International, 2009. **42**: p. 42–46.

84. Rus, T., Dular, M., Širok, B, Hocvar, M., Kern. I, *An investigation of the relationship between acoustic emission, vibration, noise, and cavitation structures on a kaplan urbine.* ASME, Journal of fluid engineering, 2007. **129**: p. 1112-1121.

85. Gill, J.D., Reuben, R. L., and Steel, J. A. *A study of small HSDI diesel engine fuel injection equipment faults using acoustic emission.* in *Proceedings of the 24th European Conference on Acoustic Emission Testing, EWGAE.* 2000. France, pp. 281-286.

86. Gill, J.D., Reuben, R. L., Scaife, M., Brown, E. R., and Steel, J. A. *Detection of diesel engine faults using acoustic emission.* in *Proceedings of the 2nd International Conference: Planned Maintenance, Reliability & Quality.* 1998. pp. 57-61.

87. Shuster, M., Combs, D., Karrip, K., and Burke, D., *Piston ring cylinder liner scuffing phenomenon studies using acoustic emission technique.* Advances in Powertrain Tribology, SP-1548, SAE, 2000: p. 23-35.

88. Nivesrangsan, P., Steel, J. A. and Reuben, R. L. , *Source location of acoustic emission in diesel engines.* Mechanical systems and signal processing, 2007. **21**(2): p. 1103-1114.

89. Nivesrangsan, P., *Multi-source, multi-sensor approaches to diesel engine monitoring using acoustic emission. PhD thesis.* December 2004, Heriot-Watt University: Edinburgh, UK.

90. Douglas, M.R., *Monitoring of the piston ring-pack and cylinder liner interface in diesel engines through acoustic emission measurements, PhD. Thesis.* 2007, Heriot-Watt university: Edinburgh, UK.

91. Douglas, R.M., Hymers, D. A., Steel, J. A., and Reuben, R. L. *Source identification of piston ring and cylinder liner interaction using acoustic emission.* in *Proceeding of the 17th International Conference on Condition Monitoring and Diagnostic Engineering Management, COMADEM.* Cambridge, UK, 2004, pp. 305-314.

92. Stephen, O., Riti, S., *Advanced engine diagnostics using artificial neural networks.* Applied soft computing, 2003. **2**: p. 259–271.

93.	Fast, M., Assadi, M., Deb, S., *Development and multi-utility of an ANN model for an industrial gas turbine.* Applied Energy 2009. **86**: p. 9–17.

94.	Fast, M., Palme´ , T. , *Application of artificial neural networks to the condition monitoring and diagnosis of a combined heat and power plant.* Energy, 2009: p. 1-7.

95.	Mu, J., Rees, D., Liu, G.P, *Advanced controller design for aircraft gas turbine engines.* Control Engineering Practice 2005 **13**: p. 1001–1015.

96.	Kosel, T., Grabec, I., Muzic, P., *Location of acoustic emission sources generated by air flow.* Ultrasonics, 2000. **38**: p. 824–826.

97.	Cyrus, B., Homji, M., Bromley, A. *Gas turbine axial compressor fouling and washing.* in *proceedings of the thirty-third turbomachinery symposium.* 2004.

98.	Kurz, R., Brun, K., *Degradation in Gas Turbine Systems.* Transaction of the ASME, Januray 2001. **123**: p. 70- 77.

99.	Mann, B.S., *Particle erosion- anew concept of flow visualization and boundary layer investigation of machines at high reynolds number.* wear, 1998. **223**: p. 110-118.

100.	Metwally, M.T., Hamed, W. A, *Blade erosion in automotive gas turbine engine.* Journal of Engineering for Gas Turbine and Power,Transactions of the ASME, 1995. **117**: p. 213-219.

101.	Carter, T.J., *Common failures in gas turbine blades.* Engineerin Failure Analysis, July 2004. **12**: p. 237-247.

102.	Oakley, S.Y., Nowell, D. , *Prediction of the combined high- and low-cycle fatigue performance of gas turbine blades after foreign object damage.* International journal of fatigue, 2007. **29**(1): p. 69-80.

103.	Bhaumik, S.K., Sujata, M., Venkataswamy, M. A., Parameswara, M.A., *Failure of a low pressure turbine rotor blade of an aeroengine.* Engineerin Failure Analysis, 2006.

104.	Hou, j., Wicks, B.J., Antoniou, R.A. , *An investigation of fatigue failures of turbine blades in a gas turbine engine by mechanical analysis.* Engineering Failure Analysis, 2002. **9**: p. 201-211.

105.	Bhaumik, S.K., Bhaskaran, T. A., Rangaraju, R., Venkataswamy, M. A., Parameswara, M.A., Krishnan, R. V., *Failure of Turbine rotor blisk of an aircraft engine.* Engineerin Failure Analysis, 2002. **9**: p. 287-301.

106.   Mazur, Z., Luna-amirez, A., Juarez-Islas, J. A., Campos-Amezcua, A., *Failure analysis of a gas turbine blade made of Iconel 738LC alloy.* Engineerin Failure Analysis, 2005. **12**: p. 474-486.

107.   Eliaz, N., Shemesh, G., Latanision, R.M., *Hot corrosion in gas turbine components.* Engineering Failure Analysis, 2002. **9**: p. 31-43.

108.   Khajavi, M.R., Shariat, M. H., *Failure of first stage gas turbine blades.* Engineerin Failure Analysis, 2004. **11**: p. 589-597.

109.   Bentley, D.E., *Forced subratative speed dynamic action of rotating machinery.* ASME, 1974. **74**.

110.   YU, J.J., Goldman, P., Bentley, D. E., Muzynska, A., *Rotor/Seal experimental and analytical study on full annular rub.* Transactions of the ASME, April 2002. **124**.

111.   Mba, D., Cooke, A., Roby, D., and Hewitt, G., *Detection of shaft-seal rubbing in large-scale power generation turbines with acoustic emission. Case study* Proceedings of the Institution of Mechanical Engineers, Part A: Journal of Power and Energy, 2004. **218**(2): p. 71-81.

112.   Fa, Y.E., Gu, F., Ball, A., *Condition monitoring of rolling element bearings using advanced acoustic emission signal analysis technique.* COMADEM, 2004: p. 491-498.

113.   Jamaludin, N., Mba. D., *Monitoring extremely slow rolling element bearings: part I & part II.* NDT&E international, 2002. **35**(6): p. 349-358, 359-366.

114.   Li, C.J., Li, S. Y., *Acoustic emission analysis for bearing condition monitoring.* Wear, 1995. **185**: p. 67-74.

115.   Al-Ghamd, A.M., Mba, D, *A comparative experimental study on the use of acoustic emission and vibration analysis for bearing defect indentification and estimation of defect.* Mechanical systems and signal processing, 2006. **20**(7): p. 1537-1571

116.   Tandon, N., Choudhury, A., *A review of vibration and acoustic measurement method for the detection of defects in rolling element bearings.* Tribology, 1999. **32**: p. 469-480

117.   Mubarak, M.A., Leahy, M., Mba, D, *A fundamental study on the source location capabilities of acoustic emission for shaft-seal rubbing on large power generation turbine.* COMADEM, 2004: p. 589-597.

118. Physical, A., *Differential Acoustic Emission Sensors*. 2010, MISTRAS Group, Inc, available at: http://www.pacndt.com/index.aspx?go=products&focus=/sensors/differential.htm.

119. Physical, A., *High Temperature Sensors*. 2010, MISTRAS Group, Inc, available at: http://www.pacndt.com/index.aspx?go=products&focus=/sensors/high_temp.htm.

120. E976-99, A., *Standard guild for determining the reproducibility of acoustic emission sensor response.* annual book of ASTM standards, 1999. **3.03**: p. 395-404.

121. Higo, Y., and Inaba, H., *"The general problems of AE sensors," Acoustic Emission: Current Practice and Future Directions, ASTM STP 1077, Sachse, W., Roget, J. and Yamaguchi, K., Eds.*, in *American Society for Testing and Materials Evaluation*. (1991: Philadelphia, USA. p. 7-24.

122. Cussons, T.l., *P9005_8 – Cussons Technology – Two Shaft Gas Turbine*. (2004.

123. Dzenis, Y.A., and Qian, J., *Analysis of microdamage evolution histories in composites.* International Journal of Solids and Structures, 2001. **38**(10-13): p. 1831-1854.

124. Bialkowski, M.T., Pekdemir, T., Reuben, R. L., Brautsch, M., Towers, D. P. and Elsbett, G., *Preliminary approach towards a CDI system modification operating on neat rapeseed oil*, in *31st Intl. Scientific Conference on Internal Combustion Engines, KONES, 12(1-2), 14 p,* . 4-7 September (2005: Wroclaw, Poland.

125. Berjger, A. *An investigation of acoustic emission in fuel injection*. in *Proc. of 3rd European Conference of Young Research and Science Workers in Transport and Telecommunications, TRANSCOM,* . 29-30 June (1999. Žilina, Slovakia.

126. Miettinen, J., and Siekkinen, V., *Acoustic emission in monitoring sliding contact behaviour.* Wear, 1995. **Vol.181-183**(2): p. 897-900.

127. Thakkar, N.A., Steel, J. A.,Reuben, R. L. , *Railway wheel flat diagnosis using Acoustic Emission: A laboratory study.* Submitted for publication in. Proceedings of the Institution of Mechanical Engineers, Part F, Journal of Rail and Rapid Transit, 2010.

Appendix A: AE sensors calibration certificates

AE SENSOR CALIBRATION CERTIFICATE

PHYSICAL ACOUSTICS CORPORATION
A MISTRAS Holdings Company

Sensor Name:	MICRO-80D	Test Date: 5/31/00
Sensor S/N:	119	Tested By: C.P.
Comment:		

Max. Value (dB): -62.76
Peak Freq.(kHz): 937.50

PAC Certifies that this sensor meets all performance, environmental and physical standards established in applicable PAC specifications.
Calibration methodology based on ASTM standard E976- "Guide for Determining the Reproducibility of Acoustic Emission Sensor Response."

Sensitivity dB ref 1V/ubar

MHz